



Norwegian University of
Science and Technology

Modelling and Analysis of Floating Bridge Concepts Exposed to Environmental Loads and Ship Collision

Kristine Senderud

Marine Technology

Submission date: June 2018

Supervisor: Bernt Johan Leira, IMT

Norwegian University of Science and Technology
Department of Marine Technology

Master Thesis, Spring 2018
for
Master Student Kristine Senderud

Modeling and Analysis of Floating Bridge Concepts Exposed to Environmental Loads and Ship Collision

Modellering og analyse av flytebro utsatt for miljølaster og skipskollisjon

Long-span bridges with floating supports are relevant for crossing of very deep and wide fjords along the Norwegian Coast. In order to compute the static and dynamic response of these bridges, the joint properties of the whole hydro-elastic system needs to be accounted for.

The following subjects are to be addressed as part of this work:

- A review is to be made of existing marine bridges and future plans for such bridges. Similarities and differences between the different bridge types are to be highlighted.
- Loads acting on the floating bridge are described together with associated structural models. Methods for both static and dynamic response analysis are elaborated and relevant numerical algorithms are outlined.
- A simplified global model of a particular bridge is to be established in relation to a proper computer program selected in cooperation with the supervisor. The hydrodynamic and structural properties are to be determined. As a completely new feature, support of the bridge by jacket structures is to be considered.
- Static response analysis and eigenvalue calculations are to be performed for the global model with a corresponding analysis of the results.
- Dynamic response analyses for regular wave loading shall be performed.
- Dynamic time domain simulation of ship collision with the bridge using USFOS is to be carried out. The ship is to be represented by a nodal mass with a given initial velocity. A literature review related to ship collision analysis is also to be included.

The work scope may prove to be larger than initially anticipated. Subject to approval from the supervisor, topics may be deleted from the list above or reduced in extent.

In the thesis the candidate shall present his personal contribution to the resolution of problems within the scope of the thesis work. Theories and conclusions should be based on mathematical derivations and/or logic reasoning identifying the various steps in the deduction.

The candidate should utilise the existing possibilities for obtaining relevant literature.

The thesis should be organised in a rational manner to give a clear exposition of results, assessments, and conclusions. The text should be brief and to the point, with a clear language. Telegraphic language should be avoided. The thesis shall contain the following elements: A text defining the scope, preface, list of contents, summary, main body of thesis, conclusions with recommendations for further work, list of symbols and acronyms, references and (optional) appendices. All figures, tables and equations shall be numbered.

The supervisor may require that the candidate, in an early stage of the work, presents a written plan for the completion of the work. The original contribution of the candidate and material taken from other sources shall be clearly defined. Work from other sources shall be properly referenced using an acknowledged referencing system.

The thesis shall be submitted in electronic form:

- Signed by the candidate
- The text defining the scope included
- Drawings and/or computer prints which cannot be bound should be organised in a separate folder.

Supervisor: Professor Bernt J. Leira

Deadline: June 11th 2018

Trondheim, January 15th, 2018

Bernt J. Leira




Preface

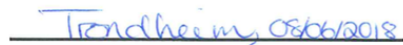
This Master's Thesis is the concluding work to the Master of Science (MSc) degree in Marine Technology at The Norwegian University of Science and Technology (NTNU). The degree specialization is in marine structures. As preliminary work for this thesis, a specialization project was performed by the author during fall 2017.

The thesis is carried out for the Norwegian Public Roads Administration (NPRA) supporting "The Ferry Free Coastal Route E39" project. The topic is modeling and analysis of floating bridge concepts supported by floating pontoons and a fixed offshore jacket for additional support and stiffness contribution. The floating bridge concepts are exposed to static and dynamic environmental loads using ANSYS Mechanical APDL 18.2. A ship collision scenario is analyzed in USFOS.

It is assumed that the reader is familiar with marine structural engineering and hydrodynamics.



Kristine Senderud



Trondheim, 08/06/2018

Acknowledgements

A special thank you is given to supervisor Professor Bernt Johan Leira (Department of Marine Technology) for your availability throughout the final semester and during the project thesis work. Your guidance and support along with close to weekly meetings has significantly contributed to the learning outcome and high motivation towards this Thesis.


Also, thank you to co-supervisors from the NPRA, Mathias Eidem and Bruno Villiora for your enthusiasm towards the concept study and providing useful information on short notice throughout the semester.

An additional thank you to Professor Jørgen Amdahl and Postdoctoral Fellow Yanyan Sha for great guidance on ship collision modelling.

I would also like to thank my fellow students at Marine Technology for contributing to a cherished working environment and valuable discussions throughout all five years of the Master's program.



Kristine Senderud



Trondheim, 08/06/2018

Abstract

The need for improving the infrastructure in Norway meets challenges when developing solutions to cross the wide and deep fjords along the coastline. The Norwegian Public Roads Administration (NPRA) is behind the ongoing project "The Ferry Free Coastal Route E39" where by replacing seven ferry crossings with floating bridges and submerged tunnels, today's travel- and transportation time between Kristiansand and Trondheim will be reduced from 21 to 11 hours. The fjords to be crossed are wide and deep with water depths up to 1300 meters. The project has faced major economic and technological challenges related to the solutions when advanced offshore technology and existing bridge solutions have been combined to establish concepts that satisfy the design criteria. This has lead to an increase in product cost from 150 to 340 billion NOK. The future project progress will depend on economic constraints and development of future technological solutions.

This thesis carries out a concept study of a floating bridge concept for crossing the Halsafjord along E39. The planned distance reaches 2.1 km from Halsneset to Urdneset. The concept is based on the proposed curved bridge for crossing the 4 km long Bjørnafjord. The thesis is carried out for the NPRA with the long term goal of reduced response at lower costs than presented for the Ferry Free Coastal Route E39 project up until today. Two concepts are analysed, where a curved bridge girder is supported by the undercarriage of offshore jackets, cable stay bridges and floating pontoons.

Concept 1, I-jacket: Curved bridge supported by one steel jacket placed 400 m from the east abudment. The span between the abudment and jacket is given additional support from cable stays. The remaining bridge girder is supported by nine floating pontoons.

Concept 2, II-jacket: Curved bridge supported by two steel jackets, each placed 400 m from the east and west abudments. The span between the jackets and the shoreline is given additional support from cable stays. The bridge girder between the jackets is supported by six floating pontoons.

The concepts are modeled in the finite element software ANSYS Mechanical APDL 18.2. Properties to represent global mass and stiffness properties of the jacket are obtained from analyses using the USFOS software and implemented in the ANSYS model.

Response from a static analysis during environmental loading conditions including wind, current and tidal variation is measured for both concepts. A regular wave analysis is performed on the II-jacket bridge for characteristic waves in the relevant area, as this concept indicated more careful considerations regarding dynamics. The static and regular wave analysis show that the response is within the design criteria limits, except for a small exceedance in vertical deflection during low tide, and a small exceedance for the acceleration component during wave conditions with a 1 year return period. Neither of the concepts exhibit critical response in terms of moments or stresses, but cyclic loading and fatigue should be assessed in further work. Considering the exceeded criteria and modeling approach, redesign and further work on hydrodynamics will be necessary.

A modal analysis shows that the first natural periods range from 82 seconds and lower (I-Jacket) and 54.5 seconds and lower (II-Jacket). Swell generated waves with 1, 100 and 10 000 year return periods overlap when the wave period is between 6 and 18 seconds for both concepts. For local wind generated sea, lower modes coincide. The first dynamic modes indicate that low frequency induced dynamic response will be important to assess as this indicates chance of resonant response.

A ship collision scenario is modeled in USFOS to measure the jackets response when exposed a collision with a RORO-vessel of similar mass and velocity as those that operate in the Halsafjord. The collision energy is 209 MJ. Results from the ship collision analysis indicate that jacket suffers severe damage, which may cause critical damage to the bridge. A full dynamic analysis of ship collision with a global bridge model must be performed to substantiate whether the bridge will survive or collapse in case of a collision.

The analyses performed in this thesis are insufficient to verify that the concept is feasible, but gives an indication of the global static and dynamic behaviour of the structure as well as highlighting of further work.

Sammendrag

Behovet for utvikling av infrastrukturen i Norge møter utfordringer når det blir nødvendig å krysse brede og dype fjorder. Dette gjelder spesielt langs kysten der fjorder i dag krysses med ferge. Statens Vegvesen står for tiden bak et stort prosjekt med navnet "Fergefri E39". Ved å erstatte syv fergeoverganger med flytebroer og undersjøiske tunneler vil dagens reise- og transporttid mellom Kristiansand og Trondheim kunne reduseres fra 21 til 11 timer. Fjordene som skal krysses er gjerne flere kilometer brede og med dybder ned til 1300 meter. Det er knyttet store økonomiske og teknologiske utfordringer til løsningene, når avansert offshoreteknologi og eksisterende broløsninger kombineres for å etablere konsepter som kan tilfredstille designkriteriene. Dette har ført til en økning i prosjektkostnader fra 150 til 340 milliarder kroner. Prosjektets fremgang vil sterkt påvirkes av økonomiske rammer og utvikling av fremtidige teknologiske løsninger.

Denne masteroppgaven er en konseptstudie som tar for seg et brokonsept for å krysse Halsafjorden langs E39. Oppgaven utføres for Statens Vegvesen. Den planlagte strekningen over Halsafjorden strekker seg 2.1 km fra Halsneset til Urdneset. Konseptstudien tar utgangspunkt i den tidligere foreslåtte krumme broen for krysningen av den 4 km lange Bjørnafjorden. Et langsiktig mål er å etablere et konsept som viser redusert respons i brokonstruksjonen og til et lavere kostnadsnivå enn konseptene som er lagt frem for Fergefri E39-prosjektet frem til i dag. To konsepter sammenliknes i denne oppgaven. Begge konseptene består av en buet brobane støttet av fagverksplattformer i stål, flytende pontonger og kabelbroer.

Konsept 1: Buet brobane støttet av en fagverksplattform bygget i stål plassert 400 m fra østlig landfeste. Brobanen mellom fagverksplattformen og østlig landfeste gir seilåpning og er konstruert som en kabelbro. Den gjenværende brokassen støttes av ni flytende pontonger.

Konsept 2: Buet brobane støttet av to fagverksplattformer bygget i stål, hver plassert 400 m fra østlig og vestlig landfeste. Brobanen mellom fagverksplattformene støttes av seks flytende pontonger. Dette gir to høybroer, hver konstruert som en kabelbro.

Konseptene er modellert ANSYS Mechanical APDL 18.2. Relevante parametere for fagverksplattformen er hentet fra analyser i programvaren USFOS og implementert i ANSYS-modellen.

Konstruksjonsrespons for begge konseptene er evaluert for last fra vind, strøm og tidevannsvariasjon. Dette måles i en statisk analyse. En regulærbølgeanalyse utføres på konsept 2 for karakteristiske bølger i det aktuelle området, ettersom resultatene indikerte at konsept 1 var i større grad dynamisk krevende enn konsept 1. Analysene viser at målt respons ligger innenfor regelverkets designkriterier, foruten vertikal nedbøyning på grunn av tidevann og vertikal akselerasjon som såvidt overstiger kriteriene. Disse overskridelsene indikerer at redesign og videre arbeid på parametere relatert til hydrodynamikk og blandt annet demping vil være nødvendig.

Broenes egenperioder spenner fra 82 sekunder og lavere (konsept 1), og 54.5 sekunder og lavere

(konsept 2). Bølger med 1-, 100- og 10 000 års returperioder overlapper lavere egenperioder i området 6-18 sekunder for begge konseptene. Dette indikerer muligheten for resonans og kan være en medvirkende årsak til at kriteriene for akselerasjon ble overskredet. For periodene til lokal vindgenerert sjø faller disse sammen med konstruksjonenes lavere perioder. De første dynamiske egenperiodene indikerer at respons fra lavfrekvente laster vil være viktig å evaluere i fremtidig arbeid.

Et skipskollisjonsscenario er modellert i USFOS for å måle fagverksplattformens respons når den utsettes for en kollisjon med et RORO-fartøy tilsvarende et av de operative fartøyene rundt Hal-safjorden. Kollisjonsenergien tilsvarer 209 MJ. Resultatene fra skipskollisjonsanalysen indikerer at plattformen får alvorlige skader, noe som kan forårsake kritisk skade på broen. En full dynamisk analyse av skipskollisjon med en global modell av broen må utføres for å underbygge om broen vil overleve eller kollapse ved kollisjon.

Analysene utført i oppgaven er ikke tilstrekkelig for å verifisere at konseptet er gjennomførbart, men gir en indikasjon på statisk og dynamisk respons samt en vurdering av viktige parametere og videre arbeid.

Table of Contents

Thesis Description	I
Preface	III
Acknowledgements	V
Abstract	VII
Sammendrag	IX
Table of Contents	X
List of Tables	XV
List of Figures	XVI
Dictionary	XXVII
1 Introduction	1
1.1 Motivation	1
1.2 Proposed Concepts	1
1.2.1 I-Jacket Concept	3
1.2.2 II-Jacket Concept	4
1.3 Literature	4
1.4 Thesis Structure	5
2 Industry Insight	7
2.1 Continuous and Separated Pontoon Bridges	8
2.2 Existing Designs of Floating Bridges	8
2.2.1 Evergreen Point Floating Bridge	8
2.2.2 Bergsøysund Floating Bridge	9
2.2.3 Nordhordaland Bridge	9
2.2.4 Solutions for Vessel Traffic	10
2.3 Future Plans for Floating Bridges	11
2.3.1 The Ferry Free Coastal Route E39	11
2.3.2 Suspension Bridge on Floating Foundations	12
2.3.3 Floating Bridge using TLP Technology	13
2.3.4 Submerged Floating Tunnel	14
First- and Second Order Wave Induced Dynamic Response	14
2.3.5 Social Impacts	15
2.3.6 Environmental Impacts	15

2.4	Jacket Structures	16
2.4.1	Structural Aspects	16
2.4.2	Market Analysis	17
2.4.3	Installation Procedures	18
2.4.4	Cost Engineering	19
2.5	Jacket Structures Subjected to Ship Impact	20
2.5.1	Research and Development	20
2.5.2	Standards and Recommended Practice	21
	Development of Regulations	21
3	Theory	23
3.1	Coordinate System and Rigid Body Motions	23
3.2	Beam Theory	24
3.2.1	Load Resistance Through Axial-, Shear Forces and Bending Moments	24
3.2.2	Curved Bridge Design: Arch Action	26
3.3	Mechanics of a Cable-Stayed Bridge	27
3.4	Jacket Structures	28
3.4.1	Global Forces	28
3.5	Hydrostatic Forces	29
3.5.1	Specific Gravity	29
3.5.2	Buoyancy	29
3.5.3	Stability	29
3.5.4	Loads from Current	30
3.6	Wave Theory	31
3.6.1	Regular Waves	31
3.6.2	Irregular Waves and Wave Spectra	31
3.6.3	Standardized Wave Spectra	33
3.7	Wave Forces	34
3.7.1	The Radiation and Diffraction Problem	34
3.7.2	Froude-Kriloff and Diffraction Forces	35
3.7.3	Drag and Inertia Forces On a Tubular Member	36
3.8	Static Response	37
3.9	Static Nonlinearity	37
3.10	Dynamic Response	38
3.10.1	Dynamic Behaviour and The Equation of Motion	38
3.10.2	Added Mass	39
3.10.3	Damping	39
3.10.4	Frequency Dependence of Added Mass and Damping	40
3.10.5	Restoring	40
3.10.6	Eigenfrequencies and Mode Shapes	40
3.11	The Finite Element Method	42
3.11.1	Method Outline	42
3.11.2	Method Outline for a Simple Beam Element	44
3.12	Ship Collision	46
3.12.1	General Considerations	46
3.12.2	Static vs. Dynamic Analysis	47
4	Design Loads and Permitted Response	49
4.1	Considerations on Weather Measurements	50
4.2	Tidal Variations	50

4.3	Static Wind Load	50
4.4	Current Load	51
4.5	Regular Wave Loads	52
4.6	Traffic and Pedestrian Loads (Eurocode)	53
4.7	Permitted Response	53
4.8	Ship Collision	54
4.8.1	Summary of Findings From Vessel Traffic and Collision Analysis	54
5	Applied Software	55
5.1	ANSYS Mechanical APDL	55
5.2	Matlab	55
5.3	USFOS	56
6	Model Formulation	57
6.1	Model development and geometry	57
6.2	ANSYS Elements and Load Types	58
6.2.1	Beam Element - BEAM189	58
6.2.2	Concentrated Mass Element - MASS21	59
6.2.3	Combination Spring Element - COMBIN14	59
6.3	Main Girder	60
6.4	Pontoons	62
6.4.1	Added Mass, Damping and Restoring	62
6.5	Cable Stays	63
6.6	Boundary Conditions	63
6.7	Jacket	64
6.8	Global Ship Collision Modeling in USFOS	65
7	Analysis Approach	67
7.1	ANSYS Analysis	67
7.1.1	Static Analysis	67
7.1.2	Modal Analysis	67
7.1.3	Regular Wave Analysis	68
7.1.4	APDL Command Flow Chart and File Description	68
7.2	USFOS Ship Collision Analysis	69
8	Analysis Results	71
8.1	Convergence Test	72
8.2	Static Response	73
8.2.1	Global Displacements	73
8.2.2	Global Rotations	75
8.2.3	Bending Moments and Shear Forces	77
8.2.4	Von Mises Stress	79
8.3	Effect of High Bridge Modeling	80
8.4	Eigenvalue Analysis	82
8.4.1	I-Jacket Concept	82
8.4.2	II-Jacket Concept	83
8.4.3	Evaluation of Coincidence With Wave Periods	85
8.5	Regular Wave Analysis	86
8.5.1	Global Displacements and Rotations	86
8.5.2	Global Accelerations	87
8.5.3	Global Bending Moments	88

8.5.4	Von Mises Stress	90
8.6	Ship Collision	91
9	Discussion and Further Work	93
10	Concluding Remarks	97
	Bibliography	98
	Appendix	103
A	Appendix	103
A.1	Literature Review	104
A.2	Pontoons: Hydrodynamic Parameters	105
A.2.1	Added Mass Parameters	105
A.2.2	Damping Parameters	105
A.3	Main Girder Cross Section Properties	106
A.4	Force-Displacement Results from USFOS	107
A.5	Static Results	108
A.6	I-Jacket: Static Results for the Highbridge Models - Additional Plots	109
A.7	Selfweight	110
A.8	Traffic Load	114
A.9	Wind (1 Year Return Period)	118
A.10	Wind and current (1 Year Return Period)	122
A.11	Wind and current (100 Year Return Period)	126
A.12	Low Tide	130
A.13	High Tide	134
A.14	Static Results for the Highbridge Models - Additional Plots	138
A.15	II-Jacket	138
A.16	Selfweight	138
A.17	Traffic Load	142
A.18	Wind (1 Year Return Period)	146
A.19	Wind and current (1 Year Return Period)	150
A.20	Wind and current (100 Year Return Period)	154
A.21	Low Tide	158
A.22	High Tide	162
A.23	Effect of Including High Bridge - Additional Plots	166
A.24	Modal Analysis	169
A.24.1	I-Jacket: Modeshape 11-30	169
A.24.2	II-Jacket: Modeshape 11-30	171
A.25	Coincidence with wave periods	172
A.25.1	Coincidence with wave periods for mode 1-30 (I-Jacket)	173
A.25.2	Coincidence with wave periods for mode 1-30 (II-Jacket)	174
A.26	Regular Wave Analysis: Additional Bending Moment Result Plots	175
Wave Period T = 5 s	175
Wave Period T = 6 s	176
A.27	Digital Appendix	178

List of Tables

2.1	Net Change in CO ₂ Emission associated with a Ferry Free E39 (Avinor, 2016) . . .	15
2.2	Jacket structures ranging from water depth 25 to 190 m installed in the UK and North Sea	17
2.3	Brief estimate of the cost related to fabrication and installation of the jacket (Visser, 1993)	19
4.1	Categorized loads for floating bridges (Watanabe and Utsunomiya, 2003)	49
4.2	Calculated static forces on the floating bridge, including current speed, direction and corresponding return periods for the Halsafjord	51
4.3	Values for estimated significant wave height (H_s) and peak period (T_p) for the Halsafjord, used in previous face of the Halsafjorden bridge development project (NPRA).	52
4.4	Traffic and pedestrian loads for associated bridge model (Statens Vegvesen, 2015) .	53
4.5	Permitted Response Parameters ($r\theta$)	54
6.1	Assigned element and load types types to the modeling sections and forces of the ANSYS model	58
6.2	Modeled plate thicknesses	60
6.3	Assigned Pontoon Parameters(Statens Vegvesen, 2015)	62
6.4	Applied Linear Spring Properties	63
6.5	Modeling parameters for the jacket configurations	64
7.1	Description of input APDL commands applied in the ANSYS APDL model	68
8.1	Time Step Convergence	72
8.2	Bending Moment and shear force results for I-jacket	77
8.3	Bending moment and shear force results for II-jacket	77
8.4	Eigenfrequencies for mode 1-10 (I-jacket)	82
8.5	Eigenfrequencies for mode 1-10 (II-jacket)	83
8.6	Maximum displacement and rotations and corresponding node location	86
8.7	Maximum accelerations from regular wave analysis	88
8.8	Maximum positive and negative bending moment results from the regular wave analysis	88
8.9	Maximum Von Mises stress from the regular wave analysis	90
8.10	Maximum displacement, velocity and acceleration and corresponding time of occurrence for node 10055	91
A.1	Frequency Dependent Added Mass for pontoons(Statens Vegvesen, 2015)	105
A.2	Frequency Dependent Damping Parameters for pontoons(Statens Vegvesen, 2015) .	105
A.3	Additional main girder cross section properties	106

A.4	Displacement, Rotation, Von Mises Stress, Bending Moments and Shear Force Results for I-jacket	108
A.5	Displacement, Rotation, Von Mises Stress, Bending Moments and Shear Force Results for II-jacket	108

List of Figures

1.1	Location of the Halsafjord along E39 (Google Maps)	2
1.2	Close-Up of the planned location for the bridge. Figure includes topography in the relevant area.	2
1.3	Concept of inspiration - the floating bridge solution for crossing the Bjørnafjord	2
1.4	Sketch of the II-Jacket concept proposed for crossing the Halsafjord	3
1.5	USFOS Model of the Kvitebjørn jacket with removed topside and riser/drilling equipment (USFOS Software)	3
1.6	Sketch of the II-Jacket concept proposed for crossing the Halsafjord	4
2.1	Evergreen Point Bridge, Washington State (Marshall, 2016)	8
2.2	Bergøysund Bridge, Møre and Romsdal, Norway (NTNU, 2017)	9
2.3	Nordhordaland Bridge, Hordaland, Norway (Bergensavisen, 2007)	9
2.4	"Bucket handle alternative" for crossing of the Sognefjord (NPRA, 2011)	10
2.5	Drawspan on Evergreen Point floating bridge, Washington, USA (Jembatan, 2013)	10
2.6	Coastal Highway E39 Route (NPRA, 2012b)	11
2.7	Concept drawing of suspension bridge on floating pontoons across the Sognefjord (Vegvesen, 2013)	12
2.8	Design proposal for the floating bridge proposes for the Sognefjord (Vegvesen, 2013)	12
2.9	Floating Bridge concept using TLP technology for crossing of Halsafjorden, Norway (NPRA, 2015a)	13
2.10	TLP platform (left), Horizontal motion of pontoon tower supported by TLP (right) (NPRA, 2015a)	13
2.11	Birdsview of SFT for Sognefjorden showing pontoon and ship channel location (NPRA, 2012a)	14
2.12	Side view of the SFT over the Sognefjord showing submerged pipe, pontoon and navigation channel (NPRA, 2012a)	14
2.13	Concept Sketch of a Steel Jacket (Amdahl, 2009)	16
2.14	Four stages of the lift and upending phase during installation of an offshore steel jacket (FGG, 2013)	18
2.15	Model of ship element and barrier for the analysis of the tension-leg bridge (Moe et al., 2017b)	20
3.1	Coordinate system for the floating bridge proposed for the Bjørnafjord crossing (rø)	23
3.2	Shear force (V) and bending moment (M) diagram for a fixed beam	25
3.3	(a) Illustration of arch with reaction forces and "C" representing concentric axial compression	
	(b) Effect of arch shape on stress distribution corresponding to 1-4 in (a).	26

3.4	(a) Illustration of arch with reaction forces and "C" representing concentric axial compression	
	(b) Effect of arch shape on stress distribution corresponding to 1-4 in (a).	27
3.5	Tension in the cables and compression in the tower of a cable-stayed bridge (Morrissey, 2000)	27
3.6	Simple model of linear varying wave loads acting on a jacket structure (right), global and reaction forces on a jacket structure (left) (Amdahl, 2009)	28
3.7	Global forces acting on a jacket structure with reacting axial and shear forces (Amdahl, 2009)	28
3.8	Stability parameters of a partially submerged body(White, 2008)	30
3.9	Principle sketch of a wave spectrum ($s\phi$)	32
3.10	The Radiation and Diffraction Problem (Faltinsen, 1993)	34
3.11	Rectangular barge exposed to incoming regular waves (Greco, 2012)	35
3.12	System of connected elastic springs (Ottosen, 1992)	42
3.13	Discretized system (Ottosen, 1992)	42
3.14	Discretized single element (Ottosen, 1992)	43
3.15	Strain energy distribution between ship and offshore installation for a fictive collision scenario (Det Norske Veritas, 2010)	46
3.16	Force-deformation curve between ship and jacket (Det Norske Veritas, 2010)	47
4.1	Pontoon force at $T = 5s$, Unit Amplitude = 1 m	52
4.2	Pontoon force at $T = 6s$, Unit Amplitude = 1 m	52
4.3	Eurocode LMV: Traffic Loading ($r\phi$).	53
6.1	I-jacket bridge with high bridge	57
6.2	II-jacket bridge with high bridge	57
6.3	Meshed ANSYS model of the I-Jacket bridge	58
6.4	ANSYS element BEAM189 (ANSYS, 2018)	58
6.5	ANSYS element MASS21 (ANSYS, 2018)	59
6.6	COMBIN14 Spring Element (ANSYS, 2018)	59
6.7	Cross section sketch of the main girder for the floating and strengthened sections	60
6.8	Custom ANSYS cross section ($r\phi$)	60
6.9	Distribution of floating, strengthened and high bridge section for the concept evaluated for the Bjørnafjorden curved bridge. The distribution is used as basis for the distribution in this model.	61
6.10	Pontoon Design	62
6.11	Modeling of pontoon column that connects the pontoon to the main girder	62
6.12	Spring and damper (heave and roll) attached to pontoon	63
6.13	Force-displacement relation analysis in USFOS performed on the KvitteBjørn Jacket	64
6.14	Impact Scenario (Birds View)	65
6.15	Modelling of non-linear springs in USFOS	65
7.1	Flowchart of static, modal and regular wave analysis scripts setup in ANSYS Mechanical	69
8.1	Maximum vertical displacement during mesh size reduction (section S1 and F1)	72
8.2	Variation in Von Mises stress as mesh size reduces from 20 to 0.01	72
8.3	Maximum x-component of displacement for both concepts with high bridge	73
8.4	Maximum z-component of displacement for both concepts with high bridge	73
8.5	Maximum y-component of displacement for both concepts with high bridge	74
8.6	Global y-component of displacement due to self weight (I-jacket concept)	74

8.7	Global y-component of displacement due to self weight (II-jacket concept)	74
8.8	Global y-component of displacement during low tide sea level (-1.0m). It is seen that the deflection of the neighbouring pontoon of the jacket exceeds the L/350 deflection criteria by 0.08 m	75
8.9	Global y-component of displacement due to low tide sea level (-1.0m). It is seen that the deflection of the neighbouring pontoons of the jackets exceeds the L/350 deflection criteria by 0.14 m	75
8.10	I-jacket: Maximum global x-component of rotation during wind and current with 100 year return period	76
8.11	Maximum and minimum global x-component of rotation for all load cases	76
8.12	Maximum and minimum global y-component of rotation for all load cases	76
8.13	Maximum and minimum global z-component of rotation for all load cases	76
8.14	Maximum and minimum global torsion moment M_x	78
8.15	Maximum and minimum global bending moment M_y	78
8.16	Maximum and minimum global bending moment M_z	78
8.17	Maximum and minimum global bending moment M_z for the I-jacket concept during low sea level (-1.0m)	78
8.18	Maximum Von Mises stress for all load cases	79
8.19	Von Mises stress for the II-jacket concept during high tide	79
8.20	Comparison of global rotations about the global y-axis for the I-jacket concept . .	80
8.21	Comparison of global rotations about the global y-axis for the II-jacket concept .	80
8.22	Global y-component of displacement during low tide sea level (-1.0m) for the I-jacket concept with the high bridge	81
8.23	Global y-component of displacement during low tide sea level (-1.0m) for the II-jacket concept with the high bridge	81
8.24	Comparison of global rotations about the global z-axis for the I-jacket concept . .	81
8.25	Comparison of global rotations about the global z-axis for the II-jacket concept .	81
8.26	Comparison of the Von Mises stress for the I-Jacket bridge, with and without the high bridge	81
8.27	Comparison of the Von Mises stress for the II-Jacket bridge, with and without the high bridge	81
8.28	Mode 1: Horizontal, T = 82.21 s	82
8.29	Mode 2: Horizontal, T = 45.86 s	82
8.30	Mode 3: Horizontal, T = 25.67 s	82
8.31	Mode 4: Horizontal, T = 20.67 s	82
8.32	Mode 5: Horizontal, T = 17.00 s	83
8.33	Mode 6: Horizontal, T = 12.81 s	83
8.34	Mode 7: Horizontal, T = 9.90 s	83
8.35	Mode 8: Horizontal, T = 8.03 s	83
8.36	Mode 9: Horizontal, T = 7.05 s	83
8.37	Mode 10: Vertical, T = 5.94 s	83
8.38	Mode 1: Horizontal, T = 54.55 s	84
8.39	Mode 2: Horizontal, T = 31.20 s	84
8.40	Mode 3: Horizontal, T = 24.02 s	84
8.41	Mode 4: Horizontal, T = 17.93 s	84
8.42	Mode 5: Horizontal, T = 12.62 s	84
8.43	Mode 6: Horizontal, T = 9.27 s	84
8.44	Mode 7: Vertical, T = 6.40 s	84
8.45	Mode 8: Vertical, T = 5.94 s	84
8.46	Mode 9: Vertical, T = 5.78 s	84

8.47	Mode 10: Vertical, $T = 5.58$ s	84
8.48	I-Jacket concept: Conditionally formatted values of the 10 first eigenperiods coinciding with wave periods with 1, 100 and 10 000 years return period from locally wind generated sea and swell.	85
8.49	II-jacket concept: Conditionally formatted values of the 10 first eigenperiods coinciding with wave periods with 1, 100 and 10 000 years return period from locally wind generated sea and swell.	85
8.50	Maximum x-component of displacement	86
8.51	Maximum y-component of displacement	86
8.52	Maximum z-component of displacement	86
8.53	Selected pontoons for vertical displacement in Figure 8.54	87
8.54	Vertical displacement over time for the three westmost pontoons	87
8.55	Maximum x-component of rotation	87
8.56	Maximum y-component of rotation	87
8.57	Maximum z-component of rotation	87
8.58	Maximum Global Bending Moment M_y for wave periods 5 and 6 seconds	89
8.59	Maximum Global Bending Moment M_x for wave periods 5 and 6 seconds	89
8.60	Maximum Global Bending Moment M_z for periods 5 and 6 seconds	89
8.61	Largest positive bending moment, M_x , at $T = 6$ s	89
8.62	Largest positive bending moment, M_y , at $T = 5$ s	89
8.63	Largest positive bending moment, M_z , at $T = 5$ s	90
8.64	Maximum Von Mises stress from time 20 to 40 seconds for wave period $T=5$ s and $T=6$ s	90
8.65	Global displacement when the impact load is activated after 10 seconds	91
8.66	Contour plot of maximum global displacements, occurring at 14.7 seconds.	91
8.67	Members with plastic utilization factor 1.0 at time 4.5 seconds after the impact.	92
A.1	Force and displacement analysis from USFOS	107
A.2	X-component of Displacement in the Bridge Girder due to Selfweight	110
A.3	Y-component of Displacement in the Bridge Girder due to Selfweight	110
A.4	Z-component of Displacement in the Bridge Girder due to Selfweight	110
A.5	X-component of Rotation in the Bridge Girder due to Selfweight	111
A.6	Y-component of Rotation in the Bridge Girder due to Selfweight	111
A.7	Z-component of Rotation in the Bridge Girder due to Selfweight	111
A.8	Global Bending Moment M_X in the Bridge Girder due to Selfweight	112
A.9	Global Bending Moment M_Y in the Bridge Girder due to Selfweight	112
A.10	Global Bending Moment M_Z in the Bridge Girder due to Selfweight	112
A.11	Global Shear Force V_y in the Bridge Girder due to Selfweight	113
A.12	Global Shear Force V_z in the Bridge Girder due to Selfweight	113
A.13	Global Von Mises Stress in the Bridge Girder due to Selfweight	113
A.14	X-component of Displacement in the Bridge Girder due to Traffic Load	114
A.15	Y-component of Displacement in the Bridge Girder due to Traffic Load	114
A.16	Z-component of Displacement in the Bridge Girder due to Traffic Load	114
A.17	X-component of Rotation in the Bridge Girder due to Traffic Load	115
A.18	Y-component of Rotation in the Bridge Girder due to Traffic Load	115
A.19	Z-component of Rotation in the Bridge Girder due to Traffic Load	115
A.20	Global Bending Moment M_X in the Bridge Girder due to Traffic Load	116
A.21	Global Bending Moment M_Y in the Bridge Girder due to Traffic Load	116
A.22	Global Bending Moment M_Z in the Bridge Girder due to Traffic Load	116
A.23	Global Shear Force V_y in the Bridge Girder due to Traffic Load	117

A.24	Global Shear Force V_z in the Bridge Girder due to Traffic Load	117
A.25	Global Von Mises Stress in the Bridge Girder due to Traffic Load	117
A.26	X-component of Displacement in the Bridge Girder due to Wind (1 Year Return Period)	118
A.27	Y-component of Displacement in the Bridge Girder due to Wind (1 Year Return Period)	118
A.28	Z-component of Displacement in the Bridge Girder due to Wind (1 Year Return Period)	118
A.29	X-component of Rotation in the Bridge Girder due to Wind (1 Year Return Period)	119
A.30	Y-component of Rotation in the Bridge Girder due to Wind (1 Year Return Period)	119
A.31	Z-component of Rotation in the Bridge Girder due to Wind (1 Year Return Period)	119
A.32	Global Bending Moment M_X in the Bridge Girder due to Wind (1 Year Return Period)	120
A.33	Global Bending Moment M_Y in the Bridge Girder due to Wind (1 Year Return Period)	120
A.34	Global Bending Moment M_Z in the Bridge Girder due to Wind (1 Year Return Period)	120
A.35	Global Shear Force V_y in the Bridge Girder due to Wind (1 Year Return Period)	121
A.36	Global Shear Force V_z in the Bridge Girder due to Wind (1 Year Return Period)	121
A.37	Global Von Mises Stress in the Bridge Girder due to Wind (1 Year Return Period)	121
A.38	X-component of Displacement in the Bridge Girder due to Wind and current (1 Year Return Period)	122
A.39	Y-component of Displacement in the Bridge Girder due to Wind and current (1 Year Return Period)	122
A.40	Z-component of Displacement in the Bridge Girder due to Wind and current (1 Year Return Period)	122
A.41	X-component of Rotation in the Bridge Girder due to Wind and current (1 Year Return Period)	123
A.42	Y-component of Rotation in the Bridge Girder due to Wind and current (1 Year Return Period)	123
A.43	Z-component of Rotation in the Bridge Girder due to Wind and current (1 Year Return Period)	123
A.44	Global Bending Moment M_X in the Bridge Girder due to Wind and current (1 Year Return Period)	124
A.45	Global Bending Moment M_Y in the Bridge Girder due to Wind and current (1 Year Return Period)	124
A.46	Global Bending Moment M_Z in the Bridge Girder due to Wind and current (1 Year Return Period)	124
A.47	Global Shear Force V_y in the Bridge Girder due to Wind and current (1 Year Return Period)	125
A.48	Global Shear Force V_z in the Bridge Girder due to Wind and current (1 Year Return Period)	125
A.49	X-component of Displacement in the Bridge Girder due to Wind and current (100 Year Return Period)	126
A.50	Y-component of Displacement in the Bridge Girder due to Wind and current (100 Year Return Period)	126
A.51	Z-component of Displacement in the Bridge Girder due to Wind and current (100 Year Return Period)	126
A.52	X-component of Rotation in the Bridge Girder due to Wind and current (100 Year Return Period)	127

A.53	Y-component of Rotation in the Bridge Girder due to Wind and current (100 Year Return Period)	127
A.54	Z-component of Rotation in the Bridge Girder due to Wind and current (100 Year Return Period)	127
A.55	Global Bending Moment M_X in the Bridge Girder due to Wind and current (100 Year Return Period)	128
A.56	Global Bending Moment M_Y in the Bridge Girder due to Wind and current (100 Year Return Period)	128
A.57	Global Bending Moment M_Z in the Bridge Girder due to Wind and current (100 Year Return Period)	128
A.58	Global Shear Force V_y in the Bridge Girder due to Wind and current (100 Year Return Period)	129
A.59	Global Shear Force V_z in the Bridge Girder due to Wind and current (100 Year Return Period)	129
A.60	Global Von Mises Stress in the Bridge Girder due to Wind and current (100 Year Return Period)	129
A.61	X-component of Displacement in the Bridge Girder due to Low Tide	130
A.62	Y-component of Displacement in the Bridge Girder due to Low Tide	130
A.63	Z-component of Displacement in the Bridge Girder due to Low Tide	130
A.64	X-component of Rotation in the Bridge Girder due to Low Tide	131
A.65	Y-component of Rotation in the Bridge Girder due to Low Tide	131
A.66	Z-component of Rotation in the Bridge Girder due to Low Tide	131
A.67	Global Bending Moment M_X in the Bridge Girder due to Low Tide	132
A.68	Global Bending Moment M_Y in the Bridge Girder due to Low Tide	132
A.69	Global Bending Moment M_Z in the Bridge Girder due to Low Tide	132
A.70	Global Shear Force V_y in the Bridge Girder due to Low Tide	133
A.71	Global Shear Force V_z in the Bridge Girder due to Low Tide	133
A.72	Global Von Mises Stress in the Bridge Girder due to Low Tide	133
A.73	X-component of Displacement in the Bridge Girder due to High Tide	134
A.74	Y-component of Displacement in the Bridge Girder due to High Tide	134
A.75	Z-component of Displacement in the Bridge Girder due to High Tide	134
A.76	X-component of Rotation in the Bridge Girder due to High Tide	135
A.77	Y-component of Rotation in the Bridge Girder due to High Tide	135
A.78	Z-component of Rotation in the Bridge Girder due to High Tide	135
A.79	Global Bending Moment M_X in the Bridge Girder due to High Tide	136
A.80	Global Bending Moment M_Y in the Bridge Girder due to High Tide	136
A.81	Global Bending Moment M_Z in the Bridge Girder due to High Tide	136
A.82	Global Shear Force V_y in the Bridge Girder due to High Tide	137
A.83	Global Shear Force V_z in the Bridge Girder due to High Tide	137
A.84	Global Von Mises Stress in the Bridge Girder due to High Tide	137
A.85	X-component of Displacement in the Bridge Girder due to Selfweight	138
A.86	Y-component of Displacement in the Bridge Girder due to Selfweight	138
A.87	Z-component of Displacement in the Bridge Girder due to Selfweight	138
A.88	X-component of Rotation in the Bridge Girder due to Selfweight	139
A.89	Y-component of Rotation in the Bridge Girder due to Selfweight	139
A.90	Z-component of Rotation in the Bridge Girder due to Selfweight	139
A.91	Global Bending Moment M_X in the Bridge Girder due to Selfweight	140
A.92	Global Bending Moment M_Y in the Bridge Girder due to Selfweight	140
A.93	Global Bending Moment M_Z in the Bridge Girder due to Selfweight	140
A.94	Global Shear Force V_y in the Bridge Girder due to Selfweight	141

A.95	Global Shear Force V_z in the Bridge Girder due to Selfweight	141
A.96	Global Von Mises Stress in the Bridge Girder due to Selfweight	141
A.97	X-component of Displacement in the Bridge Girder due to Traffic Load	142
A.98	Y-component of Displacement in the Bridge Girder due to Traffic Load	142
A.99	Z-component of Displacement in the Bridge Girder due to Traffic Load	142
A.100	X-component of Rotation in the Bridge Girder due to Traffic Load	143
A.101	Y-component of Rotation in the Bridge Girder due to Traffic Load	143
A.102	Z-component of Rotation in the Bridge Girder due to Traffic Load	143
A.103	Global Bending Moment M_X in the Bridge Girder due to Traffic Load	144
A.104	Global Bending Moment M_Y in the Bridge Girder due to Traffic Load	144
A.105	Global Bending Moment M_Z in the Bridge Girder due to Traffic Load	144
A.106	Global Shear Force V_y in the Bridge Girder due to Traffic Load	145
A.107	Global Shear Force V_z in the Bridge Girder due to Traffic Load	145
A.108	Global Von Mises Stress in the Bridge Girder due to Traffic Load	145
A.109	X-component of Displacement in the Bridge Girder due to Wind (1 Year Return Period)	146
A.110	Y-component of Displacement in the Bridge Girder due to Wind (1 Year Return Period)	146
A.111	Z-component of Displacement in the Bridge Girder due to Wind (1 Year Return Period)	146
A.112	X-component of Rotation in the Bridge Girder due to Wind (1 Year Return Period)	147
A.113	Y-component of Rotation in the Bridge Girder due to Wind (1 Year Return Period)	147
A.114	Z-component of Rotation in the Bridge Girder due to Wind (1 Year Return Period)	147
A.115	Global Bending Moment M_X in the Bridge Girder due to Wind (1 Year Return Period)	148
A.116	Global Bending Moment M_Y in the Bridge Girder due to Wind (1 Year Return Period)	148
A.117	Global Bending Moment M_Z in the Bridge Girder due to Wind (1 Year Return Period)	148
A.118	Global Shear Force V_y in the Bridge Girder due to Wind (1 Year Return Period)	149
A.119	Global Shear Force V_z in the Bridge Girder due to Wind (1 Year Return Period)	149
A.120	Global Von Mises Stress in the Bridge Girder due to Wind (1 Year Return Period)	149
A.121	X-component of Displacement in the Bridge Girder due to Wind and current (1 Year Return Period)	150
A.122	Y-component of Displacement in the Bridge Girder due to Wind and current (1 Year Return Period)	150
A.123	Z-component of Displacement in the Bridge Girder due to Wind and current (1 Year Return Period)	150
A.124	X-component of Rotation in the Bridge Girder due to Wind and current (1 Year Return Period)	151
A.125	Y-component of Rotation in the Bridge Girder due to Wind and current (1 Year Return Period)	151
A.126	Z-component of Rotation in the Bridge Girder due to Wind and current (1 Year Return Period)	151
A.127	Global Bending Moment M_X in the Bridge Girder due to Wind and current (1 Year Return Period)	152
A.128	Global Bending Moment M_Y in the Bridge Girder due to Wind and current (1 Year Return Period)	152
A.129	Global Bending Moment M_Z in the Bridge Girder due to Wind and current (1 Year Return Period)	152

A.130	Global Shear Force V_y in the Bridge Girder due to Wind and current (1 Year Return Period)	153
A.131	Global Shear Force V_z in the Bridge Girder due to Wind and current (1 Year Return Period)	153
A.132	Global Von Mises Stress in the Bridge Girder due to Wind and current (1 Year Return Period)	153
A.133	X-component of Displacement in the Bridge Girder due to Wind and current (100 Year Return Period)	154
A.134	Y-component of Displacement in the Bridge Girder due to Wind and current (100 Year Return Period)	154
A.135	Z-component of Displacement in the Bridge Girder due to Wind and current (100 Year Return Period)	154
A.136	X-component of Rotation in the Bridge Girder due to Wind and current (100 Year Return Period)	155
A.137	Y-component of Rotation in the Bridge Girder due to Wind and current (100 Year Return Period)	155
A.138	Z-component of Rotation in the Bridge Girder due to Wind and current (100 Year Return Period)	155
A.139	Global Bending Moment M_X in the Bridge Girder due to Wind and current (100 Year Return Period)	156
A.140	Global Bending Moment M_Y in the Bridge Girder due to Wind and current (100 Year Return Period)	156
A.141	Global Bending Moment M_Z in the Bridge Girder due to Wind and current (100 Year Return Period)	156
A.142	Global Shear Force V_y in the Bridge Girder due to Wind and current (100 Year Return Period)	157
A.143	Global Shear Force V_z in the Bridge Girder due to Wind and current (100 Year Return Period)	157
A.144	Global Von Mises Stress in the Bridge Girder due to Wind and current (100 Year Return Period)	157
A.145	X-component of Displacement in the Bridge Girder due to Low Tide	158
A.146	Y-component of Displacement in the Bridge Girder due to Low Tide	158
A.147	Z-component of Displacement in the Bridge Girder due to Low Tide	158
A.148	X-component of Rotation in the Bridge Girder due to Low Tide	159
A.149	Y-component of Rotation in the Bridge Girder due to Low Tide	159
A.150	Z-component of Rotation in the Bridge Girder due to Low Tide	159
A.151	Global Bending Moment M_X in the Bridge Girder due to Low Tide	160
A.152	Global Bending Moment M_Y in the Bridge Girder due to Low Tide	160
A.153	Global Bending Moment M_Z in the Bridge Girder due to Low Tide	160
A.154	Global Shear Force V_y in the Bridge Girder due to Low Tide	161
A.155	Global Shear Force V_z in the Bridge Girder due to Low Tide	161
A.156	Global Von Mises Stress in the Bridge Girder due to Low Tide	161
A.157	X-component of Displacement in the Bridge Girder due to High Tide	162
A.158	Y-component of Displacement in the Bridge Girder due to High Tide	162
A.159	Z-component of Displacement in the Bridge Girder due to High Tide	162
A.160	X-component of Rotation in the Bridge Girder due to High Tide	163
A.161	Y-component of Rotation in the Bridge Girder due to High Tide	163
A.162	Z-component of Rotation in the Bridge Girder due to High Tide	163
A.163	Global Bending Moment M_X in the Bridge Girder due to High Tide	164
A.164	Global Bending Moment M_Y in the Bridge Girder due to High Tide	164

A.165	Global Bending Moment M_Z in the Bridge Girder due to High Tide	164
A.166	Global Shear Force V_y in the Bridge Girder due to High Tide	165
A.167	Global Shear Force V_z in the Bridge Girder due to High Tide	165
A.168	Global Von Mises Stress in the Bridge Girder due to High Tide	165
A.169	Comparison of global rotations about the global x-axis for the I-jacket concept . .	166
A.170	Comparison of global rotations about the global x-axis for the II-jacket concept .	166
A.171	Comparison of global rotations about the global x-axis for the I-jacket concept . .	166
A.172	Comparison of global rotations about the global x-axis for the II-jacket concept .	166
A.173	Comparison of global rotations about the global y-axis for the I-jacket concept . .	166
A.174	Comparison of global rotations about the global y-axis for the II-jacket concept .	166
A.175	Comparison of global rotations about the global z-axis for the I-jacket concept . .	167
A.176	Comparison of global rotations about the global z-axis for the II-jacket concept .	167
A.177	Comparison of maximum and minimum global bending moment M_x for the II-jacket concept	167
A.178	Comparison of maximum and minimum global bending moment M_x for the II-jacket concept	167
A.179	Comparison of maximum and minimum global bending moment M_y for the I-jacket concept	167
A.180	Comparison of maximum and minimum global bending moment M_y for the II-jacket concept	167
A.181	Comparison of maximum and minimum global bending moment M_z for the I-jacket concept	168
A.182	Comparison of maximum and minimum global bending moment M_z for the II-jacket concept	168
A.183	Mode 11: Vertical, $T = 5.80$ s	169
A.184	Mode 12: Vertical, $T = 5.78$ s	169
A.185	Mode 13: Vertical, $T = 5.71$ s	169
A.186	Mode 14: Vertical, $T = 5.53$ s	169
A.187	Mode 15: Vertical, $T = 5.24$ s	169
A.188	Mode 16: Vertical, $T = 4.86$ s	169
A.189	Mode 17: Vertical, $T = 4.60$ s	169
A.190	Mode 18: Vertical, $T = 4.48$ s	169
A.191	Mode 19: Vertical, $T = 4.25$ s	169
A.192	Mode 20: Vertical, $T = 3.68$ s	169
A.193	Mode 21: Horizontal, $T = 2.87$ s	170
A.194	Mode 22: Vertical, $T = 2.29$ s	170
A.195	Mode 23: Horizontal, $T = 2.20$ s	170
A.196	Mode 24: Vertical, $T = 2.09$ s	170
A.197	Mode 25: Vertical, $T = 1.91$ s	170
A.198	Mode 26: Vertical, $T = 1.85$ s	170
A.199	Mode 27: Vertical, $T = 1.73$ s	170
A.200	Mode 28: Vertical, $T = 1.71$ s	170
A.201	Mode 29: Vertical, $T = 1.61$ s	170
A.202	Mode 30: Vertical, $T = 1.61$ s	170
A.203	Mode 11: Vertical, $T = 5.21$ s	171
A.204	Mode 12: Vertical, $T = 4.99$ s	171
A.205	Mode 13: Vertical, $T = 4.96$ s	171
A.206	Mode 14: Vertical, $T = 4.56$ s	171
A.207	Mode 15: Vertical, $T = 3.91$ s	171
A.208	Mode 16: Vertical, $T = 3.22$ s	171

A.209	Mode 17: Vertical, T = 2.69 s	171
A.210	Mode 18: Vertical, T = 2.51 s	171
A.211	Mode 19: Vertical, T = 2.44 s	171
A.212	Mode 20: Vertical, T = 2.22 s	171
A.213	Mode 21: Vertical, T = 2.11 s	172
A.214	Mode 22: Vertical, T = 2.08 s	172
A.215	Mode 23: Vertical T = 2.01s	172
A.216	Mode 24: Horizontal, T = 1.84 s	172
A.217	Mode 25: Horizontal, T = 1.63 s	172
A.218	Mode 26: Horizontal,, T = 1.56 s	172
A.219	Mode 27: Horizontal, T = 1.48 s	172
A.220	Mode 28: Horizontal,, T = 1.39 s	172
A.221	Mode 29: Horizontal,, T = 1.38 s	172
A.222	Mode 30: Horizontal, T = 1.35 s	172
A.223	Conditionally formatted values of eigenperiods coinciding with wave periods with 1, 100 and 10 000 years return period from locally wind generated sea and swell.	173
A.224	Conditionally formatted values of eigenperiods coinciding with wave periods with 1, 100 and 10 000 years return period from locally wind generated sea and swell.	174
A.225	Largest negative bending moment, M_x , at T = 5 s	175
A.226	Largest negative bending moment, M_y , at T = 5 s	175
A.227	Largest negative bending moment, M_z , at T = 5 s	175
A.228	Largest positive bending moment, M_x , at T = 6 s	176
A.229	Largest positive bending moment, M_y , at T = 6 s	176
A.230	Largest positive bending moment, M_z , at T = 6 s	176
A.231	Largest negative bending moment, M_x , at T = 6 s	176
A.232	Largest negative bending moment, M_y , at T = 6 s	177
A.233	Largest negative bending moment, M_z , at T = 6 s	177

Dictionary

Abbreviations

NPRA	Norwegian Public Roads Administration	APDL	ANSYS Parametric Design Language
TLP	Tension Leg Platform	USFOS	Ultimate Strength of Framed Offshore Structures
SFT	Submerged Floating Tunnel	VIV	Vortex Induced Vibration
NTP	National Transportation Plan	VIM	Vortex Induced Motions
NOK	Norwegian Kroner (Currency)	DOF	Degree of Freedom
DNV	Det Norske Veritas	DNV GL	Det Norske Vertias Germanischer Lloyd

Hydrodynamic and Structural

U_x	Surge	R	External Load Vector
U_y	Sway	K	Stiffness Matrix
U_z	Heave	K(r)	Secant Stiffness
θ_x	Roll	r	Response Vector
θ_y	Pitch	m	mass
θ_z	Yaw	c	damping
ω	Wave circular frequency	k	stiffness
η	Wave elevation	Q(t)	external load
η_a	Wave amplitude	M	mass matrix
k	Wave number	A	added mass matrix
T	Wave period	C	damping property matrix
g	Gravitational acceleration	K	stiffness (restoring) property matrix
T_v	Vortex shedding period	Q(t)	external load vector
σ	Stress	$\ddot{\mathbf{r}}$	acceleration vector
ϵ	Strain	$\dot{\mathbf{r}}$	velocity vector
N	Newtown (force, kg m/s ²)	r	displacement vector
kN	KiloNewton (10 ³ N)	ϕ	Eigenvector
Pa	Pascal (N/m ²)	ω_n	Natural Frequency
α_1	Mass damping coefficient (Rayleigh Damping)	T_n	Natural Period
α_2	Stiffness damping coefficient (Rayleigh Damping)	COG	Center Of Gravity
λ_i	Damping Ratio, frequency i	COB	Center of Buoyancy
ρ	Sea Water Density	M_r	Rotational Moment
A_w	Water Plane Area	MG	Metacentric Height
V	Displaced Volume	θ	Angle of heel
F_B	Buoyancy Force		
ρ_a	mass density of air	Measuring units (SI)	
$U_{T,z}$	average wind velocity	m	meter (length)
z	Distance [m] above sea level or ground	m ²	square meters (area)
F_w	Static Wind Force	s	seconds (time)
		m/s ²	acceleration

Introduction

1.1 Motivation

The motivation for the concept study is to introduce a floating bridge with improved structural performance and reduced response that can come out to lower costs than presented for the Ferry Free Coastal Route E39 up until today. It is discussed with the NPRA and supervisor that a reduced number of pontoons and structural support by the undercarriage of an offshore jacket might become an interesting and competitive concept.

1.2 Proposed Concepts

The two curved brudge concepts are presented in Section 1.2.1 and 1.2.2. The perception behind the concepts is to partially transfer compressive forces to a jacket that can carry them as axial forces. This will reduce the load on the arch and conceivably prevent buckling of the bridge girder. This is achieved by placing a jacket structure to support the connection between the floating span and the navigation channel. The girder will be free to move horizontally on the jacket to which allows for thermal expansion. The base concept designed for the Halsafjord has a similar geometrical design as for the concept proposed for the Bjørnafjord, Figure

The Halsafjord reaches 2.1 km from Halsneset to Urdneset along the coastal highway E39 (1.1). Due to the water depth of 493 m at the center of the Halsafjord, a jacket supporting the girder at the fjord midpoint has been considered not to be a feasible solution. The concept, therefore, suggests support by a jacket where the water depth is 137 and 141 m in Figure 1.2. With a required sailing height of 50 m required jacket height will be approximately 190 m. After a review of existing jacket structures (Section 2.4.2), the integrated drilling and processing platform Kvitebjørn with its height of 215 m is found as a suitable base model. A provided USFOS model of the Kvitebjørn jacket allowed for modification of the model height, and to extract the mass and stiffness properties applied to the bridge. The modeling procedure is described in Chapter 6. Further development of jacket design specifically for this floating bridge has been left outside the scope of this Thesis.

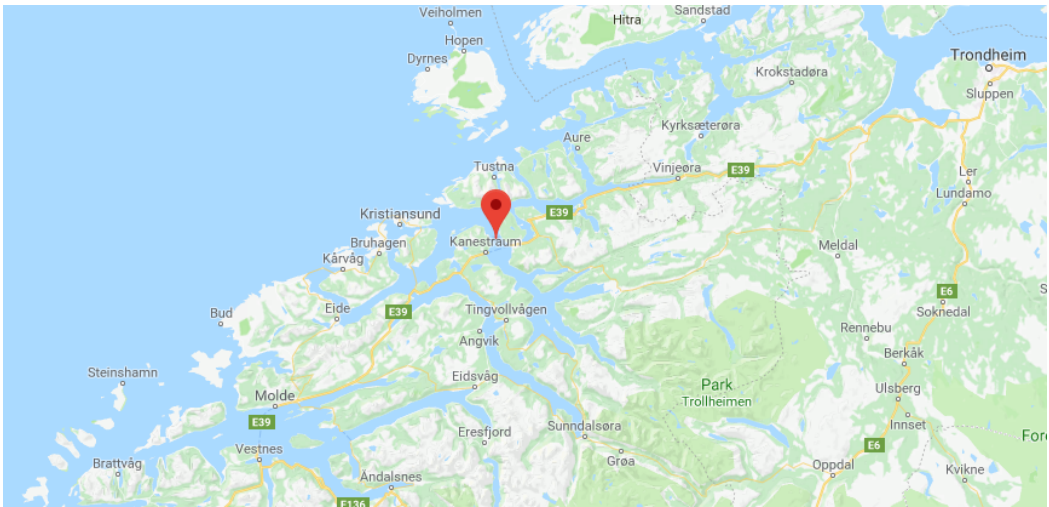


Figure 1.1: Location of the Halsafjord along E39 (Google Maps)

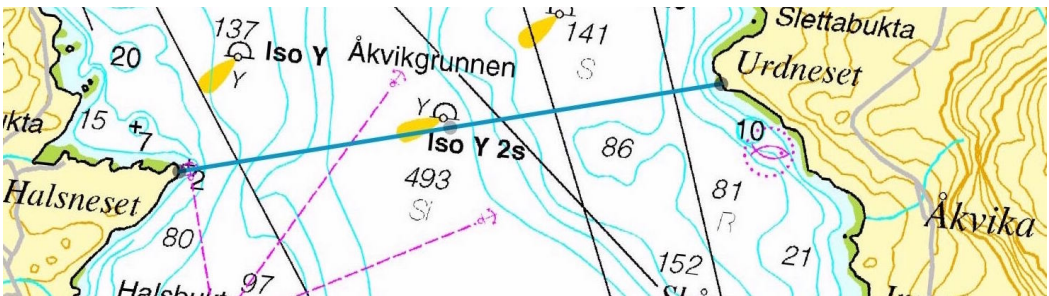


Figure 1.2: Close-Up of the planned location for the bridge. Figure includes topography in the relevant area.

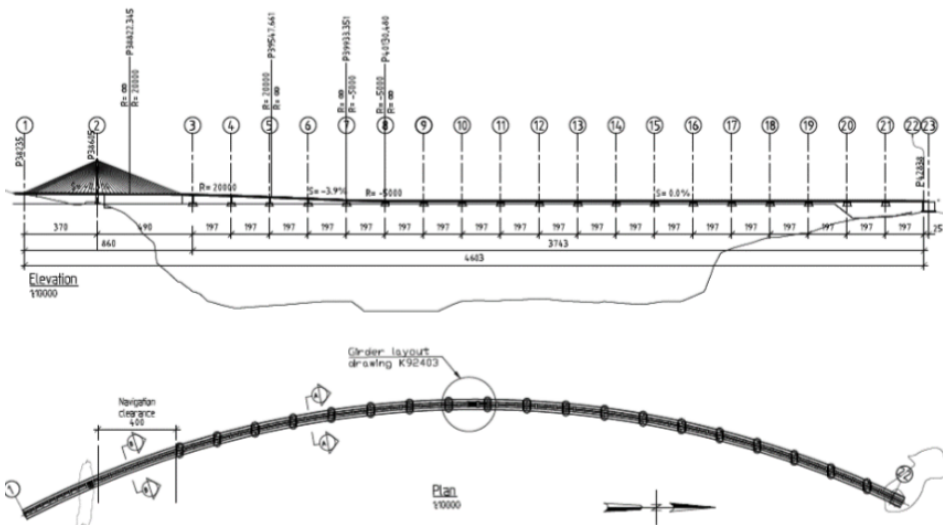


Figure 1.3: Concept of inspiration - the floating bridge solution for crossing the Bjørnafjord

1.2.1 I-Jacket Concept

The I-Jacket concept proposes a curved bridge supported by the undercarriage of a jacket 400 m north-west from Urdneset as shown in Figure ???. The bridge has an arc length of 2100 m and radius 1870 m. The navigation channel is 400 m wide as recommended from the NPRA, which is, combined with available water depth the argument for the jacket placing. Twenty stay cables support the girder over the navigation channel. Floating pontoons support the remaining distance of 1700 m. With a spacing of 200 m, nine pontoons support the remaining section of the bridge. Figure 1.4 shows a sketch of the proposed concept. The pontoons are of the same dimensions as for the Bjørnafjord concept and are in detail described in Chapter 6.

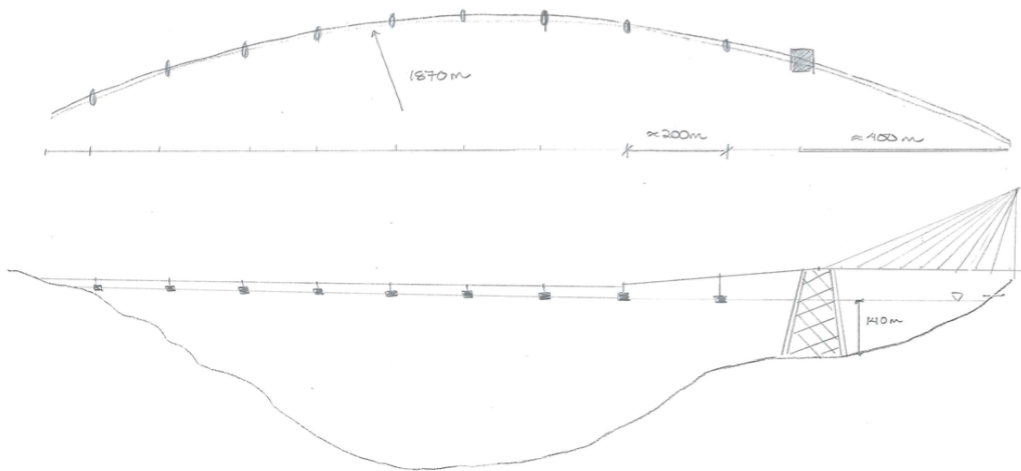


Figure 1.4: Sketch of the II-Jacket concept proposed for crossing the Halsafjord

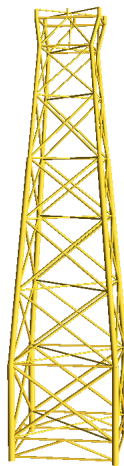


Figure 1.5: USFOS Model of the Kvitebjørn jacket with removed topside and riser/drilling equipment (USFOS Software)

1.2.2 II-Jacket Concept

The II-Jacket concept proposes a curved bridge supported by two jackets, the first is placed 400 m north-west from Urdneset and the second is placed 400 m north-east from Halsneset. This is shown in Figure 1.6. The arc length and radius is equal to the I-Jacket concept. With two cable-stayed bridges, a central section of 1300 m is left to be supported by floating pontoons. With a spacing of 200 m, six pontoons support the remaining section of the bridge. Twenty stay cables support each navigation channel. Also here, the pontoon dimensions are equal to for the Bjørnafjord concept and are in detail described in Chapter 6.

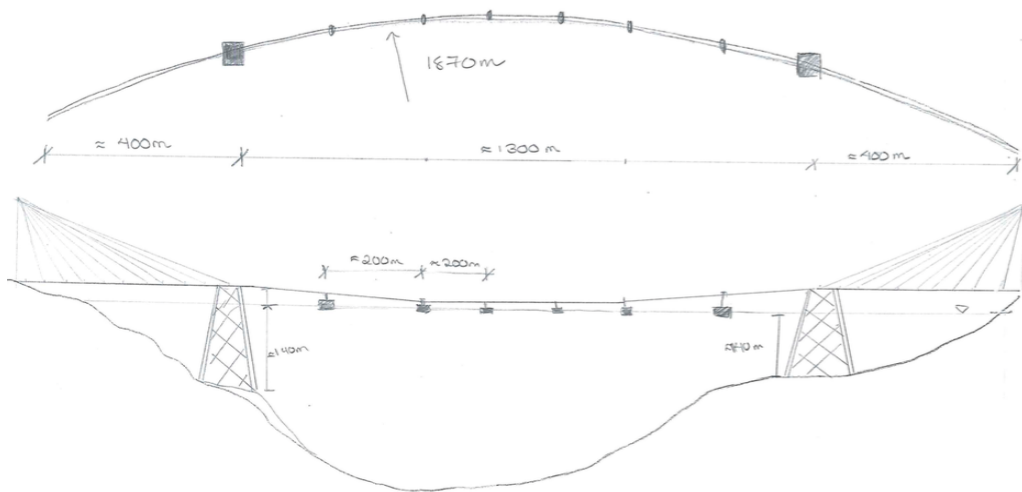


Figure 1.6: Sketch of the II-Jacket concept proposed for crossing the Halsafjord

1.3 Literature

Rules and Regulations

The rules and regulations for the bridge design are the NPRA's handbooks "N100 Veg og gateutforming" and "N400 Bruprosjektering". Limit states shall be according to Norwegian Standard NS-EN199X. Rules and regulations from DNV GL have been considered as the bridge includes components from marine structures and also for environmental and accidental loading. Applied rules have been commented throughout the thesis.

Lectured Material and Scientific Articles

Theory regarding structural mechanics, hydrostatics and hydrodynamics are partially collected from scientific articles but mainly from literature used in courses lectured during the master program at NTNU. Information about ship collision analysis has mainly been collected from scientific articles and rules and regulations. Accidental load from ship collision is presented in Chapter 4.8 according to information provided by the NPRA.

Literature Review

A summary of scientific articles used for this thesis along with extractions from their abstract is attached in the appendix.

1.4 Thesis Structure

Chapter 2 presents a review of existing marine bridges and solutions for vessel traffic. Future plans for such bridges are described along with social and environmental impacts of "The Ferry Free Coastal Route E39" project. An introduction to offshore jackets along with relevant research and regulations for ship collision is presented.

Chapter 3 presents relevant theory for computation of environmental and accidental loads. The finite element method is also described.

Chapter 4 describes the relevant loads for the floating bridge and ship collision scenario.

Chapter 5 presents the software applied in the Thesis along with model setup and description of relevant codes.

Chapter 6 presents how the sections of the global bridge model from Chapter 1.2 are modeled in ANSYS Mechanical 18.2. Element types used for the different structural sections of the model are described, along with geometry set-up and prescribed parameters to represent structural features.

Chapter 7 describes the procedure of the static, modal and regular wave analysis carried out in the ANSYS Mechanical along with a description of relevant codes. The ship collision modeling approach in USFOS is also described.

Chapter 8 presents results from the conducted analysis.

Chapter 9 includes discussion of the models applicability and recommendations of further work.

Chapter 10 presents the final conclusions.

Bibliography includes all applied literature for the thesis. An additionally detailed summary of the most relevant books and articles is attached in the appendix.

Appendix contains additional information on literature review, modeling parameters, and additional results is attached at the end of the thesis. Necessary codes and files for load calculations and analysis are provided in a digital appendix.

Industry Insight

Historically, floating bridges have existed since 2000 BC. In 480 BC, millions of troops were led over the Darnelles by use of floating bridges. The bridges were made by boats placed side by side over crossings (Watanabe and Utsunomiya, 2003). Today, technology and design have developed while the fundamental physics remain the same. When taking full advantage of water's density and the law of buoyancy, floating bridges, and submerged tunnels can withstand the forces occurring from the environment without pillars or foundations. Floating structures are commonly held in place by an anchoring system such as: mooring lines, anchors, fixed guide structures, caissons or other designs depending on water depth and seabed conditions. The structural loads are carried by floating elements, mooring lines and (or) by the structure itself. The latter approach is by establishing a curved bridge girder where the transverse loading is carried as compression or tension forces, influenced by the loading direction. This provides an advantage in deep waters and e.g soft foundations where mooring installations become complex and expensive. This arch action is further described in Section 3.2.2.

While a floating bridge has of purpose to ease and ensure safe passing for vehicles and pedestrians, it creates an obstacle for the ship traffic. Floating bridges and submerges tunnels must, therefore, in areas with vessel traffic, be designed such that the opportunity for vessel passage can be accommodated. Designs allowing for vessel passage are presented in Section 2.2.

Increasing quality of infrastructure in Norway meets challenges due to the necessity of crossing wide and deep fjords where conventional bridge technology is inadequate, primarily for fjords located along the Norwegian coastline. The environmental loading is one of the main challenges (Moe et al., 2017a). In 2017, the Norwegian Parliament presented a goal of improving the 1100 km long coastal highway E39 from Kristiansand to Trondheim, with the aim of reducing travel time by 50 percent. By replacing all ferry crossings with appropriate bridge and tunnel concepts and upgrade existing road conditions, the travel distance will decrease by approximately 50 km (Avinor, 2016). This project and social benefits are further elaborated in section 2.3. The project has faced major economic and technological challenges related to the solutions demanding advanced offshore technology to satisfy the structural criteria. This has lead to an increase in product cost and will depend on the economic limitations and development of future solutions (Romsdals-Budstikke, 2018).

2.1 Continuous and Separated Pontoon Bridges

Two floating bridge concepts can be defined by the structuring of pontoons; floating bridges with continuous or separate pontoons. Both concepts are feasible and can be designed to satisfy requirements on resistance of gravity and environmental loads as well as extreme scenarios (Chen and Duan, 2013).

For the continuous pontoon floating bridge, the pontoons are connected forming a continuous structure across the route. The roadway for carrying traffic can either be located directly on the pontoons or as a separate structure that uses the pontoons for support. The separate pontoon bridge has a various number of individual pontoons installed with required spacing depending on the bridge configuration. In between the pontoons are superstructures and bridge spans where the roadway is located. An increased number of pontoons may allow for lighter beams in the bridge floor (Seehusen, 2017).

The pontoons can have different designs to meet requirements towards the environment and structural integrity. In order to remain afloat in case of collision or severe damage, the pontoons are usually constructed with several internal bulkheads to prevent progressive flooding and capsizing (Chen and Duan, 2013).

2.2 Existing Designs of Floating Bridges

2.2.1 Evergreen Point Floating Bridge

An example of a continuous pontoon floating bridge is the Evergreen Point Bridge in Washington State connecting the two cities Seattle and Medina (Figure 2.6). The bridge as it stands today was opened in April 2016, replacing the formerly existing bridge in the same location that was built in 1963. The purpose of the reconditioning was to create a safer structure less vulnerable to high winds and earthquakes. A wider road span was also built to accommodate the heavy traffic. The floating bridge span has a length of 2310 m and is supported by 77 pontoons. As of today, the Evergreen Point Bridge is the worlds longest floating bridge (Chen and Duan, 2013).



Figure 2.1: Evergreen Point Bridge, Washington State (Marshall, 2016)

2.2.2 Bergsøysund Floating Bridge

The Bergsøysund floating bridge (Figure 2.2) is located on the north-west coast of Norway in Møre and Romsdal county. This bridge is the second longest of its kind; a floating bridge spanned over 931 m where oval pontoons support the superstructure with no mooring to the seabed. The floating span of the bridge is 845 meters with a curvature radius of 1700m. The superstructure rests on seven pontoons, each 20 m wide and 34 m long with a concrete volume of 4800 m³. The bridge is horizontally curved with a radius of 1300 m. The curved superstructure adsorbs lateral forces from wind, wave and current as axial forces transferred to the connection on shore (HjellnesConsult, 2017). The structural concept showed great resistance to roll motion and the pontoon structures provided little disturbance in the 325 m deep fjord (Watanabe and Utsunomiya, 2003).



Figure 2.2: Bergsøysund Bridge, Møre and Romsdal, Norway (NTNU, 2017)

2.2.3 Nordhordaland Bridge

The Nordhordaland floating bridge was completed in 1994 and is located north in Hordaland County, Norway. The total length of the bridge is 1614 m, whereas the floating section extends over 1246 m. The structure is a combination of a floating pontoon bridge and a cable-stayed bridge to accommodate passing of ship traffic. The latter structure has a 50 m wide navigational channel and clearance height of 32 m (Watanabe and Utsunomiya, 2003). The structural design of the Nordhordaland Bridge is similar to the Bergsøysund Bridge in Section 2.2.2. Both bridges are curved in the horizontal plane, while for the Nordhordaland Bridge the curve radius is 1700 m. The bridge superstructure consists of flexible plates that transmit forces from shear, axial forces, and torsion. Due to tidal changes, vertical displacements arise, but the design shows good structural resistance against these displacements (Watanabe and Utsunomiya, 2003).



Figure 2.3: Nordhordaland Bridge, Hordaland, Norway (Bergensavisen, 2007)

2.2.4 Solutions for Vessel Traffic

While the floating bridge eases crossing for vehicles and pedestrians, it creates an obstacle for the ship traffic. Floating bridges and submerged tunnels must, therefore, be designed such that vessel traffic in the size range from smaller pleasure boats to larger vessels can pass by. To allow that vessel traffic can pass, several structural designs for floating bridges have been developed, but only a few have been built.

For submerged floating tunnels supported by floating pontoons, the number of pontoons may vary depending on the structural design. Usually, vessels may pass between assigned pontoons where the passing can be done safely with little risk of collision or damage to either of the structures. The space between the assigned pontoons may be longer than between remaining pontoons to reduce the risk of collision. Floating bridge structures may also be designed with a ship channel close to shore. Here, the floating bridge elevates to a suspension bridge at one of the shorelines, creating an elevated passage for vessels. This concept is used for e.g., the Nordhordaland Bridge (Figure 2.3).

Floating bridges may also be constructed with a ship channel at the bridge center. For the concept in Figure 2.4, the bridge span is curved and has a remote elevation towards the center of the crossing. Columns on pontoons support the bridge. This structure may be referred to as the “bucket handle alternative” due to its structural design and has been developed as an alternative for the crossing of the Sognefjord (NPRA, 2011).

Another solution is the construction of a drawspan located on the bridge. This concept was built for The Evergreen Point Bridge, allowing passage for vessels that were too high to pass under the bridges ship channel (Figure 2.5). However, an electrical issue in December 1989 caused the drawspan of the bridge to raise about 1.5 meters. Three vehicles drove head-on into the wall, leading to six injuries and one casualty. (Jembatan, 2013).

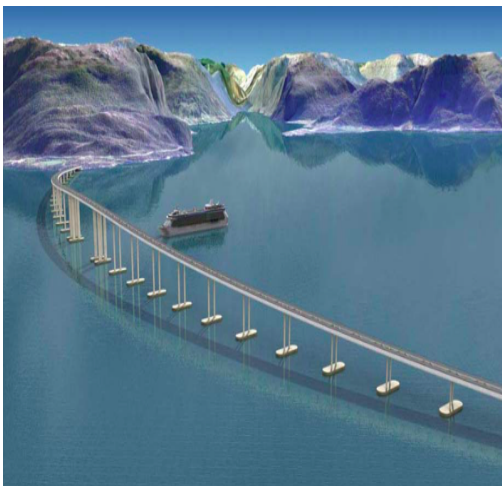


Figure 2.4: "Bucket handle alternative" for crossing of the Sognefjord (NPRA, 2011)



Figure 2.5: Drawspan on Evergreen Point floating bridge, Washington, USA (Jembatan, 2013)

2.3 Future Plans for Floating Bridges

2.3.1 The Ferry Free Coastal Route E39

The coastal route E39 is located on the west of Norway, a distance of 1100 km from Kristiansand in south and north to Trondheim. Along this distance, E39 connects the largest cities located on the Norwegian west coast such as Bergen, Stavanger, and Ålesund. The fastest transportation over the wide and deep fjords along E39 is today by ferry, which still is considered time-consuming and demanding with regards to maintenance. Traveling the coastal highway from Kristiansand to Trondheim today implies use of seven ferry crossings; Rogfast, Bjørnefjorden, Sognefjorden, Nordfjorden, Sulafjorden, Romsdalsfjorden, and Halsafjorden. Today's travel time is estimated to be 21 hours, which implies an average speed close to 50 km/h. The road conditions are considered as insufficient with regards to expected future traffic volumes (Norman and Norman, 2012).



Figure 2.6: Coastal Highway E39 Route (NPRA, 2012b)

When the National Transportation Plan (NTP) was passed in 2017, the Norwegian Parliament presented the goal of improving the coastal highway through the project "Ferry Free Coastal Highway E39". The project is to be completed in 2029, where the aim is to reduce travel time by approximately 50 percent. By replacing all ferry crossings with appropriate bridge and tunnel concepts and upgrade existing road conditions, the travel distance will decrease by approximately 50 km (Norman and Norman, 2012).

Challenges in the project are among designing bridges for the extremely wide and deep crossings where conventional bridges are not sufficient. The crossings can be over 4 km wide and over 1 km deep, meaning that even the concept of the longest bridges yet designed cannot withstand the environmental loads. A few of the concepts for the wide fjord crossings have been presented in this chapter.

The project demands complex technological solutions, while still focusing on safety aspects regarding planning, construction, and use. Furthermore, there will be improvements in conditions for business and associated living and working regions, while satisfying the environmental aspects of construction, operation and maintenance (Ulstein et al., 2015).

2.3.2 Suspension Bridge on Floating Foundations

A feasibility study has been carried out by Aas-Jakobsen, John. Holt As, Cowi, NGI, and Skansk, regarding a suspension bridge on floating foundations. The concept is suggested for crossing the 3700 m wide and 1250 m deep Sognefjord. It is concluded in the study that the solution is feasible.

The floating suspension bridge concept consists of three bridge spans with an equal length of 1234 m. The total length of the bridge is 4400 m (Figure 2.7). Connecting the bridge spans are two steel towers supported by large concrete foundations and mooring lines. The towers reach 206 m above sea level. The stiffening girder for traffic is located approximately 80 meters above sea level. Each tower is supported by a floating concrete pontoon and anchor lines moored to the seabed by use of suction anchors. This anchoring system is a technology used on the offshore industry (Vegvesen, 2013). The anchoring system consists of eight mooring lines attached to each lateral side of the pontoon. Figure 2.7 shows the described concept. Each pontoon has a diameter of 75 m and a height of 180 m. The bottom of the pontoon is located 175 m below sea level, leaving a freeboard of approximately 5 meters, depending on tidal variations. The pontoons are ballasted with olivine.

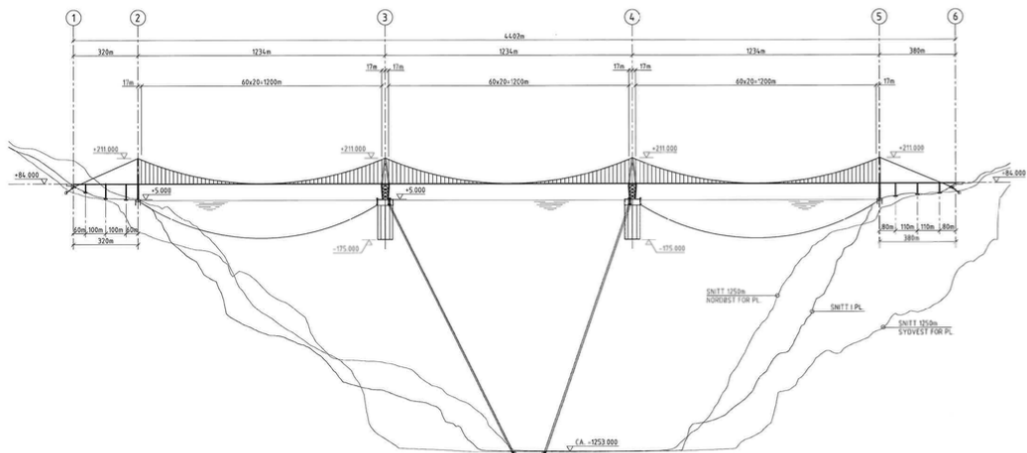


Figure 2.7: Concept drawing of suspension bridge on floating pontoons across the Sognefjord (Vegvesen, 2013)

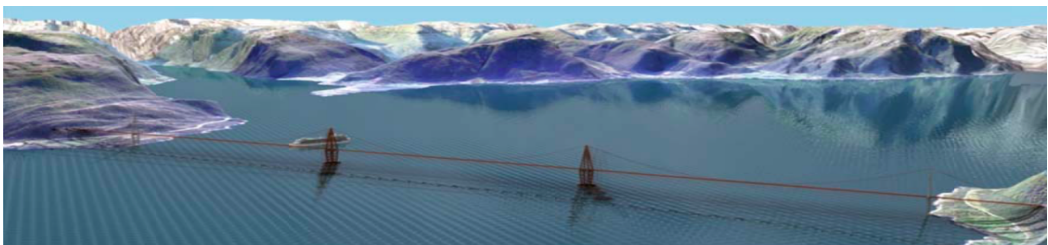


Figure 2.8: Design proposal for the floating bridge proposes for the Sognefjord (Vegvesen, 2013)

2.3.3 Floating Bridge using TLP Technology

Another concept reviewed for the Ferry Free E39 project is a multi-span suspension bridge on floating foundations, combining a suspension bridge and technology from Tension Leg Platforms (TLP). The TLP technology is frequently used in the offshore industry on large platforms i.e as installed on the Heidrun field (OffshoreTechnology, 2017). The offshore structures consist of excess buoyancy foundations anchored to the seabed through tendons in high tension, normally installed at each corner of the structure. This vertically stabilizes the structure by providing the required restoring force. For the bridge concept, the stiffness of the spans will stabilize the horizontal motion. A TLP platform is illustrated in Figure 2.10 along with the horizontal motion that will appear when the concept is applied on a pontoon-tower for a floating bridge.

This concept has been evaluated for the crossing of Bjørnafjorden and Halsafjorden (NPRA, 2015b). To allow crossing for ship traffic, the bridge roadway will be installed with a distance above sea level such that ship traffic can pass between the floating foundations. The total bridge span is 4185 m, supported by one shore tower on each landside and two TLP foundations located in the fjord. The spacing between the shore towers and floating TLP-foundations are equal and each 1395 meters (NPRA, 2015a). This structural design is similar to the suspension bridge with floating foundations in 2.3.2; both are constructed with floating foundations to obtain shorter spans. The main difference lies beneath the sea surface and regards the anchoring system.

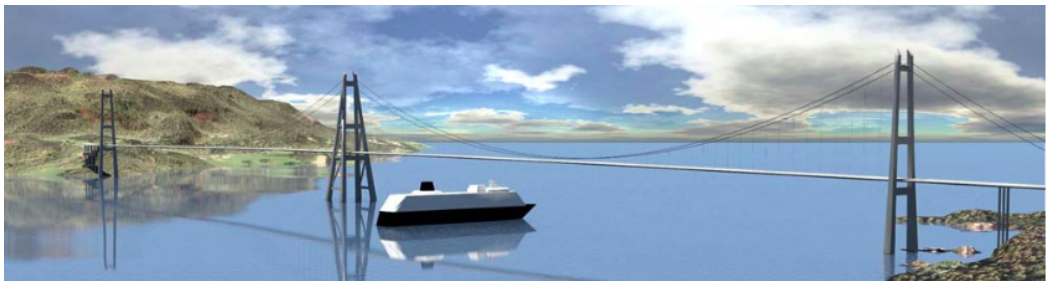


Figure 2.9: Floating Bridge concept using TLP technology for crossing of Halsafjorden, Norway (NPRA, 2015a)

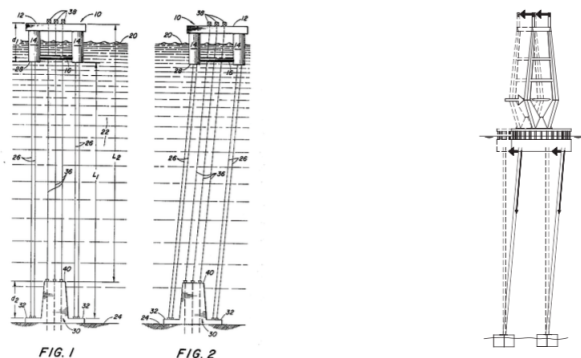


Figure 2.10: TLP platform (left), Horizontal motion of pontoon tower supported by TLP (right) (NPRA, 2015a)

2.3.4 Submerged Floating Tunnel

Submerged floating tunnels (SFT) are among the evaluated solutions for replacing the ferry crossings along E39. The concept is a submerged tube-structure that accommodates traffic and pedestrian lanes. The structure is made of steel and concrete, where the static behavior is controlled by the relation between the self-weight of the structure and buoyancy (Kawade and Meghe, 2014). Solutions for SFT's have been reviewed with one and two pipes. The solution with one pipe provides a lower horizontal stiffness. This concept has been concluded as a feasible solution for the crossing of Sognefjorden, but due to the high installation and maintenance costs, the concept has been rejected (Seehusen, 2017). The suggested concept is a submerged floating tunnel with two parallel concrete pipes moored to floating pontoons at sea level. The parallel pipes are situated in an arc, with a horizontal length of 4063 m. The tunnel is submerged 12 m below sea level, providing enough clearance for vessels to pass.

What separates the types of SFT's are mainly their anchoring systems. The anchoring systems rely on either positive or negative buoyancy and can be supported by pontoons, columns, tethers attached to the seabed or unanchored. For structural designs where the SFT is supported on columns or connected to the seafloor with tethers, the main limitation for application of these structures is water depth of the crossing. The length is not considered of importance for the feasibility. The difference between these two anchoring systems is that the columns are in compression while the tethers are in tension. Tethers will be applicable for a water depth of several hundred meters, while columns require a water depth limited to a few hundred meters. While the columns need to be vertically installed, the tethers allow for vertical and inclined installation.

The submerged floating tunnel supported by pontoons at the surface is, on the other hand, independent of water depth. The pontoons at the sea surface are exposed to higher loads from wind, waves and current loads, compared to the columns and tethers. The SFT supported by floating pontoons is also more exposed to ship collisions, which also holds for the floating pontoon bridges. A fourth solution is constructing a free tunnel with no support. This solution will be independent of water depth but highly limited by the length of the crossing (Kawade and Meghe, 2014).



Figure 2.11: Bird's view of SFT for Sognefjorden showing pontoon and ship channel location (NPRA, 2012a)



Figure 2.12: Side view of the SFT over the Sognefjord showing submerged pipe, pontoon and navigation channel (NPRA, 2012a)

First- and Second Order Wave Induced Dynamic Response

Leira (Leira, 2016) studied the first and second order wave induced response of submerged floating tunnels for the OMAE conference in Busan, South Korea, 2016. The first dynamic modes of floating bridges and submerged tunnels are found to be typically around 1 minute, and therefore wave- and low frequency regimes must be assessed. The importance of damping level is significant, as Leira writes *'the response amplitude is inversely proportional to the square root of the non-dimensional damping level'*. Considering second order response, the study found that the bending moment caused by horizontal motion was about 140 % of the same response induced by first order. Bending moment caused by vertical motion was 180 % of first order wave response.

2.3.5 Social Impacts

Investigations indicating improvements in social divisions, essentially productivity, value creation, regional and national economy and export value have been carried out (Ulstein et al., 2015). The travel time between cities and local areas along E39 implies a geographical limitation of the labor markets. A research on the impact on labor markets and value creation of Ferry-Free E39 from Nordfjord to Kristiansund performed by E.B Norman and V.D Norman, investigated the potential socioeconomic benefit of the project. The research divided the coastal distance into four main labor areas and studied the effect of local, partial and full integration. The long-term, annual profit was approximated to be 1.3 billion NOK at, and only at full integration. The results were based on simplified estimates (Norman and Norman, 2012).

A common conclusion from research on the correlation between productivity and geographical density states that increased geographical density increases the productivity in the investigated area. (Ulstein et al., 2015). The increase is assumed to contribute to increased productivity through large-scale manufacturing, increased labor market compliance and improved exchange of knowledge. The improvement of the Coastal Highway E39 is indicated as a "game changer" with long-term benefits for health and education services, trade, politics and public administration (NPRA, 2015b).

2.3.6 Environmental Impacts

Climate calculation for a ferry-free E39 is complicated. Construction of roads, tunnels, and bridges imply major emissions in the construction and transportation phase, and also throughout the operation and maintenance period. Improving roads to satisfy a minimum of two lanes imply a minimum amount of construction area. This demand may cause considerable intervention in valuable coastal and mountain territories and conflict with agricultural land. The NPRA has developed an architectural strategy to ensure the protection of involved areas and that solutions are of high architectural quality (Avinor, 2016).

A development strategy report developed in collaboration between Avinor, The Norwegian National Rail Administration, The Coastal Administration and the NPRA evaluate seven aspects of Ferry Free E39 (Avinor, 2016). Considering CO₂ emission, a comparison is made between today's coastal highway with ferry crossings and a coastal highway where floating bridges and submerged tunnels replace ferry crossings. A rough calculation of emissions over a period of 40 years showed that a reduction of CO₂ emission is realistic to expect. The research allowed for a contribution to reduced emission from improved technology, along with emission contribution from construction and maintenance. Table 2.1 shows the contributing factors to increased and reduced CO₂ emission.

Table 2.1: Net Change in CO₂ Emission associated with a Ferry Free E39 (Avinor, 2016)

Factors Contributing to Increased Emission	Factors Contributing to Reduced Emission
Increased traffic	Improved road geometry
Increased driving speed	Increased speed stability
Construction and maintenance of fjord crossing	Removal of ferries
Construction and maintenance of roads	Decreased aviation traffic
	Removal of fast ferries

2.4 Jacket Structures

2.4.1 Structural Aspects

Information presented in this section is collected from literature written by Amdahl (Amdahl, 2009). A steel jacket is a fixed structure piled to the seabed, commonly seen as a truss structure designed for supporting the topside of offshore platforms. In addition, the structure shall stand firm against environmental loads such as wave impact and wind pressure, and also be capable of resisting critical damage from corrosion and fatigue through the structures life cycle. The term "jacket" may be confusing as the structure looks nothing similar to its name, but actually comes from the tower acting as a coat for the piles hammered into the seabed.

The structural elements are commonly circular pipe elements where the vertical columns have the largest dimensions. The horizontal members contribute to the higher stiffness of the vertical columns while they ensure that the horizontal forces from environmental loading are transferred to the bearings. Diagonal members also prevent the vertical columns from buckling. The pipe elements are welded, meaning jackets commonly have multiple joints. This implies that fatigue is a relevant threat to this structure type.

The structure in Figure 2.13 has additional vertical and diagonal members between column 1 and 2. These members provide additional strength during the installation phase when the structure is tilted of the transport barge. Further explanation of the installation procedure is described in section 2.4.3. During the phase of the tilt, the weight of the structure will rest on the members in contact with the barge causing need of additional reinforcement of the structure. After installation, the additional reinforcement does not provide significant strength to the structure.

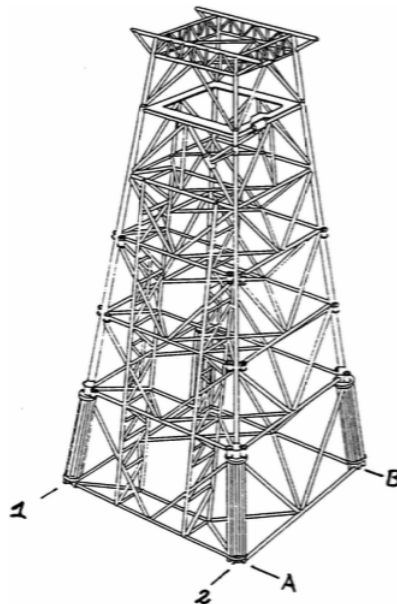


Figure 2.13: Concept Sketch of a Steel Jacket (Amdahl, 2009)

2.4.2 Market Analysis

Jacket structures are commonly used in the offshore industry both in the UK and the North Sea. The table below (Table 2.2) shows a compressed collection of jacket structures examined when searching for appropriate jacket structures for the floating bridge model. The information is collected from The North Sea Field Development Guide (10th edition) (OPL, 2005). The jackets range from 80 m to 160 m water depth and are installed in the UK or North Sea field. The availability of USFOS models also influenced the choice of jacket.

Table 2.2: Jacket structures ranging from water depth 25 to 190 m installed in the UK and North Sea

Name	Field	Country	Water Depth [m]	Legs	Piles	Weight Base [MT]	Weight Total [MT]
Comorant North	Comorant	UK	161	8	32	20052	40210
South Comorant "A"	Comorant	UK	150	4		294655	323093
Dunlin A	Dunlin Field	UK	151	4		228611	252001
Eider	Eider Field	UK	157	8	24	17000	28200
Fulmar A	Fulmar Field	UK	84	8	32	12400	40510
Fulmar AD	Fulmar Field	UK	84	4	8	1406	1666
Galleon PG	Galleon	UK	24	4	4	760	1730
Galleon PN	Galleon	UK	25	4	4	880	1680
Gannet A	Gannet A-D	UK	95	4	12	7750	20100
Goldeneye	Goldeneye	UK	120	4	8	3500	4700
Nelson	Nelson Field	UK	84	4	12	8500	18000
Schooner	Schooner Field	UK	71	4	4	2200	3600
Shearwater PUQ	Shearwater Field	UK	90	4	8	6500	18000
Shearwater WHP	Shearwater Field	UK	90	4	4	2600	5300
Tern	Tern Field	UK	167	8	32	20000	38000
Claymore CAP	Claymore Field	UK	110	4		4500	8100
Claymore CPP	Claymore Field	UK	110	8	30	12200	25700
Clyde	Clyde Field	UK	80	8	26	12300	31959
Piper B	Piper Field	UK	145	8	20	23000	51330
Tartan A	Tartan Field	UK	140	4	28	14500	30400
Alwyn North NAA	Alwyn North Field	UK	130	8	32	15900	35900
Alwyn North NAB	Alwyn North Field	UK	130	8	24	14500	32100
Dunbar	Dunbar Field	UK	145	4	16	9300	20300
Elgin PUQ	Elgin Field	UK	92	3	18	24150	43000
Elgin WHP1	Elgin Field	UK	92	4	4	2737	4485
Franklin WHP	Franklin Field	UK	93	4	4	2811	4727
Kittiwake	Kittiwake	UK	85	4	12	6250	15250
Hod	Hod Field	Norway	72	4	4	1400	2400
Kvitebjørn	Kvitebjørn Field	Norway	190	4	-	12200	25200
Tambar	Tambar Field	Norway	67	3	3	1350	2250
Ula Drilling Platform	Ula Field	Norway	70	4	12	5031	11000
Ula Production	Ula Field	Norway	70	4	12	3751	10637
Ula Quarters Platform	Ula Field	Norway	70	4	8	3718	11760
Valhall DP	Valhall Field	Norway	69	8	24	5500	12500
Valhall Flanke Nord	Valhall Field	Norway	70	4	4	2250	3850

2.4.3 Installation Procedures

The following information is collected from the lecture on installation of structural offshore systems (FGG, 2013). Installation of an offshore jacket is mainly carried out as a lift-, launch- or self-floating operation, a choice dependent on accessible equipment, cost, and water depth. Installation by lifting has become a more preferred method as the capacity of offshore lifting vessels has increased. This eliminates the need for additional steel support as described in 2.4.1. Besides the design purpose of the jacket, the structure will during installation be exposed to load out stresses increasing the need for adequate framing configuration and avoiding seabed collapse. Installation of the offshore jacket is not treated extensively in this thesis but is important as low installation costs can contribute to reducing the total project cost.

The installation of a steel jacket can mainly be divided into four project phases; loadout, seafastening, offshore transportation and installation. Detailed installation plans describe the procedures during all phases, which becomes important for conducting safe execution of this type of marine operation. Multiple analyses are necessary and required for jacket launch and installation on the seabed, e.g. seabed clearance, jacket stability to determine the temporary buoyancy arrangement, position the leg bulkheads, determine the number and location of flood valves.

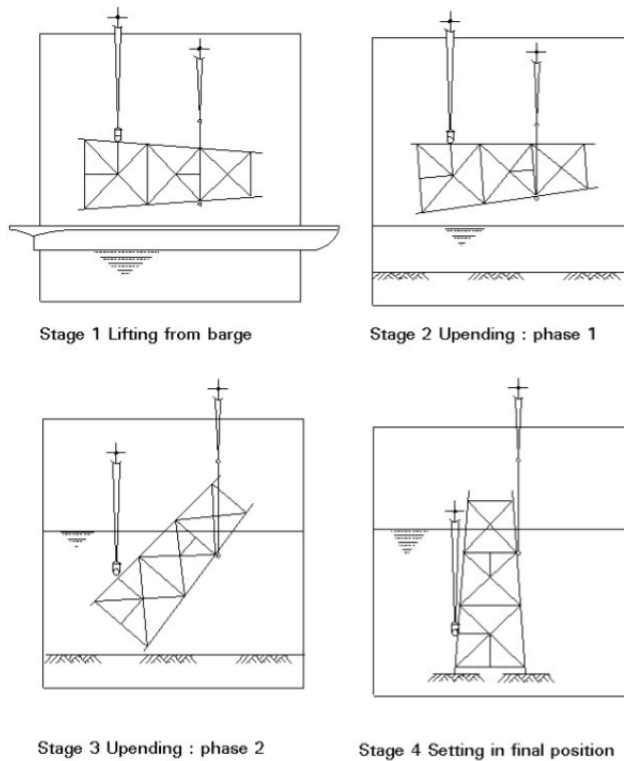


Figure 2.14: Four stages of the lift and upending phase during installation of an offshore steel jacket (FGG, 2013)

2.4.4 Cost Engineering

Specific cost data is limited due to information held by vendors. The following subsection provides a brief estimate of the cost related to fabrication and installation of the jacket, but are only meant as indicative and will strongly rely on the structures weight and design conditions (Visser, 1993).

Table 2.3: Brief estimate of the cost related to fabrication and installation of the jacket (Visser, 1993)

Parameter	Cost/Duration/Percentage
Pile Weight	Jacket Weight
Anode Weight	0.08·Jacket Weight
Transportation	200 km/day + 4 days
Installation	10-15 days
Installation and Fabrication Cost per Unit Weight	
Steel Procurement	
Jacket	US \$ 900/t
Piles	US \$ 700/t
Anodes	US \$ 4000/t
Fabrication	
Jacket	US \$ 3000-5000/t
Piles	US \$ 1000/t
Load Out and Seafastening	
Labour and mat.	5 % of fabrication cost
Barge Hire	US \$ 150k-400k
Transportation Barge	US \$ 20k-40k per day
Offshore Installation	US \$ 100k-350k per day
Additional cost (% of total above)	
Engineering/Design	10 %
Project Management	10 %
Insurance	2.5 %

2.5 Jacket Structures Subjected to Ship Impact

2.5.1 Research and Development

Analysis of ship collision scenarios is recommended to be done by non-linear finite element analysis or simplified analytical methods (Det Norske Veritas, 2010). The analysis is supported by experimental and empirical methods (Amdahl).

In the early 1980's, Hagiwara et al. proposed approaches for ship collision analysis, especially considering ship damage estimation (Hagiwara et al., 1983). It is suggested that strength estimations are done separately for the striking and struck vessel. To validate simulations, a sufficient amount of data from experiments is required for this to be a reliable source. Wevers and Vredvelt (?) have done experiments on collision with two tankers for collision force, strain and damage estimation. Work done by Haris and Amdahl (?) verifies that there is a correspondence between simulations and measured data from experiments which indicates that the finite element approach is reliable.

For the Ferry Free Coastal Route E39 project, accidental ship collisions are of critical concern due to the structural members close to the water surface. The vessels of interest are large and operate at high speeds. Extensive work is being done at the Norwegian University of Science and Technology by e.g. Wang for analyzing large floating bridges exposed to ship collisions in Bjørnafjorden. Amdahl et al. (Moe et al., 2017b) analysed a floating bridge supported by tension leg foundations and floater barriers exposed to ship collision with impact energy 1200 MJ. The analysis showed that the collision barriers reduce the damage to the ship bulkhead but increase the collision impulse on the bridge. Bridge response when the structure is subjected to ship collision loads will be important in the design process of floating bridges.

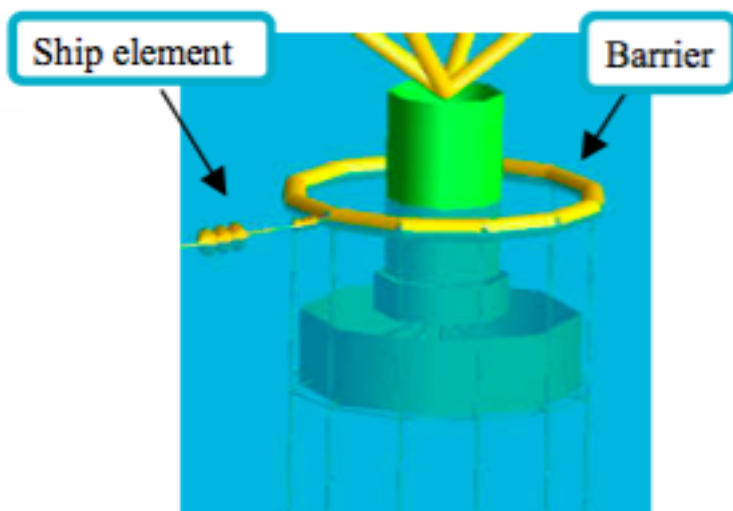


Figure 2.15: Model of ship element and barrier for the analysis of the tension-leg bridge (Moe et al., 2017b)

2.5.2 Standards and Recommended Practice

In NORSOK N-400, Design of Steel Structures (NORSOK, 2004) Annex A, Design against Accidental Actions, ship collision is one of the extensively considered accidental load cases for offshore steel structures. NORSOK Annex A covers collision mechanics, dissipation of strain energy, collision forces, force-deformation relationships for denting of tubular members, force-deformation relationships for beams, strength of connections, strength of adjacent structures, ductility limits, resistance of large diameter stiffened columns, energy dissipation in floating production vessels and global integrity during impact.

The NORSOK N-400 states that accidental actions shall be appraised through risk assessments. The structure shall be designed to maintain the load-bearing function under the impact of an accidental event. In addition, the standard states a performance criteria holding for a certain time after the accidental impact such that escape ways and shelter areas are usable (risk of human life) and criteria for the global load bearing capacity (harm to the environment, loss of property). The NORSOK N-400 and DNV GL RP C204 "Design Against Accidental Loads" share common formulations for ship collision analysis (Det Norske Veritas, 2010).

For the Norwegian Continental Shelf, accidental actions shall according to NORSOK Z-013, and S-001 be appraised through risk assessments including any influencing factors related to human, technology, operation, and installation (NORSOK, 2010). Damage to e.g. riser and drilling equipment must also be considered, but this will not be relevant when the jacket undercarriage is used to support the bridge girder.

In DNV GL's recommended practice (RP) DNV-RP-C204, chapter 3, ship collision load and analysis approach is stated. The collision load shall be characterized as kinetic energy determined from the ship mass (including the hydrodynamic added mass) and impact velocity. The kinetic energy must be distributed to the vessel and installation, however it is not required that all the energy is dissipated. The damage shall be analyzed with non-linear dynamic FEM analysis or by combining elastic plastic methods with energy considerations (Det Norske Veritas, 2010).

The collision impact load under consideration shall involve the authorized service vessel with the largest speed and mass operating in the area. Sideways and head on collisions shall be considered. Collision vessel data for the Halsafjord is provided by the NPRA and presented in Section 4.8.

Development of Regulations

Amdahl and Yu (Yu and Amdahl, 2001-2018) have investigated the response on tubular members on offshore structures subjected to ship impact. Background for the work is that the DNV GL RP C204 and NORSOK N-004 standard were developed decades ago (Yu and Amdahl, 2001-2018) such that the procedures on analysis methods and collision energy are outdated. Purpose of the research was to establish suggestions to improve the standard. The work involved the use of the software LS DYNA to perform a large number of non-linear finite element simulations to examine jacket members subjected to bow and stern impact. Amdahl and Yu recommend that strength or shared energy design approach might be necessary as the ductile energy design (legs absorb the entire energy) is virtually impossible.

Theory

3.1 Coordinate System and Rigid Body Motions

This section defines the coordinate system and body motions relevant for the floating bridge model. In linear seakeeping, oscillatory motions (translation and rotation) are defined in the inertial reference frame. This can be done because the motion amplitudes and the difference between inertial and the body-fixed reference frames is small. This way of definitions allows for motions to be expressed by application of Newton's second law (Faltinsen, 1993).

Linear seakeeping defines motions in three translational and three rotational degrees of freedom as described below.

Translational degrees of freedom

- (1) U_x - surge
- (2) U_y - sway
- (3) U_z - heave

Rotational degrees of freedom

- (4) θ_x - roll
- (5) θ_y - pitch
- (6) θ_z - yaw

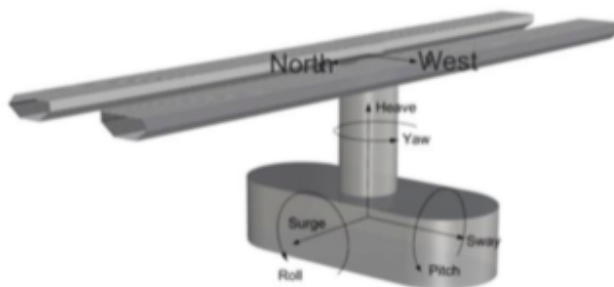


Figure 3.1: Coordinate system for the floating bridge proposed for the Bjørnafjord crossing (rø)

3.2 Beam Theory

The theory presented in this chapter (3.2) is collected from literature written by Bell (Bell, 2015).

3.2.1 Load Resistance Through Axial-, Shear Forces and Bending Moments

When the plane section in a beam remains plane, stress and strain may from testing be proven to have an approximately linear relationship through Hookes Law (Equation 3.1).

$$\sigma = E\epsilon \quad (3.1)$$

Where E is the modulus of elasticity and ϵ is the relative elongation of the beam. Further, the axial force is given by 3.2.

$$\epsilon = \frac{EA}{N} \quad (3.2)$$

The moment about the y- and z-axis are given by Equation 3.3 and 3.4.

$$M_y = EI_{yy}\kappa_y \quad (3.3)$$

$$M_z = EI_{zz}\kappa_z \quad (3.4)$$

Combined, the strain may be written as Equation 3.5 or 3.7 by defining the curvature κ as 3.6.

$$\epsilon_x = \frac{N}{EA} - \frac{M_z}{EI_{zz}}y + \frac{M_y}{EI_{zz}}z \quad (3.5)$$

$$\kappa = \frac{d^2u}{dx^2} \quad (3.6)$$

$$\epsilon_x = \epsilon_C - \kappa_{yy}y + \kappa_{zz}z \quad (3.7)$$

Where κ_{zz} is the curvature due to a displacement in z-direction. Combined and inserted to Hooks law, the axial force due with contribution from axial load and bending moments can be expressed as,

$$\sigma = \frac{N}{A} + \frac{M_z}{I_z}y + \frac{M_y}{I_z}z \quad (3.8)$$

Shear Forces and Bending Moments in Specific Cases

Beam structures carry loading by primarily resisting bending. Transverse loading is carried by shear forces and bending moments, inducing internal stresses and strains causing deformation. Simple calculations on bending moment and shear force may in relatively short time provide a coarse estimate of the force magnitudes the structure is dealing with. Despite the inaccuracy of such calculations for the treated bridge structures, it can be useful in a preliminary design stage. For a simple beam with uniformly distributed loading, the shear forces and bending moments are expressed as equation set 3.10. Corresponding shear and bending moment diagrams are shown in Figure 3.2. This configuration may, as a rough estimate, represent the bridge girder when examining the total length of the bridge or the single spans between the supporting jacket or pontoons. For the base concept, e.g. the high bridge would rather have one fixed and one pinned end.

$$V = \frac{wl}{2} \quad M = \frac{wl^2}{24} \quad M_{max} = \frac{wl^2}{12} \quad u_{max} = \frac{wL^4}{384EI} \quad (3.9)$$

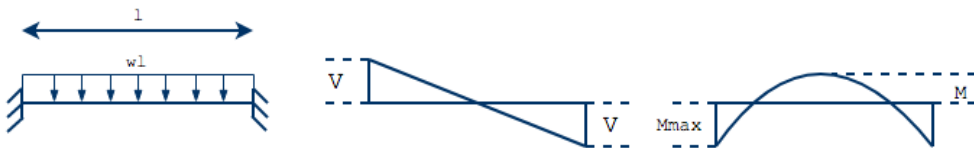


Figure 3.2: Shear force (V) and bending moment (M) diagram for a fixed beam

$$V_1 = \frac{3wl}{8} \quad V_2 = \frac{5wl}{8} \quad M_{max} = \frac{wl^2}{8} \quad M_x = \frac{9wL^2}{128} \quad u_{max} = \frac{wL^4}{185EI} \quad (3.10)$$

For an arbitrary beam cross section, the stress condition will uniquely be described by the axial force, shear force, and bending moment. Vertical equilibrium gives the relation between moment and shear force. It is worth noting that a linear distributed moment will give a constant shear force.

$$V = \frac{dM}{dx} \quad (3.11)$$

For a closed, thin walled cross section the shear stress may be assumed to act constant over the thickness, providing a shear flow through the cross section profile. This stress distribution gives a torsional moment defined by the enclosed area A_C and the average of the thickness.

$$I_V = \frac{4A_C^2}{\int_C \frac{ds}{t(s)}} \quad (3.12)$$

The maximum shear stress occurs at the smallest wall thickness,

$$\tau_{max} = \frac{M_v}{2A_C t_{min}} \quad (3.13)$$

The von Mises Yield Criterion

Continuing on the assumption of plane stress, the von Mises yield criterion defines the yield limit for a metal material. The Mises criterion is expressed as Equation 3.14, stating that the material will exhibit plastic behaviour (yield) when the equivalent tensile stress exceeds the yield limit, f_y

$$\sigma_j = f_y \tag{3.14}$$

For a plane stress condition, the equivalent stress is expressed as

$$\sigma_v = \sqrt{\sigma_x + \sigma_y + \sigma_x\sigma_y + 3\tau_{xy}^2} \tag{3.15}$$

3.2.2 Curved Bridge Design: Arch Action

The following presented theory is collected from Zallen Engineering (Zallen, 2008).

A straight floating bridge will most likely require mooring lines or tethers to ensure sufficient horizontal stiffness to withstand the horizontal loading from wind, waves and current. Installing mooring systems into deep water is very costly considering both design and operation. The curved bridge concept that is suggested withdraws the need for additional stiffness from mooring, due to the arch action.

In contrast to a straight bridge that will resist the load by beam action, transverse loads are enabled to be carried by arch action in the curved bridge design. As described by Watanabe and Utsunomiya (2003): When the current is coming from the convex side, the curved bridge shape will act as an arch rib, providing higher stiffness in the horizontal plane compared to a straight beam. In the latter case, the bridge action is closer to a catenary cable. It is important to distinguish between an arch and a curved beam. In addition to the shear and bending moment, the arch experiences a concentric axial compression that can be seen as "C" in Figure 3.4a. This occurs as an effect of the present thrust and vertical reaction at the end supports.

Comparing the stress distribution over the cross section in the straight beam and arch, it is observed that the only stress present in cross section 2-2 and 3-3, Figure 3.4a, and that compressive stress dominates the tensile stress in cross section 1-1 and 1-4.

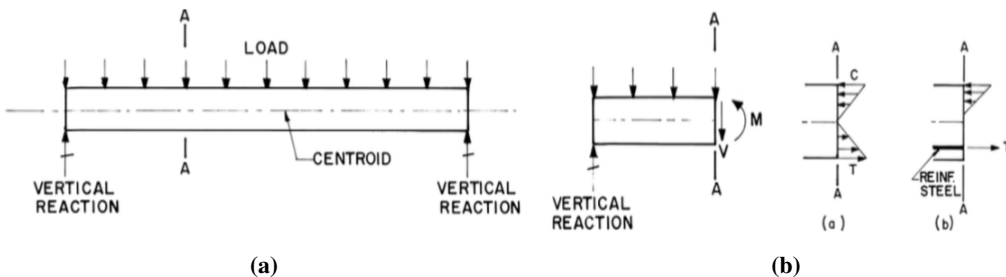


Figure 3.3: (a) Illustration of arch with reaction forces and "C" representing concentric axial compression (b) Effect of arch shape on stress distribution corresponding to 1-4 in (a).(Zallen, 2008)

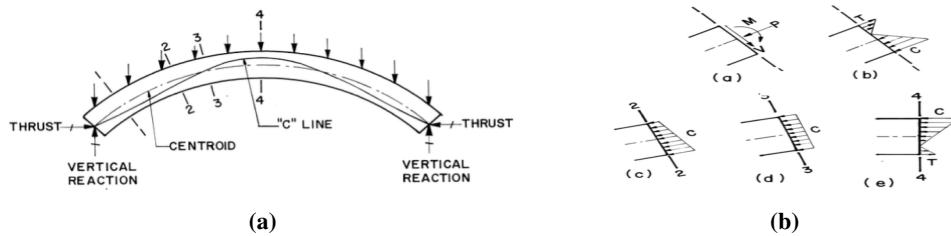


Figure 3.4: (a) Illustration of arch with reaction forces and "C" representing concentric axial compression (b) Effect of arch shape on stress distribution corresponding to 1-4 in (a). (Zallen, 2008)

3.3 Mechanics of a Cable-Stayed Bridge

Cable-stayed bridges are usually installed over spans where the properties of suspension bridges become excessive due to an economic benefit. The cables are attached from the girder directly to the tower, supporting the bridge deck by tension, transferring forces to the tower in a compressive state as seen in Figure 3.5. Cable-stayed bridges are, however, more sensitive to wind than suspension bridges due to their lower flexibility. The purpose of the stay-cables for the chosen concept is to reduce bending moments the girder exhibits from primarily self weight (of Bridges, 2018).

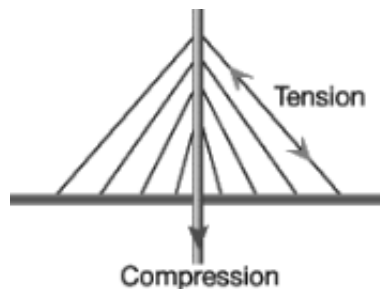


Figure 3.5: Tension in the cables and compression in the tower of a cable-stayed bridge (Morrissey, 2000)

3.4 Jacket Structures

3.4.1 Global Forces

The weight of the topside acting vertically on the structure will be absorbed as axial forces in the structural members. The environmental forces, as can be assumed acting in the horizontal plane, will, roughly speaking, cause shear forces and moments. Simply, one can state that the vertical legs carry the axial forces and moments, while the horizontal and diagonal braces carry the shear forces (Amdahl, 2009).

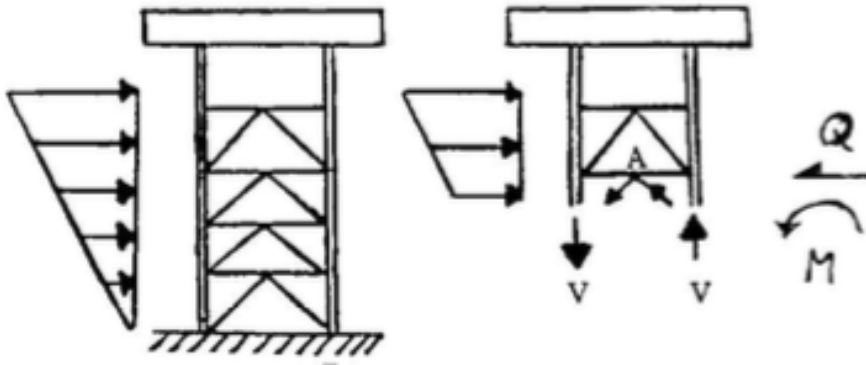


Figure 3.6: Simple model of linear varying wave loads acting on a jacket structure (right), global and reaction forces on a jacket structure (left) (Amdahl, 2009)

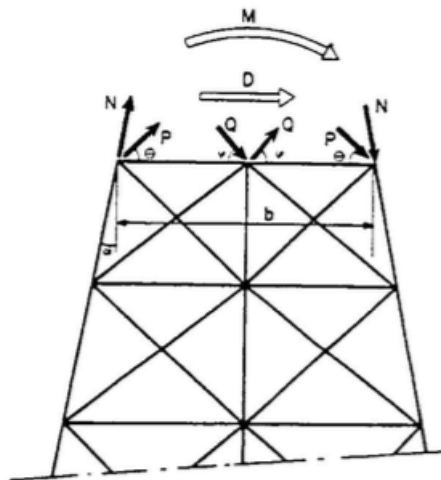


Figure 3.7: Global forces acting on a jacket structure with reacting axial and shear forces (Amdahl, 2009)

3.5 Hydrostatic Forces

3.5.1 Specific Gravity

All contributions to the weight of the structure are included in the specific gravity. Permanent weight contribution is the weight of material of all components of the structure, such as weight of concrete pontoons and pontoon towers, cable system, structural elements and asphalt. When placed in a marine environment, the structure will absorb water. This, along with marine growth and ballast will add up to the variable weight contribution of the specific gravity (Reinertsen, 2013).

3.5.2 Buoyancy

As stated in Archimedes principle, the buoyant force on a partially or fully submerged structure works on the body with a magnitude of the weight of the fluid volume displaced by the body (Amdahl, 2014). The buoyant force on the suspension floating bridge will equal the force from the displaced volume from the submerged volume of pontoons, as stated in Equation 3.16.

$$F_B = V \cdot g \cdot \rho_w \quad (3.16)$$

Where

- F_B = buoyancy force [N],
- V = displaced volume of water [m^3]
- g = acceleration due to gravity [$\frac{m}{s^2}$]
- ρ_w is the density of water, typically 1025 [$\frac{kg}{m^3}$] for sea water.

3.5.3 Stability

The restoring stiffness can be found from a linear relation between the restoring moment and the angle of heel. In an angular direction, the stiffness will be a function of the buoyancy force and the distance between the metacenter, and center of gravity, MG. For the vertical direction, the restoring component will depend on the submerged volume and weight of the displaced fluid, assuming a constant water plane area (Greco, 2012). By assuming small angles, $\sin \theta \approx \theta$, and the following relation is obtained,

$$k_\theta = \frac{M_r}{\theta} = F_B \cdot MG \quad (3.17)$$

Sufficient stability is a fundamental requirement for all marine structures and is defined as a body's ability to return to an upright position when exposed to an angle of heel. A body will heel when a rotational moment is applied.

At any given position, stable or in heel, the gravitational force on a partially submerged body will

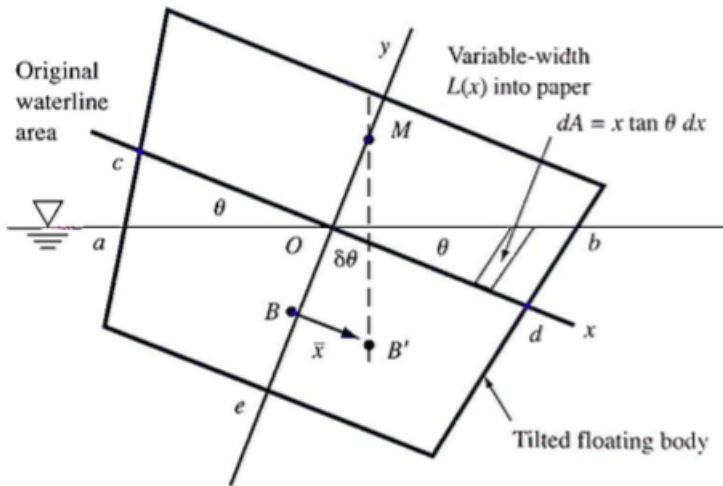


Figure 3.8: Stability parameters of a partially submerged body(White, 2008)

act vertically along the body’s symmetry line and through the body *center of gravity* (COG). COGs location will depend on the body’s mass distribution.

The buoyancy force will work upwards through the center of buoyancy (B). Bs location depends on the shape of the submerged volume. During heel, the center of buoyancy will change to B’, as the condition in Figure 3.8. The line of the buoyancy force will now intersect with the symmetry line at the *metacenter*, M. The distance between the G and metacenter is defined as the metacentric height (MG). As long as MG is positive, the body is in a stable condition (SkipperKlassen, 2012).

The restoring moment the body can create will work about the metacenter. By mechanics, the restoring moment is the product of the buoyancy force and metacentric height, as in Equation 3.18.

$$M_r = F_B \cdot MG \cdot \sin\theta \tag{3.18}$$

3.5.4 Loads from Current

Loads from current are important when studying the effects of the wave-current-wind environment. The current mainly contributes to viscous loading (Faltinsen, 1993). Viscous forces occur due to tangential stresses (causing frictional resistance) and pressure losses when fluid passes the body surface. The former causes a shear (drag) force, while the latter induced a pressure drag force.

An important parameter is the Reynolds number, which classifies the degree of turbulence in the flow. As the Reynolds number increases to a certain level, turbulent flow occurs along the surface of the body. This generally leads to a higher friction drag contribution and a lower contribution from pressure drag (Faltinsen, 1993).

3.6 Wave Theory

3.6.1 Regular Waves

Sine and cosine graphically present smooth and continuously oscillating functions, and are mathematically used to represent any type of wave motion. By application of linear wave theory, a single regular ocean wave propagating in the horizontal x-direction can be described by the function

$$\zeta = \zeta_a \sin(\omega t - kx) \quad (3.19)$$

Where x and t denote the horizontal position in reference to the chosen coordinate system and the time variable. ζ_a , ω , and k determine wave characteristics. ζ_a denotes the wave amplitude, ω is the circular frequency related to the wave period, T, by $\omega = \frac{2\pi}{T}$. The wave number, k is related to natural frequency through $k = \frac{\omega^2}{g}$.

When applying linear wave theory comes assumptions regarding the surrounding environment. In order to derive linear wave theory, one assumed a horizontal sea floor and infinite horizontal extent. The above expression is derived by satisfying the Laplace Equation and governing kinematic and dynamic boundary conditions (Faltinsen, 1993).

3.6.2 Irregular Waves and Wave Spectra

The following theory is collected from literature written by Myrhaug (Myrhaug, 2004). When looking at a real sea state, it is obvious that the sea does not consist of only regular waves behaving after a sinusoidal pattern. The ocean behaviour seems to behave randomly and chaotic. This is described as an irregular sea state, and can be approximated as a superposition of N numbers of regular, long crested waves.

$$\zeta(x, t) = \sum_{n=1}^N \zeta_{A_n} \cos(\omega_n t - k_n x + \epsilon_n) \quad (3.20)$$

Where for wave component n,

- A_n is the wave component amplitude
- ω_n is the circular frequency
- k_n is the wave number
- ϵ_n is the phase angle, uniformly distributed between 0 and 2π

Equation 3.20 can be modified to hold for short crested waves, where the sine wave propagates with an angle θ relative to the horizontal axis.

It is further assumed that the wave process is *stationary* and *ergodic*, implying that the mean and variance is constant within a short time frame (20 min - 3 hours), and that a single time serie can represent the complete wave process. In addition, the wave elevation is assumed to be *uniformly*

distributed with mean equal to zero and standard deviation σ^2 .

Considering linear waves, the total energy density per unit area is given by Equation 3.21.

$$\frac{E}{\rho g} = \sum_{n=1}^N \frac{1}{2} \zeta_{An}^2 \quad (3.21)$$

The wave spectrum $S(\omega)$ is introduced such that within the frequency interval $\Delta\omega$ the energy equals the sum of energy from each wave component within the frequency interval. The total energy is then given as Equation 3.22.

$$\frac{E}{\rho g} = \sum_{n=1}^N \frac{1}{2} \zeta_{An}^2 = \sum_{n=1}^N S(\omega) \Delta\omega \quad (3.22)$$

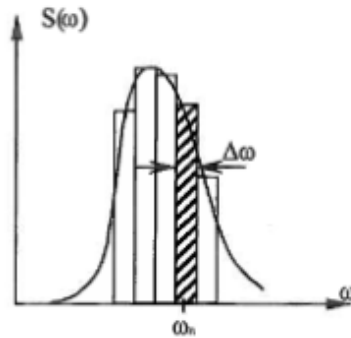


Figure 3.9: Principle sketch of a wave spectrum ($s\emptyset$)

Parameters of interest are often the significant wave height (H_s) and the peak period (T_p). These are expressed by the moments of the wave spectrum, defined as,

$$m_n = \int_0^{\infty} \omega^n S(\omega) d\omega, n = 0, 1, 2... \quad (3.23)$$

Where H_s , the significant wave height, is a definition of the average value of the 1/3 highest waves in a measured time serie. m_0 provides an estimate for H_s if the significant wave height is computed from the spectra (Equation 3.24).

$$H_s = H_{m0} = 4\sqrt{m_0} \quad (3.24)$$

The peak period, T_p (commonly given in seconds) is defined from the frequency that indicates the peak of the spectrum. The corresponding peak frequency is related to the peak period through $\omega_p = 2\pi/T_p$.

If the number of waves in a given sea state is known (which can be estimated by the duration of

the sea state and the mean zero upcrossing period), the most probable largest wave height can be determined by Equation 3.25.

$$H_M = H_{m0} \sqrt{\frac{\ln N}{2}} \quad (3.25)$$

3.6.3 Standardized Wave Spectra

Standardized wave spectra are commonly used in design phases. This is because obtaining detailed wave spectra would be time consuming and require a lot of data and resources to establish for each specific area of interest. Multiple standardised wave spectra are developed, such as Pierson Moskowitz (PM), ITTC (International Towing Tank Conference), ITTS (International Ship Structures Congress) and JONSWAP (JOint North Sea WAve Project). In this thesis the JONSWAP spectrum will be briefly described. It is not applied in the regular wave analysis, but the theoretical background on wave spectra is important for understanding the estimation of extreme value statistics.

The JONSWAP spectrum is developed from wave data measured in the North Sea during 1968-1969. It's basis is the PM spectrum, but counts in addition for limited wind fetch (the free distance of the propagating wind).

The spectrum is according to DNV GL RP C205 (DNV-GL, 2010) defined as,

$$S_J(\omega) = A_\gamma S_{PM}(\omega) \gamma^{exp(-0.5(\frac{\omega - \omega_p}{\sigma \omega_p})^2)} \quad (3.26)$$

Where

- $S_{PM}(\omega)$ is the PM spectra as defined in equation 3.27
- σ is the spectral width parameter ($\sigma = \sigma_a$ when $\omega \leq \omega_p$, $\sigma = \sigma_b$ when $\omega > \omega_p$)
- γ is the spectral peak shape parameter, typically $\gamma = 3.3$ for the JONSWAP spectrum
- $A_\gamma = 1 - 0.287 \ln(\gamma)$

Where Pierson Moskowitz spectrum is defined as,

$$S_{PM}(\omega) = \frac{5}{16} H_s^2 \omega_p^4 \omega^{-5} exp(-\frac{5}{4} (\frac{\omega}{\omega_p})^{-4}) \quad (3.27)$$

The remaining parameters are defined as,

- H_s , the significant wave height in meters
- ω_p is the peak frequency as defined above

Values for σ_a and σ_b are typically 0.07 and 0.09 for the JONSWAP spectrum. The JONSWAP spectrum is acceptable when $3.6 < \frac{T_p}{\sqrt{H_s}} < 5$ (DNV-GL, 2010).

3.7 Wave Forces

3.7.1 The Radiation and Diffraction Problem

The following theory is from literature written by Faltinsen (Faltinsen, 1993). When studying the linear wave induced motions, accelerations and structural loads, the problem can be split into two subproblems, described below and illustrated in Figure 3.14

- *Diffraction problem*: The body is assumed fixed, while exposed to incident waves. Relevant loads are Froude-Kriloff loads and diffraction loads. Froude-Kriloff loads are hydrodynamic loads due to incident waves. Diffraction loads occur due to the impermeable body's presence, creating so called diffraction waves (Greco, 2012).
- *Radiation problem*: The body is not exposed to incident waves and forced to oscillate with a frequency corresponding to the incident waves in the diffraction problem. This motion will generate waves, meaning energy is dissipated from the body (Greco, 2012). With regards to large volume structures, wave creating ability is an important force contribution (DNV-GL, 2011). Relevant hydrodynamic loads associated with dynamic pressure are added mass and damping. Variation of buoyancy due to body motions causes associated restoring terms.

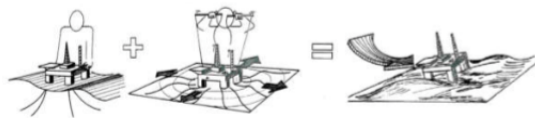


Figure 3.10: The Radiation and Diffraction Problem (Faltinsen, 1993)

Leira, Viuff and Øiseth, (Viuff et al., 2016), studied the dynamics of floating bridges and presented the first-order wave load using linear potential theory as will be described here. The radiation and diffraction problem can be expressed in the velocity potential in a fluid that satisfies the Laplace equation as,

$$\Phi = \underbrace{\varphi_0 e^{i\omega t} + \varphi_\eta e^{i\omega t}}_{\text{Diffraction problem}} + \underbrace{\sum_{k=1}^6 \phi_k \dot{u}_k}_{\text{Radiation problem}} \quad (3.28)$$

Where the subscript for the velocity potential φ and ϕ represents

- φ_0 , incident waves
- φ_η , diffracted waves
- ϕ_k , radiated waves

By satisfying the Laplace equation, and in addition the boundary conditions holding for the free surface, kinematics, the wetted body surface and the radiation. Combining Greens second identity and indirect boundary integral formulation, the velocity potential can be expressed and further the

Bernoulli equation can be applied to obtain the fluid pressure.

The wave excitation force is then obtained by integrating over the wetted surface, and further only considering velocity potential from the radiation problem the hydrodynamic action is expressed as,

$$q_j = \rho Re \left[\int_{S_d} \phi_j n_k dS \right] \ddot{u}_j + \rho \omega Im \left[\int_{S_d} \phi_j n_k dS \right] \dot{u}_j \quad (3.29)$$

Where the former expression on the right hand of the equation represents the added mass multiplied by the acceleration term, \ddot{u}_j , and the latter expression represents the damping term multiplied by the velocity, \dot{u}_j .

3.7.2 Froude-Kriloff and Diffraction Forces

The equations in the following section are obtained from literature provided by Greco (Greco, 2012). Excitation forces acting on the pontoons due to the presence of waves may be obtained by considering potential flow theory. The incident wave potential is examined. The Froude-Kriloff force is expressed as the integral of the total hydrodynamic pressure on the structure, 3.30.

$$F_{F-K} = \iint_s p_D \hat{n} ds \quad (3.30)$$

The integral is taken over the wetted surface. \hat{n} denotes the unit vector, directed normal to the body surface. For a propagating wave along the x axis, the dynamic pressure is expressed as

$$p_D = \rho g \xi_a e^{kz} \sin(\omega t - kx) \quad (3.31)$$

As a simplification, the pontoons are considered as rectangular shaped. The problem then becomes similar as to in Figure 3.11

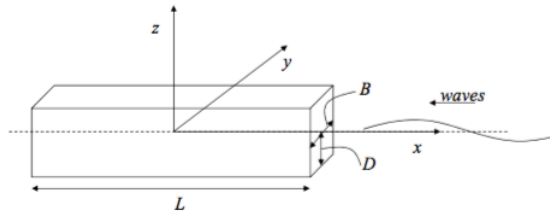


Figure 3.11: Rectangular barge exposed to incoming regular waves (Greco, 2012)

The force from the incoming wave may be decomposed into a contribution in surge and heave, while it also will contribute to a pitch moment. By integration over the wetted surface, the force (moment) components are expressed as

$$F_{F-K,1} = \rho g \xi_a B \left(\frac{1 - e^{kz}}{k} \right) 2 \sin\left(\frac{2L}{2}\right) \cos(\omega t) \quad (3.32)$$

$$F_{F-K,3} = \rho g \xi_a B e^{kz} \frac{2}{k} \sin\left(\frac{kL}{2}\right) \sin(\omega t) \quad (3.33)$$

$$F_{F-K,5} = \rho g \xi_a B e^{kz} \left(\frac{L}{k} \cos\left(\frac{kL}{2}\right) - \frac{2}{k^2} \sin\left(\frac{kL}{2}\right) \right) \quad (3.34)$$

Given the diffraction problem, motion of the structure causes disturbance in the pressure field of the fluid edging the structure. The fluid is accelerated, and by Newtons second law, diffraction force in a given direction ,i, is expressed as the added mass multiplied by the acceleration,

$$F_{D,i} = A_{ii} a_i \quad (3.35)$$

Where the acceleration is expressed as (e.g, heave)

$$a_3 = -\omega^2 \xi_a e^{kz} \sin(\omega t - kx) \quad (3.36)$$

By integration over the wetted surface of the body, the following force contributions are obtained,

$$F_{D,1} = \zeta_a A_{11}^{2D} \omega^2 \left(\frac{1 - e^{kz}}{k} \right) \cos(\omega t) \quad (3.37)$$

$$F_{D,3} = -\zeta_a A_{33}^{2D} \omega^2 e^{kz} \left(\frac{2}{k} \right) \sin\left(\frac{kL}{2}\right) \sin(\omega t) \quad (3.38)$$

$$F_{D,5} = -\zeta_a A_{33}^{2D} \omega^2 e^{kz} \left(\frac{L}{k} \cos\left(\frac{kL}{2}\right) - \frac{2}{k^2} \sin\left(\frac{kL}{2}\right) \right) \quad (3.39)$$

3.7.3 Drag and Inertia Forces On a Tubular Member

The drag and inertia forces (F_D and F_M) on a tubular member subjected to a fluid with velocity u and acceleration a may be expressed by the Morison equation (Equation 3.40) (Pettersen, 2007).

$$F_D = F_D + F_M = \frac{1}{2} \rho C_D D L u^2 + \frac{\pi D^2}{4} C_M L a \quad (3.40)$$

Where

- C_D = Drag coefficient [-]
- C_M = Added mass coefficient [-]
- D = tubular diameter [m]
- L = tubular length [m]

The drag and added mass coefficient when below mean sea level may be assumed $C_D = 0.74$ and $C_M = 2.0$. A drag coefficient of 0.9 includes the contribution from marine growth.

3.8 Static Response

The static response analysis is without consideration of the time domain. The equation for the global model relates the global external load vector, \mathbf{R} to the global nodal displacement vector \mathbf{r} through the global stiffness matrix, \mathbf{K} as stated in Equation 3.41.

$$\mathbf{R} = \mathbf{K}\mathbf{r} \quad (3.41)$$

The response is calculated by solving Equation 3.41 with respect to \mathbf{r} , and Equation 3.42 is obtained. The solution provides linear equations for the displacement of each degree of freedom in the global system.

$$\mathbf{r} = \mathbf{K}^{-1}(\mathbf{R}) \quad (3.42)$$

Where \mathbf{K}^{-1} denotes the inverse global stiffness matrix (Moan, 2003).

3.9 Static Nonlinearity

A linear static analysis can be applied long as displacements are regarded as small and the material properties are linear and elastic. Then the stiffness relationship expressed in Equation 3.41 yields. This implies a relation where the strains are linear functions of the displacement derivatives. When non linearity's occur the linear system stiffness relationship no longer yields, as the equilibrium equations no longer can be established with reference to the initial configuration. This implies that changes in geometry, material properties, and boundary conditions must be accounted for in incremental steps (Moan, 2011).

Geometrical nonlinear behavior is accounted for by modifying the system relationship to,

$$\mathbf{K} = \mathbf{K}(\mathbf{r})\mathbf{r} \quad (3.43)$$

Where $\mathbf{K}(\mathbf{r})\mathbf{r}$ is the secant stiffness, containing a linear stiffness term and a non-linear geometrical stiffness term. An analytic solution of this non linear stiffness relationship can in general not be done, and iterative methods are necessary. For solution through iterative methods, a new stiffness term is introduced as,

$$K_I(r) = \frac{d}{dr}(K(r)r) \quad (3.44)$$

$K_I(r)$, the incremental stiffness, represents the sum of stiffness contributions from linear stiffness

and additional stiffness contribution that arise due to non-linear deformations.

Material nonlinearity becomes relevant when the stress exceeds the proportionality limit and the material exhibits elasto-plastic behavior, at viscoelastic/viscoplastic behavior and creep at high temperatures. For the former, this leaves a residual plastic strain in the material when stress is reduced to zero. Hook's law as yields for linear elastic behavior changes to Equation 3.45, introducing the tangent modulus E_T , the gradient of the tangent of the stress-strain relationship curve above the proportionality limit.

$$\Delta\sigma = E_T \Delta\epsilon \quad (3.45)$$

Boundary nonlinearity is relevant for contact problems and large deformations where the relationship between the applied load and surface no longer is linear. Contact problems are complex involving several non-linear problems such as slick-slip due to friction. (Moan, 2011)

3.10 Dynamic Response

3.10.1 Dynamic Behaviour and The Equation of Motion

Vibrations in marine offshore marine structures, due to various environmental loads, can reduce platform productivity, endanger safety, affect the serviceability of the structure and have been attributing factors in several major accidents and failures in the marine and offshore industry over the last few decades. Vibrations occur due to the continuous interaction between kinetic- and strain energy (elasticity) during deformation of the system (Langen I., 1979).

The dynamic analysis implies, in contrast to a static analysis, a time dependent solution. What mainly separates static and dynamic response are the inertia loads arising throughout the structure i.e the body's ability to resist change in velocity and acceleration due to irregular, time-varying loads. By application Newton's 2nd law, d'Alembert's principle, the principle of virtual work and demand equilibrium (Langen I., 1979) the dynamic equation of motion for a system consisting of a spring and damper, is formulated as Equation 3.46.

$$m\ddot{u} + c\dot{u} + ku = Q(t) \quad (3.46)$$

$Q(t)$ denotes the external load vector. m , c and k denote the mass, damping and stiffness properties of the system. \ddot{u} , \dot{u} and u denote the system acceleration, velocity and displacement. When applied to a structure subjected to hydrodynamic waves the equation expands to 3.47 when translational and rotational degrees of freedom as described in 3.1 are included. For Equation 3.47, the terms listed below are involved. \mathbf{A} , \mathbf{C} and \mathbf{K} are further described in Section 3.10.2 to 3.10.5.

$$(\mathbf{M}+\mathbf{A})\ddot{\mathbf{r}} + \mathbf{C}\dot{\mathbf{r}} + \mathbf{K}\mathbf{r} = \mathbf{Q}(t) \quad (3.47)$$

Where

- \mathbf{M} = 6x6 mass matrix
- \mathbf{A} = 6x6 added mass matrix
- \mathbf{C} = 6x6 damping property matrix
- \mathbf{K} = 6x6 stiffness matrix
- $\mathbf{Q}(t)$ = 6x1 external load vector
- $\ddot{\mathbf{r}}$ = 6x1 acceleration vector
- $\dot{\mathbf{r}}$ = 6x1 velocity vector
- \mathbf{r} = 6x1 displacement vector

3.10.2 Added Mass

The hydrodynamic load from added mass occurs as an additional force when the body oscillates in a fluid and the pressure field around the body changes (Faltinsen, 1993). Acceleration of the fluid particles requires an additional force, and the added mass is the component of the force that oscillates in phase with the body (Pettersen, 2007).

The added mass can be obtained analytically by potential theory (Faltinsen, 1993). This method combines an assumed expression for flow around a cylinder with the Bernoulli equation to obtain an expression for the distributed pressure acting on the body. The force is obtained by integrating pressure over the projected area. The expression for the hydrodynamic force over the projected area will be a product of mass and acceleration, where the former expresses the added mass.

Another method is by use of strip theory. Strip theory will provide the same expression for added mass as previously described, however, strip theory is more applicable for obtaining the added mass of rotational motions. For strip theory the submerged section of the body is divided into thin transverse "strips", allowing expressions for the corresponding pressure on each section. The total hydrodynamic force is obtained by integration over the sections (Faltinsen, 1993). The above approaches are valid for 2D problems treating simple cross sections. However, for arbitrary shapes, added mass is obtained by experiments and numerical approximations (Pettersen, 2007).

3.10.3 Damping

Hydrodynamic damping on an oscillating body may occur as viscous damping or wave damping as described below. The damping forces are mainly of interest near the free surface (Faltinsen, 1993).

- *Viscous damping*: Due to the body's presence, flow disturbance will cause separation. The friction occurring between the structure and the fluid causes viscous damping.
- *Radiation damping*: Considering the radiation problem in Section 3.7.1, energy dissipates from the body by generated surface waves. The wave damping is related to this energy dissipation.

Damping is often related to slow drift motions that can excite large resonance behavior (Greco, 2012). Anchor lines may also contribute to damping (Faltinsen, 1993), however, this is not relevant for this thesis.

The damping coefficient implemented in the equation of motion may be expressed as a linear combination of \mathbf{M} and \mathbf{K} by the Rayleigh-damping (Langen I., 1979)

$$\mathbf{C} = \alpha_1 \mathbf{M} + \alpha_2 \mathbf{K} \quad (3.48)$$

Where α_1 and α_2 can be determined if the damping ratio is known, as,

$$\alpha_1 = \frac{2\omega_1\omega_2}{\omega_2^2 - \omega_1^2}(\lambda_1\omega_2 - \lambda_2\omega_1) \quad (3.49)$$

$$\alpha_2 = \frac{2(\omega_2\lambda_2 - \omega_1\lambda_1)}{\omega_2^2 - \omega_1^2} \quad (3.50)$$

3.10.4 Frequency Dependence of Added Mass and Damping

The hydrodynamic added mass and damping shows strong frequency dependence because it is related to the mode of oscillation. As Faltinsen states, in *Sea Loads on Ships and Offshore Structures* (Faltinsen, 1993), 'that means that added mass in heave for a body is not necessarily the same as added mass in sway'. Numerical estimations have been done that show e.g. large differences in added mass and damping when the frequency goes towards 0 or oppositely, towards infinity.

As described in the model formulation in Chapter 6, the frequency dependent added mass and damping values implemented in the floating bridge model are taken from the NPRA's report on the Bjørnafjorden bridge. The modeling allows for the added mass and damping corresponding to the chosen wave period for the incoming, regular wave is included in the model.

3.10.5 Restoring

The restoring forces will act to bring the structure to equilibrium when it is forced out of this state. In the feasibility study, the restoring forces were given for heave and pitch. Mathematically, these can be found from the following equations (Greco, 2012)

$$C_{33} = \rho g A_{wp} \quad (3.51)$$

$$C_{55} = \rho g V GM_L \quad (3.52)$$

A_{wp} represents the waterplane area of the submerged structure, here the cross sectional area of the pontoon. V is the displaced volume of the pontoon. GM_L is the longitudinal metacentric height (Faltinsen, 1993). Implemented values for restoring in heave and pitch are located in the model formulation. As seen in equation 3.52, the restoring force changes with the displaced volume of the pontoon. Variations of displaced volume are not implemented in the solution formulation in the model, but is assumed to be accounted for by modelling the stiffness as spring elements with stiffness contributions.

3.10.6 Eigenfrequencies and Mode Shapes

The dynamic equilibrium equation for a body is stated as Equation 3.53. The equation can be modified to an eigenvalue problem on the general form to obtain structural eigenfrequencies (Langen I., 1979).

$$\mathbf{M}\ddot{\mathbf{r}} + \mathbf{C}\dot{\mathbf{r}} + \mathbf{K}\mathbf{r} = \mathbf{Q}(t) \quad (3.53)$$

By studying a free, undamped vibration, the natural frequencies of a system can be found by applying

$$\mathbf{C} = 0 \quad (3.54)$$

$$\mathbf{Q}(t) = 0 \quad (3.55)$$

The equation of motion is then,

$$\mathbf{M}\ddot{\mathbf{r}} + \mathbf{K}\mathbf{r} = 0 \quad (3.56)$$

Assuming harmonic vibration,

$$\mathbf{r} = \phi \sin(\omega t) \quad (3.57)$$

$$\ddot{\mathbf{r}} = -\omega^2 \phi \sin(\omega t) \quad (3.58)$$

Where,

- ω : frequency [rad/s]
- ϕ : eigenvector

The modified equilibrium Equation 3.56 can then be expressed as an eigenvalue problem on general form, Equation 3.59.

$$(\mathbf{K} - \omega^2 \mathbf{M})\phi = 0 \quad (3.59)$$

Solving will provide a set of eigenfrequencies for the undamped, free vibration system along with ϕ , the eigenvector that determines the shape (mode) of vibration the structure oscillates with at the frequency ω_n (Langen I., 1979). This natural eigenfrequency depends on the stiffness to mass ratio for the system, as Equation 3.60,

$$\omega_n = \sqrt{\frac{k}{m}} \quad (3.60)$$

With the corresponding natural period,

$$T_n = \frac{2\pi}{\omega_n} \quad (3.61)$$

3.11 The Finite Element Method

The following theory is collected from literature written by Ottosen and Petterson (Ottosen, 1992). The finite element method is a well known numerical approach in the field of engineering to obtain an approximate solution to complex differential equations that are challenging to solve for models covering a wide range of physical phenomena. One of the reasons for the finite element methods popularity lies in the methods versatility. The method can be applied to a wide range of body shapes exposed to different loads and environments and many well-established computer programs for this type of structural analysis exist (e.g ANSYS, ABAQUS, SESAM, DYNA2D and DYNA3D). However, users of the finite element method should study the concept and assumptions that lie behind such that the program can be used with greater benefit and avoid misinterpretation. Sufficient training in applying the method along with good judgement are necessary to evaluate the vailidity of complex models.

Differential equations are characterized by their validity within a certain expanse. By dividing the expanse of interest into a finite number of elements with one-, two-, or three dimensions, approximated solutions to the differential equations valid within each element expanse may be obtained. The division of a structure is named the "mesh", where the solution should converge as the mesh size decreases.

3.11.1 Method Outline

To briefly describe the method outline, the finite element method applied to a simple spring structure presented by Ottosen and Petterson (Ottosen, 1992) will be applied. The example systematically presents how the system response can be obtained by following the steps. The system is a fictive structure consisting of two elastic springs attached longitudinally (parallel to the x-axis). The springs have stiffness k_1 and k_2 and exposed to the external loads F_{x1} , F_{x2} , F_{x3} .

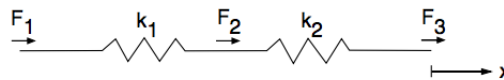


Figure 3.12: System of connected elastic springs (Ottosen, 1992)

Discretisation

The Figure below shows the division of the structure into elements (numbers enclosed by circle), nodes and with the spring stiffness properties.

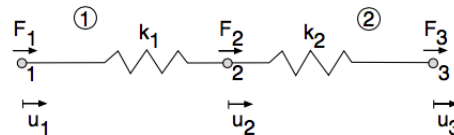


Figure 3.13: Discretized system (Ottosen, 1992)

Element Analysis

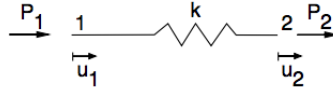


Figure 3.14: Discretized single element (Ottosen, 1992)

For a single element, equilibrium of can be expressed through Equation 3.62, which expresses the system response through Hook's law.

$$N = k(u_2 - u_1) \quad (3.62)$$

The link between the element forces and displacements can then be written,

$$P_2 = k(u_2 - u_1) \quad P_1 = k(u_1 - u_2) \quad (3.63)$$

Considering system equilibrium, the sum of external forces is zero, $P_1 + P_2 = 0$. These equations can be written on matrix form,

$$\begin{bmatrix} k & -k \\ -k & k \end{bmatrix} \begin{bmatrix} u_1 \\ u_2 \end{bmatrix} = \begin{bmatrix} P_1 \\ P_2 \end{bmatrix}$$

Also known as the element stiffness relation

$$\mathbf{K}^e \mathbf{a}^e = \mathbf{F}^e \quad (3.64)$$

Where \mathbf{K} is the element stiffness matrix containing material properties, \mathbf{a} is the nodal displacement vector containing the nodal degrees of freedom, and \mathbf{F} is the element force vector.

System Analysis

Equation 3.64 expresses the element stiffness relation for a single element. By global equilibrium, a relation between the local elements and global system is established as u_i^j , where i denotes the local node number and j the element number. For the system of two springs connected at node 2, the following yields,

$$u_2 = u_1^2 = u_2^1 \quad (3.65)$$

The element stiffness relation for element 1 can be expressed as,

$$\begin{bmatrix} k_1 & -k_1 \\ -k_1 & k_1 \end{bmatrix} \begin{bmatrix} u_1 \\ u_2 \end{bmatrix} = \begin{bmatrix} P_1^1 \\ P_2^1 \end{bmatrix} \quad \begin{bmatrix} k_2 & -k_2 \\ -k_2 & k_2 \end{bmatrix} \begin{bmatrix} u_1 \\ u_2 \end{bmatrix} = \begin{bmatrix} P_1^2 \\ P_2^2 \end{bmatrix} \quad (3.66)$$

Globally, we obtain the expanded element stiffness matrices for element 1 and 2,

$$\begin{bmatrix} k_1 & -k_1 & 0 \\ -k_1 & k_1 & 0 \\ 0 & 0 & 0 \end{bmatrix} \begin{bmatrix} u_1 \\ u_2 \\ 0 \end{bmatrix} = \begin{bmatrix} P_1^1 \\ P_2^1 \\ 0 \end{bmatrix} \quad \begin{bmatrix} 0 & 0 & 0 \\ 0 & k_2 & -k_2 \\ 0 & -k_2 & k_2 \end{bmatrix} \begin{bmatrix} 0 \\ u_1 \\ u_2 \end{bmatrix} = \begin{bmatrix} 0 \\ P_1^2 \\ P_2^2 \end{bmatrix} \quad (3.67)$$

When establishing relations for the global system, we get

$$\mathbf{K}\mathbf{a} = \mathbf{F} \quad (3.68)$$

$$\begin{bmatrix} k_1 & -k_1 & 0 \\ -k_1 & k_1 + k_2 & -k_2 \\ 0 & -k_2 & k_2 \end{bmatrix} \begin{bmatrix} u_1 \\ u_2 \\ u_3 \end{bmatrix} = \begin{bmatrix} F_1 \\ F_2 \\ F_3 \end{bmatrix}$$

Boundary Conditions

Due to \mathbf{K} 's symmetry properties, $\det[\mathbf{K}] = 0$. The system above has no prescribed a priori displacements and the system is therefore not possible to solve. To avoid rigid body motions, e.g nodal point u_1 is restricted against displacement. This effect is applied to the system by setting the first row in the system relation and the first column of the system stiffness matrix to zero such that,

$$\begin{bmatrix} k_1 + k_2 & -k_2 \\ -k_2 & k_2 \end{bmatrix} \begin{bmatrix} u_2 \\ u_3 \end{bmatrix} = \begin{bmatrix} F_2 \\ F_3 \end{bmatrix}$$

Finding Global Displacements

The expression above is now transformed to a linear set of equations that may be solved for the displacements by Equation 3.69. Stresses may further be obtained from strain and displacement functions.

$$\mathbf{a} = \mathbf{K}^{-1}\mathbf{F} \quad (3.69)$$

3.11.2 Method Outline for a Simple Beam Element

The deflection for one beam element can be expressed through the shape function, \mathbf{N} , and displacement vector \mathbf{a} . The displacement vector contains the number of unknowns, not the number of nodal points as in the 1-D problem described in the previous section.

$$w = \mathbf{N}^e \mathbf{a}^e \quad (3.70)$$

As bending moments are a function of the second derivative of deflections, the following is defined,

$$B^e = \frac{d^2 \mathbf{N}^e}{dx^2} \quad (3.71)$$

When establishing the element stiffness relation for a beam element, the element boundary vector, \mathbf{f}_B , and element load vector, \mathbf{f}_l must be considered such that,

$$\mathbf{K}\mathbf{a} = \mathbf{f} = \mathbf{f}_B + \mathbf{f}_l \quad (3.72)$$

The components of the stiffness relation are,

$$\mathbf{K} = \int_a^b \mathbf{B}^T EI \mathbf{B} dx \quad (3.73)$$

$$\mathbf{f}_b^e = [\mathbf{N}^{eT} V]_{L\alpha} - \left[\frac{d\mathbf{N}^{eT}}{dx} M \right]_{L\alpha} \quad (3.74)$$

$$\mathbf{f}_l^e = \int_{L\alpha} \mathbf{N}^{eT} q dx \quad (3.75)$$

With the lateral load, shear force and bending moment is expressed as,

$$q = -\frac{dV}{dx} \quad V = \frac{dM}{dx} \quad M = -EI \frac{d^2w}{dx^2} \quad (3.76)$$

3.12 Ship Collision

3.12.1 General Considerations

According to DNV GL CP C204, ship collisions with offshore structures commonly distinguish between powered and drifting collisions. For an analysis purpose, the collision is characterized by large amounts of kinetic energy absorbed as strain energy purely in the ship, jacket or distributed between both. Analysis of global damage on steel jackets subjected to ship collision is commonly performed for single cases due to the uniqueness of each ship-jacket system. For reduced complexity and time consumption, the collision analysis often separates the external hydrodynamic loads and collision mechanics from the internal energy distribution between the collision elements. When analysing the internal mechanics it is assumed that the contact point between the struck structure and the vessel is in equilibrium and that force-deformation curves (Figure 3.16) for the two elements is representative.

In DNV GL RP C204 there are three design stages for energy dissipation in ship collision analysis as can be seen in Figure 3.15. The ductile design approach anticipates that the installation dissipates much more energy than in the ship and therefore faces large plastic deformations. The shared energy design is the most realistic scenario where the energy is dissipated in both the vessel and installation. The strength design considers the energy in the ship to be opposite of the ductile design.

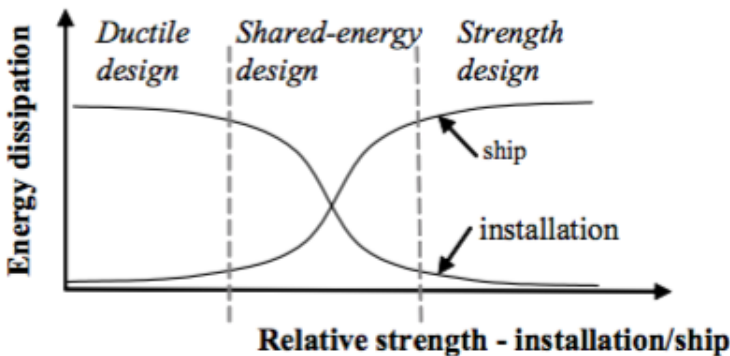


Figure 3.15: Strain energy distribution between ship and offshore installation for a fictive collision scenario (Det Norske Veritas, 2010)

The dissipated amount of strain energy can be expressed through conservation of energy before and after the collision. The strain energy, E_s is taken as Equation 3.77.

$$E_s = \frac{1}{2} M_s V_s^2 \quad (3.77)$$

Where M_s is the mass of the ship (including hydrodynamic added mass) and V_s is the impact velocity.

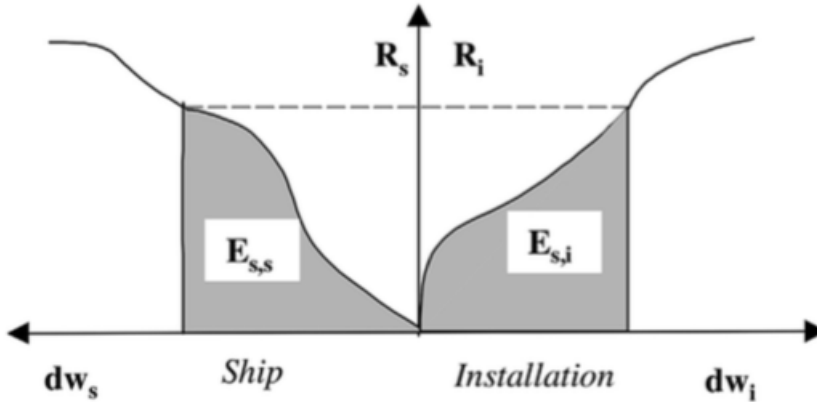


Figure 3.16: Force-deformation curve between ship and jacket (Det Norske Veritas, 2010)

The amount of dissipated strain energy equals the area under the force/deformation curve and satisfies the following conservation of energy where subscripts s and i denote the ship and installation, respectively.

$$E_s = E_{s,s} + E_{s,i} = \int_0^{w_i, max} R_s dw_s + \int_0^{w_i, max} R_i dw_i \quad (3.78)$$

3.12.2 Static vs. Dynamic Analysis

There are significant differences in the approach for static and dynamic analysis of ship collision. Using USFOS, the static impact is considered with a constant velocity. This analysis method gives a result without using significant computational time. All dynamic effects are however disregarded. In a dynamic analysis, the mass is given an initial velocity. During the analysis, the mass velocity is reduced and may eventually experience change of sign when exposed to the movement of kinetic energy. Modeling of the ship collision in this thesis is further described in Section 6.8.

According to Amdahls research in 1993 (Yu and Amdahl, 2001-2018), the results from static and dynamic analysis in collision with jackets do not show great differences, supported by the argument that *'the jacket response for the impact scenario considered can be reasonably well predicted by a static approach, because the impact duration is relatively long compared to the fundamental period of the governing motion...'*. Considering the jacket model in USFOS and the full model in ANSYS, these structures will have completely different eigenperiods, where the floating bridge will have periods around one minute while the jacket might have eigenperiods close to only a few seconds. The dynamic effects will therefore be of importance when evaluating collision with the floating bridge. As found in Furnes and Amdahls publication "Ship Collisions with Offshore Platforms", a dynamic analysis is due to the excited vibrations in the platform from the kinetic energy (Furnes and Amdahl, 1980).

Design Loads and Permitted Response

Floating bridges will, in addition to service loads from traffic, be exposed to powerful forces from the environment. Compared to conventional bridges that mainly are exposed to loads from wind, floating bridges must, in addition, withstand forces from the marine environment. Waves, hydrostatic pressures, tidal variations, marine growth and in special cases ice loads must be accounted for when establishing a sufficient structural design (Chen and Duan, 2013). The loads will strongly depend on site conditions.

Characterising the correct behavior of the specific marine environment for the structure is very important to ensure the safe and efficient performance of activities (Greco, 2012). Watanabe and Utsunomiya (Watanabe and Utsunomiya, 2003), classify loads for floating bridges into four categories as presented in Table 4.1. The main categories are principle, secondary and particular equivalent to the above mentioned.

This section presents a description of the relevant loads applied to the model in ANSYS Mechanical. The applied loads are from wind and current and considered as static loads with return periods of 1, 100 and 10 000 years. The weather data is provided from the co-supervisor in the NPRA.

Table 4.1: Categorized loads for floating bridges (Watanabe and Utsunomiya, 2003)

Primary Loads	Secondary Loads
Dead load	Wind load
Live load	Wave and Swell effects
Impact load	Effect of earthquake
Earth Pressure	Temperature effect
Hydrostatic pressure	Current load
Particular Primary Loads	Particular Secondary Loads
Tidal variation effect	Effect of tsunami and storm
Effect of seabed deformation	Collison loads from ships and drifting materials
Effect of support movement	Effect of marine growth
Snow/Ice load	
Centrifugal load	

4.1 Considerations on Weather Measurements

The weather data from the Halsafjord provided from the NPRA show large deviations between extreme calculated statistics based on data and observations. Most likely, model results from the middle of the fjord are the most representative for larger sections of the bridge.

Deviations occur due to shielding from land and effects of swirls that are easily set up further south of the fjord. This means that results may easily be distracted depending on the methodology and choice of reference data. This has probably led to an underestimate of extreme wind from the south on both measuring masts. It is therefore proposed that the 100-year value of 10-minute medium wind velocity of 36.0 m/s be used in the "design basis" for wind across the bridge, while a direction coefficient of 0.85 is used for wind along the bridge at Halsafjorden.

4.2 Tidal Variations

The tide in the relevant area of the bridge will cause an increase and decrease in sea level at the installation area for the bridge. High tide will increase the buoyant force on the pontoon structure due to larger displaced volume, while low tide will affect oppositely and decrease the buoyant force on the pontoon structure (Reinertsen, 2013).

Tidal variations at the installation site is an increase/decrease of +/-0.75 m measured relative to the mean sea level. It is of high prioritization that the tidal variation does not impose misalignment between girder sections during installation. The effect of tidal variation will be included in the analysis as an additional applied load, and conservatively, a tidal variation of 1 m is assumed. Multiplied by the water plane stiffness in heave, this opposes a load of 17 450 kN (rø).

4.3 Static Wind Load

The load contribution from wind is estimated based on guidance from Eurocode NS-EN 1991-1-4:2005 combined with experience from former comparable projects. Wind measurements performed in the wake of the chosen analysis report proclaims that the estimations based on the Eurocode are slightly conservative.

Force contributions from mean wind may be calculated by Equation 4.1,

$$F_m(z) = \frac{1}{2} \rho_a V_m(z)^2 C_D H \quad (4.1)$$

The only provided information on wind speeds from the NPRA consider wind speeds with 100 year return periods where the 100-year value of 10 min medium wind velocity of 36.0 m/s should be used in the "design basis" for wind across the bridge resulting in an applied force of 4.366 kN/m.

4.4 Current Load

From currents, viscous forces occur due to tangential stresses (causing frictional resistance) and pressure losses along the body surface. The former causes a shear/drag force, while the latter induced a pressure drag force. An important parameter is the Reynolds number, which classifies the degree of turbulence in the flow. As the Reynolds number increases to a certain level, turbulent flow occurs along the surface of the body. This generally leads to a higher friction drag contribution and a lower contribution from pressure drag (Faltinsen, 1993).

As defined in the DNV RP-C205, forces from a steady current may be given as,

$$F = C \cdot U_c^2 \quad (4.2)$$

Where

- C = current coefficient, usually determined by empirical formulas
- U_c = current velocity

The current velocity may be decomposed into normal components in the cross flow and longitudinal direction. For column based structures as the jacket in this thesis, the cross-flow creates an inline drag force which is of main interest. The longitudinal component mainly contributes to shear force, which usually is not accounted for. The inline drag force may be calculated as,

$$F_D = \frac{1}{2} \cdot \rho_w \cdot C_D \cdot A \cdot U_{cN}^2 \quad (4.3)$$

The table below shows the calculated and applied forces from current applied to the model in ANSYS Mechanical. The current force on the pontoons is applied as a point load. Considering modeling of the jacket by use of a concentrated mass element situated in the bridge birder and spring elements adding the contributing horizontal stiffness, (as described in Chapter 6), the current force on the jacket will be approximated from an assumed uniform flow inducing a moment on the girder and a drag factor of 0.9 for a rough cylinder.

Table 4.2: Calculated static forces on the floating bridge, including current speed, direction and corresponding return periods for the Halsafjord

Pontoons			
Return Period [year]	Degree [deg]	Other Current Speed [m/s]	Applied Force [kN]
1	240-300	0.8	145 kN
100	240-300	1	227 kN
10 000	240-300	1.17	658 kN
Jacket			
Return Period [year]	Degree [deg]	Other Current Speed [m/s]	Applied Force [kNm]
1	240-300	0.8	479 kNm
100	240-300	1	749 kNm
10 000	240-300	1.17	2164 kNm

4.5 Regular Wave Loads

The regular wave forces applied to the pontoons and jacket are plotted in Figure 4.1 and 4.2 for unit amplitude and wave period 5 and 6 seconds. The frequency dependent added mass is read from tables and included in the load calculation where it is relevant. Hydrodynamic damping is taken from the feasibility study and added in sway, heave, and roll to the spring elements. The Rayleigh damping coefficients are estimated by the procedure described in section 3.3.3, assuming 2 % percent of critical damping for frequency 1 and 10 (Brede, 2017).

The regular waves are applied with components in sway, heave, and roll. The regular wave force is applied as a moment about the x-axis about the mass node on the jacket. The applied wave forces for the regular wave with period 5 and 6 seconds are shown in the Figures below.

The arch shape of the bridge means that the incoming waves will be at different phases when meeting the pontoons (Brede, 2017). This is accounted for by calculating a delay in the regular wave force for each regular wave period. The delay calculations are attached in the excel workbook *delay* in the digital appendix.

Table 4.3: Values for estimated significant wave height (H_s) and peak period (T_p) for the Halsafjord, used in previous face of the Halsafjorden bridge development project (NPR).

	Direction	Parameter	1 year	100 year	10 000 year
Locally Wind Generated Sea	270	Hs [s]	1.2	1.8	2.1
Locally Wind Generated Sea	270	Tp [s]	≤ 5	≤ 6	≤ 7
Locally Wind Generated Sea	225/315	Hs [s]	0.8	1.2	1.4
Locally Wind Generated Sea	225/315	Tp [s]	≤ 5	≤ 6	≤ 7
Locally Wind Generated Sea	0/180	Hs [s]	0.4	0.6	0.7
Locally Wind Generated Sea	0/180	Tp [s]	≤ 5	≤ 6	≤ 7
Swell	250-290	Hs [s]	0.3	0.45	0.53
Swell	250-290	Tp [s]	6-18	6-18	6-18

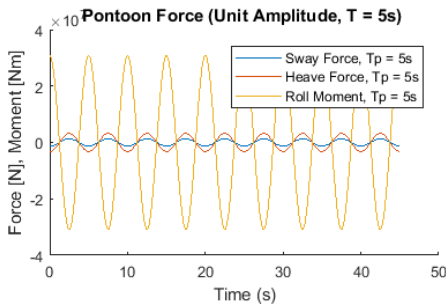


Figure 4.1: Pontoon force at T = 5s, Unit Amplitude = 1 m

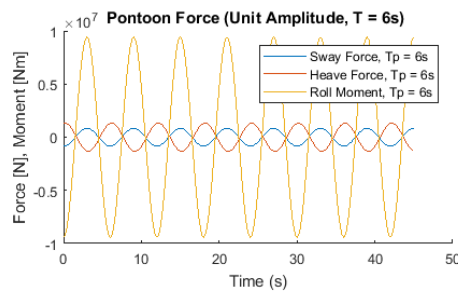


Figure 4.2: Pontoon force at T = 6s, Unit Amplitude = 1 m

4.6 Traffic and Pedestrian Loads (Eurocode)

Traffic and pedestrian loads are accounted for as the weight of vehicles and pedestrians using the roadway. Applied load parameters are similar to employed in the analysis summary. Two load cases from the Eurocode are applied, LM1 and LMV. Calculated equivalent line loads are taken from the analysis summary provided by the NPRA. Applied loads are summarized in Table 4.4. **LM1** applies to members where the influence length is below 500 m. **LMV** governs members where the length exceeds 500 m.

Table 4.4: Traffic and pedestrian loads for associated bridge model (Statens Vegvesen, 2015)

Location/Description	Axial Load	UDL
LM1		
Lane 1	$P_1 = 2 \times 300 \text{ kN}$	$q_1 = 16.2 \text{ kN/m}$
Lane 2	$P_2 = 2 \times 200 \text{ kN}$	$q_2 = 7.5 \text{ kN/m}$
Lane 3	$P_3 = 2 \times 100 \text{ kN}$	$q_3 = 7.5 \text{ kN/m}$
Remaining Area		$q_{ra} = 2.5 \text{ kN/m}$
Pedestrian Path		$q_p = 7.5 \text{ kN/m}$
LMV		
All traffic loading		$q = 9 \text{ kN/m}$
Pedestrian/Cycle		$q = 2 \text{ kN/m}$

Eurocode - LMV

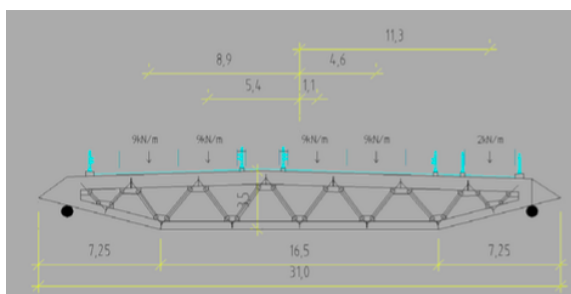


Figure 4.3: Eurocode LMV: Traffic Loading ($r\phi$).

4.7 Permitted Response

Based on the functional criteria defined in the analysis report, boundaries are set to limit permitted response in the floating bridge from external loads. The limits are presented in Table 4.5. The NPRA's handbook for bridge design N400 states that vertical deflection should be limited to $L/350$. However, as the span length is not clearly defined for the floating bridge, the report states that vertical deflection is limited to 1 m when 70 % of design traffic load is applied. Further, the requirements for deflection and rotation demand a minimum vertical pontoon stiffness of 9.1 kN/m and minimum roll stiffness of 2500 MNm/rad.

The maximum allowable accelerations are defined from N400 Ch. 5.1.3.1, stating that for bridges without pedestrian load the acceleration is limited to 1.0 m/s^2 while limited to 0.5 m/s^2 for bridges with significant pedestrian loading. These requirements yield for a one year storm, whereas the

design must be able to withstand less frequent storms causing higher impact energy. To avoid risk to human the bridge will be closed during extreme weather, however, the response of the bridge should still be limited to avoid costly damage and downtime.

Yield strength of the material, S460 grade steel, is 460 MPa ($r\sigma$).

Table 4.5: Permitted Response Parameters ($r\sigma$)

Motion	Load	Criterion
Vertical Deflection Due to Traffic	0.7xTraffic	1 [m]
Rotation about bridge axis (Roll) due to traffic loads	0.7xTraffic	1 [deg]
Rotation about bridge axis (Roll) due to environmental loads	1 year storm	1.5 [deg]
Vertical Acceleration	1 year storm	0.5 [m/s ²]
Horizontal Acceleration	1 year storm	0.6 [m/s ²]

4.8 Ship Collision

Floating bridges crossing channels with vessel traffic are exposed to ship collision scenarios. Although these accident types have a low probability, the consequences may be severe and cause flooding, loss of stability and even detachments between the girder and supporting columns. From the NPRAs report for the crossing of the Bjørnafjord, three main collision events have been identified as relevant for the proposed concept:

- Head-On-Bow collision with pontoons
- Head-On-Bow collision with the bridge girder
- Deckhouse collision with the bridge girder

Risk of head-on collision with the bridge girder may be approximately eliminated by ensuring sufficient height of the bridge deck. From NPRAs studies, the deckhouse collision with the bridge girder is of insignificant importance. This leaves the option of concern to be head on bow collision with pontoons. Monte-Carlo simulations show collision energies of up to 250 MJ for the pontoon connecting the high- and floating bridge, while for the remaining pontoons yield collision energies in 110 MJ of magnitude.

4.8.1 Summary of Findings From Vessel Traffic and Collision Analysis

AIS data provided by Norwegian Coastal Administration (through the co-supervisor in the NPRAs) in the relevant location proposed increased ship traffic of large RORO (Roll-On-Roll-Off) vessels due to the proposed weekly call from the port in Surnadalen. These vessels, with 9000 DWT are proposed as the worst case ship for the 10 000 year collision scenario in the area. The specific ice-reinforced vessel, SC Connector, is in operation today.

SC Connectors maximum summer displacement measures 14 800 tonnes, while 13 000 tonnes are applied in calculations as the cargo ship is rarely in a maximum loaded condition. By estimated collision speed of 10.5 knots (5.4 m/s) and added mass factor of 0.1 for surge motion, the collision energy may be estimated as 208 MJ from Equation 4.4.

$$E = \frac{1}{2}mv^2 \quad (4.4)$$

Applied Software

5.1 ANSYS Mechanical APDL

ANSYS Mechanical APDL is an advanced finite element program built up by over 100 000 lines of code widely used for static and dynamic analysis on electronics, mechanical structures, heat transfers and fluids. The finite element program solves great advanced problems by following the theory of the finite element analysis. ANSYS offers also ANSYS Workbench that offers a "point and click" approach in a graphical user interface. The ANSYS Mechanical APDL allows the user to write the program in ANSYS Parametric Design Language (APDL) opening for a set up more complicated operations that do not apply as standards in the Workbench GUI (Moaveni, 2015).

The modeling and analysis is approached by establishing necessary parameters, elements, materials, constant sets and cross sections in the preprocessor. The geometric modeling is based on a bottom-up approach, where lines are established between key points, areas between lines, and so on. The geometric segments are assigned their belonging properties, depending on element type. When this is established, the meshing may be performed such that the model is divided into a finite number of elements. In closing, relevant boundary conditions restraining nodes and external forces are applied.

5.2 Matlab

MATLAB (MATrix LABratory) is a programming language applied for among others mathematical computations, modeling, simulations, development of algorithms and analysis of data. Data elements are built in non-dimensional arrays making it convenient to solve matrix and vector problems through a faster build up than languages as C or Fortran would require (Attaway, 2009). It is possible to run ANSYS through Matlab in batch mode for e.g. optimization, but this was not considered required as the modifications to the ANSYS scripts were minor and a fair amount of the postprocessing was done in the ANSYS GUI. In this thesis Matlab is used mainly for postprocessing results through graphical plots and array interpretation. Scripts are also created for coarse weight and draft calculations related to buoyancy.

5.3 USFOS

USFOS (Ultimate Strength of Framed Offshore Structures) is an advanced program for non-linear static and dynamic analysis of fixed offshore structures in both intact and damaged condition. This leading software tool was developed by SINTEF Marintek in collaboration with NTNU and has been applied in the industry since 1985. The core team behind the development of USFOS consisted of Prof. Jørgen Amdahl, Dr. Tore Holmås, Dr. Øyvind Hellan and Dr. Ernst Eberg (USFOS, 2018). With its intuitive user interface, the program has contributed to significant cost savings for finite element analysis in the industry. Its combination of coarse finite element modeling while still obtaining results with excellent accuracy, and benefit for understanding safety considerations for offshore structures. The program has been developed to provide results that satisfy design equations for Ultimate Limit States (ULS) (USFOS, 2018).

USFOS can with high accuracy simulate the structural behavior from the first yield to collapse as a consequence of thermal or mechanical loading and has an effective formulation to establish structural members in a damaged condition.

In this thesis, an USFOS model of the Kvitebjørn jacket is provided by Prof. Jørgen Amdahl. The model is modified to fit length requirements regarding water depth and elements representing drilling equipment are removed. USFOS is further used to obtain structural parameters such as effective mass contribution and the horizontal stiffness contribution that was modeled in ANSYS. This is further described in chapter 6.7. A ship collision scenario is modeled and analyzed as described in section 6.8.

Chapter 6

Model Formulation

6.1 Model development and geometry

The models created in ANSYS are shown in the figures below (figure 6.1 and 6.2). Details on modeling of each section is presented throughout this chapter. The modeling approach is based on the experience the author gained during the project thesis work that treated modeling of a suspension bridge on floating towers.

For the two concepts (I-jacket and II-jacket), the effect on the response by including a high bridge is examined. Four models are therefore developed and compared in this thesis, but with main focus on the concept with the high bridge. What separates the models is the global geometry in terms of including a high bridge for the I- and II-jacket concept. The bridge arc shape, length, number and size of pontoons, number and properties of stay cables and cross-section area of the bridge girder sections are held constant when examining the effect of high bridge modeling.

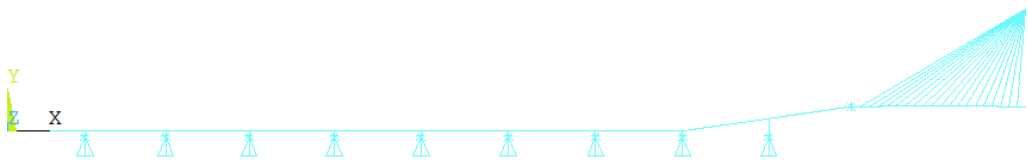


Figure 6.1: I-jacket bridge with high bridge



Figure 6.2: II-jacket bridge with high bridge

6.2 ANSYS Elements and Load Types

The ANSYS element library predefines a wide range of element types. As presented below, the three elements used in the global model are beam element BEAM189, spring element COMBIN14 and concentrated mass element MASS21. The table below presents an overview of the application of different element and load types applied to the model.

Table 6.1: Assigned element and load types types to the modeling sections and forces of the ANSYS model

Section	Element	Section	Element
Main girder	BEAM189	Buoyancy Force	Point Load
Mass contribution from jacket	MASS21	Current Force	Point Load
Pontoon	MASS21	Static Wind Pressure	Uniform Distributed Load
Structural pontoon stiffness	COMBIN14	Pedestrian Load	Uniform Distributed Load
Cable System	COMBIN14	Vehicle Load	Uniform Distributed Load

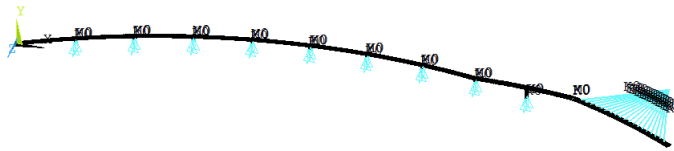


Figure 6.3: Meshed ANSYS model of the I-Jacket bridge

6.2.1 Beam Element - BEAM189

BEAM189 (figure 6.5) is a 3-D quadratic (3 noded) element suitable for modeling thick beam structures. The element relies on Timoshenko beam theory and includes shear deformation effect. At each node there are six degrees of freedom, one translational and one rotational in- and about each of the x-,y- and z-direction.

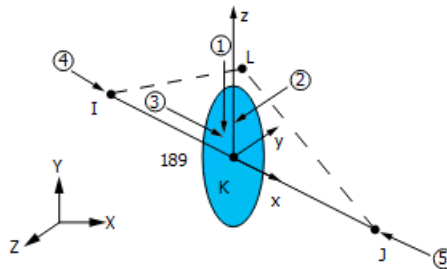


Figure 6.4: ANSYS element BEAM189 (ANSYS, 2018)

BEAM189 will be applied to model the main box girder of the bridge along with the pontoon towers.

6.2.2 Concentrated Mass Element - MASS21

MASS21 is a point element with six degrees of freedom, one translation and one rotational in and about each of the x-,y- and Z-directions. This element type allows adding properties regarding directional mass in x-,y- and z-direction along with corresponding moments of inertia.

By application of this element, mass and inertia properties can be assigned making it suitable for modelling the pontoon and the effective mass of the jacket. This is however, used to simplify the modelling of pontoons and will provide a coarse representation of e.g. the added mass.

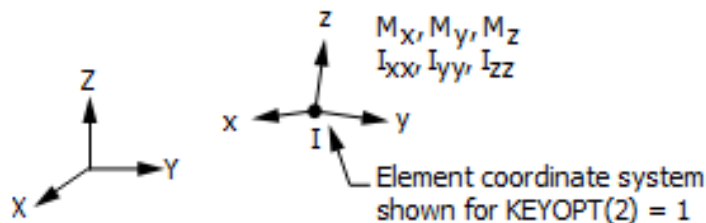


Figure 6.5: ANSYS element MASS21 (ANSYS, 2018)

6.2.3 Combination Spring Element - COMBIN14

The combination spring element COMBIN14 is used to model stiffness properties of pontoons, the jacket and the cable stays with pretension. These elements can also be used when applying damping properties for the dynamic analysis. This spring element allows for modeling of torsional and longitudinal stiffness. The former applies to roll and pitch motion. Longitudinally, it is applied for horizontal stiffness (surge or sway), and vertical restoring in heave.

The principles of the element as illustrated in the ANSYS library is shown in figure. 6.6.

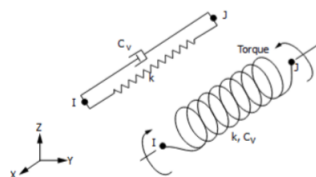


Figure 6.6: COMBIN14 Spring Element (ANSYS, 2018)

6.3 Main Girder

Equivalent Plate Thickness

The section properties vary along the main girder as shown in Figure 6.9. The cable stay bridge has girder cross section H1, while for the floating section, section F1 and a strengthened section S1 applies. The strengthened section has an increase in plate thickness by 50 %, compared to F1. The sections are modeled as BEAM189 elements. Equivalent thickness parameters of the plate components are given in the summary report. A summary of parameters are presented in Table 6.2.

Custom Cross Section

To create a cross section equivalent to modeled by the NRPA, a custom section is established as the predefined ANSYS cross sections do not offer the specific girder shape. The simplified cross section is shown in Figure 6.8, while Figure 6.7 shows the cross section including stiffeners. The hexagonal cross section is established by defining one area per plate, establish common boundaries and store the user mesh file. The custom cross sections are taken from the modeling done by Brede for the master thesis treating the Bjørnafjorden floating bridge for NTNU in 2017 (Brede, 2017). These are stored in the digital appendix as *S1.SECT*, *F1.SECT* and *H1.SECT*.

Table 6.2: Modeled plate thicknesses

General Dimensions	S1 [m]	F1 [m]	H1 [m]	Equivalent Plate Thickness	S1 [m]	F1 [m]	H1 [m]
Total width	15	15	15	Top Plate (Plate 3)	0.035	0.025	0.046
Cross Section Height	5	5	5	Upper inclined web (Plate 1)	0.03	0.02	0.020
Height Lower Inclined Web	3.5	3.5	2.5	Upper inclined web (Plate 2)	0.03	0.02	0.036
Width Upper Inclined Web	2.2	2.2	2	Lower inclined web (Plate 4)	0.03	0.02	0.036
Width Lower Inclined Web	7.25	7.25	4	Lower inclined web (Plate 5)	0.03	0.02	0.020
				Lower Plate	0.035	0.02	0.036

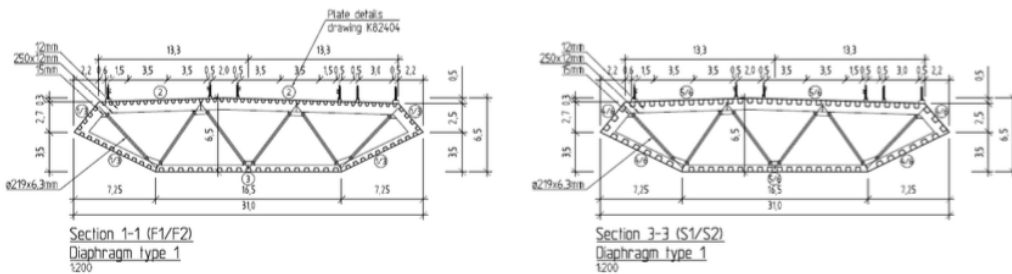


Figure 6.7: Cross section sketch of the main girder for the floating and strengthened sections

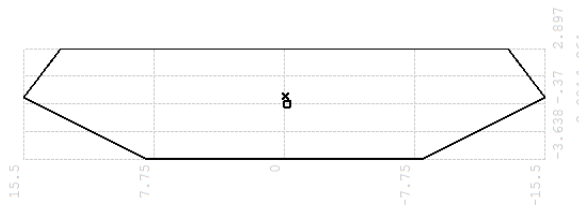


Figure 6.8: Custom ANSYS cross section ($r\ddot{o}$)

6.4 Pontoons

The floating concrete pontoons are installed with an equal span distance of 200 m. The I-jacket concept has nine pontoons installed from the cable-stayed bridge to the western abutment, while the II-jacket concept has six pontoons installed in between the two jackets. Figure 6.10 shows the pontoon outline. The 5 m wide bottom flange provides an increase in added mass, shifting the heave eigenperiod to improve heave motion ($r\theta$). When installed, the draft is 10.5 m. The pontoons are attached to the girder with a circular hollow beam with diameter 4 meters and wall thickness 35 mm ($r\theta$).

As the objective is to study the response rather than pontoon geometry, the pontoon modeling approach assigns mass properties of the pontoon to prescribed nodes opposed to creating a geometrically equivalent structure. Attached to the main girder is a stiffened beam where a MASS21 element is assigned to the end node. Buoyancy forces are found by examining forces spring elements in the static analysis.

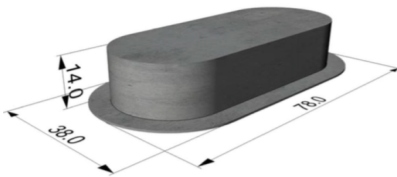


Figure 6.10: Pontoon Design

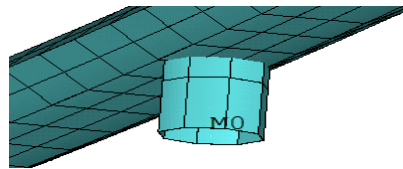


Figure 6.11: Modeling of pontoon column that connects the pontoon to the main girder

Table 6.3: Assigned Pontoon Parameters(Statens Vegvesen, 2015)

Assigned Pontoon Parameters	Value	Unit	Assigned Pontoon Parameters	Value	Unit
Mass	11300	tonns	COG(x)	0.0	m
Roll Inertia	4.90E+06	t m ²	COG(y)	0.0	m
Pitch Inertia	1.36E+06	t m ²	COG(z)	-4.2	m
Inertia	5.70E+06	t m ²	Height	14.5	m
Roll Water Plane Stiffness pgI44	5.70E+03	MNm/rad	Freeboard	4.0	m
Pitch Water Plane Stiffness pgI55	1.00E+03	MNm/rad	Draft	10.5	m
Heave Stiffness	17.5	MN/m	Width	68.0	m
			Length	28.0	m

6.4.1 Added Mass, Damping and Restoring

The MASS21 node is given material and mass properties (including frequency dependent added mass) as provided in the study done on the Bjørnafjorden bridge from the NPRA. The relevant period is defined in the code, which reads the corresponding frequency dependent added mass and damping properties and assigns them to the mass and spring-damper elements. Assigned added mass and radiation damping parameters are provided in appendix and in the digital appendix files *addedmass.txt* and *damping.txt*.

The pontoons dynamic behavior implies radiation damping and restoring forces, the former occurs due to energy dissipated from the system, while the latter appears as a consequence of the

i.e. change in buoyancy. Use of the spring-damper element COMBIN14 simulates these features. A linear spring element is chosen and appropriate spring stiffness and damping coefficients are applied. Spring stiffness are listed in Table 6.4. The damping properties are frequency dependent and listed in appendix A.2.2. Structural damping properties through α and β damping is applied by assuming a damping level of 2 % for mode 1 and 10 (?), and values for implementation are calculated. Spring elements are attached to each pontoon node in heave and sway as seen in Figure 6.12. In addition, a spring element is attached to simulate the spring stiffness and damping in roll.

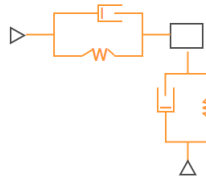


Figure 6.12: Spring and damper (heave and roll) attached to pontoon

Table 6.4: Applied Linear Spring Properties

Property	Value	Unit
Spring Stiffness (Heave)	1.7453e7	[N/m]
Spring Stiffness (Roll)	5600e7	[Nm/rad]
Damping Coefficient	Frequency Dependent	[Ns/m]

6.5 Cable Stays

Modeling the girder by neglecting the cable system turned out to be challenging, as the two outcomes were either 1) large dimensions and a weight of the main span 2-3 times given in the feasibility study, or 2) smaller dimensions, but larger deflections due to lower moment of inertia. The high bridge is therefore expanded to a suspension bridge with pretensioned cables. The cables are modeled by COMBIN14 elements, given an initial force to represent the pretension. The cable stiffness is approximated to be $k = \frac{EA}{L}$ while the pretension is given in the feasibility study.

6.6 Boundary Conditions

Boundary conditions represent external constraints in the structure usually to define a displacement or load, typically at fixed ends where translational or rotational motion is prohibited (Moan, 2013). Boundary conditions are applied to the model at the north and south ends of the bridge, and at each end of the spring elements as described below.

West end (Halsneset) and East end (Urdneset)

The west end is assumed fixed in translation and allowed to rotate about the z-axis which seems reasonable taking the movement of the bridge girder from tidal variation into account. The east end is held fixed in all degrees of freedom assuming firm support.

Spring elements - Pontoon properties, cable system and mooring system

The spring elements representing the horizontal contribution from the heave stiffness are restrained against translation. The spring element used to model the rotational stiffness of the pontoon is

restricted against rotation. Restraining all degrees of freedom in these elements is not considered necessary as the springs are purely translation and rotational springs.

6.7 Jacket

The model did not call for a complete jacket geometry in ANSYS as a more straightforward approach could provide the structural features and effect on global response. The jacket is assumed to contribute with near to infinite vertical stiffness, so boundary conditions are applied to restrain this section of the bridge to displace vertically. The boundary condition allows for horizontal displacement to account for thermal expansion due to temperature changes. The jacket support is assumed to restrain the model from rotation about the global bridge y-axis. To account for the horizontal stiffness contribution, a spring element is horizontally attached at the location of the jacket and given the horizontal stiffness found from a load/displacement analysis in USFOS, attached in appendix A.4.

The effective mass of the jacket is modeled as a MASS21 element in the bridge girder and will be of important consideration when establishing eigenfrequencies (Equation 3.60). As the jacket legs are assumed fixed to the seabed, it can be considered that only a fraction of the total mass will contribute to oscillations (Larsen, 2014). In agreement with the supervisor, it is assumed that the oscillating mass contribution from the jacket may be approximated in the same way as for a jackup-platform in literature provided by Larsen, (Larsen, 2014), by assuming that the effective mass contribution is 25 % of the leg mass.

The USFOS model is modified to satisfy the approximated length requirements. As the length will affect the horizontal stiffness, a force-displacement analysis is performed for the jacket. Assuming that the force-displacement relationship is linear, the force is proportional to the displacement and expressed as the product of the spring constant (stiffness) and the displacement. The resulting parameters for length, effective mass and stiffness contribution is given in Table 8.10 Further changes of jacket dimensions is left outside the scope of this Thesis.

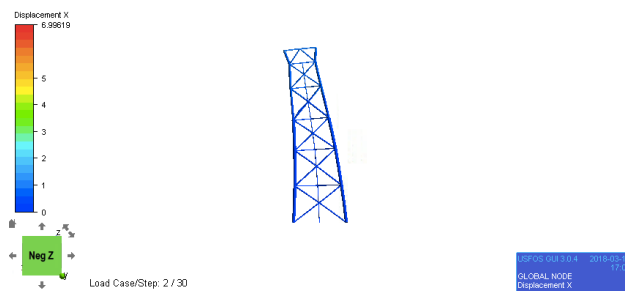


Figure 6.13: Force-displacement relation analysis in USFOS performed on the KviteBjørn Jacket

Table 6.5: Modeling parameters for the jacket configurations

Jacket Length	Effective Mass [kg]	Stiffness (k_y) [N/m]
190 m	8.24E06	3.3e06

6.8 Global Ship Collision Modeling in USFOS

The collision considered the impact between the ship bow and one of the jacket legs as shown in Figure 6.14. It is assumed that the bow strikes the jacket 20 m above the sea surface. This is an approximation.

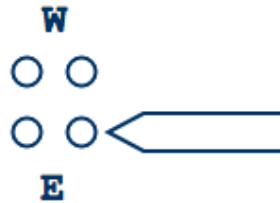


Figure 6.14: Impact Scenario (Birds View)

The global dynamic ship collision analysis is modeled as a mass-spring system with non-linear springs and a mass with a prescribed initial velocity. The mass and initial velocity will together represent the kinetic energy in the striking vessel. The non-linear springs are programmed corresponding to force-deformation curves. Force-deformation curves are normally obtained from a local bow-crushing analysis and are in this thesis predefined and implemented in the non-linear springs by assistance from postdoctoral fellow Yanyan Sha.

The mass-spring system consists of two springs attached in series to the mass node as shown in Figure 6.15. The springs are restrained such that only translation in the collision direction (in USFOS, global x-direction) is permitted. The latter spring is hyperelastic, implying high compression stiffness and low tensile stiffness. This to represent the detachment of the ship from the bridge and ensure that the non-linear spring does not follow the force-deformation curve during unloading as this would not give a correct image due to the plastic deformations.

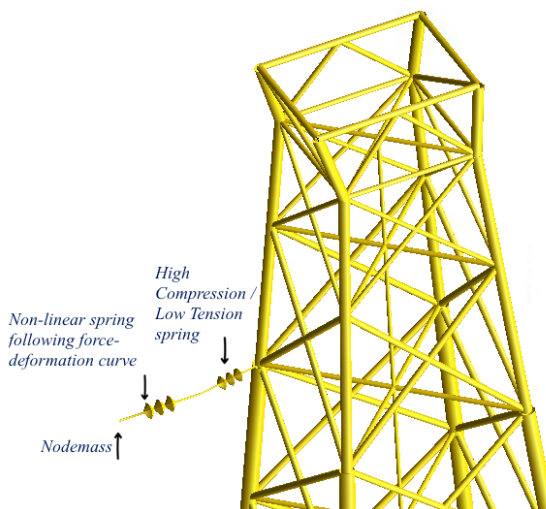


Figure 6.15: Modelling of non-linear springs in USFOS

Analysis Approach

7.1 ANSYS Analysis

7.1.1 Static Analysis

The static analysis performed in ANSYS Mechanical obtains displacement, rotations, bending moments and stress results for the model during steady loading conditions. As the loading and response are assumed to have very small variations in the time domain for this analysis, inertia and damping effects are neglected. The static analysis will be carried out for seven load cases. The first load case accounts only for the structures self-weight, while static external loads as traffic load, static wind, and current will be applied secondly.

The static analysis is performed by running the APDL code *main_static.txt*. The geometry is built bottom-up, which means that key points are established first, then lines are created between the key points, and further, areas are defined between the lines where necessary. Lines and key points are prescribed with the necessary attributes such that the different sections of the model get their geometry, material, mass and stiffness properties. The static traffic and wind loads are applied as pressure loads along the bridge girder. The buoyancy and current load is applied as point loads. The buoyancy acts vertically in the positive y-direction, and the current is applied in the positive z-direction as indicated by weather data from the NPRA.

Postprocessing of the results included examining values and location of the maximum and minimum stress and displacement values, which are presented in Chapter 8.2.

7.1.2 Modal Analysis

Modal analysis has become an advanced technological tool assisting engineers as an important part of the finite element analysis to determining dynamic behaviour of structures. Understanding vibration of structures is a relevant focus area in modern life with regards to the increasing demand of safe and reliable structures. Dynamic characteristics as natural frequencies, mode shapes and factors related to damping are combined to express a mathematical model of the structural dynamic behaviour (He, 2001).

The modal analysis will indicate which wave frequencies that possibly could coincide with the

natural modes of the system, causing resonance. No external loads are applied. In the modal analysis, the 30 first eigenfrequencies are extracted and results are presented in Section ???. The modal analysis is run through the APDL code *main_modal.txt*.

7.1.3 Regular Wave Analysis

A regular wave analysis is done in this concept study as it is a simple approach to obtain certain knowledge of the dynamics acting on the system. The regular wave analysis is performed on the II-jacket bridge, as results from the static and modal analysis could indicate that this concept was more demanding as a dynamic system. This is done in agreement with the supervisor. The regular wave analysis is only dependent on one frequency and makes it easier to include the frequency dependent added mass and radiation damping.

The forces acting on the pontoons and jacket are calculated in Matlab according to theory in Section 3.7.2. The force components for each time step are stored in a cell array and written to files for ANSYS to read. The wave period can be changed between 5 and 6 seconds. These parameters will further extract the corresponding stiffness, damping, and added mass values and assign them to their respective elements. The regular wave loads are applied in sway (global z), heave (global y) and roll (moment about the global x-axis) to the pontoons. The regular wave load is applied as a moment acting on the jacket due to the modeling approach was chosen for the pontoons.

Results are extracted by running separate scripts specified for the postprocessing. These scripts run through all nodes, searching for maximum response parameters. Results are extracted from the steady state. Matlab is further used for post-processing and results display.

7.1.4 APDL Command Flow Chart and File Description

The table below (Table 7.1) summarizes the created APDL-codes stored in txt-files. Figure 7.1 explains the setup of the commands. The APDL files are attached in the digital appendix.

Table 7.1: Description of input APDL commands applied in the ANSYS APDL model

File	Description
main_static.txt	Calls inputs for static analysis
main_modal.txt	Calls inputs for modal analysis
main_regular.txt	Calls inputs for regular wave analysis
properties.txt	Defines parameters for materials, element types, spring properties, mass properties, reads added mass and damping terms from defined tables
loads.txt	Defines calculated current and wind load parameters and allows for determination of load input by user
sections.txt	Reads input section files and defines section type
geometry_2JH.txt	Builds keypoints and lines for the bridge model with two jackets and high bridge. A similar script is made for building the model for the I-Jacket concept. Assigns element, materials and structural properties and mesh attributes to grouped lines.
mesh.txt	Model mesh command for the meshing of lines and key points.
bc_self.txt	Assigns boundary conditions and self-weight to the system
static_loads.txt	Applies self-weight, traffic loads and environmental loads to the bridge beam and pontoons. The user may modify which load types to be applied.
regular_loads.txt	Applies self-weight, traffic loads and environmental loads to the bridge beam and pontoons. The user may modify which load types to be applied.
solve_static.txt	Solve commands for static analysis
solve_modal.txt	Solve commands for modal analysis. Number of eigenfrequencies may be modified in this script.
solve_regular.txt	Runs regular analysis and applies time varying loads for each time step



Figure 7.1: Flowchart of static, modal and regular wave analysis scripts setup in ANSYS Mechanical

7.2 USFOS Ship Collision Analysis

The ship collision is set up in USFOS as described in Section 6.8. Two files are created, *head_dyn.fem* and *stru-1_dyn.fem* where the former is the primary control file and the latter is the model file establishing element geometry. The node mass is given an initial velocity implemented in the head file. The formulation of force-deformation curves are, as previously stated, provided by postdoctoral fellow Yanyan Sha. These are implemented in the model file. The non-linear springs are established in the model-file along with the remaining nodes and elements.

The analysis is set up such that gravity is applied first. After 10 seconds, the collision load is applied increasingly, step by step. The time for the dynamic analysis is set to 25 seconds and a time step of 0.01 seconds. This gives USFOS sufficient time to reach a load level close to the maximum collision load. The small time step is necessary to capture results of sufficient accuracy.

The results are examined by using the USFOS post-processor tools in the USFOS GUI.

Analysis Results

This section presents the results from the analysis types conducted in the Thesis.

The response from the static ANSYS analyses is measured in terms of global displacements, rotations, bending moments and Von Mises stress. For the regular wave analysis, accelerations are also measured. Throughout the chapter, it is commented whether the model satisfies the stated criteria from regulations presented in Section 4.7.

Presentation of results

For presentation of the static load case results, the applied load cases are numbered (from 1-7) and response extreme values are plotted according to the corresponding load case numbers as listed below. The plots in this section show the results from the models with the high bridge, while the results from the low bridge models are attached in the appendix.

- Load Case 1: Self weight
- Load Case 2: Traffic load
- Load Case 3: Wind with 1 year return period
- Load Case 4: Wind and current with 1 year return period
- Load Case 5: Wind and current with 100 year return period
- Load Case 6: High tide (mean sea level increased by 1.0 m)
- Load Case 7: Low tide (mean sea level reduced by 1.0 m)

The largest response difference between the model with and without high bridge is commented based on results from a static analysis.

Results from the modal analysis are presented in Section 8.4. The 30 first eigenmodes are extracted. The ten first eigenmodes are shown in this section, and the remaining 20 are attached in the appendix. Section 8.4.3 evaluates how eigenmodes coincide with wave periods at the installation site.

The results from the ship collision analysis measures maximum displacements and accelerations. The response in terms of plastic utilization is also commented.

8.1 Convergence Test

Mesh Size

A convergence test to measure the change in displacement and Von Mises stress with decreasing mesh size was performed to find a mesh size so small that a reduction no longer had a significant impact on the results. When reducing the mesh size, the accuracy of the analysis will increase. With reduced mesh size comes increased computational time and CPU consumption, so it is preferable to maintain a mesh size as high as possible while still obtaining sufficiently accurate results (Ottosen, 1992).

A mesh convergence test was established to measure the maximum deflection in x-, y- and z-direction for element size 20 to 0.01 and reducing the size by 0.01 m per step. An option was to obtain deflections from several points on the structure, but as the test measured both stress and displacement, this was considered sufficient at this stage. Figure 8.1 shows the maximum vertical displacement (U_y) for a decreasing mesh size. The mesh size is plotted on a logarithmic scale for easier interpretation. The variation is overall low (magnitude of 10^{-3}), and convergence is assumed obtained at mesh size 1x1 m per element. The computational time for the static analysis was overall short (approximately 10-20 seconds), so increasing the mesh size for reducing computational time was not considered of importance for the work performed in this Thesis.

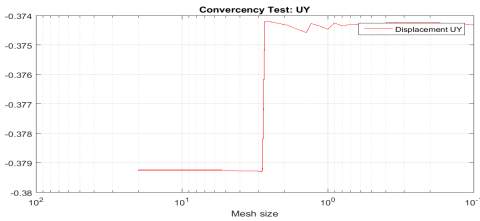


Figure 8.1: Maximum vertical displacement during mesh size reduction (section S1 and F1)

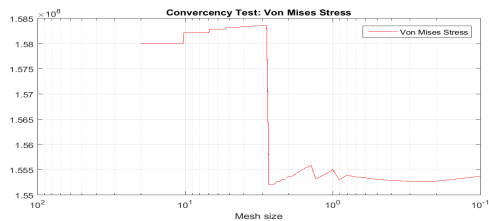


Figure 8.2: Variation in Von Mises stress as mesh size reduces from 20 to 0.01

Time Step

A convergence test for time step length was performed before the regular wave analysis. Dynamic analysis is commonly more complex and time-consuming than static analysis, so running as high time steps as possible without losing accuracy in results is preferable. A larger time step also reduces CPU consumption, which can be important depending on the computers storage capacity. It is, prior to the analysis discussed with the supervisor that a time step of 0.25-0.2 seconds, is reasonable for this analysis. For analysis examining local effects, e.g. ship collision, a lower time step would be applied. The table below (Table 8.1) summarizes the displacement results for the convergence test. The analysis time was overall short, but increased significantly when the time step was reduced. Time steps of 0.5, 0.3, 0.2 and 0.1 seconds are tested.

Table 8.1: Time Step Convergence

Node	Variable	Unit	0.5	0.3	0.2	0.1
1478	u_y	[m]	-0.2980	-0.3176	-0.3150	-0.3058
2099	u_y	[m]	-0.2691	-0.2709	-0.2646	-0.2643
Global	Time	[min:s]	1:45	2:19	2:40	5:14

8.2 Static Response

8.2.1 Global Displacements

Figure 8.3 and 8.4 show the extreme values of the x- and z-component of displacement for each of the seven load cases. For load case 1, 2, 6 and 7 (self-weight, traffic load, low tide and high tide), no external horizontal forces are applied, but still deflections in the horizontal plane are observed, both in x- and z-direction. When vertical loads are applied to the inclined section, this section will, obviously, deflect vertically and give the bridge a positive z-component of displacement. This effect is largest at the center of the floating span. Deflection of the inclined spans also causes small rotations of the pontoons about the global z-axis and one can also observe displacements in the x-direction. In addition, the deflection in x- and z-direction could also be affected by the forces induced by the cables with pretension in the ends of the bridges, the attached springs and the small rotations that occur about the x-axis. This response is (for the mentioned load cases) overall higher for the II-jacket concept, but are generally of small magnitude.

Considering the response in terms of displacement in z-direction due to the wind and current loading, the maximum displacement occurs for load case 5 when wind and current with 100 year return period is applied. This response is highest for the II-jacket bridge where the deflection is 0.75 m. The II-jacket concept has higher deflection here due to the induced tension from the vertical deflection of the inclined spans. The bridge girder is displaced -0.14 m in the negative z-direction at the easternmost high bridge. This is because of the rotation of the bridge girder about the boundary conditions at the easternmost jacket attachment. The x-component of displacement is not significantly affected by the environmental loading, but it is seen for both concepts that the high tide loading gives the largest x-component of displacement.

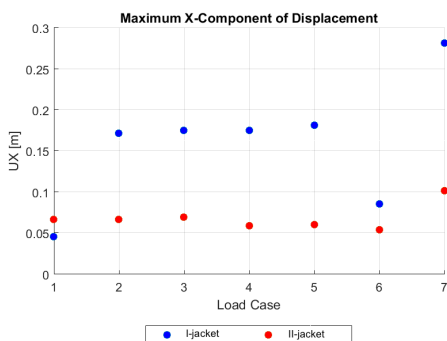


Figure 8.3: Maximum x-component of displacement for both concepts with high bridge

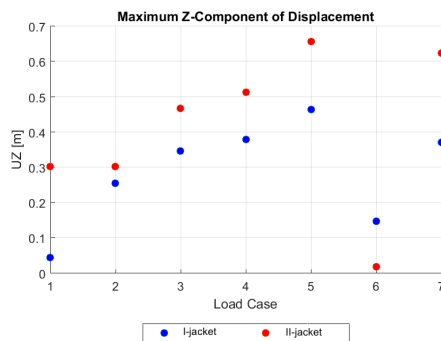


Figure 8.4: Maximum z-component of displacement for both concepts with high bridge

The maximum vertical displacements (y-direction) for all load cases are plotted in Figure 8.5. For the load cases including wind and current, both concepts seem to satisfy the deflection criteria of span deflection not exceeding $L/350$. From Figure 8.5 it can be seen that in general, the y-component of displacement is of larger magnitude for the II-jacket than the I-jacket concept. These results may be affected by the buoyancy distribution, which is commented on in the next paragraph. Figure 8.5 considers only the global maximum deflection, so to identify the local deflections, the contour plots are examined.

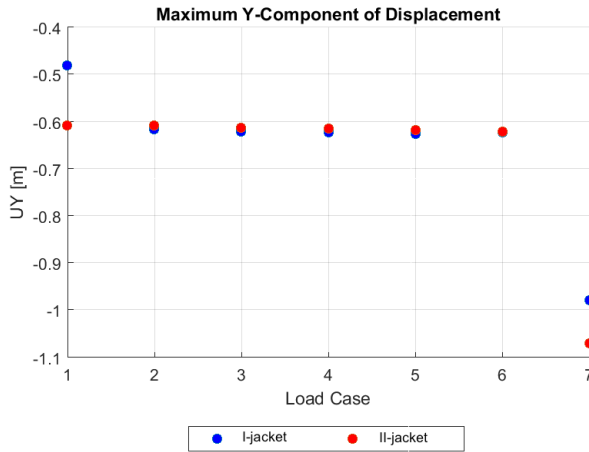


Figure 8.5: Maximum y-component of displacement for both concepts with high bridge

From Figure 8.6 and 8.7 it can be seen that the buoyancy distribution could have been modeled better. This is due to the slight positive displacement observed at the connection between the pontoon columns and the bridge girder. However, these displacements were of such small magnitude that it was assumed sufficient to continue at this stage. The largest displacements of the bridge girder occur for all load cases in the high bridge, except during low tide when the largest displacement is found at the center of the floating spans.

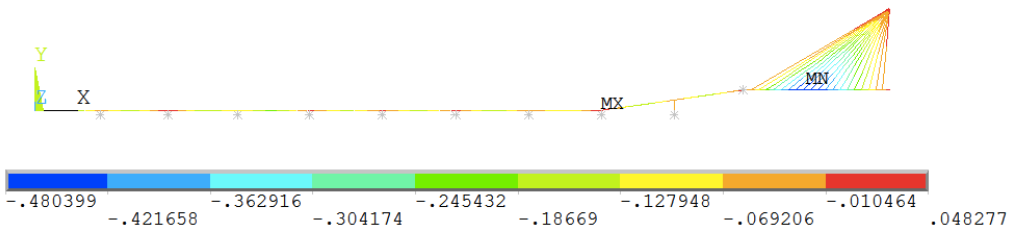


Figure 8.6: Global y-component of displacement due to self weight (I-jacket concept)

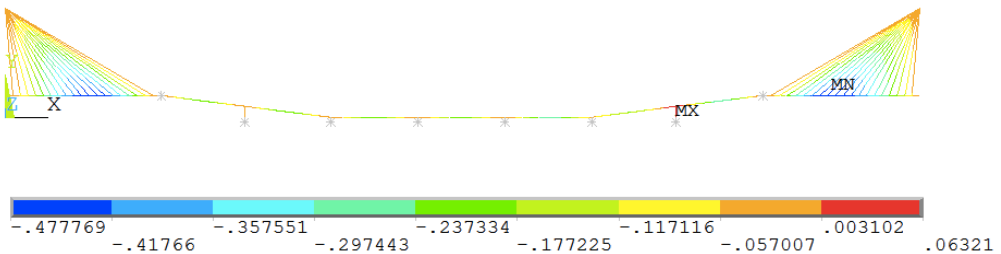


Figure 8.7: Global y-component of displacement due to self weight (II-jacket concept)

Tidal Variation

The criteria for span deflection not exceeding $L/350$ should be given extra attention for when the model is exposed to low tide. Examining Figure 8.8 and 8.9, the neighboring floating spans of the jackets are displaced -0.65 m and -0.71 m, which at an absolute maximum should have been -0.57 m. Corrective actions are discussed in Chapter 9.

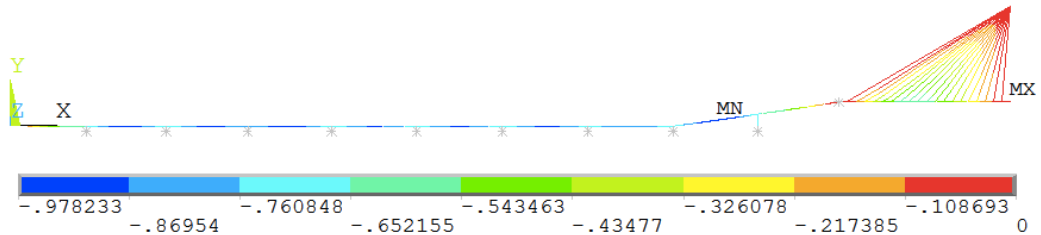


Figure 8.8: Global y-component of displacement during low tide sea level (-1.0 m). It is seen that the deflection of the neighbouring pontoon of the jacket exceeds the $L/350$ deflection criteria by 0.08 m

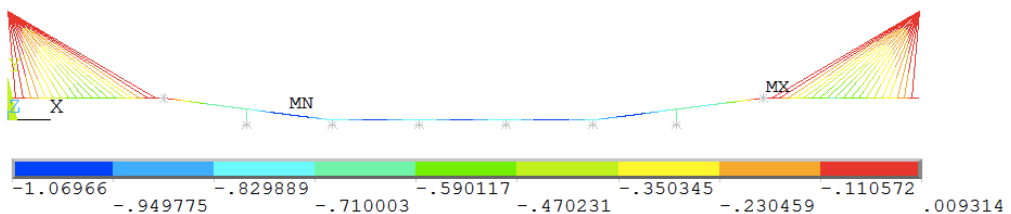


Figure 8.9: Global y-component of displacement due to low tide sea level (-1.0 m). It is seen that the deflection of the neighbouring pontoons of the jackets exceeds the $L/350$ deflection criteria by 0.14 m

8.2.2 Global Rotations

Figure 8.11 and 8.13 show the response concerning global rotations about the x-, y- and z-axis. Both the maximum values of positive and negative rotations are shown, where positive rotations are defined as clockwise about the axis.

The global rotations about the x-axis shall not exceed 1.5 degrees during a 1-year storm (Section 4.7). Neither shall the traffic load induce global rotations about the bridge girder that exceed 1 degree. This criteria is satisfied for all load cases and are in general higher for the II-jacket bridge than the I-jacket bridge. The dominating rotational response of the II-jacket concept is about the x-axis. This is thought to be because of the jackets that are resisting horizontal motions. Larger rotations are therefore induced. For the I-jacket concept, the rotation about the global z-axis dominates. The maximum y-component of rotation increases as the horizontal applied loads increase in magnitude. It can be observed that the distribution of clockwise and counterclockwise rotations for the II-jacket concept is close to symmetric. This seems reasonable due to the load acting normal on the symmetric model.

The rotations about the global z-axis are, as expected, very little affected by the applied horizontal motions. The most significant impact is observed at load case 7 when low tide is applied. The

clockwise rotations are generally slightly higher for the II-jacket concept, which can be expected as the environmental loads are applied from north.

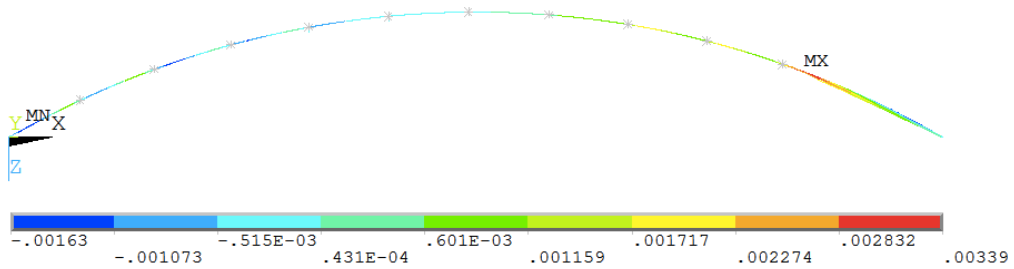


Figure 8.10: I-jacket: Maximum global x-component of rotation during wind and current with 100 year return period

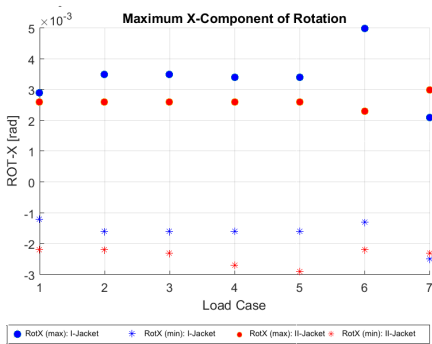


Figure 8.11: Maximum and minimum global x-component of rotation for all load cases

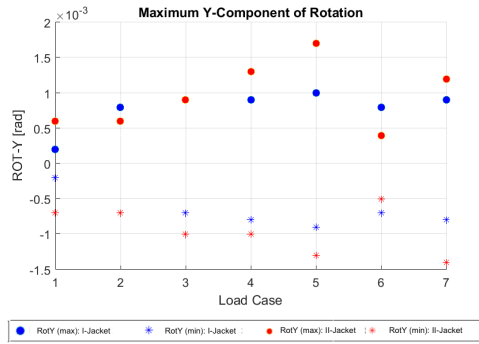


Figure 8.12: Maximum and minimum global y-component of rotation for all load cases

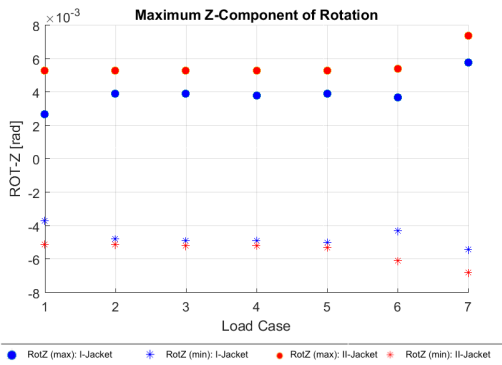


Figure 8.13: Maximum and minimum global z-component of rotation for all load cases

8.2.3 Bending Moments and Shear Forces

The maximum bending moments and shear forces for both concepts are summarized in Table 8.2 and 8.3. The global bending moment about the x-axis (torsional moment on the bridge girder) for all load cases is given in Figure 8.14. From this plot, it is seen that the model does not show significant variation in this bending moment component for the load case 1-7. This corresponds well with the response in terms of the x-component of rotations. From Figure 8.14, it is seen that the torsional moments in the II-jacket concept are larger in magnitude than the I-jacket bridge. This can be explained by that the bridge supported by one jacket is less resistant to horizontal deflection, and therefore more of the energy is taken by the global bending moment M_y than the global bending moment M_x .

The bending moments about the global y-axis for the I-jacket concept show larger variation when exposed to wind and current than the II-jacket concept, as can be seen in Figure 8.15. Also here, the bending moments are in general higher for the II-jacket concept. The higher moments are thought to be because of the II-jacket concepts ability to withstand horizontal deflection. Figure 8.17 shows the bending moment, M_z , distribution along the bridge girder. As the color shades from green to mint green, the magnitude changes from positive to negative.

The maximum bending moment about the global z-axis is, as expected, not significantly affected by the wind and current loads. It is, however, affected by the tidal variation, which is due to the change in vertical displacements. This will induce cyclic stresses, so fatigue should be assessed. Figure 8.17 shows the bending moment distribution during wind and current loading with 100 year return period (I-jacket concept). The moment distribution corresponds with the theory for bending moments in beams, presented in Chapter 3.2.1.

Table 8.2: Bending Moment and shear force results for I-jacket

	Value	Load Case	
$M_{x,max}$	2.91E+07	6	High Tide
$M_{x,min}$	-3.85E+07	7	Low Tide
$M_{y,max}$	6.23E+07	5	Wind and Current (100 year)
$M_{y,min}$	-4.04E+07	6	High Tide
$M_{z,max}$	4.442E+08	7	Low Tide
$M_{z,min}$	-1.70E+08	7	Low Tide
$V_{y,max}$	1.07E+07	7	Low Tide
$V_{y,min}$	-1.10E+07	7	Low Tide

Table 8.3: Bending moment and shear force results for II-jacket

	Value	Load Case	
$M_{x,max}$	3.79E+07	5	Wind and Current (100 year)
$M_{x,min}$	-3.18E+07	5	Wind and Current (100 year)
$M_{y,max}$	3.82E+07	5	Wind and Current (100 year)
$M_{y,min}$	-6.43E+07	5	Wind and Current (100 year)
$M_{z,max}$	1.81E+08	6 & 7	Low Tide & High Tide
$M_{z,min}$	-4.30E+08	7	Low Tide
$V_{y,max}$	1.14E+07	7	Low Tide
$V_{y,min}$	-4.99E+07	7	Low tide

In the plots below, the colored dots indicate clockwise moments while the star (*) indicates counterclockwise moments.

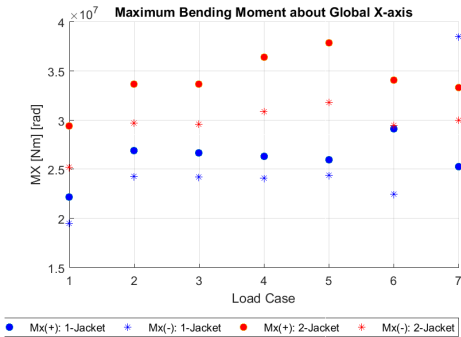


Figure 8.14: Maximum and minimum global torsion moment M_x

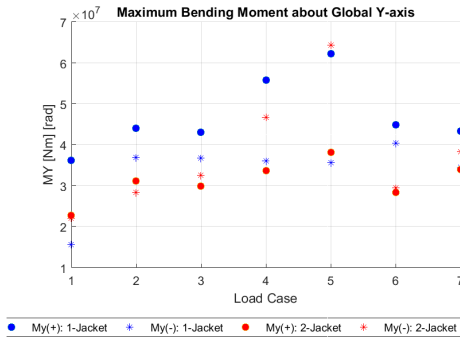


Figure 8.15: Maximum and minimum global bending moment M_y

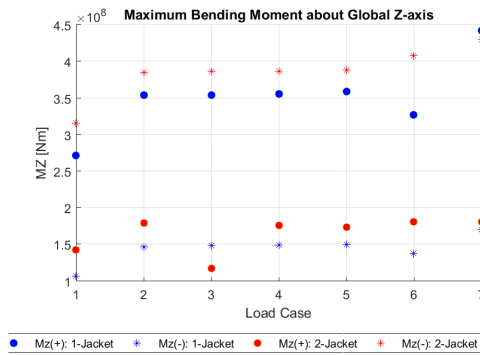


Figure 8.16: Maximum and minimum global bending moment M_z

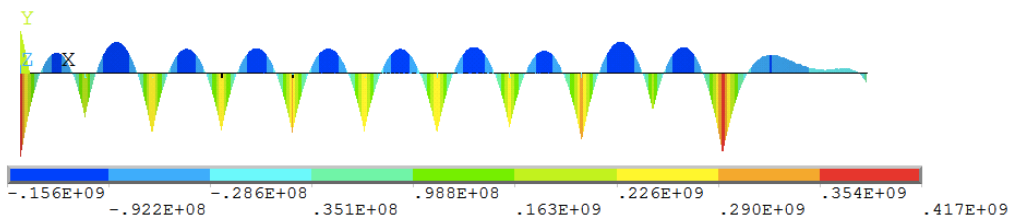


Figure 8.17: Maximum and minimum global bending moment M_z for the I-jacket concept during low sea level (-1.0m)

8.2.4 Von Mises Stress

The maximum Von Mises stress for all load cases are shown in Figure 8.18. For both concepts, the maximum Von Mises stress is found at the attachment point of the jacket, as expected since this point restrains more deflection and rotation than the pontoons. The maximum observed Von Mises stress is 222 MPa, which is well below the yield criterion.

The stress distribution corresponds well with the distribution of bending moments, where larger bending moments are seen at the strengthened girder sections. During high tide, the energy absorbed in the structure due to the vertical displacements induces stress concentration at these locations. The restriction against vertical and rotational motion at the jacket absorbs energy and induces stress concentration.

During high and low tide, the stress level at the jackets cycle from 175 MPa to 222 MPa for the I-jacket bridge and from 130 to 168 MPa for the II-jacket bridge. This is a rough estimate of the cyclic loading that the bridge will experience due to tidal variation, which can cause fatigue.

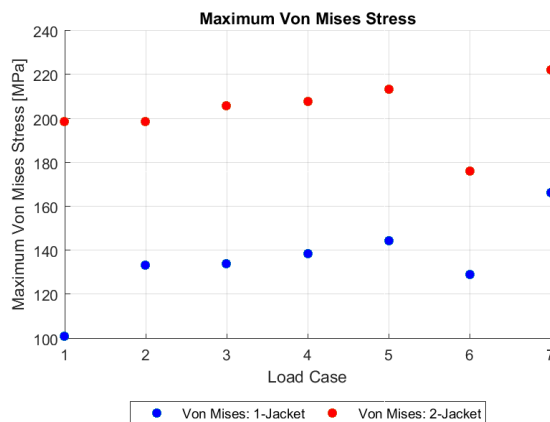


Figure 8.18: Maximum Von Mises stress for all load cases

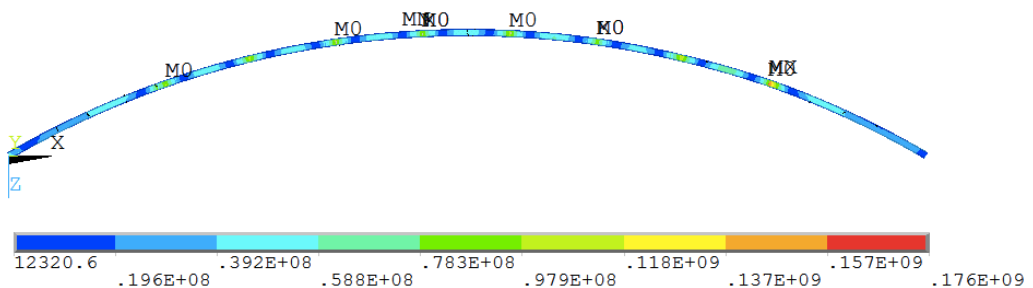


Figure 8.19: Von Mises stress for the II-jacket concept during high tide

8.3 Effect of High Bridge Modeling

The first model created for this thesis was without a high bridge to simplify the model. The following section shows the difference in measured static response between the concepts with and without the high bridge. The high bridge models are the most realistic considering the navigation channel, but it could be of interest to examine whether the high bridge has a great influence on the structural response. Of special interest was the effect on the vertical displacements during low tide, as the floating spans on the model without the high bridge exceeded the $L/350$ deflection criteria. By including a high bridge and an inclined section connecting the high bridge and the floating section, the analysis showed that deflection criteria was still exceeded.

Figure 8.20 and 8.21 show the difference in maximum y- and component of displacement for the I-jacket and II-jacket concept with and without the high bridge. The difference is practically negligible for the I-jacket concept. For the II-jacket concept, the displacement is slightly smaller for the high bridge model, except during low tide.

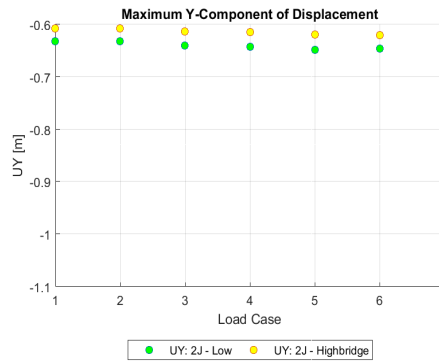
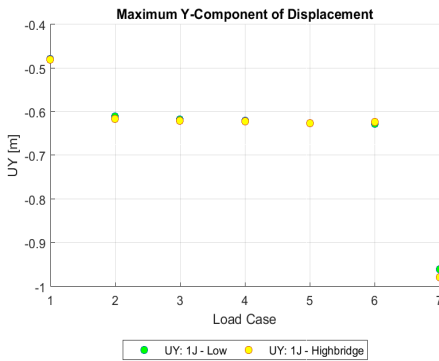


Figure 8.20: Comparison of global rotations about the global y-axis for the I-jacket concept

Figure 8.21: Comparison of global rotations about the global y-axis for the II-jacket concept

The largest difference is found in the z-component of displacement and the von Mises stress distribution as can be seen in Figure 8.26 and 8.27. The reason for the larger z-component of displacements is the deflection of the inclined spans that will cause the arced floating span to displace towards the arc circle center. The II-jacket concept has two inclined spans causing this displacement, and the z-component of displacement is, therefore, larger for the II-jacket concept. The I-jacket concept shows a larger increase in this response parameter when one goes from self-weight to traffic load.

The maximum Von Mises stress level is in general lower for the I-jacket concept when the high bridge is included. For the II-jacket concept, the von Mises stress is generally larger for all load cases. This corresponds to the displacement levels discussed in the previous section.

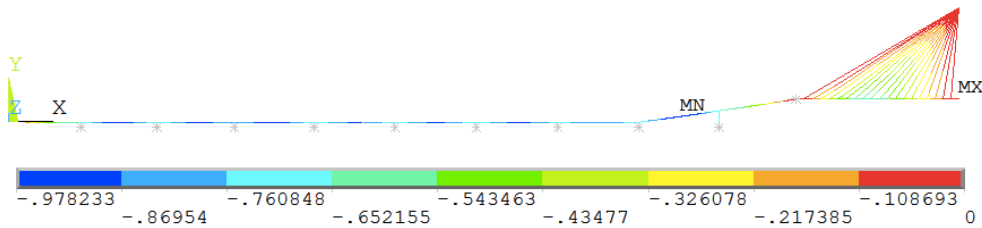


Figure 8.22: Global y-component of displacement during low tide sea level (-1.0m) for the I-jacket concept with the high bridge

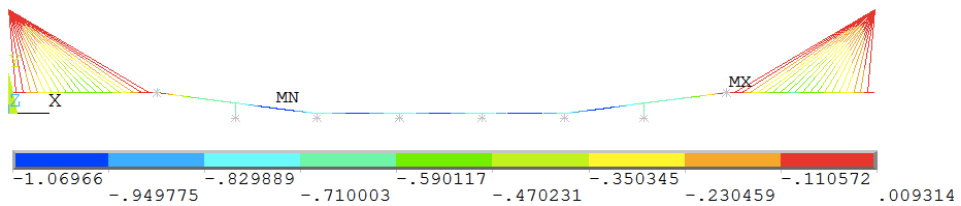


Figure 8.23: Global y-component of displacement during low tide sea level (-1.0m) for the II-jacket concept with the high bridge

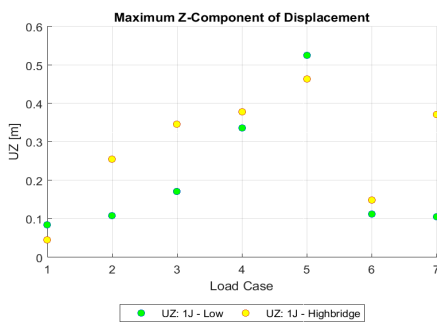


Figure 8.24: Comparison of global rotations about the global z-axis for the I-jacket concept

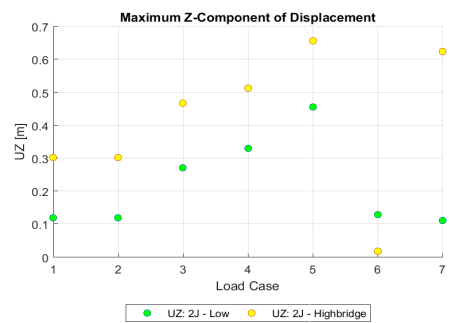


Figure 8.25: Comparison of global rotations about the global z-axis for the II-jacket concept

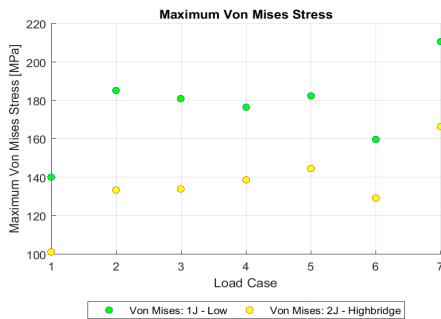


Figure 8.26: Comparison of the Von Mises stress for the I-Jacket bridge, with and without the high bridge

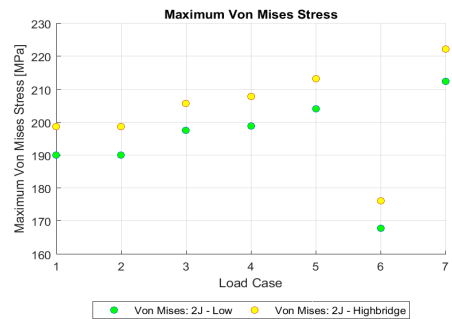


Figure 8.27: Comparison of the Von Mises stress for the II-Jacket bridge, with and without the high bridge

8.4 Eigenvalue Analysis

8.4.1 I-Jacket Concept

The 30 first eigenfrequencies of the system were extracted from a modal analysis in ANSYS Mechanical. Mode 1-10 are summarized in Table 8.4. The rightmost column denotes the direction of the mode shape, where *V* denotes *vertical* and *H* denotes *horizontal*. The ten first eigenfrequencies range from 82.21 seconds to 5.94 seconds. The range of eigenperiods indicates that dynamic response for both first order (wave frequency) and second order (low frequency) needs to be assessed. The eigenperiods coincidence with wave periods are presented in Section 8.4.3 along with provided significant wave height and peak period values from an earlier design stage for the Halsafjord (provided by the NPRA). The first dynamic modes have long periods and from the fifth eigenmode the periods start coinciding with natural periods from extreme waves. horizontal mode shapes dominate the first modes while vertical modes dominate the higher modes.

Table 8.4: Eigenfrequencies for mode 1-10 (I-jacket)

SET	FREQUENCY [Hz]	PERIOD [s]	ANGULAR FREQUENCY [rad/s]	DIRECTION
1	0.012	82.21	0.08	H
2	0.022	45.86	0.14	H
3	0.039	25.67	0.24	H
4	0.048	20.67	0.30	H
5	0.059	17.00	0.37	H
6	0.078	12.81	0.49	H
7	0.101	9.90	0.63	H
8	0.125	8.03	0.78	H
9	0.142	7.05	0.89	H
10	0.168	5.94	1.06	V

Mode Shapes

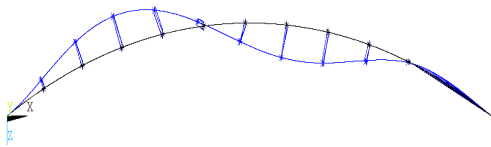


Figure 8.28: Mode 1: Horizontal, T = 82.21 s

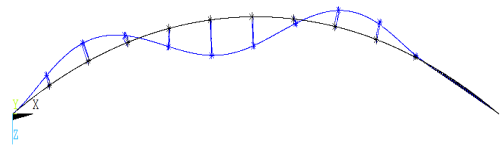


Figure 8.29: Mode 2: Horizontal, T = 45.86 s

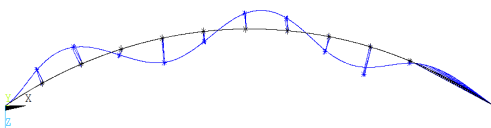


Figure 8.30: Mode 3: Horizontal, T = 25.67 s

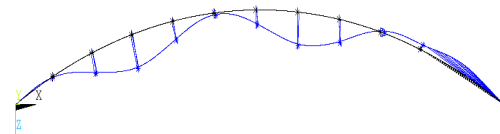


Figure 8.31: Mode 4: Horizontal, T = 20.67 s

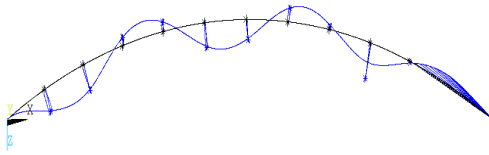


Figure 8.32: Mode 5: Horizontal, $T = 17.00$ s

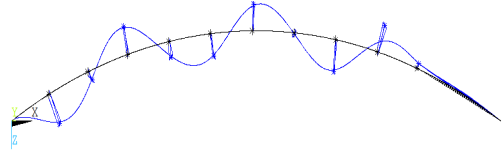


Figure 8.33: Mode 6: Horizontal, $T = 12.81$ s

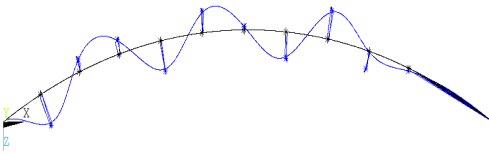


Figure 8.34: Mode 7: Horizontal, $T = 9.90$ s

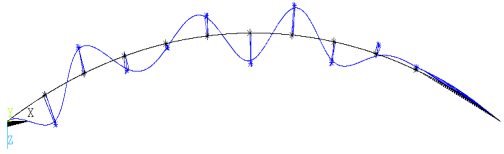


Figure 8.35: Mode 8: Horizontal, $T = 8.03$ s

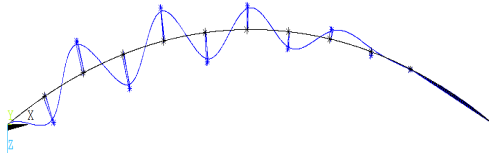


Figure 8.36: Mode 9: Horizontal, $T = 7.05$ s

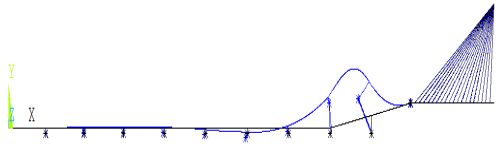


Figure 8.37: Mode 10: Vertical, $T = 5.94$ s

8.4.2 II-Jacket Concept

The 30 first eigenfrequencies of the system were extracted. The 10 first eigenfrequencies are summarized in Table 8.5. These range from 54.55 seconds to 5.58 seconds. The first three eigenperiods are long (from 54.55 seconds down to 24.02 seconds) and from the fourth eigenmode the periods start coinciding with periods from extreme waves as evaluated in the section below. As similar to the I-jacket concept, the range of eigenperiods indicates that dynamic response for both first order (wave frequency) and second order (low frequency) needs to be assessed due to the long periods for the first dynamic modes. Horizontal mode shapes dominate the first modes while vertical modes start to dominate earlier for the II-jacket concept than for the I-jacket concept.

Table 8.5: Eigenfrequencies for mode 1-10 (II-jacket)

SET	FREQUENCY [Hz]	PERIOD [s]	ANGULAR FREQUENCY [rad/s]	DIRECTION
1	0.018	54.55	0.12	H
2	0.032	31.20	0.20	H
3	0.042	24.02	0.26	H
4	0.056	17.93	0.35	H
5	0.079	12.62	0.50	H
6	0.108	9.27	0.68	H
7	0.156	6.40	0.98	V
8	0.168	5.94	1.06	V
9	0.173	5.78	1.09	V
10	0.179	5.58	1.13	V

Mode Shapes

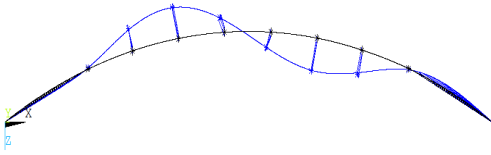


Figure 8.38: Mode 1: Horizontal, $T = 54.55$ s

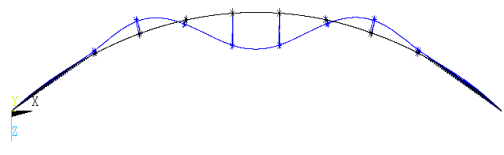


Figure 8.39: Mode 2: Horizontal, $T = 31.20$ s

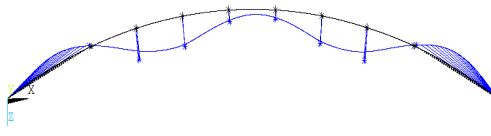


Figure 8.40: Mode 3: Horizontal, $T = 24.02$ s

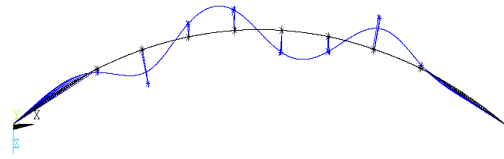


Figure 8.41: Mode 4: Horizontal, $T = 17.93$ s

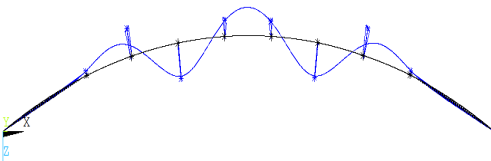


Figure 8.42: Mode 5: Horizontal, $T = 12.62$ s

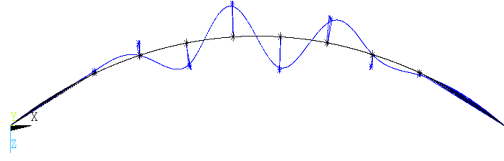


Figure 8.43: Mode 6: Horizontal, $T = 9.27$ s

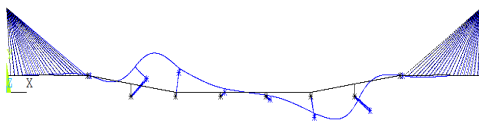


Figure 8.44: Mode 7: Vertical, $T = 6.40$ s

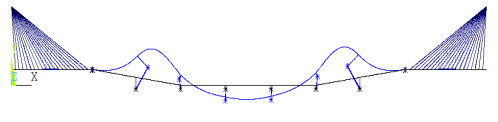


Figure 8.45: Mode 8: Vertical, $T = 5.94$ s

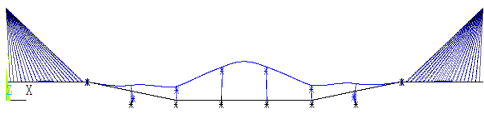


Figure 8.46: Mode 9: Vertical, $T = 5.78$ s

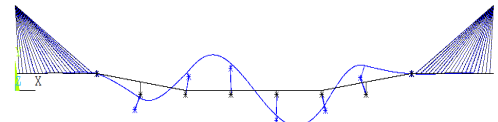


Figure 8.47: Mode 10: Vertical, $T = 5.58$ s

8.4.3 Evaluation of Coincidence With Wave Periods

As mentioned previously, deviations in weather measurements occur due to shielding from land and effects of swirls that are easily set up further south of the fjord. This means that weather parameters may easily be distracted depending on the methodology and choice of reference data. The values for peak period (T_p) and significant wave height (H_s) in Table 4.3 will for this thesis give a preliminary indication of eigenperiods that coincide with extreme wave periods. Figure 8.48 and 8.49 show the 10 first eigenperiods that coincide with the extreme wave periods marked in red. Similar tables for the 30 extracted modes for both concepts are attached in Appendix A.25.

The swell generated waves with 1, 100 and 10 000 year return period bound the highest periods, and overlap mode 5-9 for the I-jacket concept and mode 4-9 for the II-jacket concept. This indicates chance of resonance. Mode 7-9 should be evaluated for the II-jacket concept as vertical mode shapes are in this range. For swell generated waves, the lower mode shapes are outside the wave period range. For the locally wind generated sea, independent of direction, eigenperiod 10-30 (I-jacket) and 7-30 (II-jacket) coincide and there is chance that some resonance can be excited. For local wind generated sea with return period of 10 000 years, it is also mode 7-30 that coincides. The most critical sea state is the locally wind generated sea with direction 270 degrees with its significant wave height of 2.1 metres and peak period of 7 seconds or less.

Considering wind periods, these are often low and may coincide with the lower eigenmodes. As previously mentioned, low frequency response from waves is also of great importance since the first dynamic modes range from approximately 50 seconds and higher.

SET	FREQUENCY	PERIOD	Locally Wind Generated Sea									Swell		
			270			225/315			0/180			250-290		
			1 year	100 year	10 000 year	1 year	100 year	10 000 year	1 year	100 year	10 000 year	1 year	100 year	10 000 year
	[Hz]	[s]	≤ 5	≤ 6	≤ 7	≤ 5	≤ 6	≤ 7	≤ 5	≤ 6	≤ 7	6-18	6-18	6-18
1	1.23E-02	81.21	81.21	81.21	81.21	81.21	81.21	81.21	81.21	81.21	81.21	81.21	81.21	81.21
2	2.18E-02	45.86	45.86	45.86	45.86	45.86	45.86	45.86	45.86	45.86	45.86	45.86	45.86	45.86
3	3.90E-02	25.67	25.67	25.67	25.67	25.67	25.67	25.67	25.67	25.67	25.67	25.67	25.67	25.67
4	4.84E-02	20.67	20.67	20.67	20.67	20.67	20.67	20.67	20.67	20.67	20.67	20.67	20.67	20.67
5	5.88E-02	17.00	17.00	17.00	17.00	17.00	17.00	17.00	17.00	17.00	17.00	17.00	17.00	17.00
6	7.80E-02	12.81	12.81	12.81	12.81	12.81	12.81	12.81	12.81	12.81	12.81	12.81	12.81	12.81
7	0.10097	9.90	9.90	9.90	9.90	9.90	9.90	9.90	9.90	9.90	9.90	9.90	9.90	9.90
8	0.12452	8.03	8.03	8.03	8.03	8.03	8.03	8.03	8.03	8.03	8.03	8.03	8.03	8.03
9	0.14188	7.05	7.05	7.05	7.05	7.05	7.05	7.05	7.05	7.05	7.05	7.05	7.05	7.05
10	0.16828	5.94	5.94	5.94	5.94	5.94	5.94	5.94	5.94	5.94	5.94	5.94	5.94	5.94

Figure 8.48: I-Jacket concept: Conditionally formatted values of the 10 first eigenperiods coinciding with wave periods with 1, 100 and 10 000 years return period from locally wind generated sea and swell.

SET	FREQ.	PERIOD	Locally Wind Generated Sea									Swell		
			270			225/315			0/180			250-290		
			1 year	100 year	10 000 year	1 year	100 year	10 000 year	1 year	100 year	10 000 year	1 year	100 year	10 000 year
	[Hz]	[s]	≤ 5	≤ 6	≤ 7	≤ 5	≤ 6	≤ 7	≤ 5	≤ 6	≤ 7	6-18	6-18	6-18
1	0.0183	54.55	52.76	52.76	52.76	52.76	52.76	52.76	52.76	52.76	52.76	52.76	52.76	52.76
2	0.0321	31.20	31.27	31.27	31.27	31.27	31.27	31.27	31.27	31.27	31.27	31.27	31.27	31.27
3	0.0416	24.02	21.70	21.70	21.70	21.70	21.70	21.70	21.70	21.70	21.70	21.70	21.70	21.70
4	0.0558	17.93	16.14	16.14	16.14	16.14	16.14	16.14	16.14	16.14	16.14	16.14	16.14	16.14
5	0.0793	12.62	11.09	11.09	11.09	11.09	11.09	11.09	11.09	11.09	11.09	11.09	11.09	11.09
6	0.1079	9.27	8.73	8.73	8.73	8.73	8.73	8.73	8.73	8.73	8.73	8.73	8.73	8.73
7	0.1563	6.40	5.83	5.83	5.83	5.83	5.83	5.83	5.83	5.83	5.83	5.83	5.83	5.83
8	0.1683	5.94	5.81	5.81	5.81	5.81	5.81	5.81	5.81	5.81	5.81	5.81	5.81	5.81
9	0.1730	5.78	5.70	5.70	5.70	5.70	5.70	5.70	5.70	5.70	5.70	5.70	5.70	5.70
10	0.1791	5.58	5.46	5.46	5.46	5.46	5.46	5.46	5.46	5.46	5.46	5.46	5.46	5.46

Figure 8.49: II-jacket concept: Conditionally formatted values of the 10 first eigenperiods coinciding with wave periods with 1, 100 and 10 000 years return period from locally wind generated sea and swell.

8.5 Regular Wave Analysis

8.5.1 Global Displacements and Rotations

From the regular wave analysis the bridge response is measured for regular waves with peak period and significant wave height $T_p = 5$ s, $H_s = 0.4$ m and $T_p = 6$ s, $H_s = 1.2$ m, referring to the 1 year and 100 year return period conditions in Table 4.3. The wave load is adjusted for amplitude according to the significant wave heights. The purpose of this analysis is to check if the response is within the criteria stated in Table 4.5. That is, the vertical and Horizontal accelerations shall not exceed 0.5 and 0.6 m/s². In addition, the global deflections also stated in the table shall not be exceeded.

The table below summarizes the maximum displacements and rotations in x- y and z-direction along with location. The largest displacement is found for the wave with peak period $T_p = 5$ s in the y-direction. The differences in displacements and rotations are in general small when comparing results from the two wave periods.

Table 8.6: Maximum displacement and rotations and corresponding node location

Period	U_x	Location	U_y	Location	U_z	Location
$T = 5$ s	-0.16	Inclined span (east)	-0.54	Inclined span (west)	-0.14	Inclined span (east)
$T = 6$ s	-0.14	Inclined span (east)	-0.50	Inclined span (west)	-0.14	Inclined span (east)
Period	Rot_x	Location	Rot_y	Location	Rot_z	Location
$T = 5$ s	-0.003	Inclined span (east)	-0.00085	Western high bridge	-0.005	Western high bridge
$T = 6$ s	-0.003	Inclined span (east)	-0.00065	Western high bridge	-0.005	Western high bridge

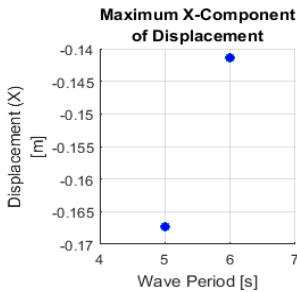


Figure 8.50: Maximum x- component of displacement

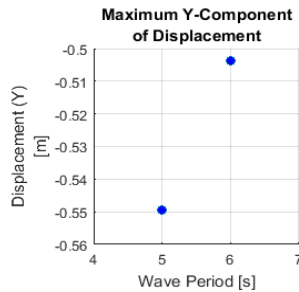


Figure 8.51: Maximum y- component of displacement

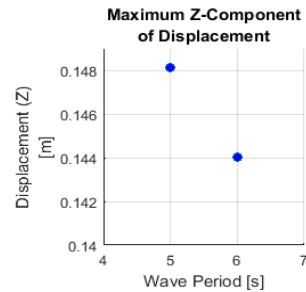


Figure 8.52: Maximum z- component of displacement

In Figure 8.54 the vertical displacement of the three westmost pontoons are plotted over 25 seconds in steady state. From this it can be seen that the amplitude of displacement increases as the pontoon location moves towards the center of the bridge. The lowest amplitude is for the pontoon neighbour to the jacket, where some of the vertical motion is restricted by the jackets presence. There is a small, but noticeable difference in amplitude from pontoon 2 to pontoon 3.

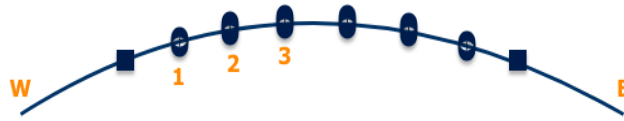


Figure 8.53: Selected pontoons for vertical displacement in Figure 8.54

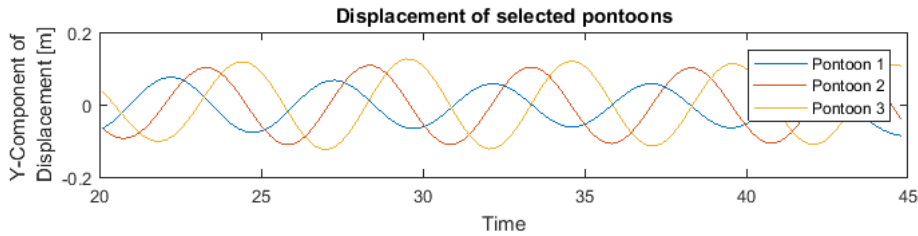


Figure 8.54: Vertical displacement over time for the three westmost pontoons

The maximum rotation is found at about the global z-axis. The rotations are overall small, and are within the criteria stated. The rotation is was expected to be symmetric along the girder due to symmetry in the bridge geometry and applied regular wave forces (including the pontoon delay). The rotation was found not to be completely symmetric because the span distance was later found to be not completely symmetric. The deviations in the spans are only on the range of 0.5-1 meters, but are large enough to explain this deviation from expected results.

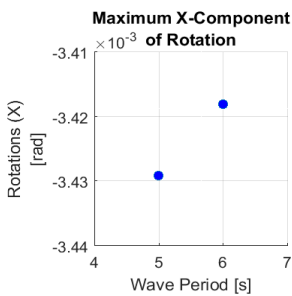


Figure 8.55: Maximum x-component of rotation

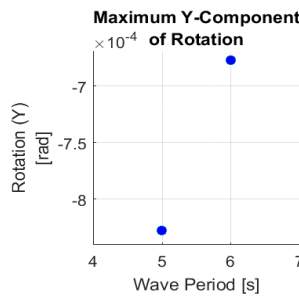


Figure 8.56: Maximum y-component of rotation

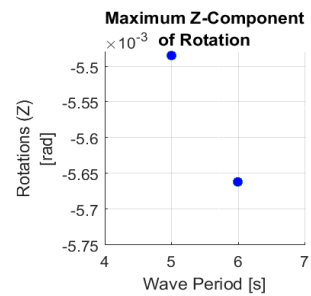


Figure 8.57: Maximum z-component of rotation

8.5.2 Global Accelerations

In Table 8.7, the maximum global accelerations in x-, y-, z- and for corresponding rotations are summarized. Located maximum accelerations are within the criteria, except for the y-component of acceleration when the wave period is 5 seconds. Here, the criteria is exceeded by 0.03 m/s². The larges accelerations occur in the vertical direction for wave period 5. A contributing effect can be because this wave period coincides with mode 5-7 which are vertical modes and some resonant behaviour is excited. It could also be affected by the structural and hydrodynamic damping parameters.

Table 8.7: Maximum accelerations from regular wave analysis

Period	A_x [m/s ²]	A_y [m/s ²]	A_z [m/s ²]	A_{rotx} [m/s ²]	A_{roty} [m/s ²]	A_{rotz} [m/s ²]
T = 5 s	0.23	0.53	0.08	2.5E-03	6.1E-04	6.4E-03
T = 6 s	0.13	0.32	-0.04	-1.5E-03	-2.5E-04	3.5E-03

8.5.3 Global Bending Moments

The presented bending and torsional moments only take the bridge girder into consideration. The stay cables and pontoon columns are not included. Table 8.8 summarizes the largest observed values for each load condition. Figure 8.58, 8.59, and 8.60 show the variation in moment components over a 20 second time period. The bending moment and stress results shows coherence between the applied regular wave load and the response. Additional plots of the maximum positive and negative bending moments are attached in the appendix.

Table 8.8: Maximum positive and negative bending moment results from the regular wave analysis

Period	$M_{x,max}$ [MNm]	$M_{x,min}$ [MNm]	$M_{y,max}$ [MNm]	$M_{y,min}$ [MNm]	$M_{z,max}$ [MNm]	$M_{z,min}$ [MNm]
T = 5 s	33.5	-26.6	-46.1	-33.1	159.7	-367.8
T = 6 s	32.6	-27.1	44.6	-31.8	159.4	-367.8

The bending moment about the global x-axis over 20 seconds, Figure 8.59, has the smallest variation in amplitude during the time of measurement. This holds for both wave periods. The largest bending moment is 33.5 MNm and occurs at the section of the girder surrounding the pontoon column on the inclined section. Due to the taller column and its coarse modeling, this section of the bridge is more exposed to movement, which is reflected in the results. It was expected that this distribution was symmetric, but it is seen that the bending moment is larger on the east side of the bridge. This could be because the distance between the spans is not completely symmetric, and the spans on the east side are slightly longer than the spans on the west side. This error in the model geometry arised because the bridge was divided from west to east on coarse arc length calculations which caused an inaccuracy.

Considering the bending moment about the global y-axis, Figure 8.58 this response shows the largest variation in amplitude for the bending moment. It is seen that the maximum and minimum bending moments have close to symmetric response, however the minimum bending moment has a lower peak amplitude. For the wave with peak period $T_p = 6$ s, this response term is smallest. The response for the wave with peak period $T_p = 5$ s is slightly larger than for the wave with peak period $T_p = 6$ s.

The bending moment about the global z-axis (Figure 8.60) dominates in magnitude, and the negative component has the largest amplitude. The bending moment contribution 8.63 corresponds well with the theory presented in Section 3.2.1. The largest clockwise bending moments occur at the inclined spans, while the largest counterclockwise bending moment occurs at the section of the inclined bridge supported by the pontoon column. This can be explained by that this section is exposed to more movement.

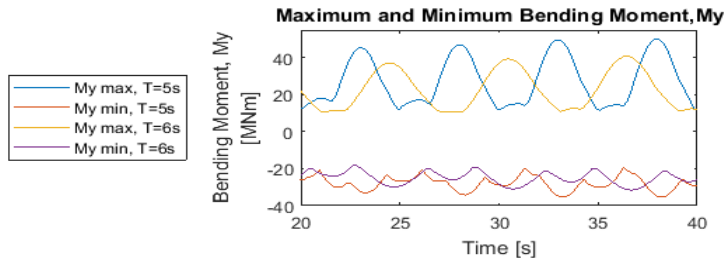


Figure 8.58: Maximum Global Bending Moment M_y for wave periods 5 and 6 seconds

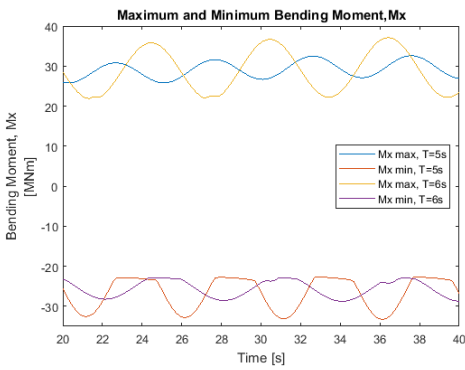


Figure 8.59: Maximum Global Bending Moment M_x for wave periods 5 and 6 seconds

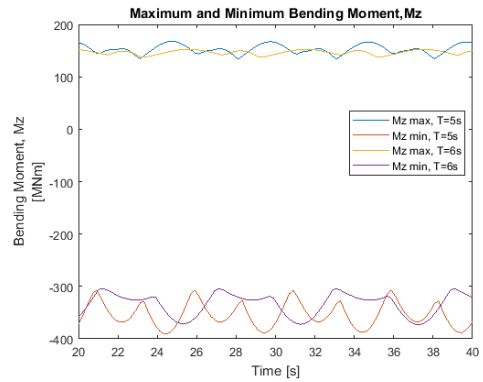


Figure 8.60: Maximum Global Bending Moment M_z for periods 5 and 6 seconds

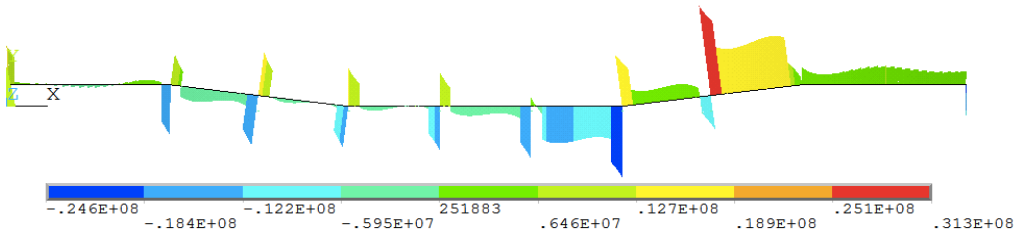


Figure 8.61: Largest positive bending moment, M_x , at $T = 6$ s

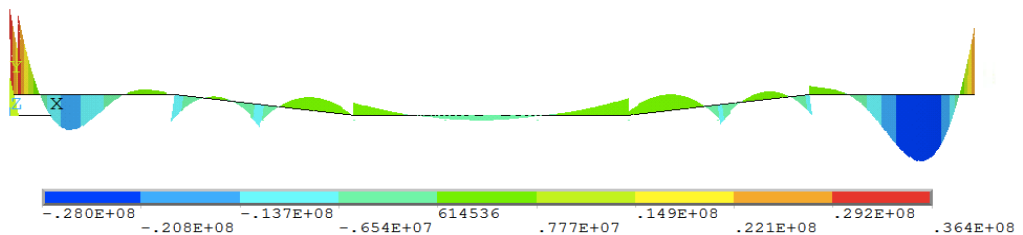


Figure 8.62: Largest positive bending moment, M_y , at $T = 5$ s

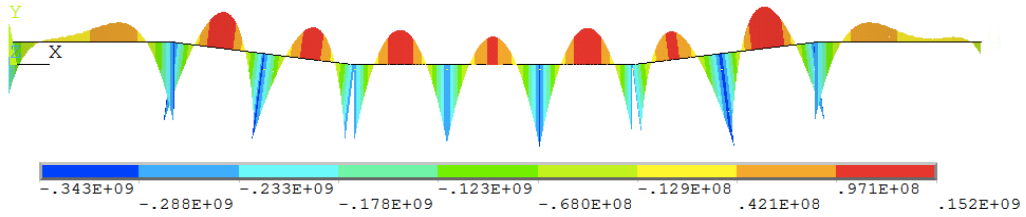


Figure 8.63: Largest positive bending moment, M_z , at $T = 5$ s

8.5.4 Von Mises Stress

The time varying measured maximum Von Mises stress from 20 to 40 seconds is shown in Figure 8.64. The maximum Von Mises stress occurs at the girder section surrounding the eastmost jacket for $T_p = 5$ s, which also holds the largest values for the bending moments M_y and M_z that can be seen in Table 8.8. This load case also has the largest amplitude for the cyclic load. This could be because the wave period excites some of the lower vertical modes, which leads to the higher stress levels. However, the difference in stress levels for the three wave periods is very small, which coincides with the small variations in the other response parameters.

Considering only the floating span, the Von Mises stress is larger at the section surrounding the pontoon column compared to the floating span. This corresponds with the large contribution from the bending moment about the global z-axis. In addition, the wave forces induce rotations on the bridge, causing stress concentrations at the pontoon columns.

Table 8.9: Maximum Von Mises stress from the regular wave analysis

Period	Unit	Von Mises Stress	Where
T = 5 s	[MPa]	164	Section surrounding the eastmost jacket
T = 6 s	[MPa]	156	Section surrounding the eastmost jacket

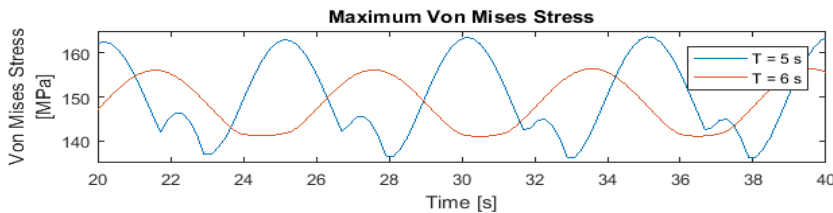


Figure 8.64: Maximum Von Mises stress from time 20 to 40 seconds for wave period $T=5$ s and $T=6$ s

8.6 Ship Collision

The jacket response in terms of displacement is governed by transverse displacement (in the x-direction) when struck by the vessel. The maximum x-component of displacement is -0.8 m and occurs at 14.7 seconds, that is 4.7 seconds after the collision load is activated. Rotation about the global z-axis is observed, but of minor magnitude.

Figure 8.65 shows the history plot of displacement throughout the analysis. The impact load is initiated after 20 seconds. After 21 seconds the mass re-obtains kinetic energy and bounces back away from the jacket. The time history plot of global displacements in Figure 8.65 shows that the largest response in terms of displacements occurs the first 10 seconds after the impact. A contour plot of global displacements is shown in Figure 8.66. After this, the curve shows that the structure exhibits small pendulum motions. The natural periods of this behaviour must be examined to check for possible resonant behaviour. From velocity and acceleration plots of the examined nodes, it is confirmed that the largest velocities and accelerations occur during analysis time 10-15 seconds.

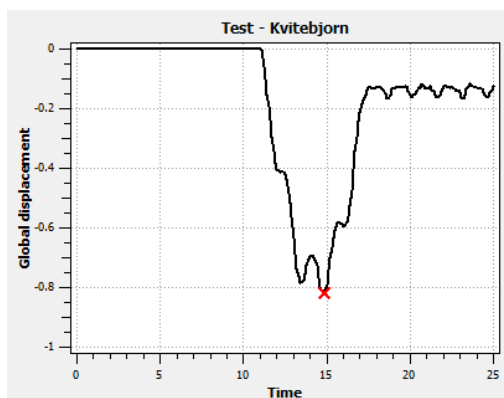


Figure 8.65: Global displacement when the impact load is activated after 10 seconds

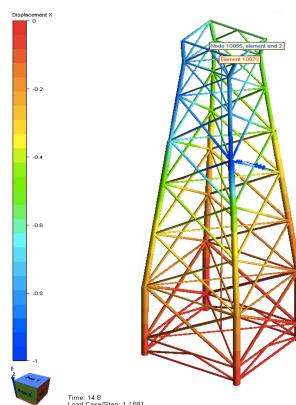


Figure 8.66: Contour plot of maximum global displacements, occurring at 14.7 seconds.

The induced displacement, velocity and acceleration due to the ship impact for the impacted node and the top of the jacket (where the bridge girder is) is summarized in the table below. Measuring the acceleration at the node of impact may, however, lead to conservative results, as all the kinetic energy from the node mass is concentrated in the x-direction, while realistically some of this energy would be dissipated through the e.g. roll, sway and heave motion. If a collision between the bridge and the ship is at risk, the bridge should be closed immediately to reduce the risk of harm to human. If however, vehicles and pedestrians are on the bridge at the time of the collision, the large induced accelerations and velocity of the bridge girder can cause vehicle collision and possibly loss of human life.

Table 8.10: Maximum displacement, velocity and acceleration and corresponding time of occurrence for node 10055

Node	U [m]	Time	V [m/s]	Time	A [m/s ²]	Time
10055	-0.82	14.7	-0.75	12.9	-17	11.1

Diagonal members are exposed to large compressing forces that causes buckling as seen in the Figure below. The member absorbs a large amount of energy, and failure occurs after the formation of a plastic hinge. Examining the plastic utilization of the jacket throughout the analysis it is seen that the plastic utilization reaches 1 for the three diagonal members pointed out with arrows in Figure 8.67. These are the members connected to, and adjacent to the struck node point. The structure suffers critical damage. USFOS however, stops the analysis if a collapse occurs. The analysis runs through the input time. This can indicate that the structure suffers critical damage, but does not collapse. This cannot be drawn as a conclusion without more extensive analysis being performed, but indicates that redesign is necessary.

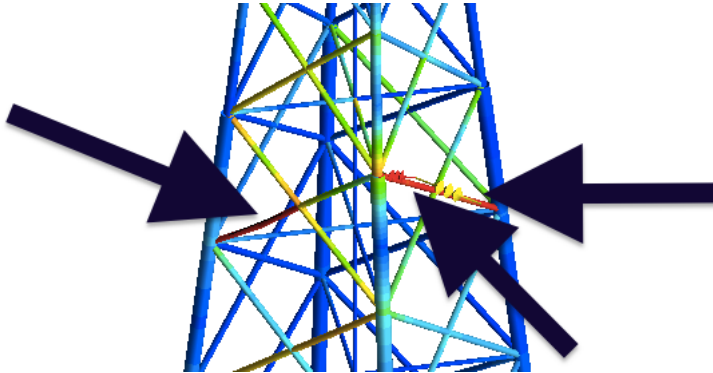


Figure 8.67: Members with plastic utilization factor 1.0 at time 4.5 seconds after the impact.

Discussion and Further Work

As a continuation of the model formulation and results presented in the previous chapters, effects of the simplifications made during the model establishment and analyses need to be addressed. This chapter presents a discussion of the main topics along with recommendations for further work and considerations that must be made to approach sufficient information about the global system behaviour to validate if the concept is feasible.

The analyses were run with a mesh size of 1.0 meters per element after evaluating convergence of stress and displacement. To advance the mesh convergence study, the optimum mesh size for each section of the model could have been run. This would have provided greater accuracy in the results. This was not considered necessary in this thesis as the interest was to examine response in the global bridge girder and not to perform detailed local analysis of certain sections. For larger dynamic analyses a larger mesh size or optimum mesh size approach could be considered as memory and software license may limit the computer performance.

The input parameters for representation of the jacket model (horizontal stiffness and effective mass) are taken from a force-displacement analysis in USFOS. The topside and equipment elements are removed from the model such that the mass and stiffness contribution is as close to a jacket undercarriage as possible. By modelling boundary conditions as spring-to-ground elements, the horizontal stiffness decreases slightly compared to fixed supports. Modelling these boundary conditions as completely fixed would provide a conservative result with higher stiffness while modelling as simply supported would underestimate the stiffness. It is not considered whether this effect will have a significant influence on the horizontal displacement of the bridge, but it will have a more significant influence for future work considering eigenvalues of the jacket.

The modelling of the buoyancy could have been improved as small vertical deflections were observed when the structure was subjected to loading from self weight and buoyancy only. When extracting forces from the buoyancy springs, a limited number of decimal points are available which are thought to cause minor effects on the results. The buoyancy distribution resulted in small vertical displacement along the structure. Further modelling of ballast could have been considered to go deeper into pontoon design, but this was outside the scope of this thesis. However, pontoon optimization should be considered for lower costs. The static analysis shows in addition to vertical displacement some horizontal displacement and rotations which may be because of the

modelling procedure and uneven distribution of buoyancy.

Considering the deflection when the model is exposed to traffic load, the results showed that the response was within the criteria. These results are somewhat conservative, as the criteria is given for when 70 % of the traffic load is applied. The static results are within the criteria except for during tidal variation, which is discussed in the next paragraph. Even though these results do not indicate anything about the dynamics of the system, they provide estimates relatively fast that can uncover sections that need redesign at an early stage. When examining the bending moment and shear force distributions along the bridge girder, these correspond well with the theory presented when considering simplified estimates.

The results from the tidal load cases need attention. The exceedance of the criteria will require that the modelling approach is changed and redesign of the bridge is necessary. E.g., the pontoon and the column supporting the inclined section should be remodelled such that this span section is prevented from such large displacements. This could also be improved by adding larger pontoons to support the inclined section. However, it is preferable that during rising and decrease of the mean sea level the bridge should partially follow the water level such that the ends are relieving the large moments that are absorbed if the bridge restrains this motion. There must, therefore, be a balance between restraining the bridge motion and allowing vertical deflections that do not exceed the criteria. Tide level parameters are taken from measurements done in the Bjørnafjord. For conservatism, a tidal variation of +/- 1.0 m instead of +/- 0.75 m is applied.

When comparing the stress results from the static and regular wave analysis, the Von Mises stress results are higher for the static analysis when tidal variation is considered. For both analysis the maximum Von Mises stress occurs at the section surrounding the jacket (eastmost), so it is clear that this section of the bridge will be particularly exposed to cyclic loading and fatigue assessments should therefore be addressed. The maximum Von Mises stress occurs due to tidal variation, so this static load case in combination with dynamics should be given further attention as it indicates that this combination can expose the bridge to large stresses.

The modal analysis indicates that the first dynamic modes range from around 50 seconds and higher, implying that low frequency induced response must be assessed. The higher modes coincide with wave periods from 6-18 seconds (swell generated), and with wave periods lower than 7 seconds (wind generated) in the relevant area. This may induce resonant response and could be a contributing cause to the results exceeding the acceleration criteria of 0.5 m/s^2 .

The structural damping parameters, α and β are found by assuming a damping level of 2 % between mode 1 and 10. It was tested to compute α and β by assuming an equivalent damping level between other modes, but it did not seem to affect the results significantly. The estimation of damping parameters was based on assumptions. The damping parameters could instead have been found by computing the modal mass contribution and include this when obtaining α and β . It is not one hundred percent certain that the damping parameters are correct, which can have contributed to the accelerations that slightly exceeded the design criteria. The radiation damping coefficients taken from the NPRAs report for the Bjørnafjord should also be re-examined. Computing new damping parameters would provide a stronger theoretical argument for whether the results are valid or not. The damping level is essential concerning the response amplitude, and also when considering the low frequency induced response. The structural damping will most likely contribute to limit the response, but it will still be very important to obtain a representative damping effect to ensure that response that causes damage to the structure is avoided. This will be especially important since the wave frequencies at the installation site coincides with some of the modes for both concepts.

Variations in frequency dependent added mass for the jacket are not included, which may lead to underestimation of the forces. However, the wave periods in the regular wave analysis are only one second apart from each other, so this assumption is not considered to have a significant impact on the results. It should, however, be included if analyses including other wave conditions are performed. The added mass contribution on the pontoons is found in the report from the NPRA on the Bjørnafjorden floating bridge and obtained from reading the graphs in the report. This is a source of uncertainty, and a change in added mass will affect the eigenfrequencies, which further can lead to different results in the static, and regular wave analysis.

The regular wave analysis is done to analyse simple dynamics of the floating bridge. For detailed design and further analysis (and in the long run, verification of the concept), it will be necessary to consider multiple sea states with extreme values. Modelling the dynamic behaviour of the system is challenging when defining structural- and hydrodynamic properties and boundary conditions. The modelling approach will affect the dynamic behaviour of the structure. Different behaviour can be expected for the concept when the bridge exposed to irregular waves. The structure needs time to respond to the wave forces, and so the duration of the wave periods will affect the response in the structure.

The collision scenario is a head-on collision, which is assumed the most probable scenario. Other impact scenarios are also likely to occur (but less than the chosen scenario), e.g. with an impact angle of 45 degrees or parallel impact between the ship hull and the jacket. Further, more extensive results on the residual strength of the jacket and total energy distribution between the ship and the jacket could have been obtained, but due to time limitation, the work scope was limited to a simple analysis. A more advanced and realistic analysis would be to include the impact of the bulb, and establish a global model of the bridge in e.g. USFOS. This was however not considered a priority at such an early stage in the design phase. Large deformations are expected to occur. The effect of collision with the pontoons and simulation of flooded compartments should be performed in a more thorough analysis of collision between the ship and components of the floating bridge. In addition, the jackets natural frequencies should be checked for evaluation of the significance of global dynamics. Redesign of the structure could be considered, e.g. with collision barriers.

A cost evaluation has not been performed in this thesis due to time limitation and limited available information on costs related to installation and fabrication of floating bridges. However, steel, sub-sea operations, and heavy lift equipment are often cost drivers. Also, if the bridge was redesigned such that the cable stay bridge and large towers could be avoided, this could further reduce costs. The cost of the undercarriage will be less than offshore jackets installed in the north sea, as they, in addition, have expensive drilling and production equipment for treating hydrocarbons.

Considering further work for comparison of the concepts, multiple dynamic analysis must be made for both concepts to make a decision on which concept that should be chosen. The I-jacket concept shows coincidence with wave periods for lower modes than the II-jacket concept and there might, therefore, be lower chance of resonant response. A cost evaluation will also be necessary. It is thought that the I-jacket bridge can come out to lower costs, as this concept needs only one jacket and one cable bridge which will require a lower steel mass. This will, however, depend on the cost of the additional pontoons needed for this concept, and of course, that the structural response is within design criteria. The work done in this thesis is however not sufficient to confirm which concept one should move forward with.

Concluding Remarks

The analyses performed in this thesis gives an indication of the global static and dynamic behaviour of the structures as well as highlighting further work that must be done for validation. The analyses performed are not sufficient to validate either of the concepts, as this would require multiple analysis of extreme response in irregular sea.

The static and regular wave analyses show that the response is within the design criteria limits, except for:

- Vertical deflection due to low tide is exceeded by -0.08 m for the I-jacket and -0.14 m II-jacket concept.
- The response in terms of the global y-component of acceleration exceeds the requirement of 0.5 m/s^2 by 0.03 m/s^2 .

That these criteria were exceeded, is believed to occur due to flaws in the modelling of structural and radiation damping features and contributions from excited resonant behavior. The bridge girder geometry with the inclined section should be improved and strengthened. More extensive work on hydrodynamic parameters for the global model must be carried out.

The modal analysis shows that the first modes range from 82 seconds (I-jacket) and lower, and 54.5 seconds (II-jacket) and lower. Swell generated waves with 1, 100 and 10 000 year return period overlap modes in the range 6-18 seconds for both concepts. For locally wind generated sea, lower modes coincide. The first dynamic modes indicate that low frequency induced dynamic response will be necessary to assess. This indicates a chance of resonant response.

The collision scenario in USFOS is modeled by using mass and spring elements. The force-deformation curve is represented through a non-linear spring element, while a hyper-elastic spring represents the unloading phase. Results from the ship collision analysis indicate that the jacket suffers severe damage, which may cause critical damage to the bridge. A full dynamic analysis of ship collision with a global bridge model must be performed to substantiate whether the bridge will survive or collapse in case of a collision. The effect of adding additional protection as braces or fenders could be investigated in further work.

Bibliography

Amdahl, e. a., 2014. Havromsteknologi. Fagbokforlaget.

Amdahl, J., 2009. TMR4167 - Marine Technology - Structures.

ANSYS, 2018. ANSYS Documentation, 18.2).

Attaway, S., 2009. Matlab: A Practical Introduction to Programming and Problem Solving.

Avinor, Jerbaneverket, K. S., 2016. Utviklingsstrategi for Ferjefri og Utbeta E39.

Bell, K., 2015. Konstruksjonsmekanikk. Fagbokforlaget.

Bergensavisen, 2007.

URL <https://www.ba.no/nyheter/nordhordland-eller-nordhordaland/s/1-41-2923806>

Brede, H., 2017. Concept Study of a Floating Bridge.

Chen, W.-F., Duan, L., 2013. Bridge Engineering Handbook. Superstructure Design, 734.

Det Norske Veritas, 2010. Design Against Accidental Loads. Recommended Practice DNV-RP-C204 (October), 7–52.

DNV-GL, 2010. Environmental conditions and environmental loads. Dnv (October), 9–123.

DNV-GL, 2011. Modelling and Analysis of Marine Operations (April).

Faltinsen, O. M., 1993. Sea Loads on Ships and Offshore Structures. Cambridge University Press.

FGG, U., 2013. Structural systems: Offshore - installation (university of ljubljana, faculty of civil and geodetic engineering).

Furnes, O., Amdahl, J., 1980. Ship Collisions with Offshore Platforms.

Greco, M., 2012. TMR4215: Sea Loads, Lecture Notes. Department of Marine Technology, Faculty of Engineering Science and Technology, NTNU.

Hagiwara, K., Takanabe, H., Kawano, H., 1983. A proposed method of predicting ship collision damage. International Journal of Impact Engineering 1 (3), 257–279.

He, Z.-F. F. J., 2001. Modal Analysis. Butterworth-Heinemann Oxford.

HjellnesConsult, 2017. Bergsøysundet flytebru.

URL <http://www.hjellnesconsult.no/wp-content/uploads/>

[Norsk-Bergsoysundet.pdf](#)

- Jembatan, D., 2013. Evergreen Point.
URL http://www.datajembatan.com/index.php?g=guest_bridge&m=bridge.detail&b=753
- Kawade, A. B., Meghe, S. P., 2014. Submerged Floating Tunnel. Civil Engineering Portal 1986, 91380.
URL <http://www.engineeringcivil.com/submerged-floating-tunnel.html>
- Langen I., S. R., 1979. Dynamisk Analyse av Konstruksjoner. Tapir Publishers.
- Larsen, C. M., 2014. TMR4182 - Marin Dynamikk.
- Leira, B. J., 2016. OMAE2016-54598, 1–9.
- Marshall, A., 2016. What It Takes to Keep a 7,700-Foot Floating Bridge From Doom. The Balance.
URL <https://www..com/2016/04/takes-keep-7700-foot-floating-bridge-doom/>
- Moan, T., 2003. TMR4190 Finite Element Modeling and Analysis of Marine Structures.
- Moan, T., 2011. Nonlinear Analysis. Nonlinear Analysis 74 (5), 1676–1689.
URL <http://dx.doi.org/10.1016/j.na.2010.10.039>
- Moaveni, S., 2015. Finite Element Analysis- Theory and application with ANSYS. Vol. 4. Pearson.
- Moe, O. H., Aas-jakobsen, K., Amdahl, J., 2017a. ScienceDirect ScienceDirect of tether anchored floating suspension bridge subjected to extreme environmental loads Analysis of Ole tether anchored floating suspension , Jørgen bridge extreme environmental loads. Procedia Engineering 199, 3033–3038.
URL <http://dx.doi.org/10.1016/j.proeng.2017.09.536>
- Moe, O. H., Sha, Y., Veie, J., Amdahl, J., 2017b. Analysis of tether anchored floating suspension bridge subjected to large ship collisions. Procedia Engineering 199, 2488–2493.
URL <http://dx.doi.org/10.1016/j.proeng.2017.09.413>
- Morrissey, R. L. . M., 2000. How bridges work.
URL <https://science.howstuffworks.com/engineering/civil/bridge7.htm>
- Myrhaug, D., 2004. Marin dynamikk (uregelmessige bølger og bølgestatistikk). Akademika Forlag.
- Norman, E. B., Norman, V. D., 2012. Mørebyen ?
- NORSOK, 2004. NORSOK: N-004: Design of steel structures. The Norwegian Oil Industry Association (OLF) and Federation of Norwegian Manufacturing Industries (TBL) (October).
- NORSOK, 2010. Risk and emergency preparedness analysis. Vol. 3.
- NPRA, 2011. A feasibility study – How to cross the wide and deep Sognefjord (March 2011).

-
- NPRA, 2012a. Feasibility study for crossing the Sognefjord - Submerged Floating Tunnel.
- NPRA, 2012b. Stor bransjeinteresse for ferjefri e39.
URL <https://www.vegvesen.no/vegprosjekter/ferjefriE39/nyhetsarkiv/stor-bransjeinteresse-for-ferjefri-e39>
- NPRA, 2015a. Ferjefri E39 - Fjordkryssingsprosjektet Brukonferansen 2015 Strukturelle komponenter.
- NPRA, 2015b. Statusrapport Ferjefri E39.
- NTNU, 2017. Floating bridges.
URL <https://www.ntnu.edu/kt/research/dynamics/research/long-span/floating-bridges>
- of Bridges, H., 2018. Cable-stayed bridge - history, facts and types.
URL <http://www.historyofbridges.com/facts-about-bridges/cable-stayed-bridges/>
- OffshoreTechnology, 2017. Heidrun Field.
URL <https://www.offshore-technology.com/projects/heidrun-field/>
- OPL, 2005. The North Sea Field Development Guide. Oilfield Publications.
- Ottosen, N. Petersson, H., 1992. Introduction to the Finite Element Method. Pearson Educated Limited.
- Pettersen, B., 2007. TMR4247 - Marin Teknikk 3 Hydrodynamikk.
- Reinertsen, 2013. Mulighetsstudie for kryssing av Sognefjorden Neddykket rørbru.
- Romsdals-Budstikke, 2018. Ferjefri e39 blir utsatt med 17 år.
URL <https://www.rbnett.no/nyheter/2018/02/20/Ferjefri-E39-blir-utsatt-med-17-%C3%A5r-16129834.ece>
- Seehusen, J., 2017. Verdens lengste flytebru: Kan bli en brukonstruksjon verden aldri tidligere har sett.
URL <https://www.tu.no/artikler/verdens-lengste-flytebru-kan-bli-en-brukonstruksjon-verden-aldri-tidligere-har-sett/407471>
- SkipperKlassen, 2012. Stabilitets video - lær deg stabilitet for skip på en grunnleggende måte.
URL <https://www.youtube.com/watch?v=n3TyDLbQOws>
- Statens Vegvesen, 2015. Håndbok N400 Bruprosjektering.
- Ulstein, H., Skogstrøm, J. F. B., Aalen, P., Grünfeld, L. A., 2015. Produktivitetseffekter av Ferjefri E39, 36.
- USFOS, 2018. Usfos: Home: Product info: Usfos.
URL <http://www.usfos.no/>
- Vegvesen, S., 2013. Sognefjorden Mulighetsstudie Flytebru.
-

Visser, D. W., 1993. The Structural Design of Offshore Jackets.

Viuff, T., Leira, B., Øiseth, O., Xiang, X., 2016. Dynamic response of a floating bridge structure. IABSE Congress Stockholm, 2016: Challenges in Design and Construction of an Innovative and Sustainable Built Environment (September), 21–23.

Watanabe, E., Utsunomiya, T., 2003. Analysis and design of floating bridges. Progress in Structural Engineering and Materials 5 (3), 127–144.

URL <http://doi.wiley.com/10.1002/pse.151>

White, F. M., 2008. Fluid Mechanics. McGraw-Hill.

Yu, Z., Amdahl, J., 2001-2018. Analysis and design of offshore tubular members against ship impacts. Marine Structures 58, 109–135.

Zallen, R. M., 2008. Beam and Arch Action - A Structural Primer for Non-Engineers. Zallen Engineering - Forensic Engineering in Construction.

Chapter **A**

Appendix

A.1 Literature Review

ARTICLES					
Title	Author	Year	Software /Model	Highlights	Keywords
Analysis of tether anchored floating suspension bridge subjected to extreme environmental loads	Ole Harald Moe, Ketil Aas-Jakobsen, Jørgen Amdahl	2017	USFOS	Substantial horizontal displacement (35m) during extreme wind and wave loads. Bridge survives 100 year storm. Tether layout should be changed. Lower eigenperiods (<100s) creates exposure to dynamic amplifications from environmental loads	Analysis, Resonance, Response
Analysis of tether anchored floating suspension bridge subjected to large ship collisions	Ole Harald Moea, Yanyan Shaa, Johannes Veieb, Jørgen Amdahl		USFOS, LS-DYNA, ABAQUS	Collision barrier installed on floater. Barrier dissipates energy. Ship may be modeled as nodal mass.	Analysis, Response
Finite element modeling for static behavious analysis of suspension bridges with varying rigidity of main cables	Tatjana Grigorjeval1, Algirdas Juozapaitis2, Zenonas Kamaitis3, Ainars Paeglitis	2004	CosmosM Mi-das/Civil	Main problem of suspension bridges: excessive deformability, especially changes in environmental temperature and the wind effects. By changing the cable to stiff- ening girder bending stiffness ratio it is possible to reduce considerably the vertical displacements. The vertical deflections can be reduced up to 30% and the bending moments up to 70%	Analysis
Submerged floating tunnel	Prof. Amol B. Kawade, Miss. Shruti P. Meghe Amrutvahini			Design technology for various submerged floating tunnels	Theory
Wave forces on adjacent floating bridges	P. McIVER Department	1986		Linear theory indicates that very large responses are possible for the fluid between the bridges, though these are likely to be severely limited by non-linear and viscous effects. Very large motions and forces are not likely to occur frequently, though the consequences of such an occurrence may be serious.	Analysis, Resonance, Response
Historical view of long-span bridge aerodynamics	Toshio Miyata	2003		Aerodynamic behaviors associated with wind-induced responses concerned are quite susceptible to configurations, variables and properties of structures or their elements as well as specified turbulent winds at the site	
Modal Analysis of a Cable-Stayed Bridge	Liuchuang Weia, Heming Chenga*, Jianyun Lia	2012	ANSYS APDL	Initial design model, fem model must be validated and corrected in future work. Initial model and establishment useful for future reference. Non linear effects will cause reduced member stiffness, larger deflection and reduced frequency.	Analysis, Modal, Nonlinear
Analysis and design of floating bridges	Eiichi Watanabe and Tomoaki Utsunomiya	2003		Basic floating bridge concepts, history, design, mooring, environmental forces	History, Design
Effect of Soil-Pile Interaction on Fixed Offshore Platform Behaviour	K.S. Arun, K. Muthukkumaran	2009	FLAC 3D	Modeling and results of static wave analysis on fixed offshore structures, study the effects of the combined lateral and vertical loads on pile group foundation	Soil
Dynamic analysis of floating bridges	Mohammad Saeed Seif ??*, Yoshiyuki Inoue	1998		Modeling and response of floating bridge exposed to environmental loads. Rational approach. Pontoon design and separation distance.	Analysis
A proposed method of predicting ship collision damage	Hagiwara, Koichi Takanabe, Hisato Kawano, Hajime O. Moe, Y. Sha, J.Veie et al.	1983		A ship collision is too complex to study using theoretical methods alone. Authors propose a method for predicting ship collision damage that resorts to three combined experiments.	Collision
Analysis of tether anchored floating suspension bridge subjected to large ship collisions	O. Moe, Y. Sha, J.Veie et al.	2017	USFOS	Global response of a floating bridge subjected to large and extreme container vessel collisions both with and without the barrier.	Collision
Energy dissipation in high-energy ship-offshore jacket platform collisions	J. Travanca, H. Hao	2015		Series of FE numerical simulations are performed with the aim of providing a clearer understanding on the strain energy dissipation phenomenon, particularly upon the ship-structure interaction.	Collision
Analysis and design of offshore tubular members against ship impacts	Z. Yu, J. Amdahl	2018	LS-DYNA	Two 7500 tons displacement supply vessels of modern design are modeled. Force-displacement curves for bow and stern indentation by rigid tubes are compared with design curves in the DNV-GL RP C204. Next, both the ship structure and the tubular braces/legs are modeled using nonlinear shell finite elements, and the effect of ship-platform interaction on the damage distribution is investigated.	Collision
BOOKS					
Title	Author	Year	Software/ Model	Highlights	Keywords
Floating Bridges	M. Myint Lwin	2000		Introduction, concept, types, design criteria analysis, fabrication, cost, inspection	Theory, Design, Cost
Vessel Collision Design of Bridges	Knott, M., Pruca, Z. "Vessel"	2000		Protection requirements result in design changes. Longer span bridges more economical with regards to additional costs. Typical costs for adding protection, or for retrofitting an existing bridge for vessel collision, have ranged from 25% to over 100% of the existing bridge costs. Typical costs for incorporating vessel collision and protection issues in the plan- ning stages of a new bridge have ranged from 5% to 50% of the basic structure cost without protection.	Theory, Design, Cost
Nonlinear Analysis of Bridge Structures	Akkari, M., Duan L.	2000		Analysis classifications, material and geometrical formulations, practical applications	Theory
Nonlinear Analysis	Moan, T.	2011		Theory on nonlinear analysis	Theory
FERRY FREE COASTAL ROUTE					
Title	Author	Year	Software/ Model	Highlights	Keywords
Utviklingsstrategi for ferjefri og utbetra E39	NPRA	2015		Economic influence and sosial benefits of the coastal highway	Economic influence
Statusrapport Ferjefri E39	NPRA				Economic influence
Curved bridge - Navigation channel in south	Aas Jakobsen, COWI, Johs Holt, Global Maritime	2016		Design parameters and analysis results of the curved bridge concept designed for Bjørfjordfjorden. Wind and waves, ship collision.	Concepts
Prosjektpresentasjon - Bruer: Bergsøysundet flytebru	Johs Holt	x			Concepts
Bjørfjordfjorden suspension bridge K1 and K2 design summary	NPRA				Concepts
Produktivitetseffekter av Ferjefri E39	Heidi Ulstein, Jens Fredrik B. Skogstrøm, Peter Aalen og Leo A. Grünfeld	2015	NOREG	FF coastal highway E39 will increase BNP from 2013-2016. The largest effects will be along the norwegian west coast.	Economic influence

A.2 pontoons: Hydrodynamic Parameters

A.2.1 Added Mass Parameters

Table A.1: Frequency Dependent Added Mass for pontoons (Statens Vegvesen, 2015)

Period [s]	Surge [kg]	Sway [kg]	Heave [kg]	Roll [kg m ²]	Pitch [kg m ²]	Yaw [kg m ²]
1	6.000E+06	1.900E+06	3.700E+07	1.125E+06	2.800E+09	1.15E+09
2	5.000E+06	1.500E+06	3.710E+07	1.118E+06	2.775E+10	9.00E+08
3	3.500E+06	1.000E+06	3.690E+07	1.115E+06	2.750E+09	6.00E+08
4	2.000E+06	8.000E+05	3.650E+07	1.100E+06	2.600E+09	2.00E+08
5	1.000E+06	1.000E+06	3.650E+07	1.117E+06	2.550E+09	5.00E+08
6	1.500E+06	2.000E+06	3.640E+07	1.148E+06	2.600E+09	2.00E+08
7	5.000E+06	2.900E+06	3.600E+07	1.160E+06	2.700E+09	2.60E+09
8	1.500E+06	4.000E+06	3.480E+07	1.162E+06	3.200E+09	4.00E+09
9	1.600E+07	5.200E+06	3.420E+07	1.155E+06	3.650E+09	4.95E+09
10	2.900E+07	5.950E+06	3.380E+07	1.149E+06	3.900E+09	4.20E+09
11	2.800E+07	6.500E+06	3.410E+07	1.145E+06	3.800E+09	3.90E+09
12	2.650E+07	6.750E+06	3.460E+07	1.145E+06	3.700E+09	3.50E+09
13	2.450E+07	6.500E+06	3.500E+07	1.146E+06	3.650E+09	3.20E+09
14	2.400E+07	6.300E+06	3.650E+07	1.146E+06	3.625E+09	3.10E+09
15	2.300E+07	6.000E+06	3.720E+07	1.147E+06	3.600E+09	3.05E+09
16	2.250E+07	5.800E+06	3.800E+07	1.145E+06	3.650E+09	3.03E+09
17	2.200E+07	5.700E+06	3.900E+07	1.145E+06	3.620E+09	3.02E+09
18	2.100E+07	5.300E+06	4.000E+07	1.145E+06	3.600E+09	3.01E+09
19	2.075E+07	5.200E+06	4.100E+07	1.145E+06	3.550E+09	3.00E+09
20	2.050E+07	5.150E+06	4.150E+07	1.146E+06	3.500E+09	2.90E+09

A.2.2 Damping Parameters

Table A.2: Frequency Dependent Damping Parameters for pontoons (Statens Vegvesen, 2015)

Period [s]	Sway [N/(m/s)]	Heave [N/(m/s)]	Roll [N/(rad/s)]
1	0	1.55E+05	0
2	0	3.20E+05	1.01E+07
3	0	9.50E+05	3.51E+07
4	2.90E+05	2.11E+06	2.80E+08
5	5.10E+05	3.21E+06	5.20E+09
6	3.60E+05	3.91E+06	5.00E+08
7	1.50E+04	3.52E+06	2.80E+09
8	2.80E+05	3.41E+06	1.00E+08
9	1.01E+06	2.94E+06	1.99E+07
10	1.69E+06	2.23E+06	9.99E+06
11	2.27E+06	1.53E+06	1.99E+07
12	2.75E+06	1.00E+06	2.99E+07
13	2.93E+06	6.70E+05	3.51E+07

A.3 Main Girder Cross Section Properties

Table A.3: Additional main girder cross section properties

	H1	F1	S1	
Plate Thickness				
Plate 1	0.025	0.035	0.046	m
Plate 2	0.02	0.02	0.02	m
Plate 3	0.025	0.025	0.036	m
Plate 4	0.025	0.025	0.036	m
Plate 5	0.02	0.02	0.02	m
Plate 6	0.025	0.02	0.036	m
Cross section properties				
Area	0.9242	1.0341	1.3562	m ²
Iyy	23.731	24.848	30.788	m ⁴
Iyz	-0.23631	-0.1459	2.89E-02	m ⁴
Izz	6.5194	7.4335	9.9787	m ⁴
Warping Constant	9.1344	5.0699	2.1715	
Torsion Constant	18.432	20.019	24.997	
Centroid Y	0.16973	0.49401	0.4341	m
Centroid Z	-0.29824	-0.26617	-0.7027	m
Shear Center Y	3.59E-02	0.56908	0.46787	m
Shear Center Z	-0.56602	-0.62629	-2.0224	m
Shear Correction-yy	0.18797	0.17217	0.16194	m
Shear Correction-yz	-1.14E-02	-8.83E-03	-1.21E-02	m
Shear Correction-zz	0.73181	0.7584	0.77149	m

A.4 Force-Displacement Results from USFOS

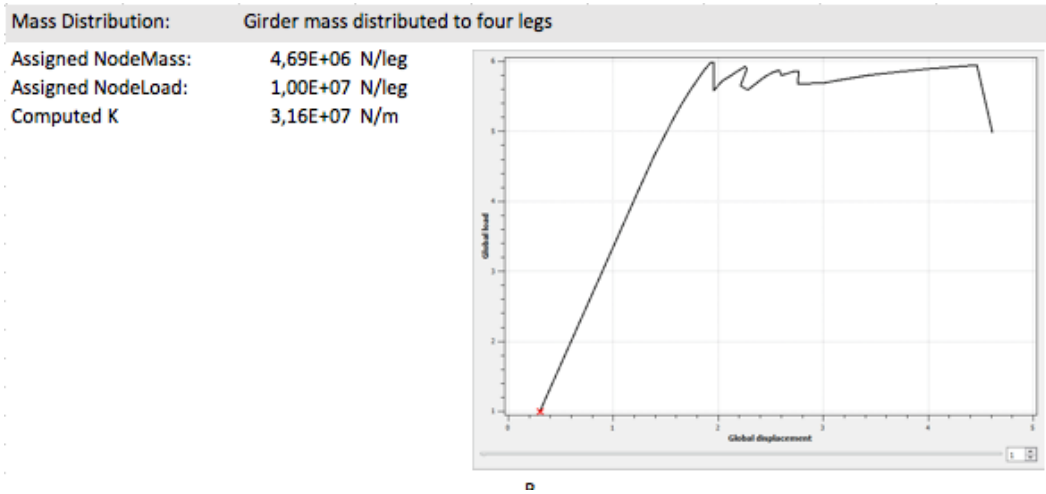


Figure A.1: Force and displacement analysis from USFOS

A.5 Static Results

Table A.4: Displacement, Rotation, Von Mises Stress, Bending Moments and Shear Force Results for I-jacket

Load Case		1	2	3	4	5	6	7
ux_{max}	[m]	0.0453	0.1713	0.1749	0.1752	0.1816	0.0858	0.2814
ux_{min}	[m]	0	0	0	0	0	0	-0.0046
uy_{max}	[m]	0.0483	0	0	0	0	0.3526	0
uy_{min}	[m]	-0.4804	-0.6159	-0.6207	-0.622	-0.6256	-0.6235	-0.9782
uz_{max}	[m]	0.0444	0.2547	0.3463	0.3785	0.4637	0.148	0.3712
uz_{min}	[m]	-0.0758	-0.2134	-0.1582	-0.1286	-0.0785	-0.3153	-0.1114
$rotx_{max}$	[rad]	0.0029	0.0035	0.0035	0.0034	0.0034	0.005	0.0021
$rotx_{min}$	[rad]	-0.0012	-0.0016	-0.0016	-0.0016	-0.0016	-0.0013	-0.0025
$roty_{max}$	[rad]	0.0002	0.0008	0.0009	0.0009	0.001	0.0008	0.0009
$roty_{min}$	[rad]	-0.0002	-0.0007	-0.0007	-0.0008	-0.0009	-0.0007	-0.0008
$rotz_{max}$	[rad]	0.0027	0.0039	0.0039	0.0038	0.0039	0.0037	0.0058
$rotz_{min}$	[rad]	-0.0037	-0.0048	-0.0049	-0.0049	-0.005	-0.0043	-0.0054
vm_{max}	[MPa]	101.13	133.45	134.05	138.73	144.63	129.27	166.29
mx_{max}	[Nm]	2.22E+07	2.69E+07	2.67E+07	2.63E+07	2.60E+07	2.91E+07	2.53E+07
mx_{min}	[Nm]	-1.95E+07	-2.43E+07	-2.42E+07	-2.41E+07	-2.44E+07	-2.25E+07	-3.85E+07
my_{max}	[Nm]	3.62E+07	4.41E+07	4.30E+07	5.58E+07	6.23E+07	4.49E+07	4.33E+07
my_{min}	[Nm]	-1.56E+07	-3.69E+07	-3.68E+07	-3.61E+07	-3.56E+07	-4.04E+07	-3.45E+07
mz_{max}	[Nm]	2.72E+08	3.54E+08	3.54E+08	3.56E+08	3.59E+08	3.27E+08	4.42E+08
mz_{min}	[Nm]	-1.07E+08	-1.47E+08	-1.48E+08	-1.49E+08	-1.50E+08	-1.38E+08	-1.70E+08
vy_{max}	[N]	7.98E+06	3.98E+05	1.00E+07	1.00E+07	9.98E+06	9.97E+06	1.07E+07
vy_{min}	[N]	-8.00E+06	-1.10E+06	-1.01E+07	-1.01E+07	-1.01E+07	-9.79E+06	-1.10E+07

Table A.5: Displacement, Rotation, Von Mises Stress, Bending Moments and Shear Force Results for II-jacket

Load Case		1	2	3	4	5	6	7
ux_{max}	[m]	0.0663	0.0663	0.0697	0.059	0.0604	0.0541	0.1014
ux_{min}	[m]	-0.0689	-0.0689	-0.0793	-0.094	-0.1086	-0.0762	-0.1638
uy_{max}	[m]	0.0018	0.0018	0.0014	0.0013	0.001	0.3083	0.0093
uy_{min}	[m]	-0.6073	-0.6073	-0.6135	-0.6144	-0.6186	-0.6207	-1.0697
uz_{max}	[m]	0.3032	0.3032	0.4674	0.5127	0.657	0.0176	0.6247
uz_{min}	[m]	-0.0375	-0.0375	-0.0356	-0.0529	-0.0625	-0.0701	-0.0439
$rotx_{max}$	[rad]	0.0026	0.0026	0.0026	0.0026	0.0026	0.0023	0.003
$rotx_{min}$	[rad]	-0.0022	-0.0022	-0.0023	-0.0027	-0.0029	-0.0022	-0.0023
$roty_{max}$	[rad]	0.0006	0.0006	0.0009	0.0013	0.0017	0.0004	0.0012
$roty_{min}$	[rad]	-0.0007	-0.0007	-0.001	-0.001	-0.0013	-0.0005	-0.0014
$rotz_{max}$	[rad]	0.0053	0.0053	0.0053	0.0053	0.0053	0.0054	0.0074
$rotz_{min}$	[rad]	-0.0051	-0.0051	-0.0052	-0.0052	-0.0053	-0.0061	-0.0068
vm_{max}	[MPa]	198.68	198.68	205.81	207.80	213.24	176.25	222.18
mx_{max}	[Nm]	2.94E+07	3.37E+07	3.37E+07	3.64E+07	3.79E+07	3.41E+07	3.33E+07
mx_{min}	[Nm]	-2.52E+07	-2.97E+07	-2.96E+07	-3.09E+07	-3.18E+07	-2.95E+07	-3.00E+07
my_{max}	[Nm]	2.27E+07	3.11E+07	2.99E+07	3.37E+07	3.82E+07	2.84E+07	3.39E+07
my_{min}	[Nm]	-2.20E+07	-2.84E+07	-3.25E+07	-4.67E+07	-6.43E+07	-2.95E+07	-3.83E+07
mz_{max}	[Nm]	1.43E+08	1.79E+08	1.17E+08	1.76E+08	1.74E+08	1.81E+08	1.81E+08
mz_{min}	[Nm]	-3.16E+08	-3.85E+08	-3.87E+08	-3.87E+08	-3.88E+08	-4.08E+08	-4.30E+08
vy_{max}	[N]	8.73E+06	1.10E+07	1.10E+07	1.10E+07	1.10E+07	1.08E+07	1.14E+07
vy_{min}	[N]	-3.86E+07	-4.94E+07	-4.92E+07	-4.92E+07	-4.90E+07	-4.90E+07	-4.99E+07

A.6 I-Jacket: Static Results for the Highbridge Models - Additional Plots

A.7 Selfweight

X-component of Displacement

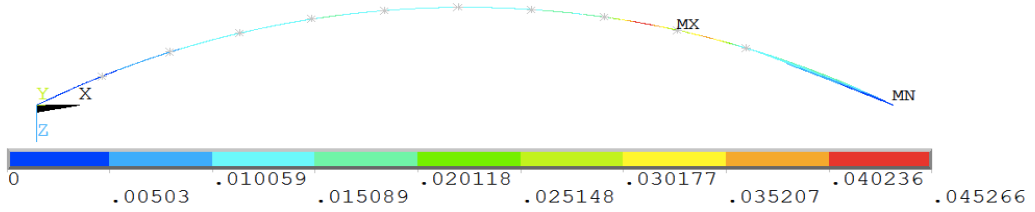


Figure A.2: X-component of Displacement in the Bridge Girder due to Selfweight

Y-component of Displacement

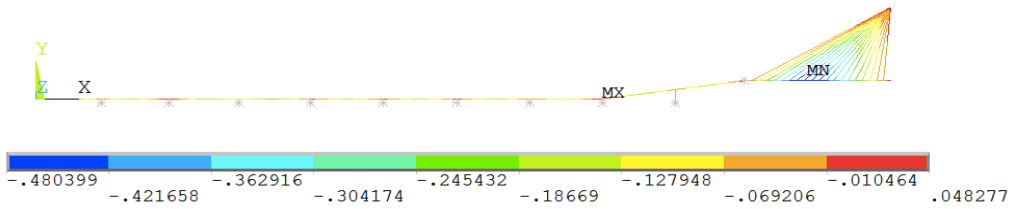


Figure A.3: Y-component of Displacement in the Bridge Girder due to Selfweight

Z-component of Displacement

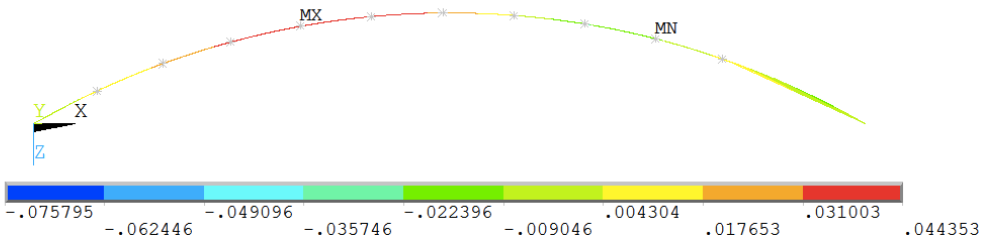


Figure A.4: Z-component of Displacement in the Bridge Girder due to Selfweight

X-component of Rotation

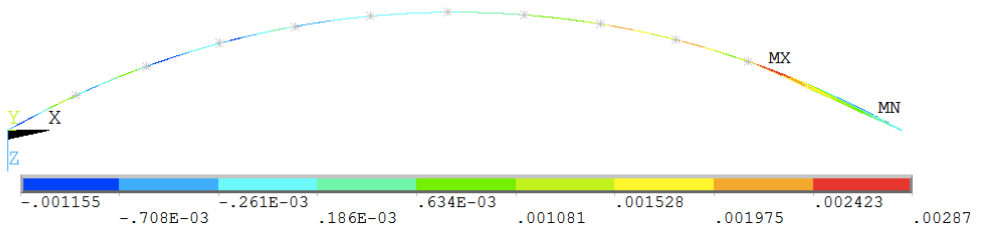


Figure A.5: X-component of Rotation in the Bridge Girder due to Selfweight

Y-component of Rotation

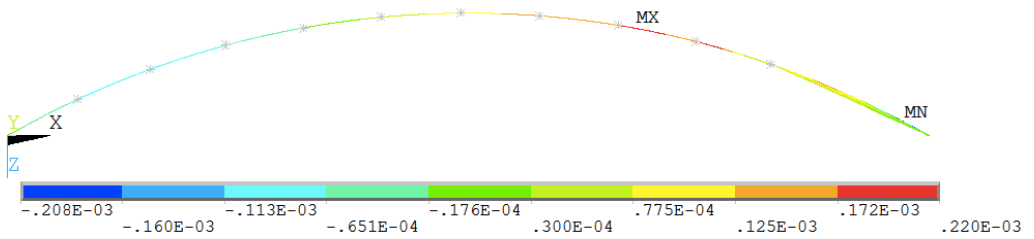


Figure A.6: Y-component of Rotation in the Bridge Girder due to Selfweight

Z-component of Rotation

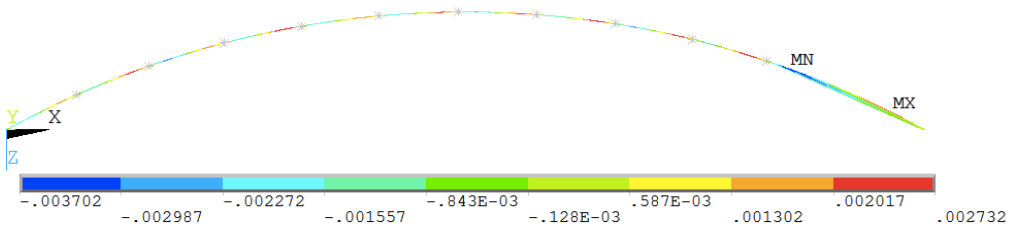


Figure A.7: Z-component of Rotation in the Bridge Girder due to Selfweight

Global Bending Moment M_X

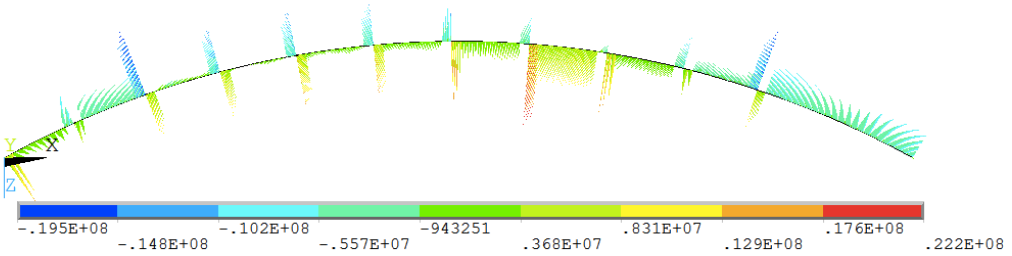


Figure A.8: Global Bending Moment M_X in the Bridge Girder due to Selfweight

Global Bending Moment M_Y

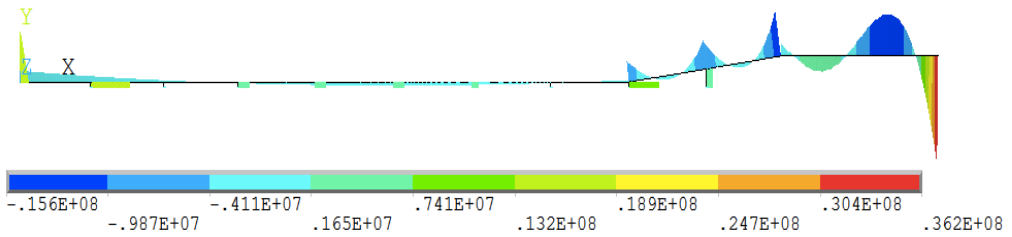


Figure A.9: Global Bending Moment M_Y in the Bridge Girder due to Selfweight

Global Bending Moment M_Z

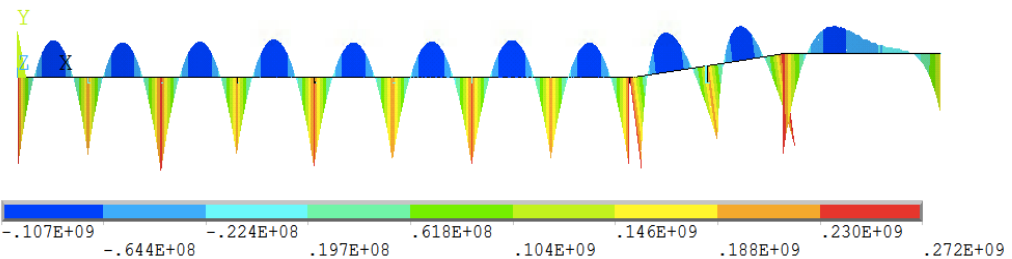


Figure A.10: Global Bending Moment M_Z in the Bridge Girder due to Selfweight

Global Shear Force V_Y

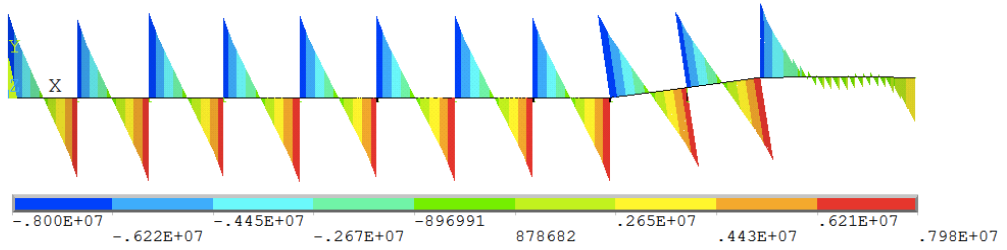


Figure A.11: Global Shear Force V_y in the Bridge Girder due to Selfweight

Global Shear Force V_Z

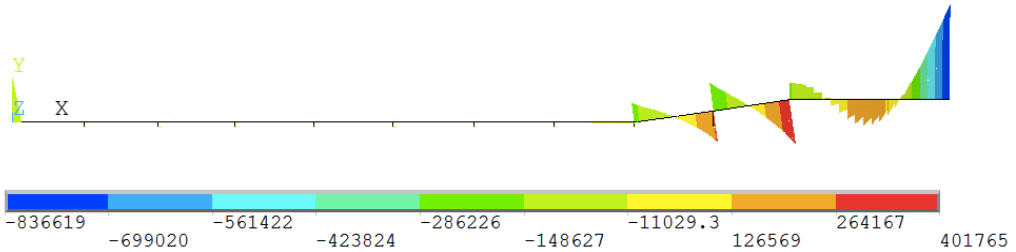


Figure A.12: Global Shear Force V_z in the Bridge Girder due to Selfweight

Global Von Mises Stress

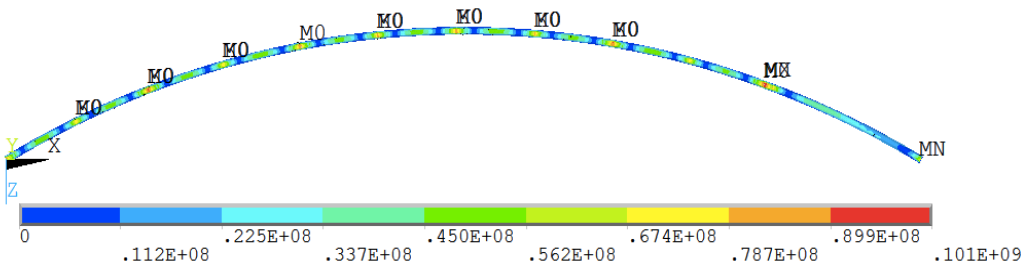


Figure A.13: Global Von Mises Stress in the Bridge Girder due to Selfweight

A.8 Traffic Load

X-component of Displacement

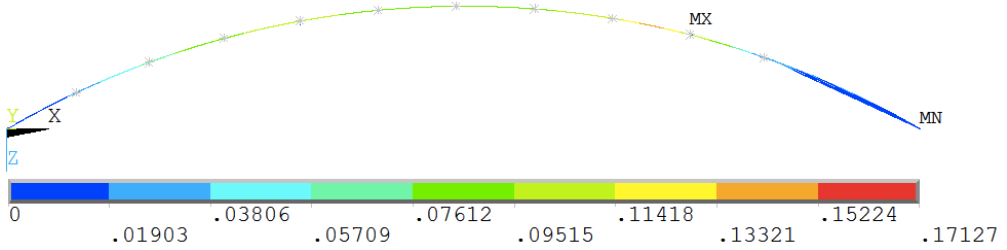


Figure A.14: X-component of Displacement in the Bridge Girder due to Traffic Load

Y-component of Displacement

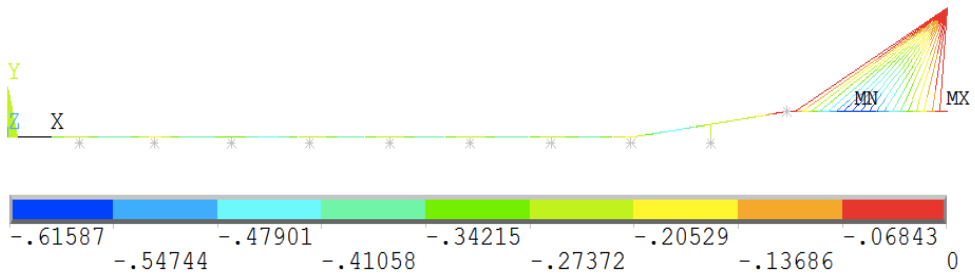


Figure A.15: Y-component of Displacement in the Bridge Girder due to Traffic Load

Z-component of Displacement

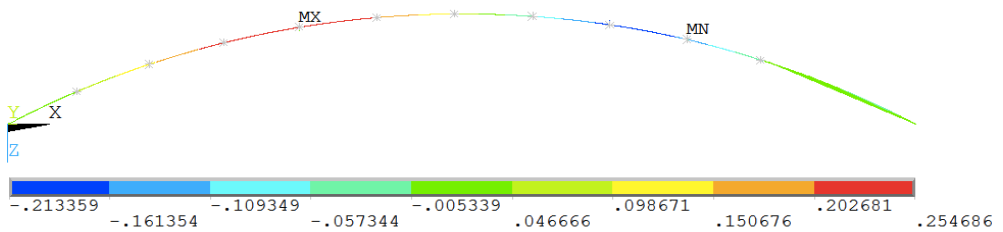


Figure A.16: Z-component of Displacement in the Bridge Girder due to Traffic Load

X-component of Rotation

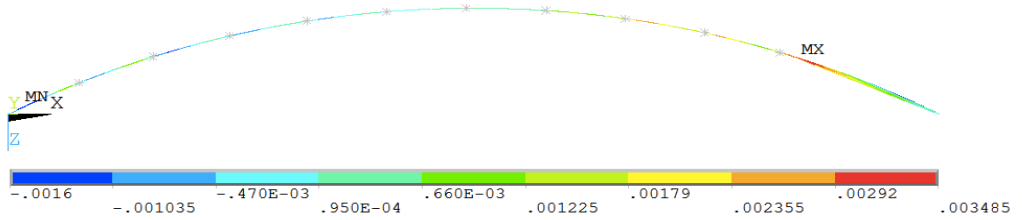


Figure A.17: X-component of Rotation in the Bridge Girder due to Traffic Load

Y-component of Rotation

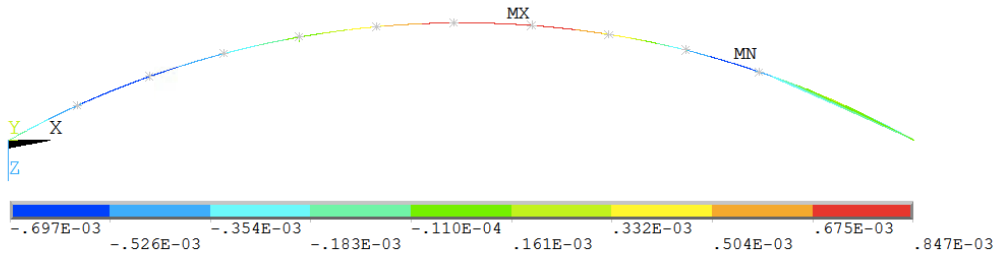


Figure A.18: Y-component of Rotation in the Bridge Girder due to Traffic Load

Z-component of Rotation

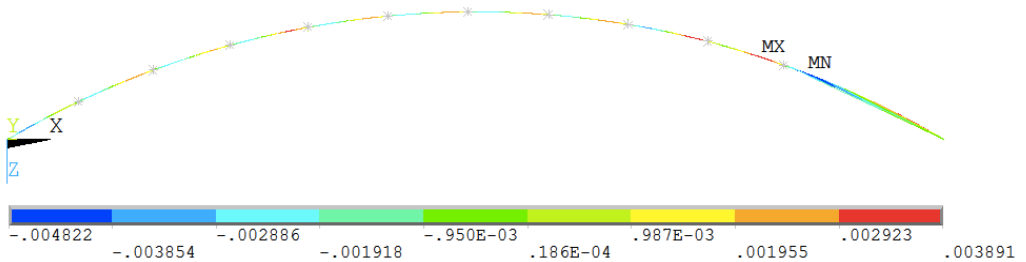


Figure A.19: Z-component of Rotation in the Bridge Girder due to Traffic Load

Global Bending Moment M_X

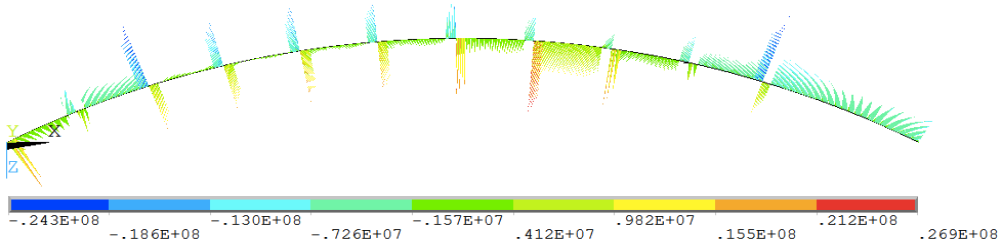


Figure A.20: Global Bending Moment M_X in the Bridge Girder due to Traffic Load

Global Bending Moment M_Y

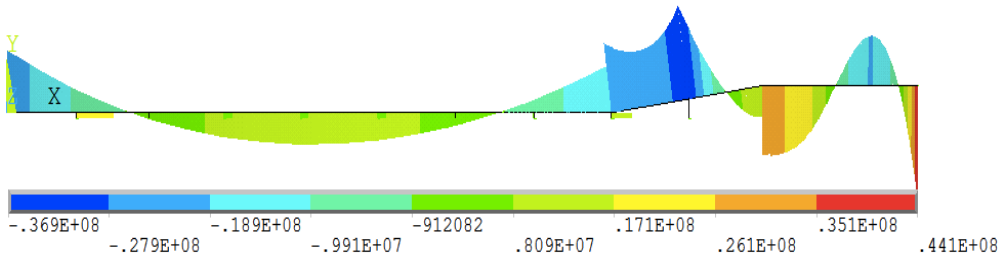


Figure A.21: Global Bending Moment M_Y in the Bridge Girder due to Traffic Load

Global Bending Moment M_Z

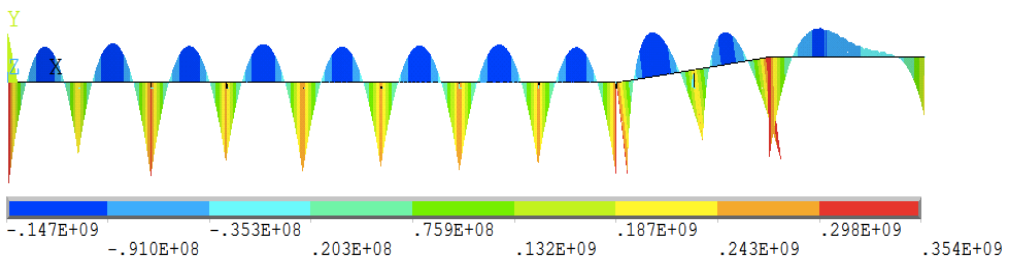


Figure A.22: Global Bending Moment M_Z in the Bridge Girder due to Traffic Load

Global Shear Force V_Y

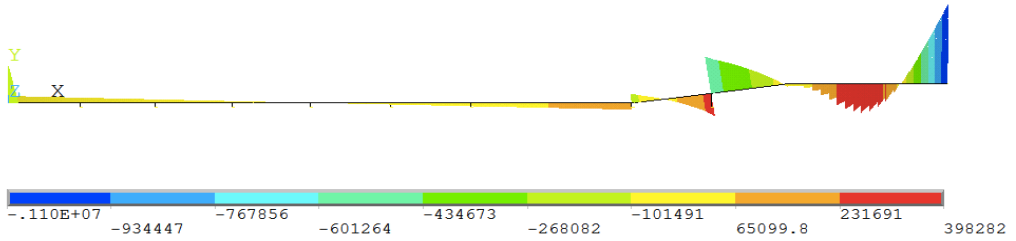


Figure A.23: Global Shear Force V_Y in the Bridge Girder due to Traffic Load

Global Shear Force V_Z

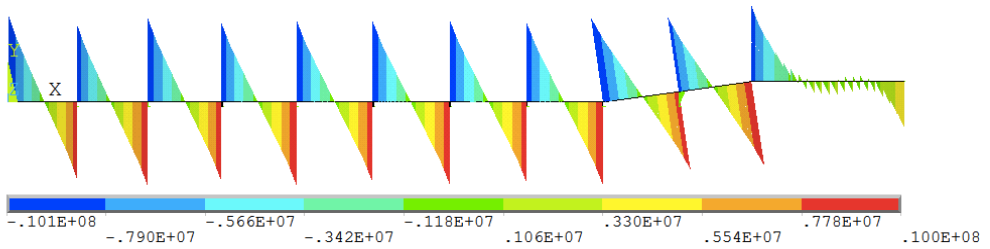


Figure A.24: Global Shear Force V_Z in the Bridge Girder due to Traffic Load

Global Von Mises Stress

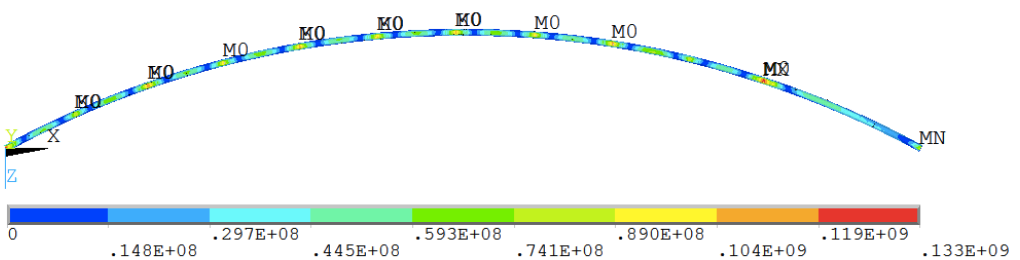


Figure A.25: Global Von Mises Stress in the Bridge Girder due to Traffic Load

A.9 Wind (1 Year Return Period)

X-component of Displacement

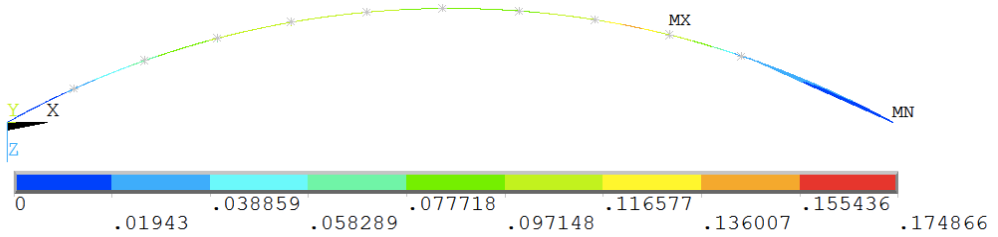


Figure A.26: X-component of Displacement in the Bridge Girder due to Wind (1 Year Return Period)

Y-component of Displacement

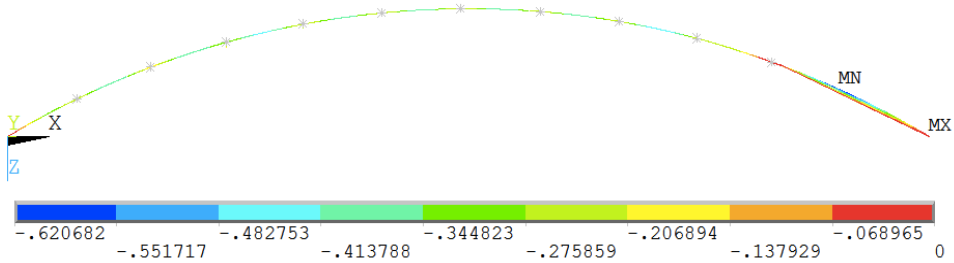


Figure A.27: Y-component of Displacement in the Bridge Girder due to Wind (1 Year Return Period)

Z-component of Displacement

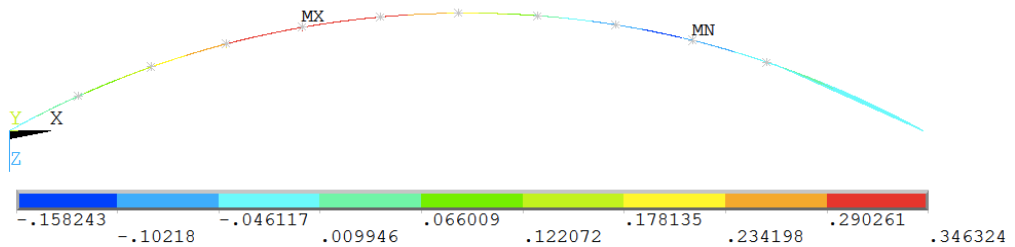


Figure A.28: Z-component of Displacement in the Bridge Girder due to Wind (1 Year Return Period)

X-component of Rotation

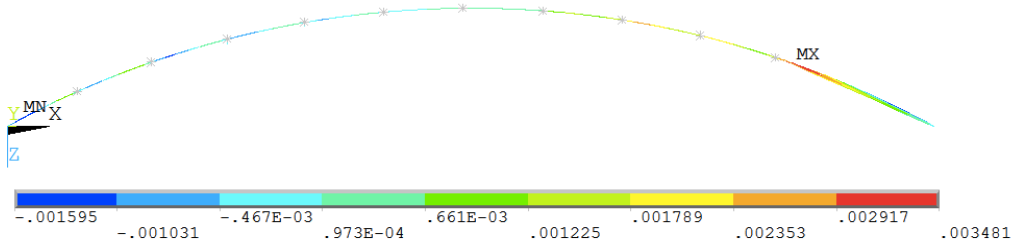


Figure A.29: X-component of Rotation in the Bridge Girder due to Wind (1 Year Return Period)

Y-component of Rotation

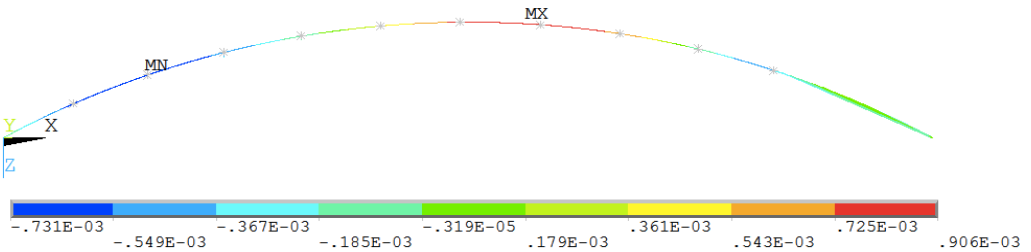


Figure A.30: Y-component of Rotation in the Bridge Girder due to Wind (1 Year Return Period)

Z-component of Rotation

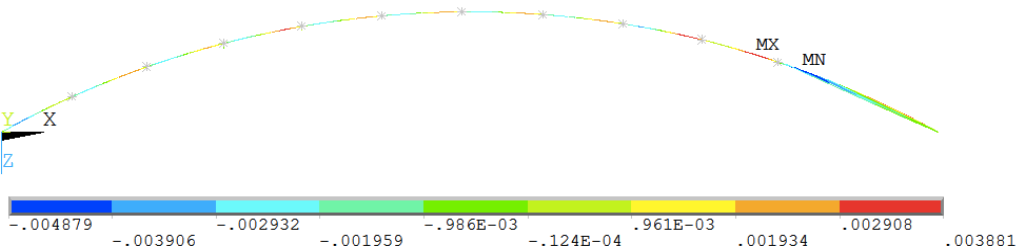


Figure A.31: Z-component of Rotation in the Bridge Girder due to Wind (1 Year Return Period)

Global Bending Moment M_X

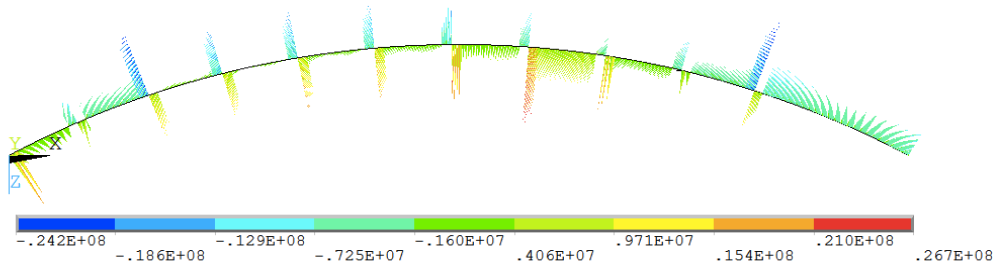


Figure A.32: Global Bending Moment M_X in the Bridge Girder due to Wind (1 Year Return Period)

Global Bending Moment M_Y

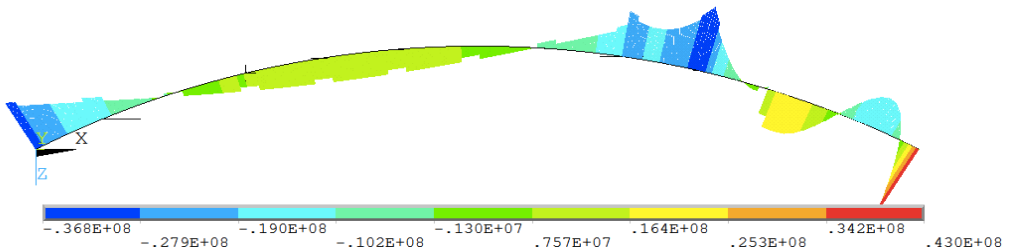


Figure A.33: Global Bending Moment M_Y in the Bridge Girder due to Wind (1 Year Return Period)

Global Bending Moment M_Z

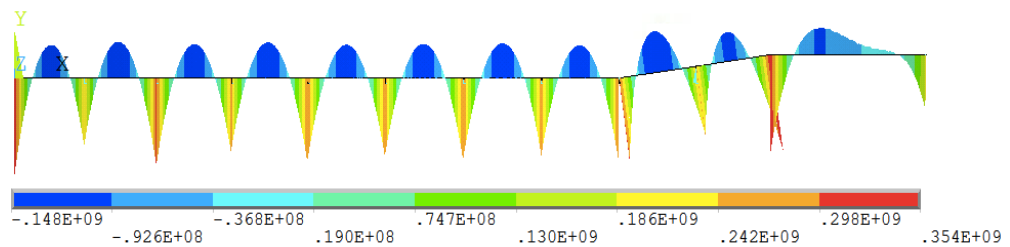


Figure A.34: Global Bending Moment M_Z in the Bridge Girder due to Wind (1 Year Return Period)

Global Shear Force V_Y

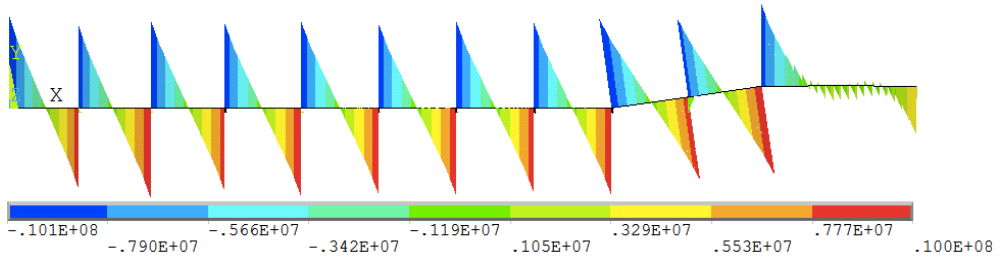


Figure A.35: Global Shear Force V_y in the Bridge Girder due to Wind (1 Year Return Period)

Global Shear Force V_Z

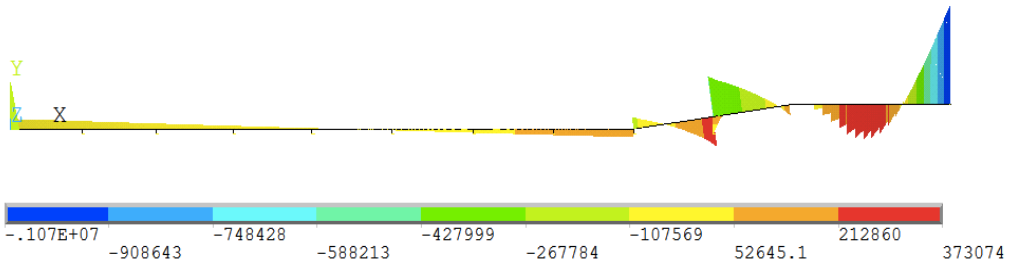


Figure A.36: Global Shear Force V_z in the Bridge Girder due to Wind (1 Year Return Period)

Global Von Mises Stress

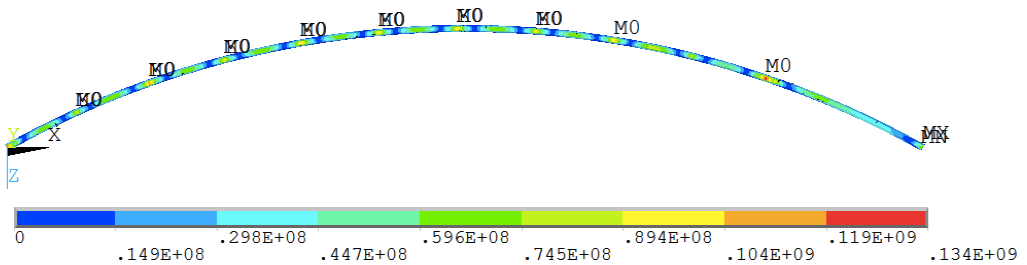


Figure A.37: Global Von Mises Stress in the Bridge Girder due to Wind (1 Year Return Period)

A.10 Wind and current (1 Year Return Period)

X-component of Displacement

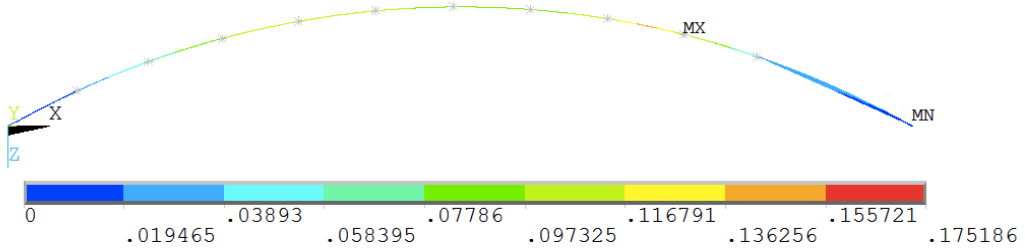


Figure A.38: X-component of Displacement in the Bridge Girder due to Wind and current (1 Year Return Period)

Y-component of Displacement

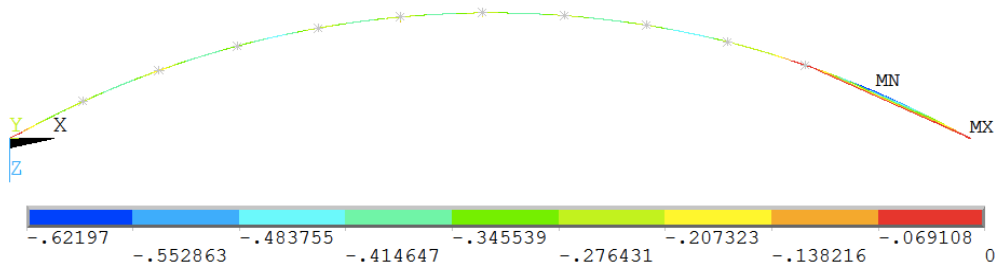


Figure A.39: Y-component of Displacement in the Bridge Girder due to Wind and current (1 Year Return Period)

Z-component of Displacement

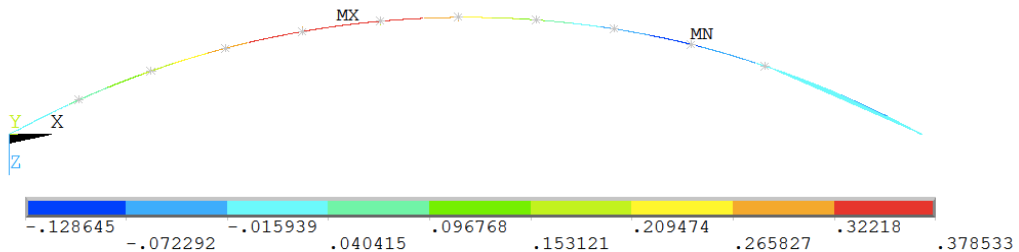


Figure A.40: Z-component of Displacement in the Bridge Girder due to Wind and current (1 Year Return Period)

X-component of Rotation

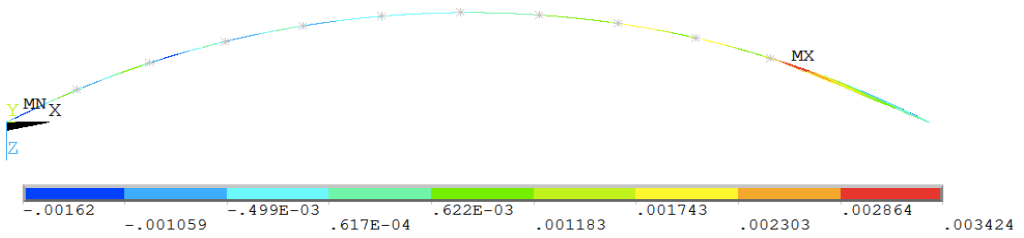


Figure A.41: X-component of Rotation in the Bridge Girder due to Wind and current (1 Year Return Period)

Y-component of Rotation

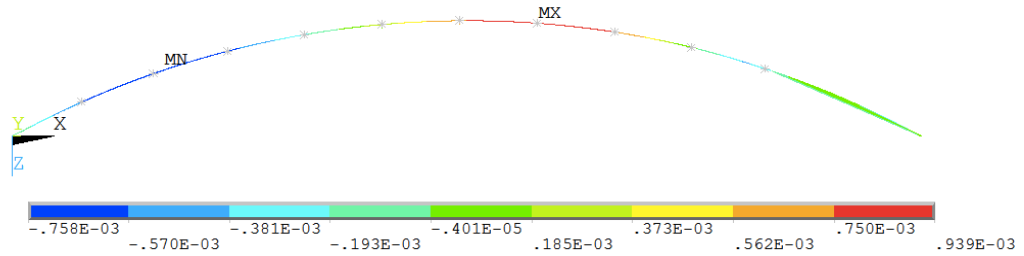


Figure A.42: Y-component of Rotation in the Bridge Girder due to Wind and current (1 Year Return Period)

Z-component of Rotation

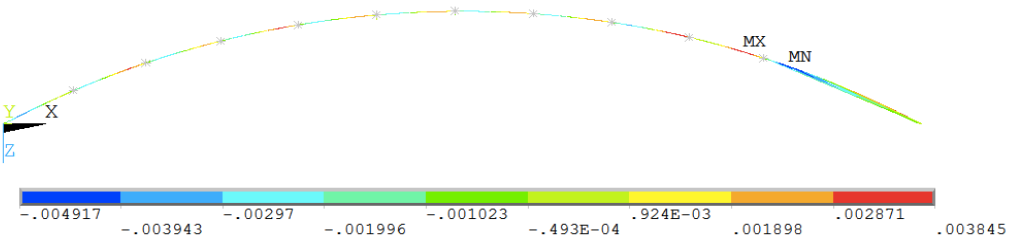


Figure A.43: Z-component of Rotation in the Bridge Girder due to Wind and current (1 Year Return Period)

Global Bending Moment M_X

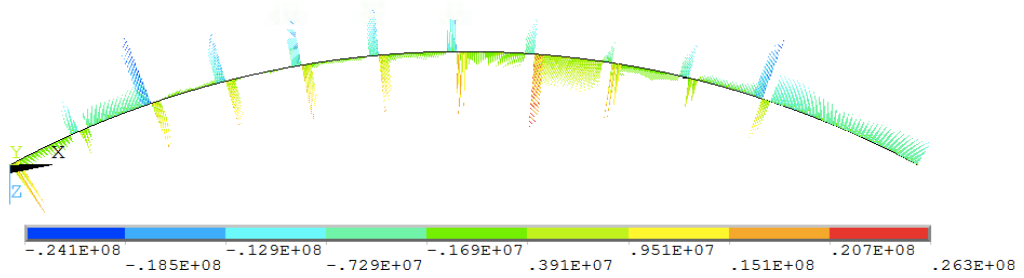


Figure A.44: Global Bending Moment M_X in the Bridge Girder due to Wind and current (1 Year Return Period)

Global Bending Moment M_Y

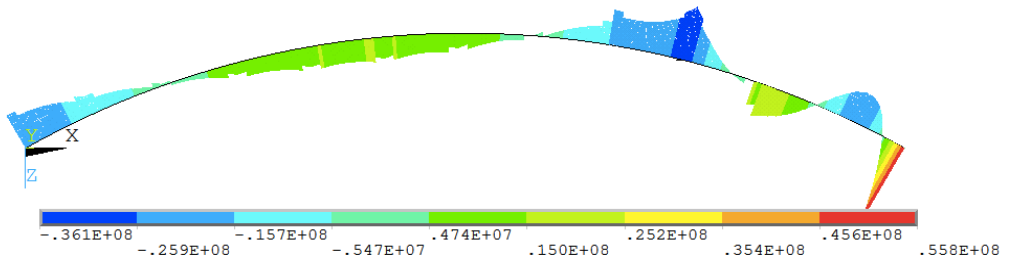


Figure A.45: Global Bending Moment M_Y in the Bridge Girder due to Wind and current (1 Year Return Period)

Global Bending Moment M_Z

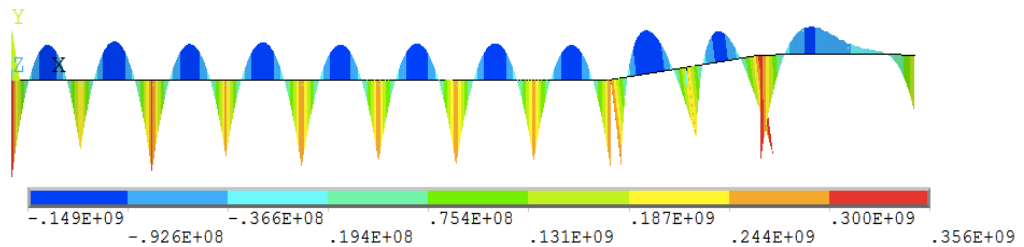


Figure A.46: Global Bending Moment M_Z in the Bridge Girder due to Wind and current (1 Year Return Period)

Global Shear Force V_Y

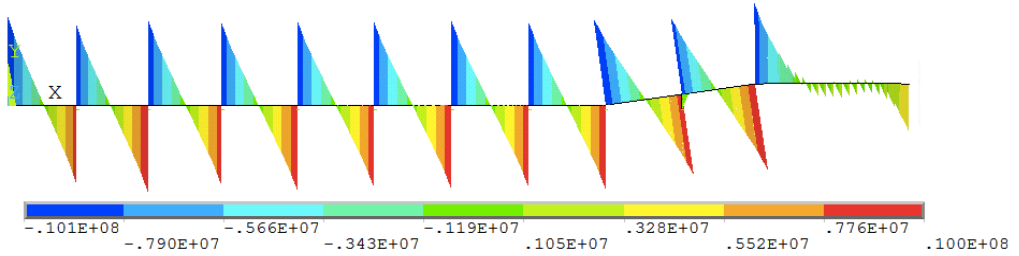


Figure A.47: Global Shear Force V_y in the Bridge Girder due to Wind and current (1 Year Return Period)

Global Shear Force V_Z

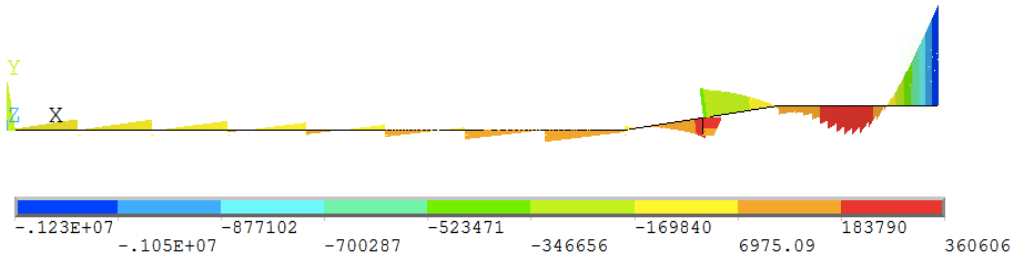


Figure A.48: Global Shear Force V_z in the Bridge Girder due to Wind and current (1 Year Return Period)

A.11 Wind and current (100 Year Return Period)

X-component of Displacement

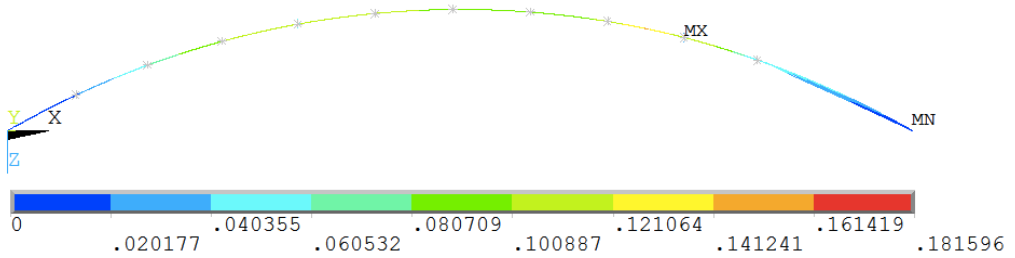


Figure A.49: X-component of Displacement in the Bridge Girder due to Wind and current (100 Year Return Period)

Y-component of Displacement

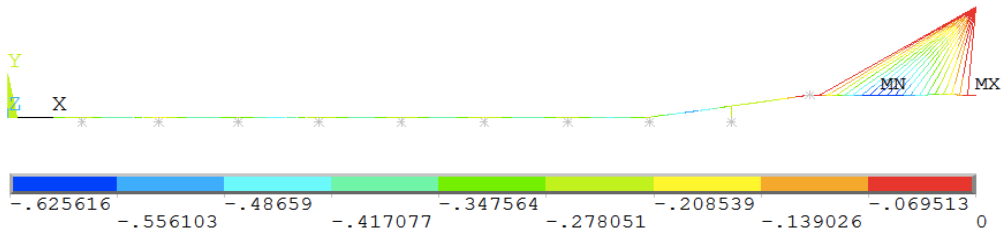


Figure A.50: Y-component of Displacement in the Bridge Girder due to Wind and current (100 Year Return Period)

Z-component of Displacement

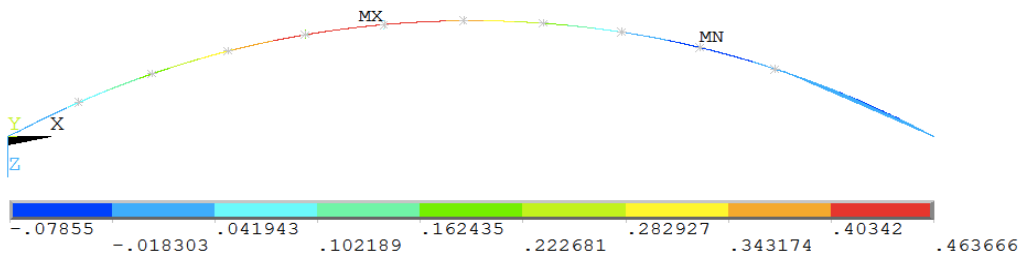


Figure A.51: Z-component of Displacement in the Bridge Girder due to Wind and current (100 Year Return Period)

X-component of Rotation

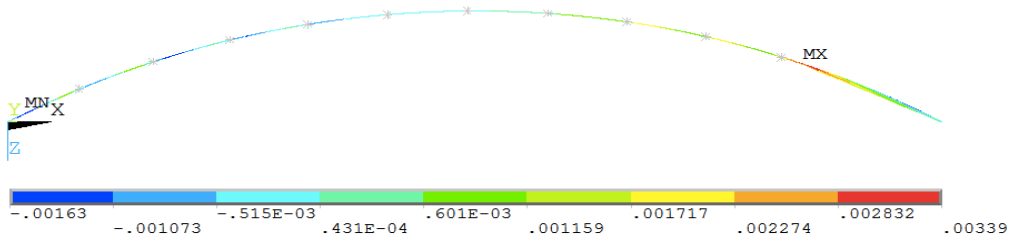


Figure A.52: X-component of Rotation in the Bridge Girder due to Wind and current (100 Year Return Period)

Y-component of Rotation

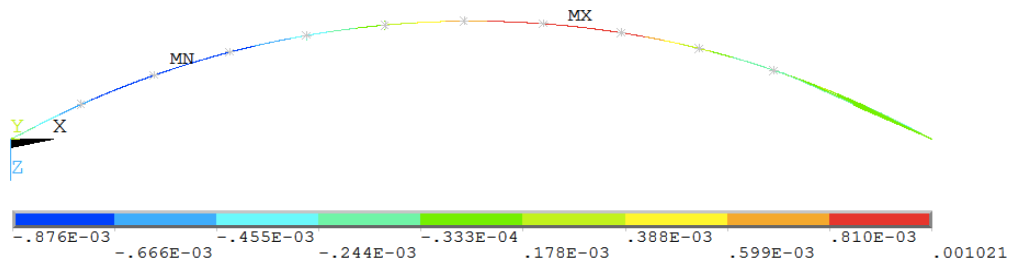


Figure A.53: Y-component of Rotation in the Bridge Girder due to Wind and current (100 Year Return Period)

Z-component of Rotation

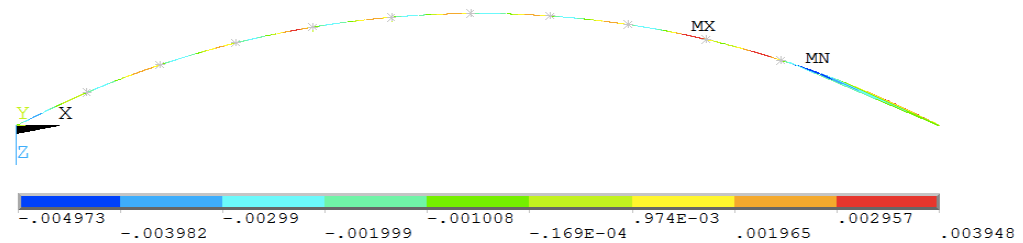


Figure A.54: Z-component of Rotation in the Bridge Girder due to Wind and current (100 Year Return Period)

Global Bending Moment M_X

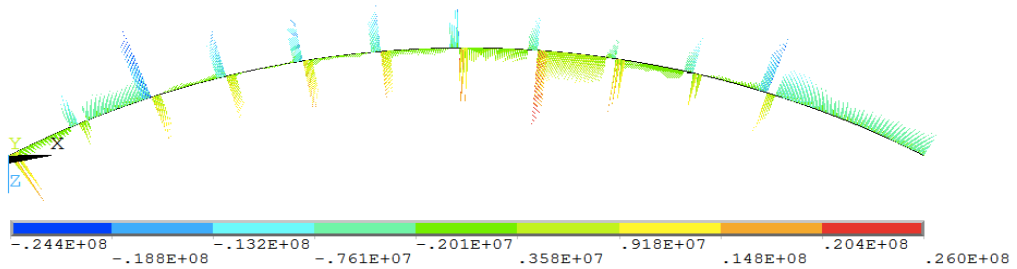


Figure A.55: Global Bending Moment M_X in the Bridge Girder due to Wind and current (100 Year Return Period)

Global Bending Moment M_Y

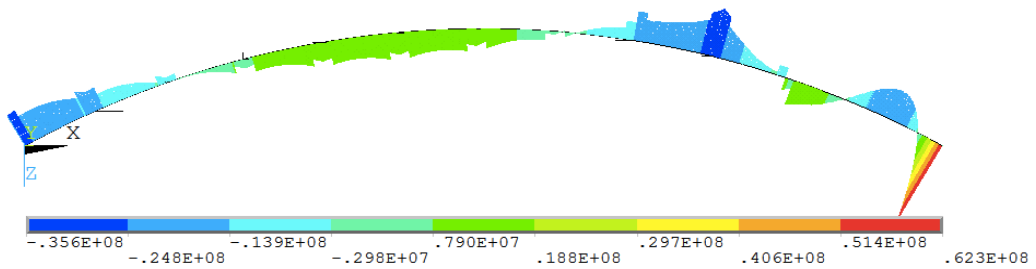


Figure A.56: Global Bending Moment M_Y in the Bridge Girder due to Wind and current (100 Year Return Period)

Global Bending Moment M_Z

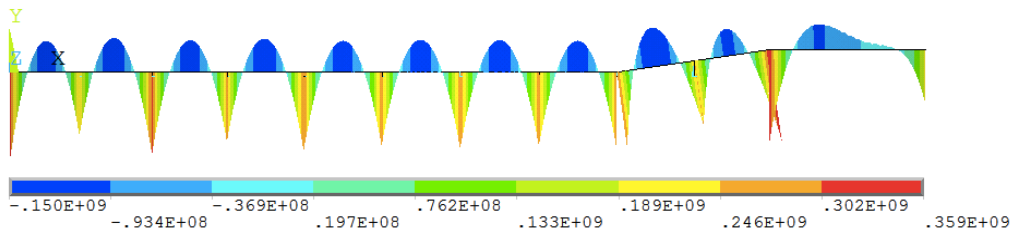


Figure A.57: Global Bending Moment M_Z in the Bridge Girder due to Wind and current (100 Year Return Period)

Global Shear Force V_y

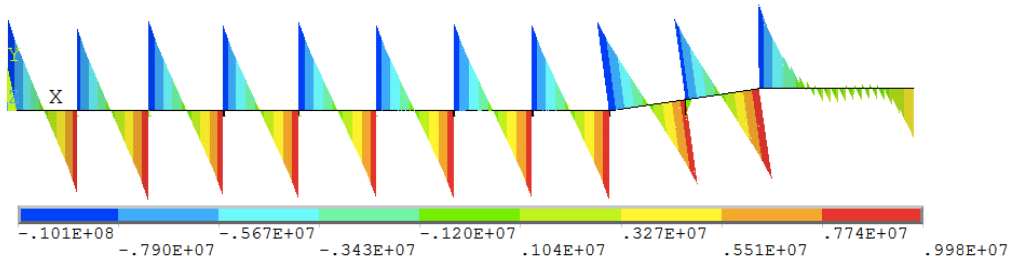


Figure A.58: Global Shear Force V_y in the Bridge Girder due to Wind and current (100 Year Return Period)

Global Shear Force V_z

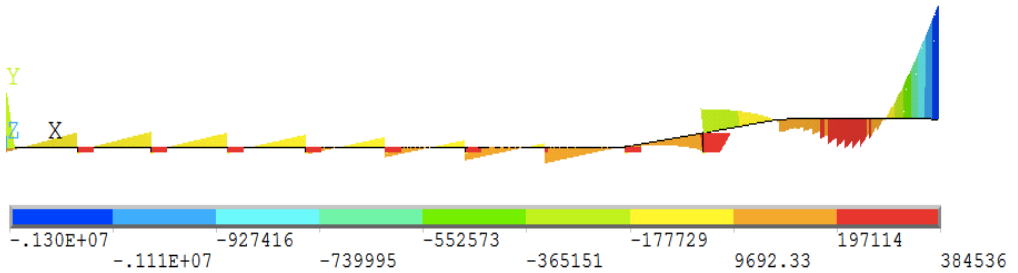


Figure A.59: Global Shear Force V_z in the Bridge Girder due to Wind and current (100 Year Return Period)

Global Von Mises Stress

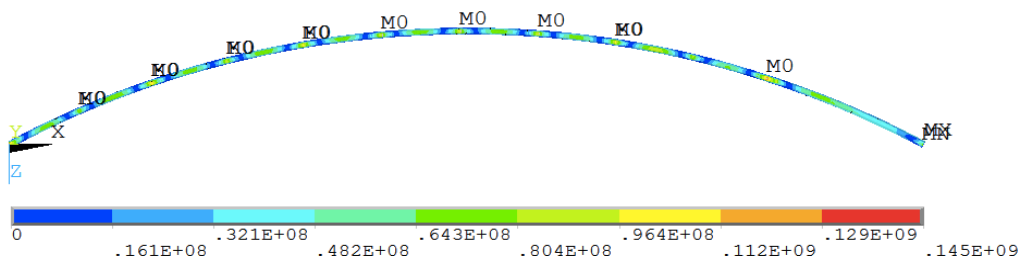


Figure A.60: Global Von Mises Stress in the Bridge Girder due to Wind and current (100 Year Return Period)

A.12 Low Tide

X-component of Displacement

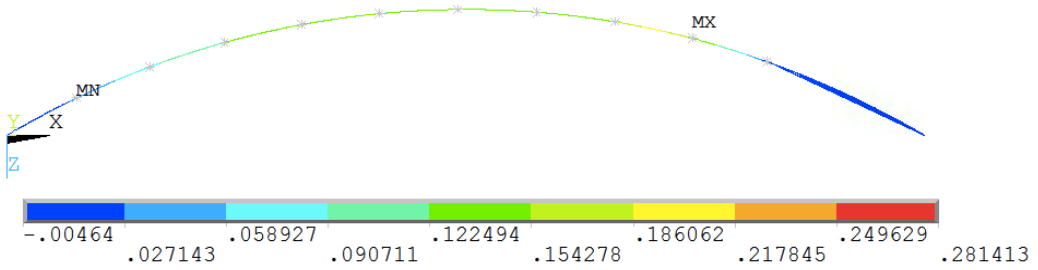


Figure A.61: X-component of Displacement in the Bridge Girder due to Low Tide

Y-component of Displacement

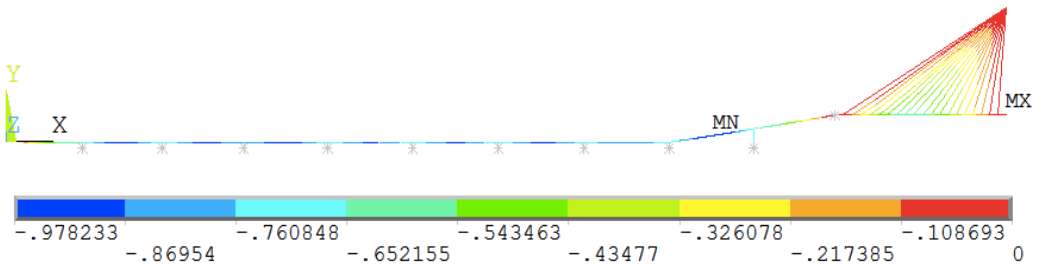


Figure A.62: Y-component of Displacement in the Bridge Girder due to Low Tide

Z-component of Displacement

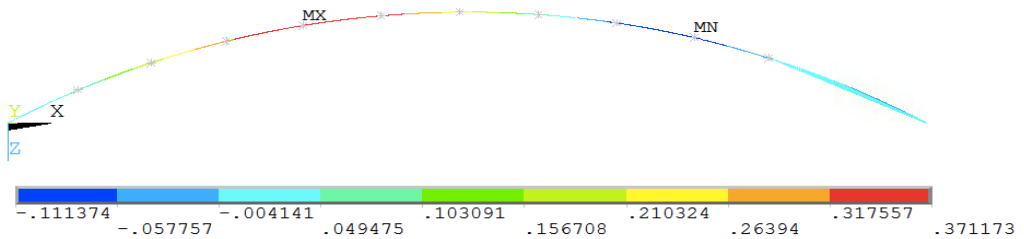


Figure A.63: Z-component of Displacement in the Bridge Girder due to Low Tide

X-component of Rotation

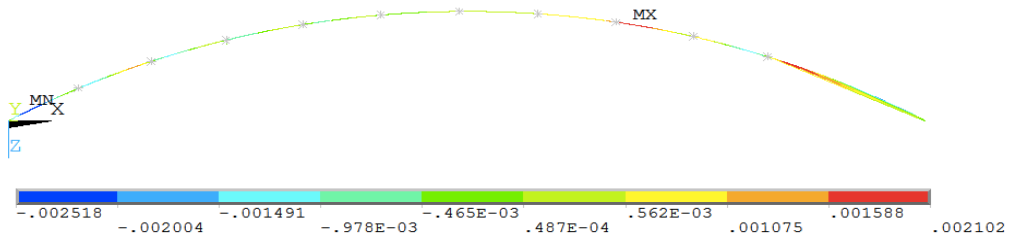


Figure A.64: X-component of Rotation in the Bridge Girder due to Low Tide

Y-component of Rotation

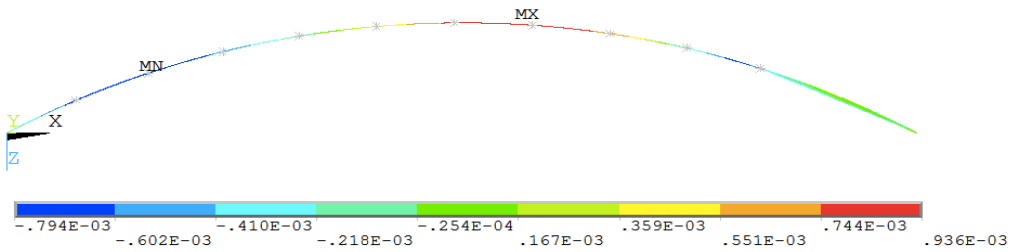


Figure A.65: Y-component of Rotation in the Bridge Girder due to Low Tide

Z-component of Rotation

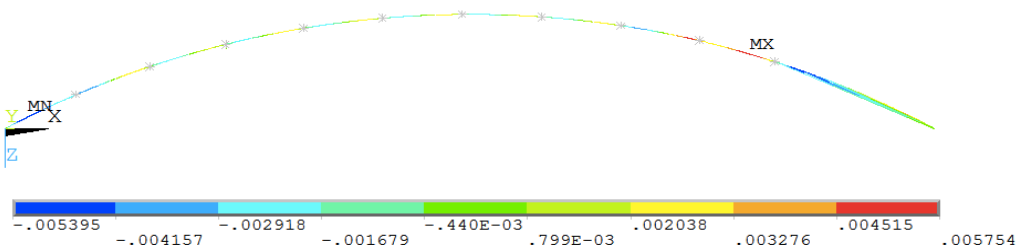


Figure A.66: Z-component of Rotation in the Bridge Girder due to Low Tide

Global Bending Moment M_X

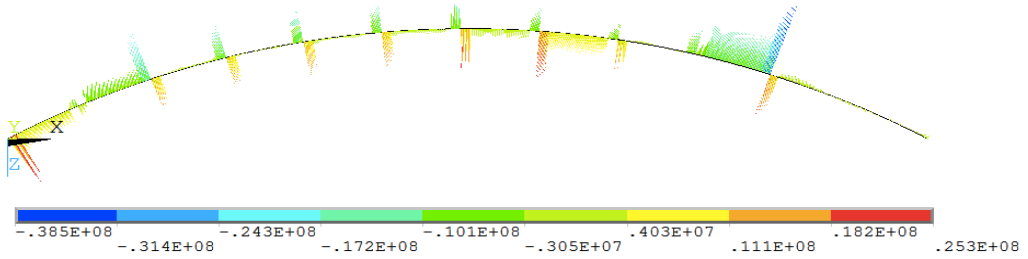


Figure A.67: Global Bending Moment M_X in the Bridge Girder due to Low Tide

Global Bending Moment M_Y

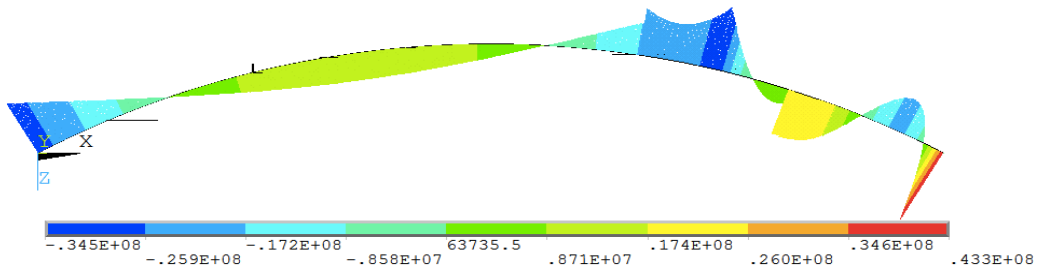


Figure A.68: Global Bending Moment M_Y in the Bridge Girder due to Low Tide

Global Bending Moment M_Z

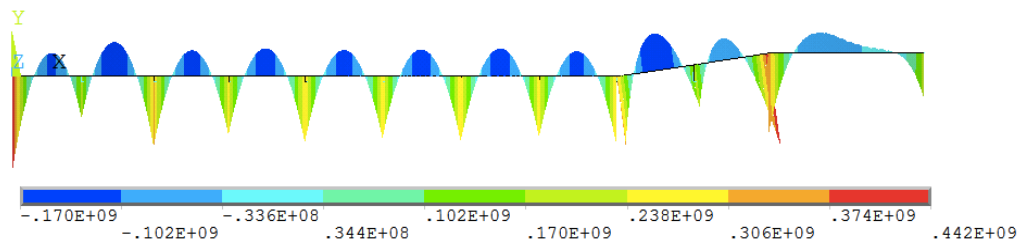


Figure A.69: Global Bending Moment M_Z in the Bridge Girder due to Low Tide

Global Shear Force V_Y

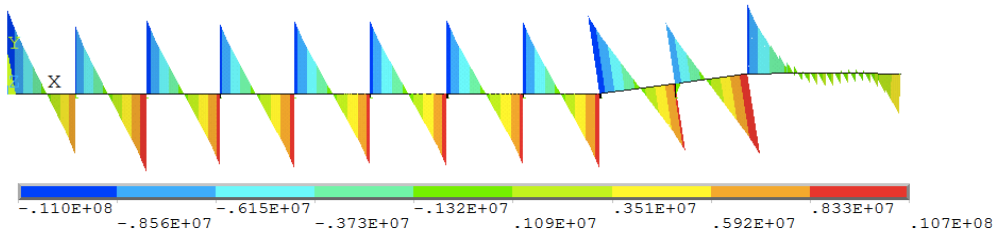


Figure A.70: Global Shear Force V_y in the Bridge Girder due to Low Tide

Global Shear Force V_Z

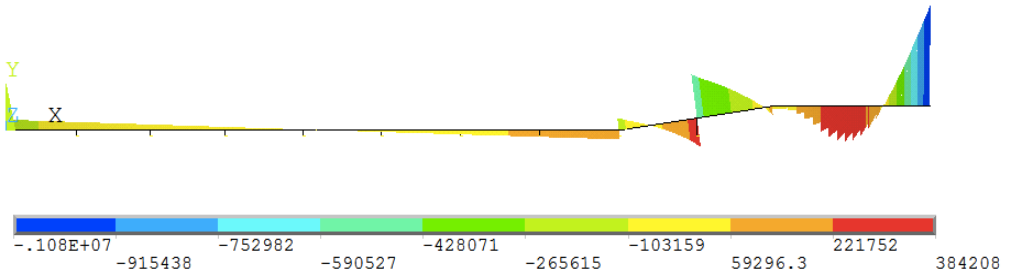


Figure A.71: Global Shear Force V_z in the Bridge Girder due to Low Tide

Global Von Mises Stress

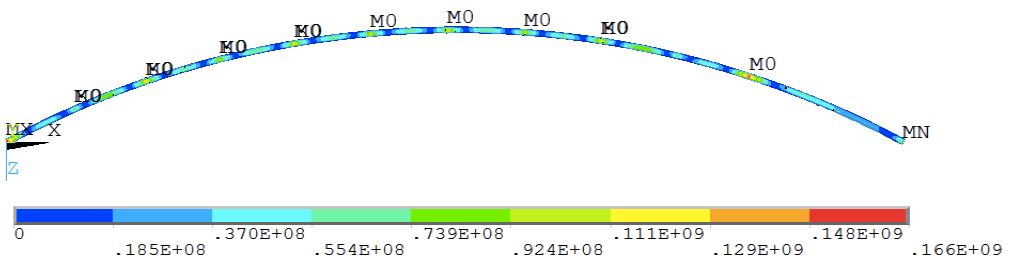


Figure A.72: Global Von Mises Stress in the Bridge Girder due to Low Tide

A.13 High Tide

X-component of Displacement

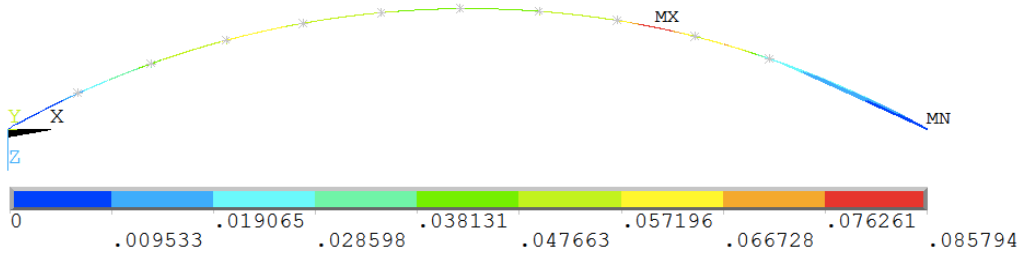


Figure A.73: X-component of Displacement in the Bridge Girder due to High Tide

Y-component of Displacement

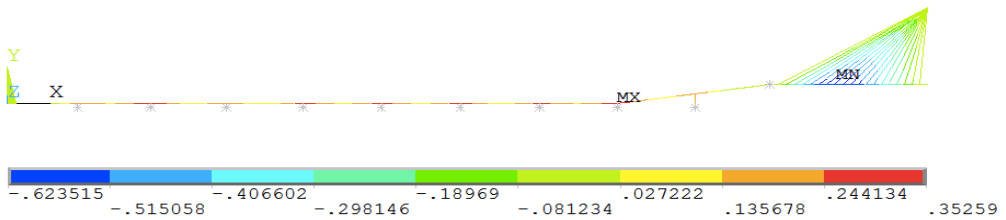


Figure A.74: Y-component of Displacement in the Bridge Girder due to High Tide

Z-component of Displacement

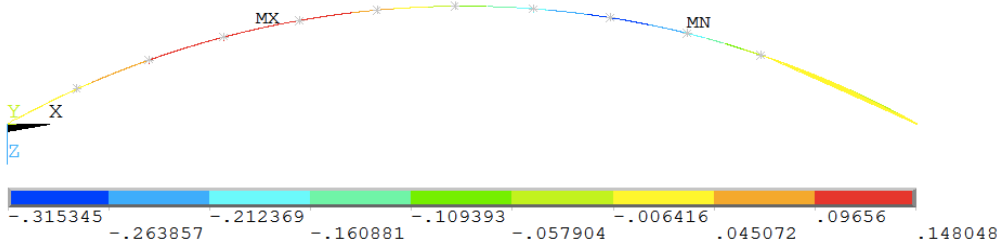


Figure A.75: Z-component of Displacement in the Bridge Girder due to High Tide

X-component of Rotation

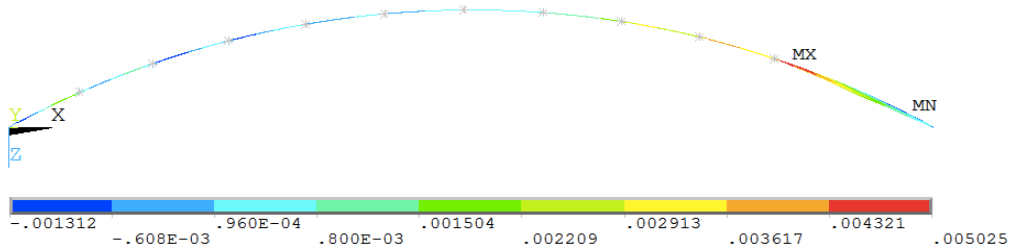


Figure A.76: X-component of Rotation in the Bridge Girder due to High Tide

Y-component of Rotation

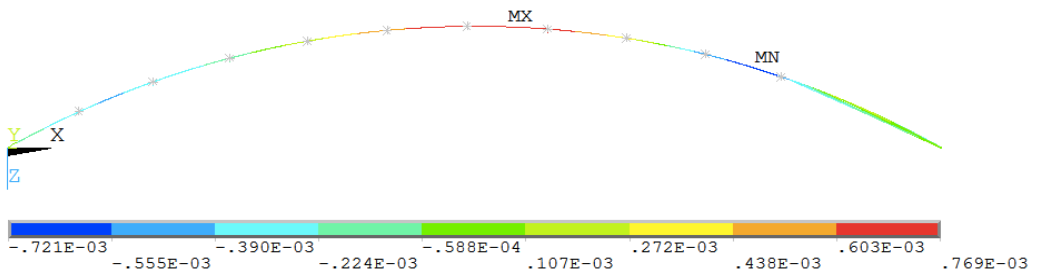


Figure A.77: Y-component of Rotation in the Bridge Girder due to High Tide

Z-component of Rotation

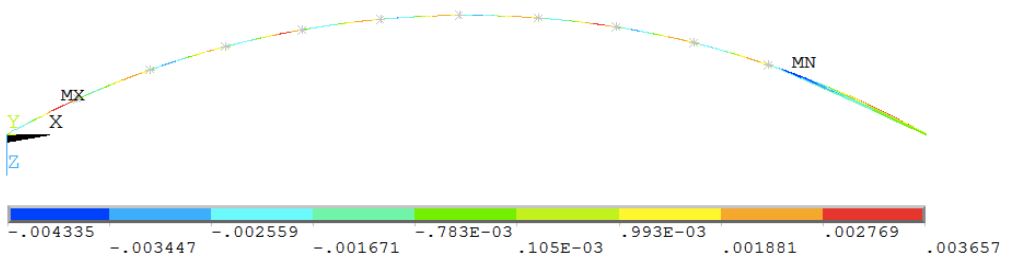


Figure A.78: Z-component of Rotation in the Bridge Girder due to High Tide

Global Bending Moment M_X

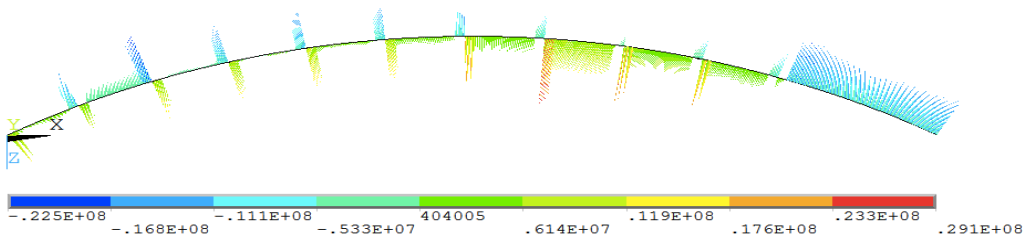


Figure A.79: Global Bending Moment M_X in the Bridge Girder due to High Tide

Global Bending Moment M_Y

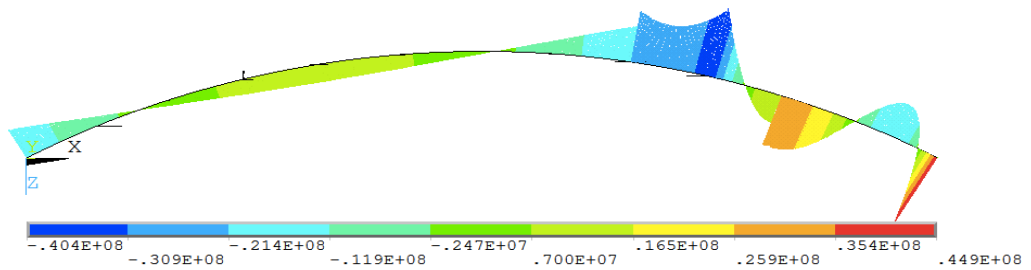


Figure A.80: Global Bending Moment M_Y in the Bridge Girder due to High Tide

Global Bending Moment M_Z

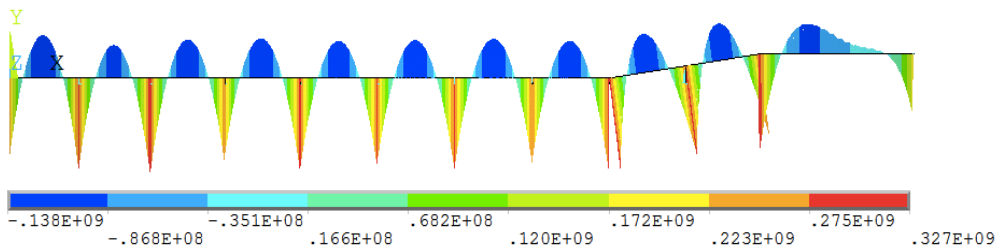


Figure A.81: Global Bending Moment M_Z in the Bridge Girder due to High Tide

Global Shear Force V_Y

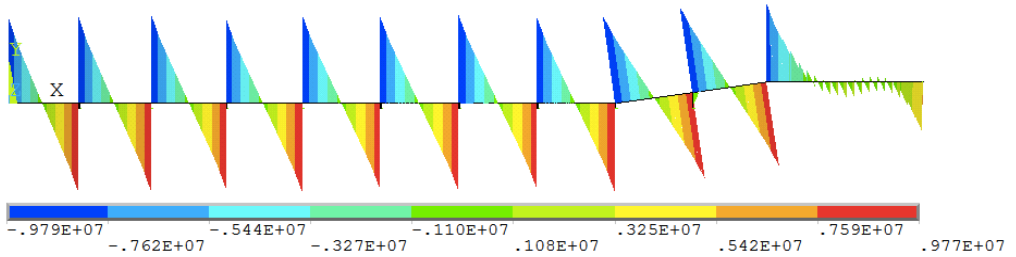


Figure A.82: Global Shear Force V_y in the Bridge Girder due to High Tide

Global Shear Force V_Z

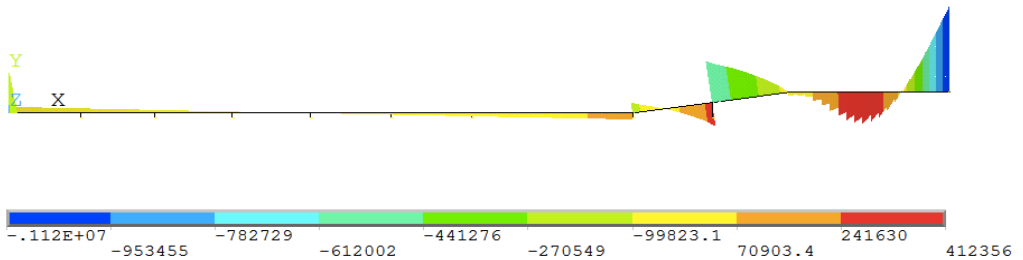


Figure A.83: Global Shear Force V_z in the Bridge Girder due to High Tide

Global Von Mises Stress

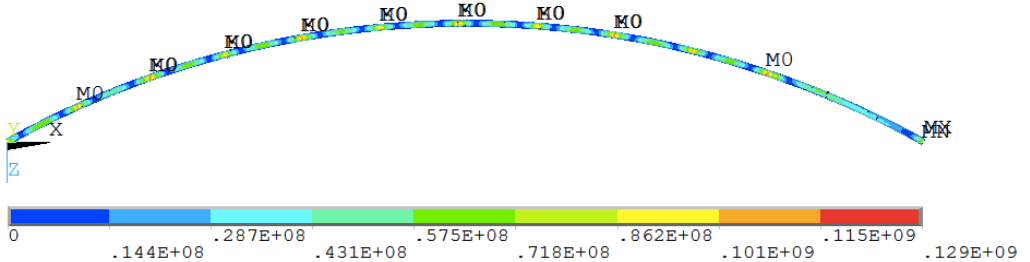


Figure A.84: Global Von Mises Stress in the Bridge Girder due to High Tide

A.14 Static Results for the Highbridge Models - Additional Plots

A.15 II-Jacket

A.16 Selfweight

X-component of Displacement

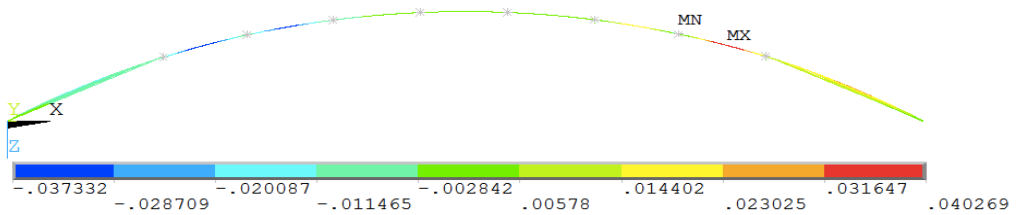


Figure A.85: X-component of Displacement in the Bridge Girder due to Selfweight

Y-component of Displacement

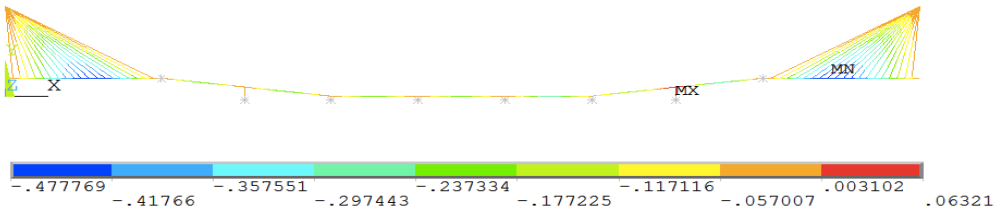


Figure A.86: Y-component of Displacement in the Bridge Girder due to Selfweight

Z-component of Displacement

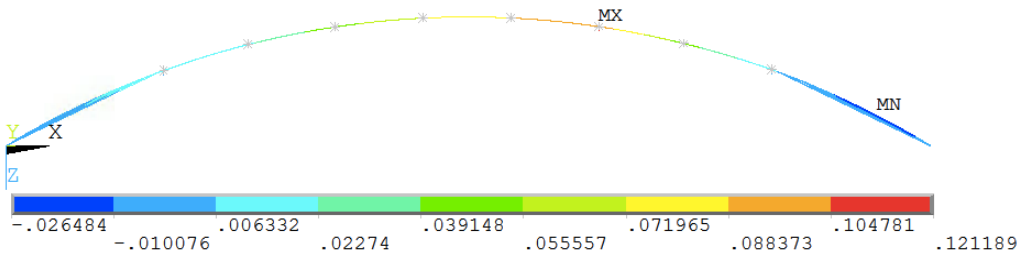


Figure A.87: Z-component of Displacement in the Bridge Girder due to Selfweight

X-component of Rotation

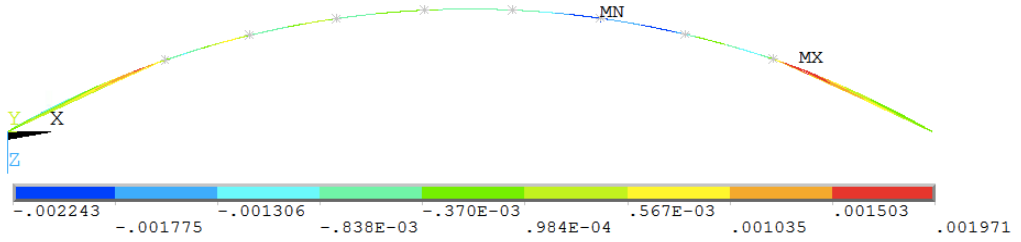


Figure A.88: X-component of Rotation in the Bridge Girder due to Selfweight

Y-component of Rotation

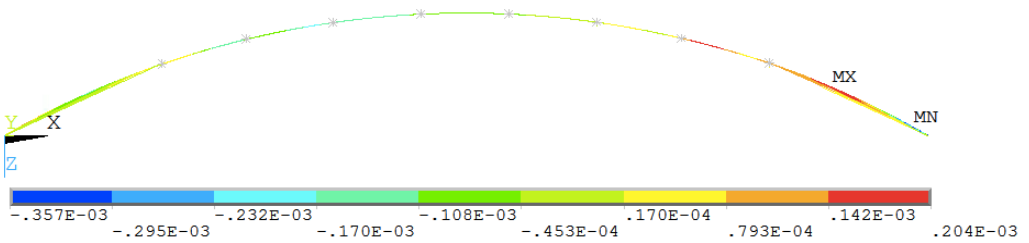


Figure A.89: Y-component of Rotation in the Bridge Girder due to Selfweight

Z-component of Rotation

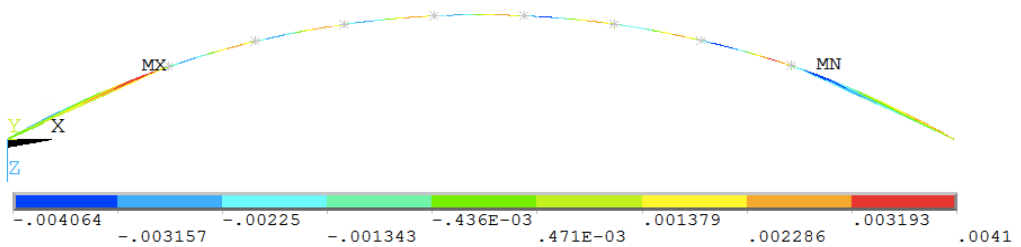


Figure A.90: Z-component of Rotation in the Bridge Girder due to Selfweight

Global Bending Moment M_X

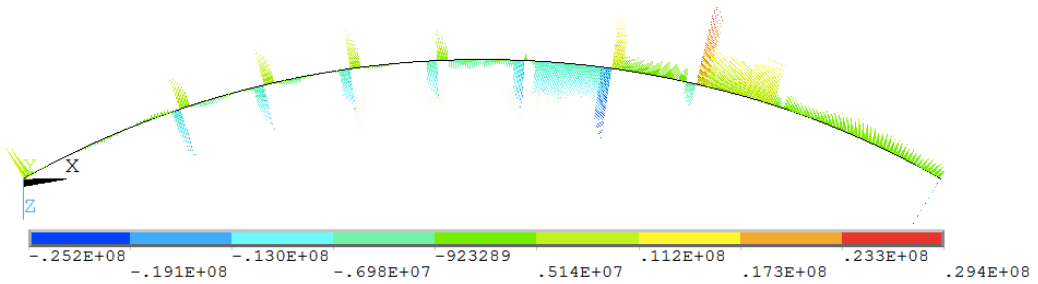


Figure A.91: Global Bending Moment M_X in the Bridge Girder due to Selfweight

Global Bending Moment M_Y

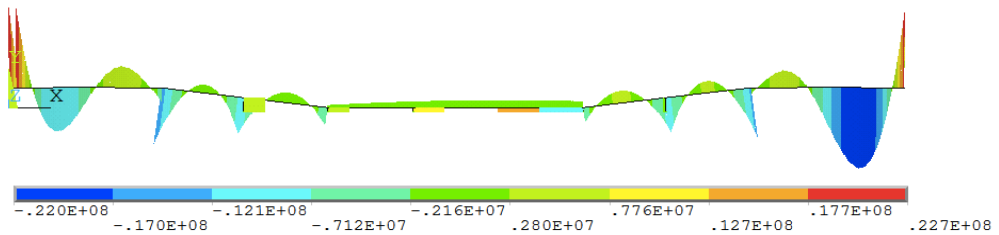


Figure A.92: Global Bending Moment M_Y in the Bridge Girder due to Selfweight

Global Bending Moment M_Z

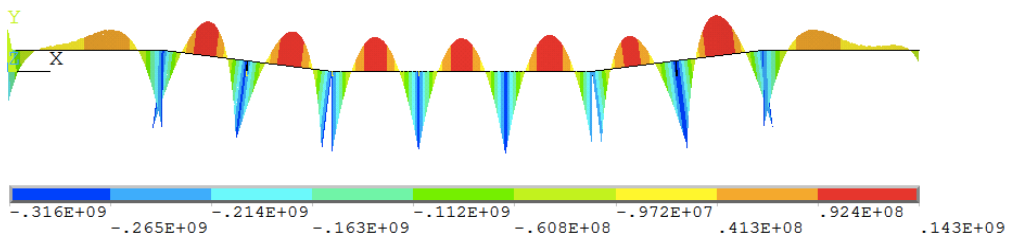


Figure A.93: Global Bending Moment M_Z in the Bridge Girder due to Selfweight

Global Shear Force V_Y

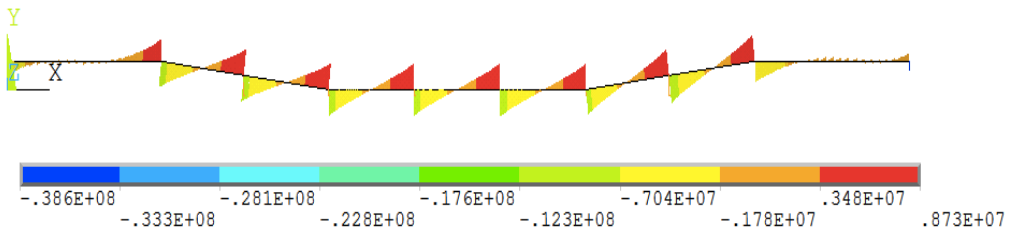


Figure A.94: Global Shear Force V_y in the Bridge Girder due to Selfweight

Global Shear Force V_Z

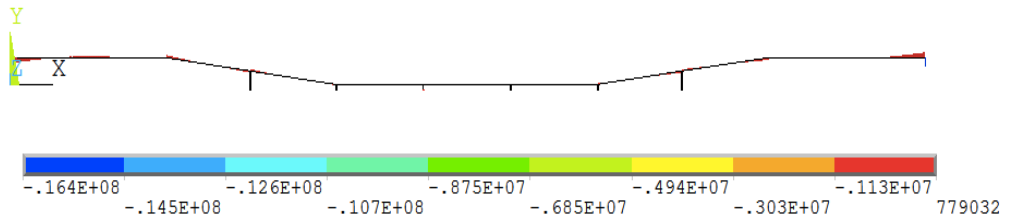


Figure A.95: Global Shear Force V_z in the Bridge Girder due to Selfweight

Global Von Mises Stress

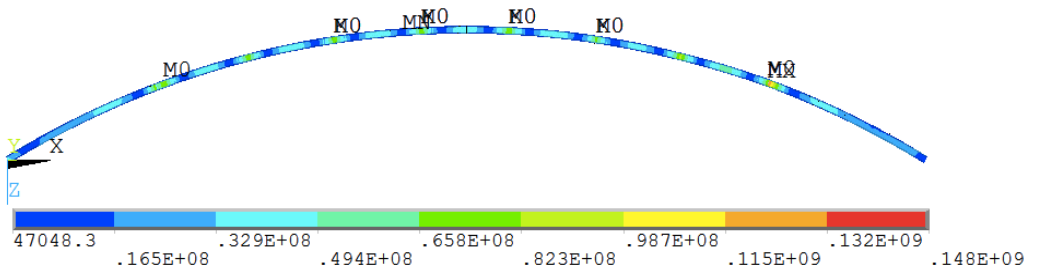


Figure A.96: Global Von Mises Stress in the Bridge Girder due to Selfweight

A.17 Traffic Load

X-component of Displacement

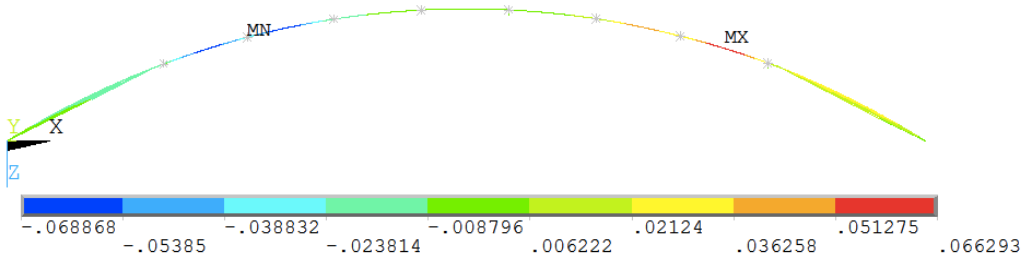


Figure A.97: X-component of Displacement in the Bridge Girder due to Traffic Load

Y-component of Displacement

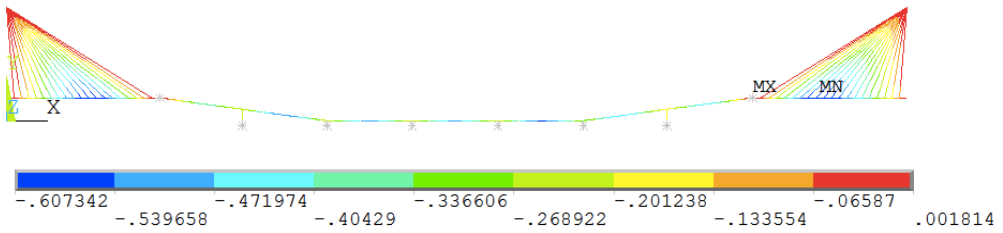


Figure A.98: Y-component of Displacement in the Bridge Girder due to Traffic Load

Z-component of Displacement

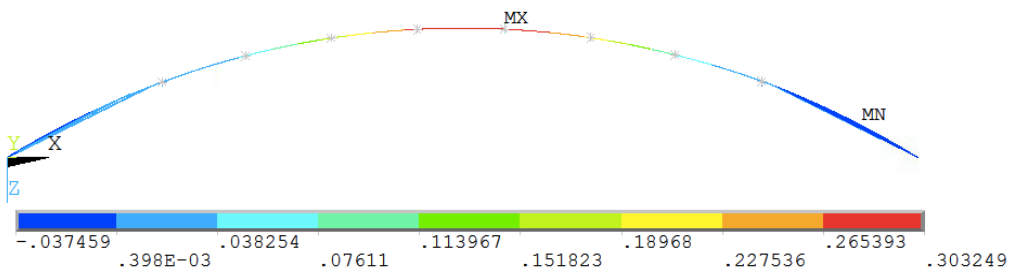


Figure A.99: Z-component of Displacement in the Bridge Girder due to Traffic Load

X-component of Rotation

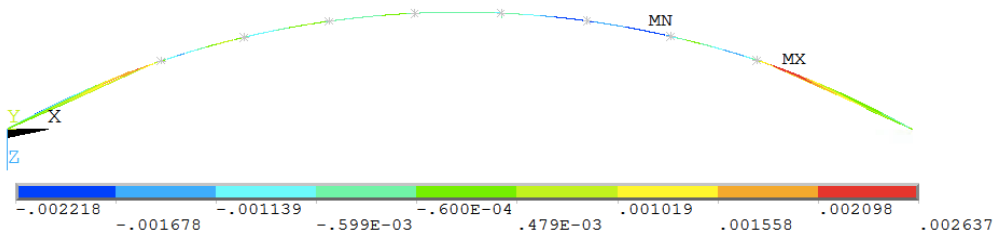


Figure A.100: X-component of Rotation in the Bridge Girder due to Traffic Load

Y-component of Rotation

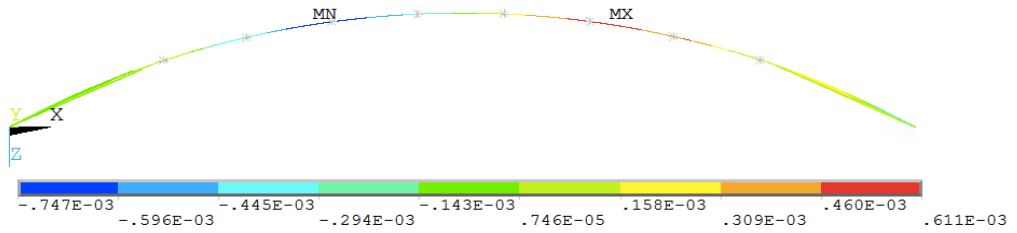


Figure A.101: Y-component of Rotation in the Bridge Girder due to Traffic Load

Z-component of Rotation

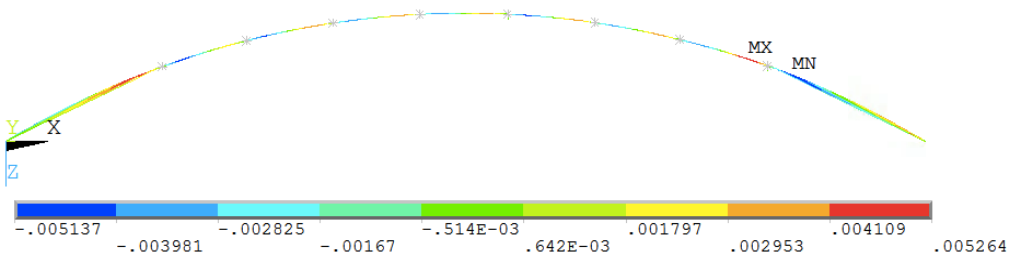


Figure A.102: Z-component of Rotation in the Bridge Girder due to Traffic Load

Global Bending Moment M_X

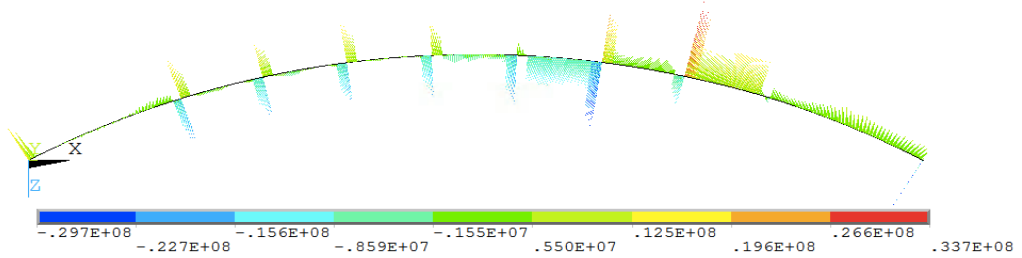


Figure A.103: Global Bending Moment M_X in the Bridge Girder due to Traffic Load

Global Bending Moment M_Y

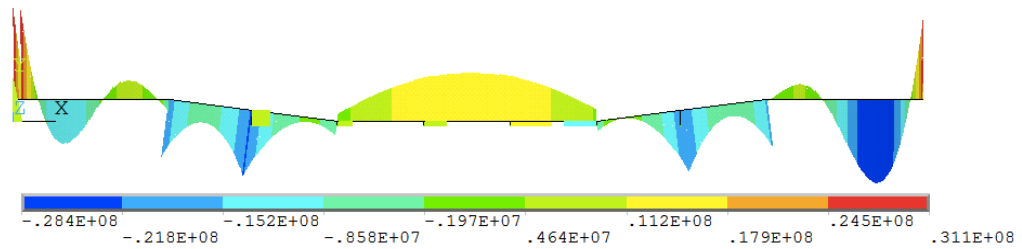


Figure A.104: Global Bending Moment M_Y in the Bridge Girder due to Traffic Load

Global Bending Moment M_Z

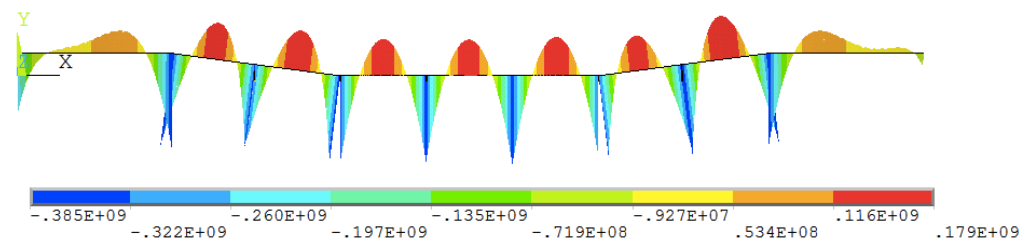


Figure A.105: Global Bending Moment M_Z in the Bridge Girder due to Traffic Load

Global Shear Force V_Y

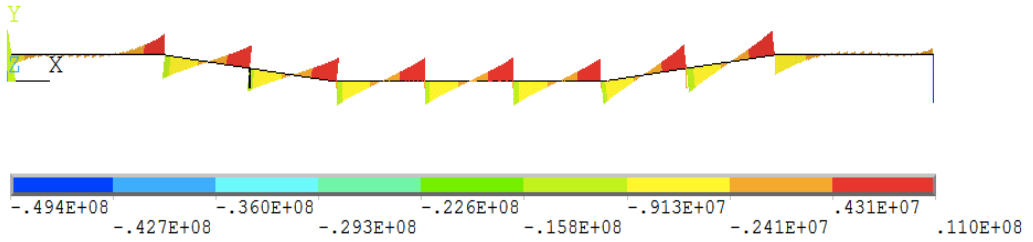


Figure A.106: Global Shear Force V_y in the Bridge Girder due to Traffic Load

Global Shear Force V_Z

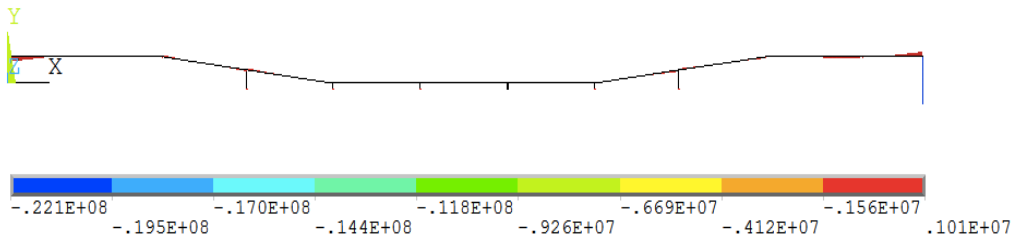


Figure A.107: Global Shear Force V_z in the Bridge Girder due to Traffic Load

Global Von Mises Stress

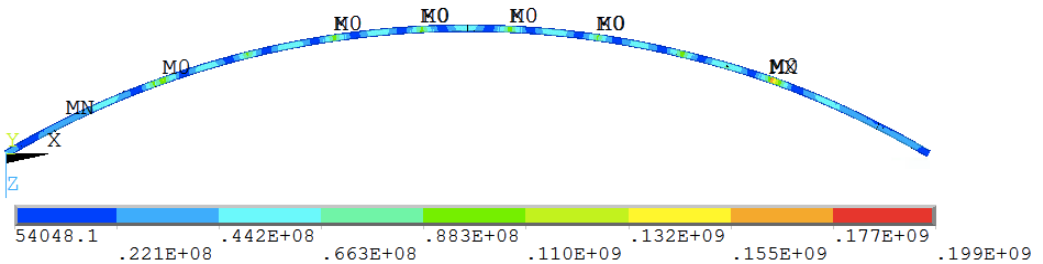


Figure A.108: Global Von Mises Stress in the Bridge Girder due to Traffic Load

A.18 Wind (1 Year Return Period)

X-component of Displacement

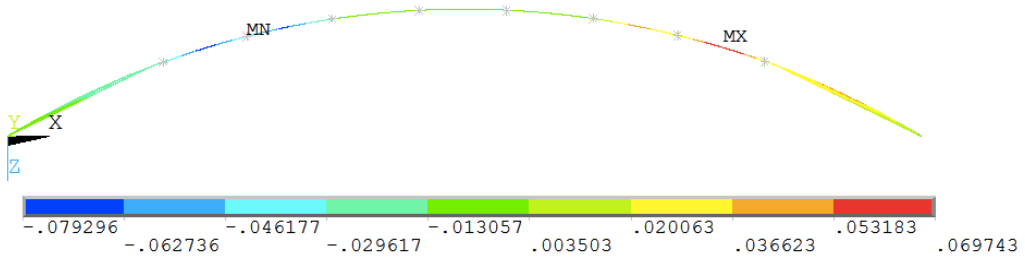


Figure A.109: X-component of Displacement in the Bridge Girder due to Wind (1 Year Return Period)

Y-component of Displacement

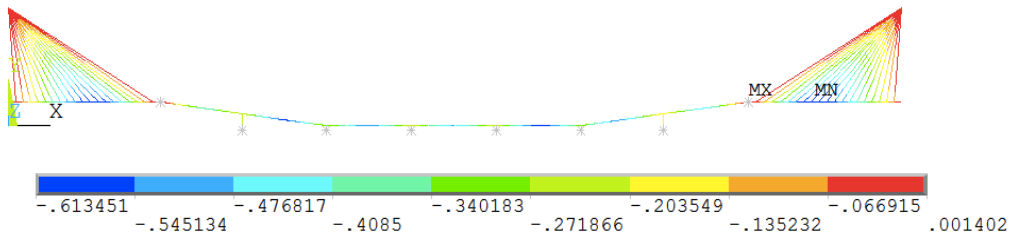


Figure A.110: Y-component of Displacement in the Bridge Girder due to Wind (1 Year Return Period)

Z-component of Displacement

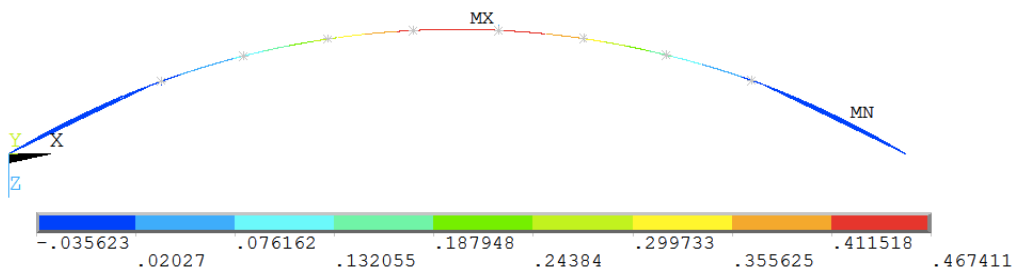


Figure A.111: Z-component of Displacement in the Bridge Girder due to Wind (1 Year Return Period)

X-component of Rotation

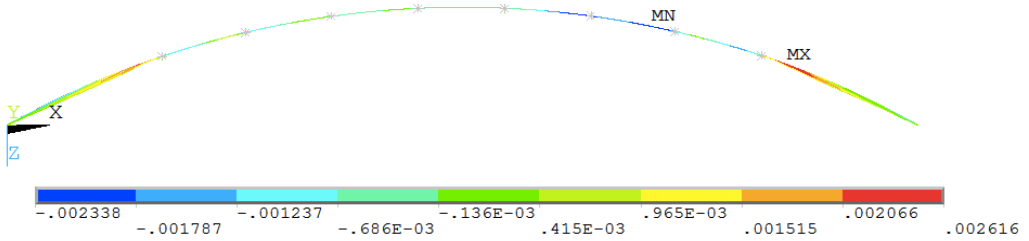


Figure A.112: X-component of Rotation in the Bridge Girder due to Wind (1 Year Return Period)

Y-component of Rotation

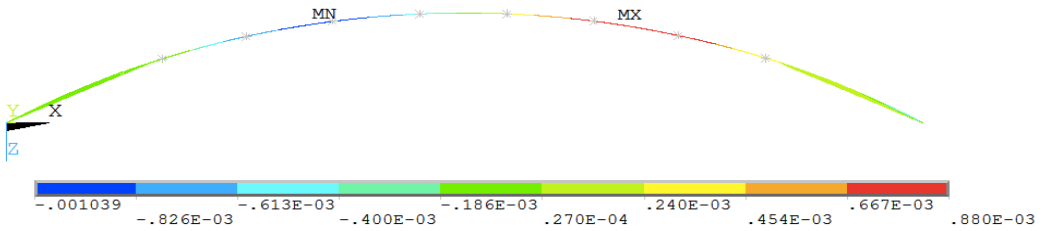


Figure A.113: Y-component of Rotation in the Bridge Girder due to Wind (1 Year Return Period)

Z-component of Rotation

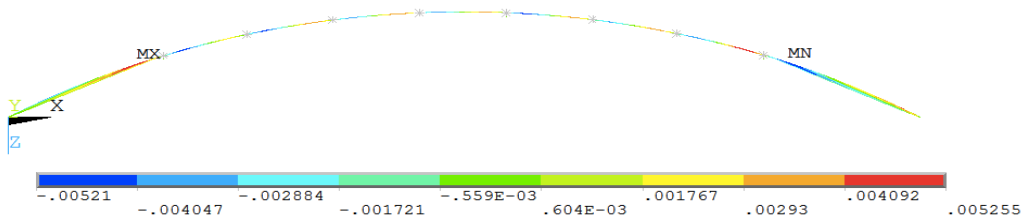


Figure A.114: Z-component of Rotation in the Bridge Girder due to Wind (1 Year Return Period)

Global Bending Moment M_X

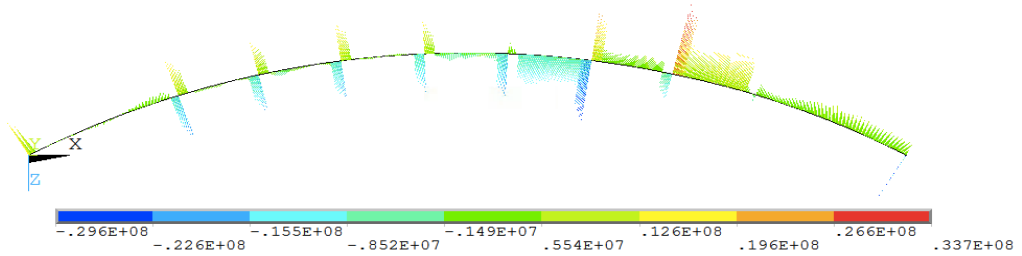


Figure A.115: Global Bending Moment M_X in the Bridge Girder due to Wind (1 Year Return Period)

Global Bending Moment M_Y

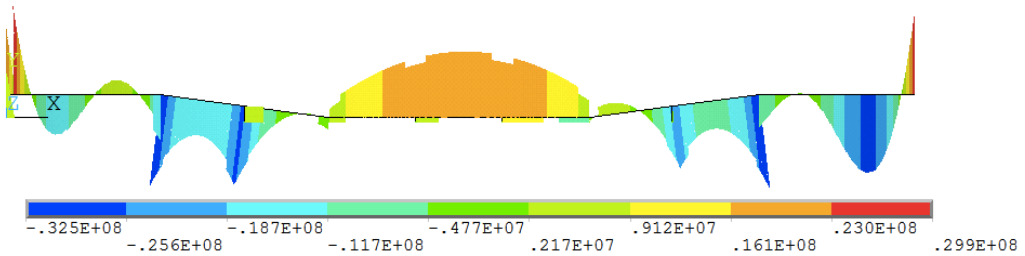


Figure A.116: Global Bending Moment M_Y in the Bridge Girder due to Wind (1 Year Return Period)

Global Bending Moment M_Z

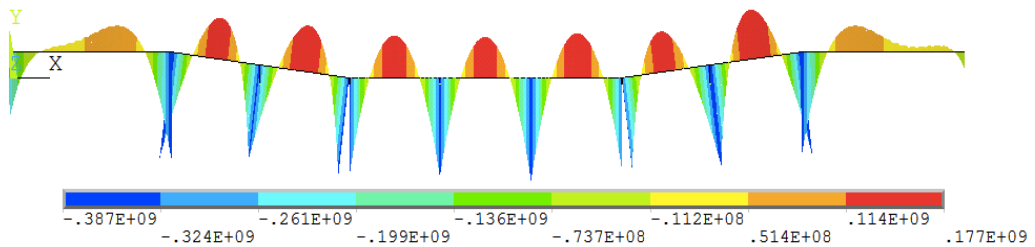


Figure A.117: Global Bending Moment M_Z in the Bridge Girder due to Wind (1 Year Return Period)

Global Shear Force V_Y

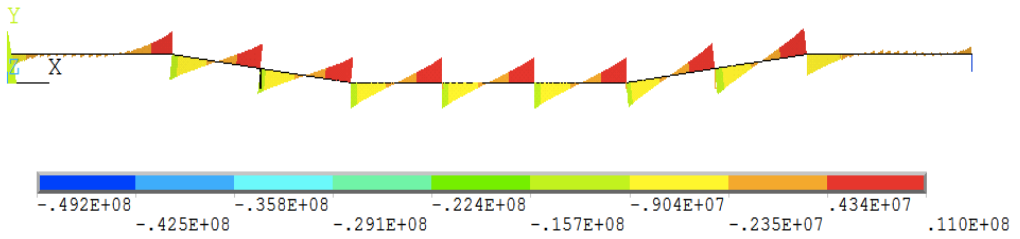


Figure A.118: Global Shear Force V_y in the Bridge Girder due to Wind (1 Year Return Period)

Global Shear Force V_Z

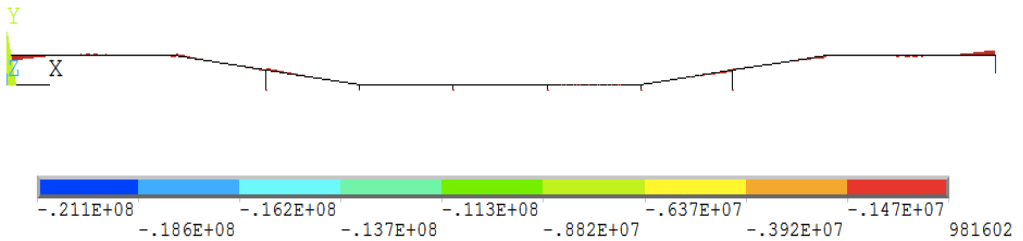


Figure A.119: Global Shear Force V_z in the Bridge Girder due to Wind (1 Year Return Period)

Global Von Mises Stress

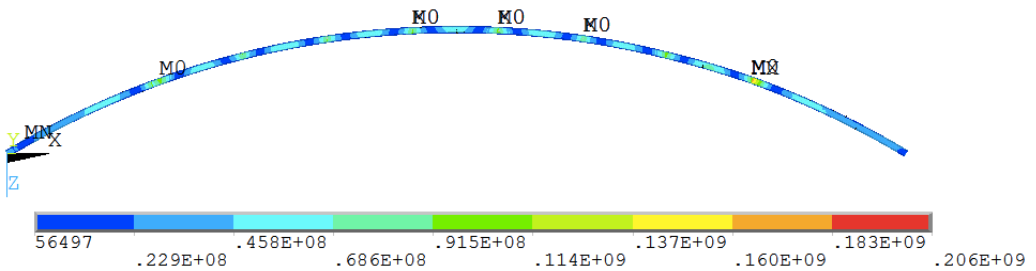


Figure A.120: Global Von Mises Stress in the Bridge Girder due to Wind (1 Year Return Period)

A.19 Wind and current (1 Year Return Period)

X-component of Displacement

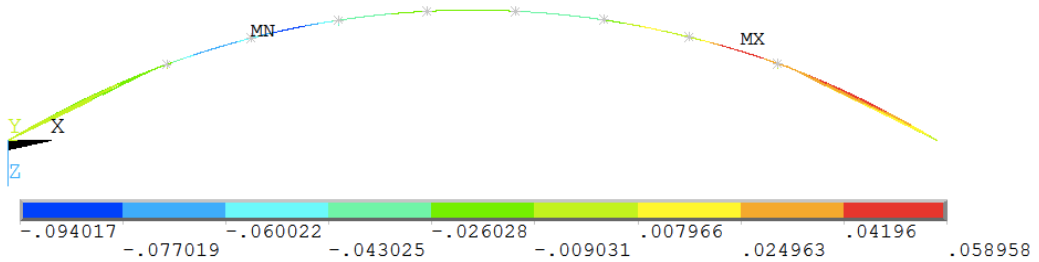


Figure A.121: X-component of Displacement in the Bridge Girder due to Wind and current (1 Year Return Period)

Y-component of Displacement

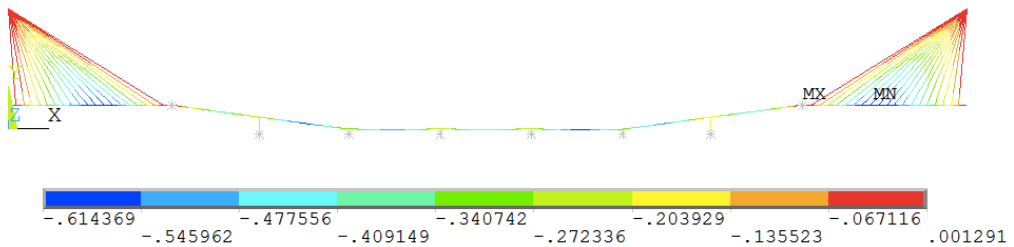


Figure A.122: Y-component of Displacement in the Bridge Girder due to Wind and current (1 Year Return Period)

Z-component of Displacement

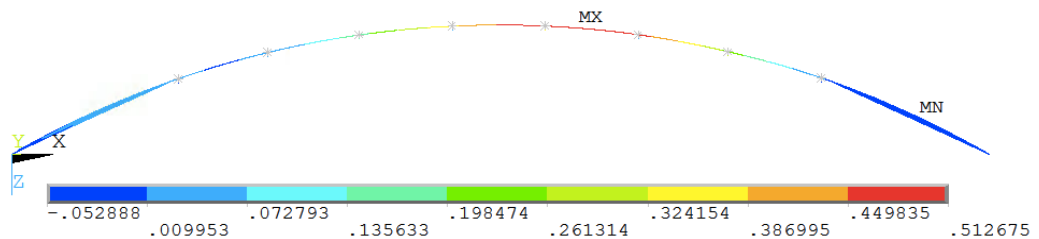


Figure A.123: Z-component of Displacement in the Bridge Girder due to Wind and current (1 Year Return Period)

X-component of Rotation

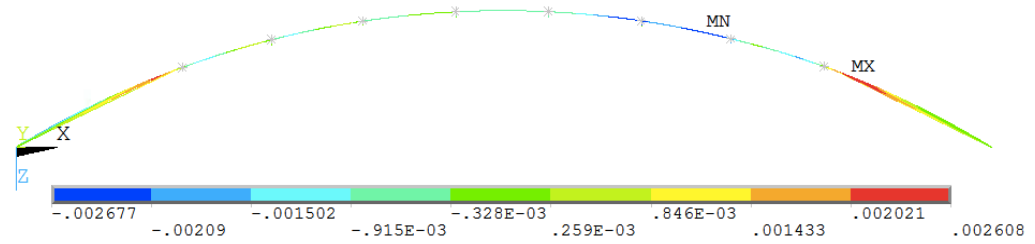


Figure A.124: X-component of Rotation in the Bridge Girder due to Wind and current (1 Year Return Period)

Y-component of Rotation

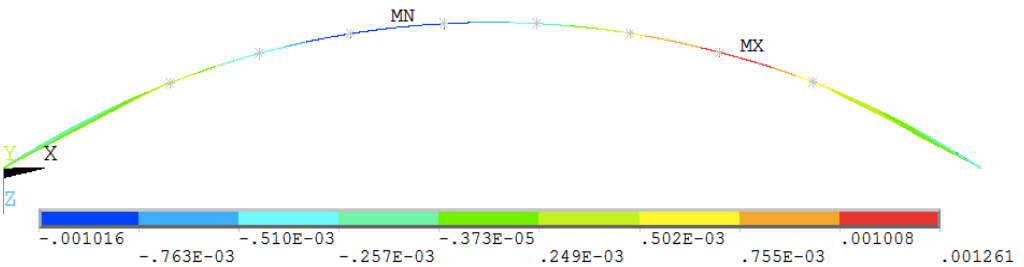


Figure A.125: Y-component of Rotation in the Bridge Girder due to Wind and current (1 Year Return Period)

Z-component of Rotation

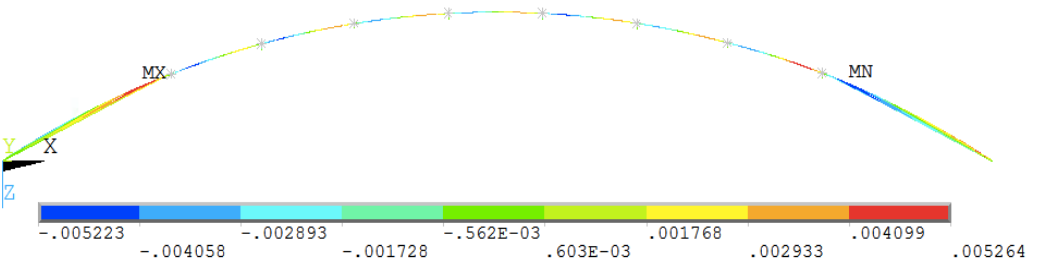


Figure A.126: Z-component of Rotation in the Bridge Girder due to Wind and current (1 Year Return Period)

Global Bending Moment M_X

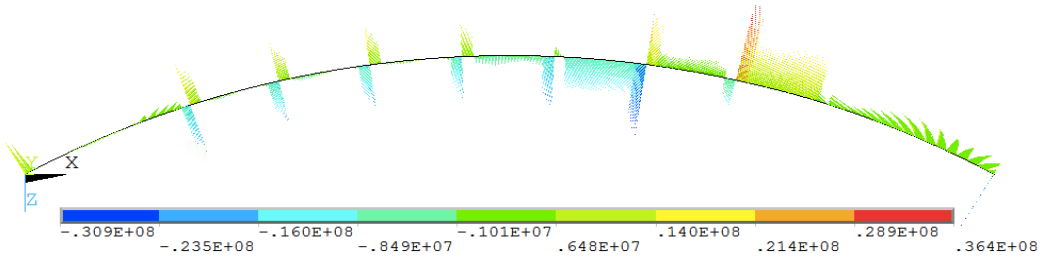


Figure A.127: Global Bending Moment M_X in the Bridge Girder due to Wind and current (1 Year Return Period)

Global Bending Moment M_Y

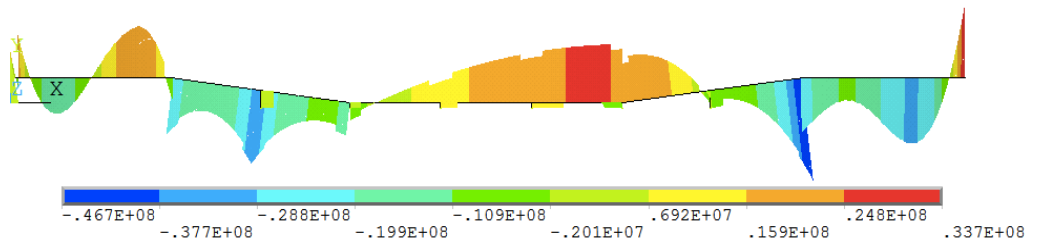


Figure A.128: Global Bending Moment M_Y in the Bridge Girder due to Wind and current (1 Year Return Period)

Global Bending Moment M_Z

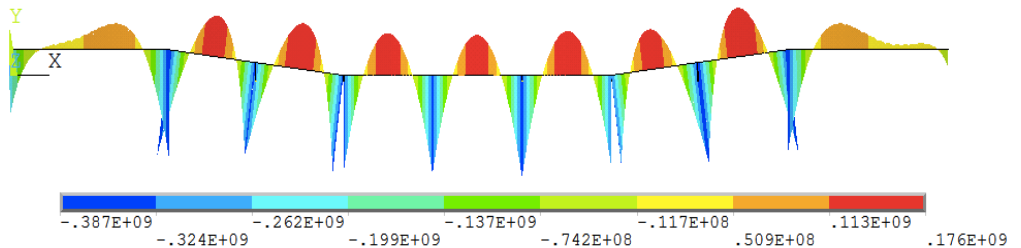


Figure A.129: Global Bending Moment M_Z in the Bridge Girder due to Wind and current (1 Year Return Period)

Global Shear Force V_Y

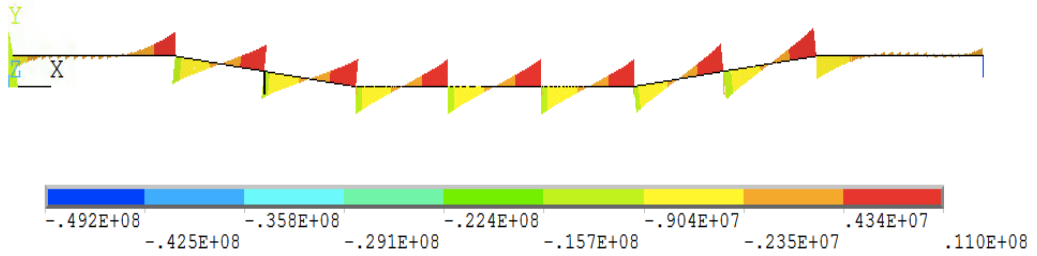


Figure A.130: Global Shear Force V_y in the Bridge Girder due to Wind and current (1 Year Return Period)

Global Shear Force V_Z

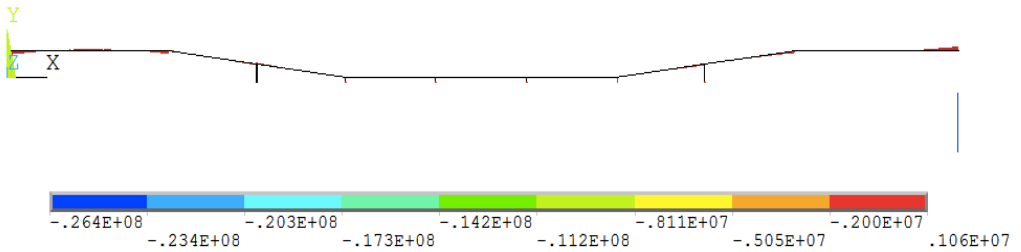


Figure A.131: Global Shear Force V_z in the Bridge Girder due to Wind and current (1 Year Return Period)

Global Von Mises Stress

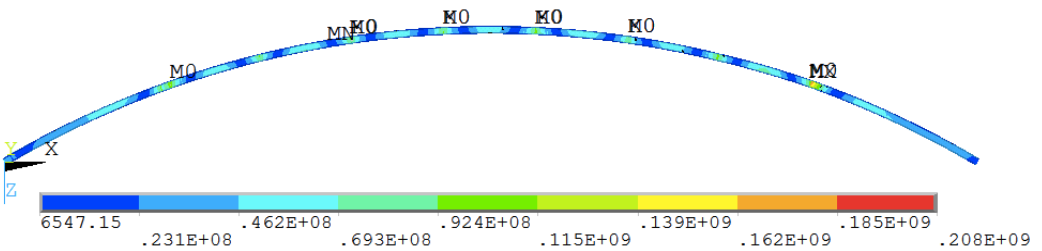


Figure A.132: Global Von Mises Stress in the Bridge Girder due to Wind and current (1 Year Return Period)

A.20 Wind and current (100 Year Return Period)

X-component of Displacement

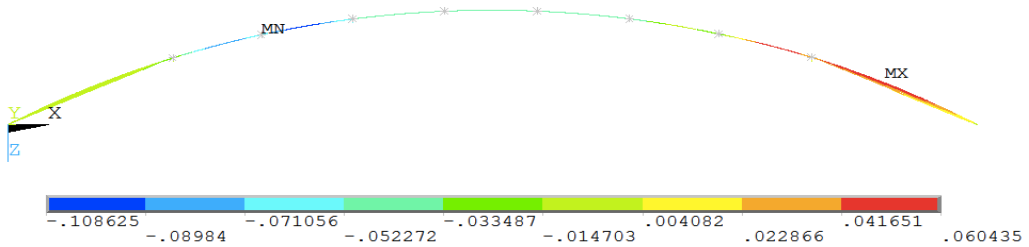


Figure A.133: X-component of Displacement in the Bridge Girder due to Wind and current (100 Year Return Period)

Y-component of Displacement

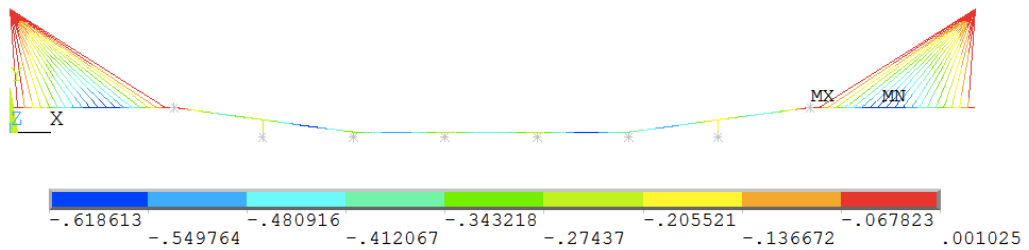


Figure A.134: Y-component of Displacement in the Bridge Girder due to Wind and current (100 Year Return Period)

Z-component of Displacement

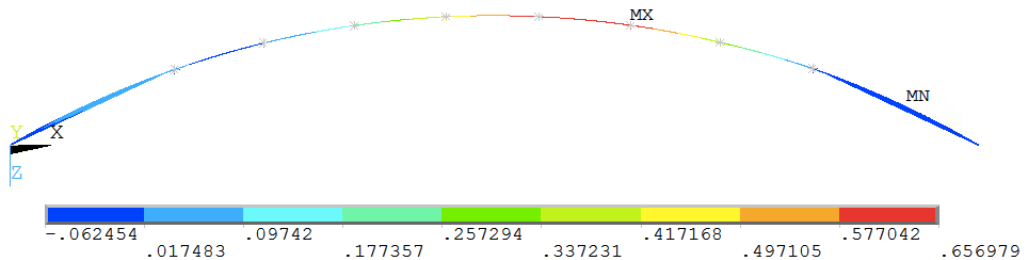


Figure A.135: Z-component of Displacement in the Bridge Girder due to Wind and current (100 Year Return Period)

X-component of Rotation

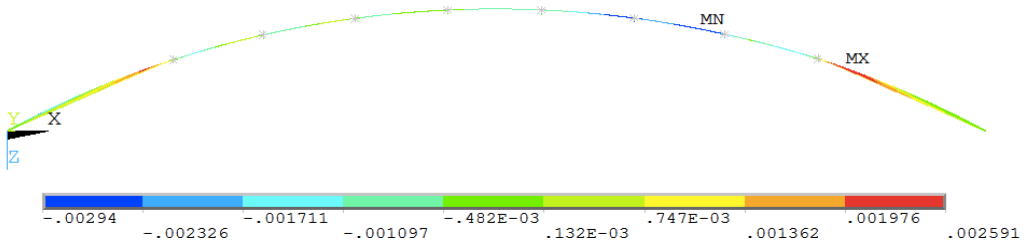


Figure A.136: X-component of Rotation in the Bridge Girder due to Wind and current (100 Year Return Period)

Y-component of Rotation

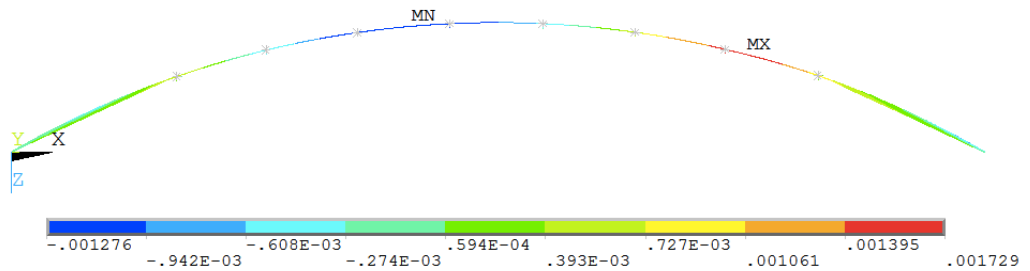


Figure A.137: Y-component of Rotation in the Bridge Girder due to Wind and current (100 Year Return Period)

Z-component of Rotation

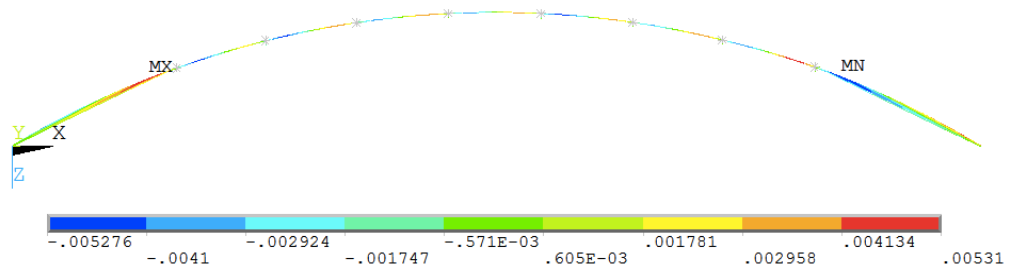


Figure A.138: Z-component of Rotation in the Bridge Girder due to Wind and current (100 Year Return Period)

Global Bending Moment M_X

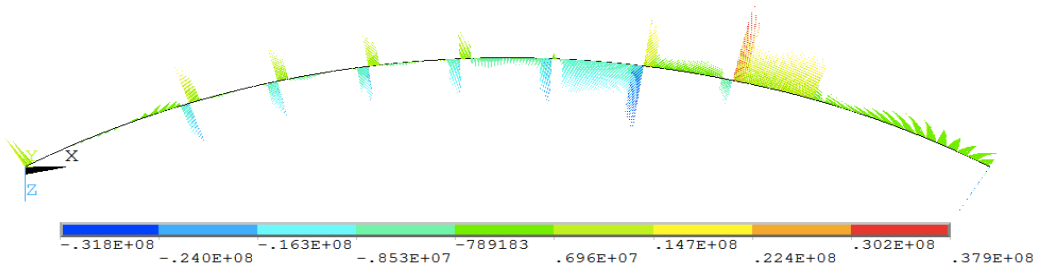


Figure A.139: Global Bending Moment M_X in the Bridge Girder due to Wind and current (100 Year Return Period)

Global Bending Moment M_Y

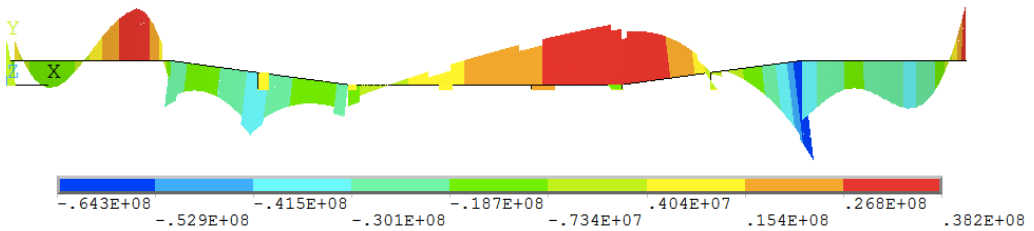


Figure A.140: Global Bending Moment M_Y in the Bridge Girder due to Wind and current (100 Year Return Period)

Global Bending Moment M_Z

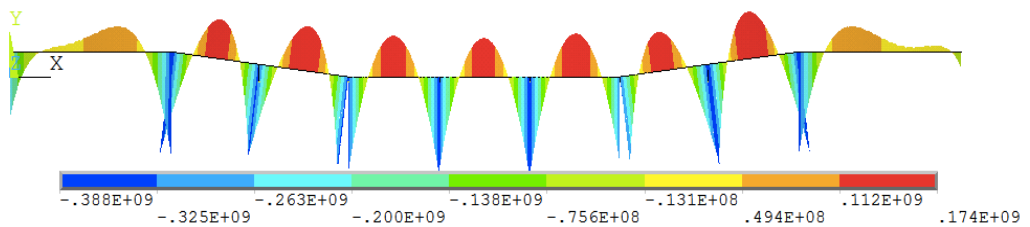


Figure A.141: Global Bending Moment M_Z in the Bridge Girder due to Wind and current (100 Year Return Period)

Global Shear Force V_y

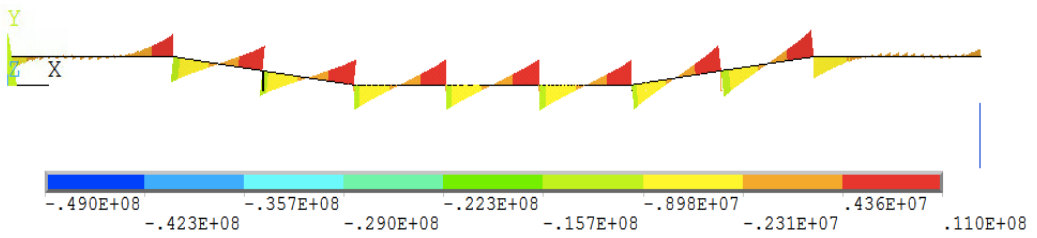


Figure A.142: Global Shear Force V_y in the Bridge Girder due to Wind and current (100 Year Return Period)

Global Shear Force V_z

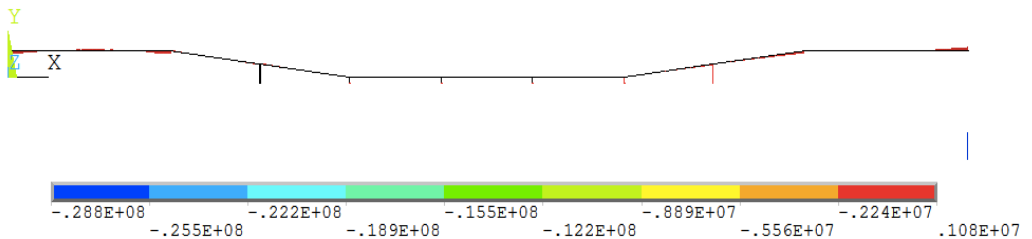


Figure A.143: Global Shear Force V_z in the Bridge Girder due to Wind and current (100 Year Return Period)

Global Von Mises Stress

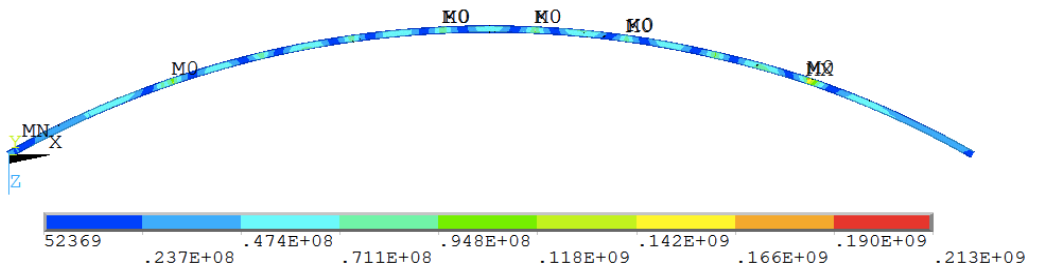


Figure A.144: Global Von Mises Stress in the Bridge Girder due to Wind and current (100 Year Return Period)

A.21 Low Tide

X-component of Displacement

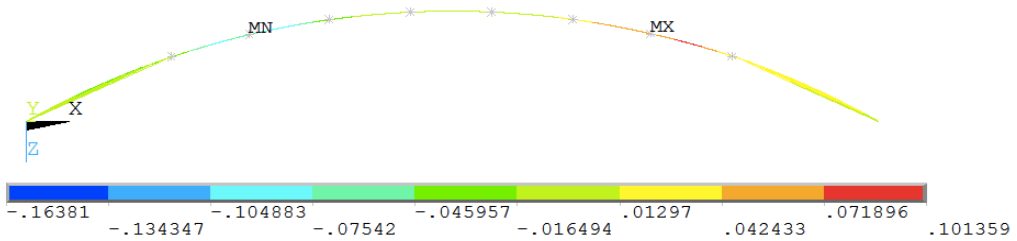


Figure A.145: X-component of Displacement in the Bridge Girder due to Low Tide

Y-component of Displacement

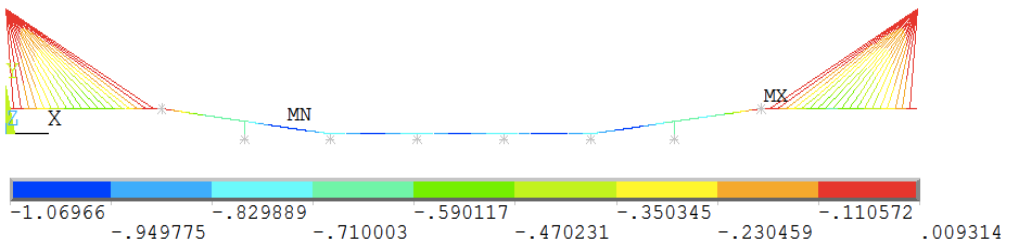


Figure A.146: Y-component of Displacement in the Bridge Girder due to Low Tide

Z-component of Displacement

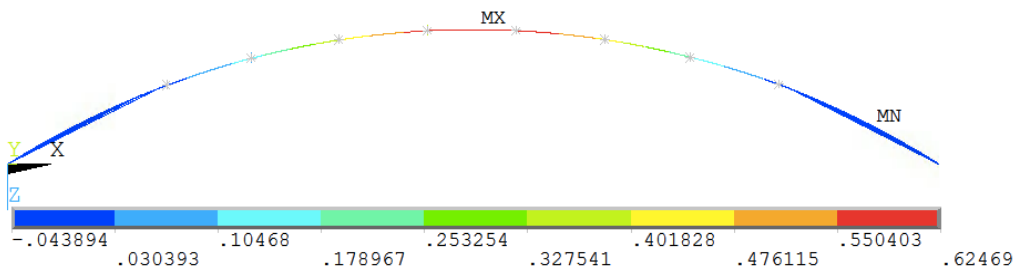


Figure A.147: Z-component of Displacement in the Bridge Girder due to Low Tide

X-component of Rotation

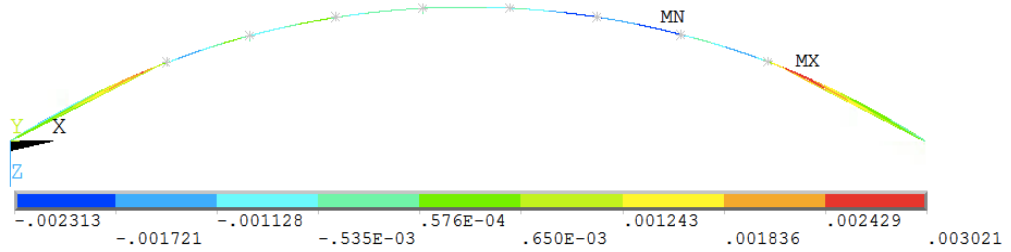


Figure A.148: X-component of Rotation in the Bridge Girder due to Low Tide

Y-component of Rotation

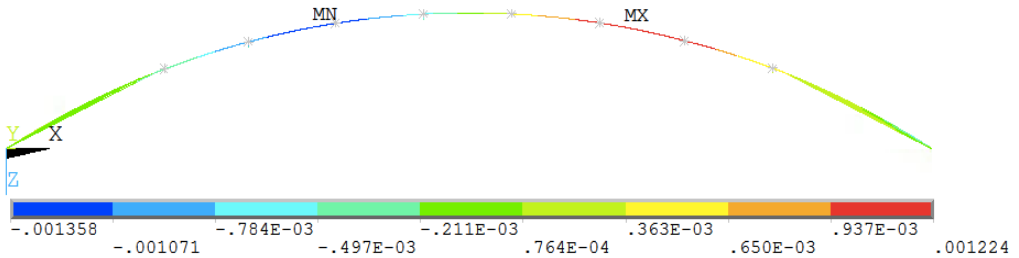


Figure A.149: Y-component of Rotation in the Bridge Girder due to Low Tide

Z-component of Rotation

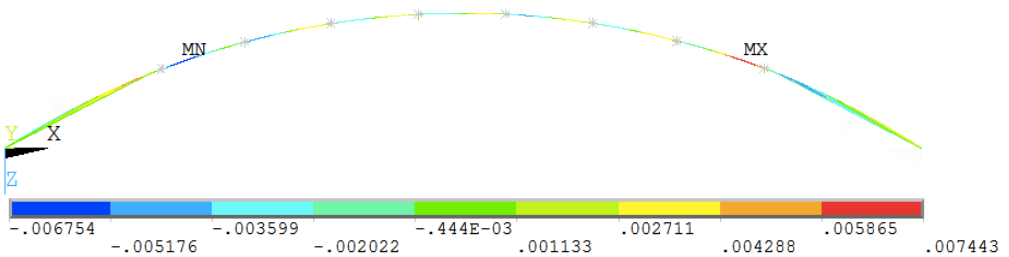


Figure A.150: Z-component of Rotation in the Bridge Girder due to Low Tide

Global Bending Moment M_X

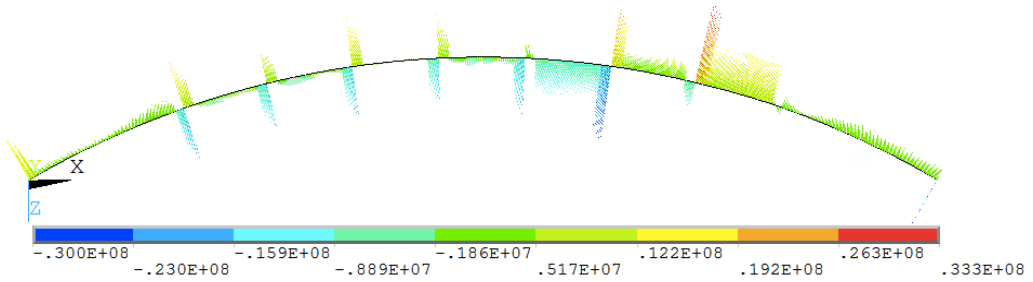


Figure A.151: Global Bending Moment M_X in the Bridge Girder due to Low Tide

Global Bending Moment M_Y

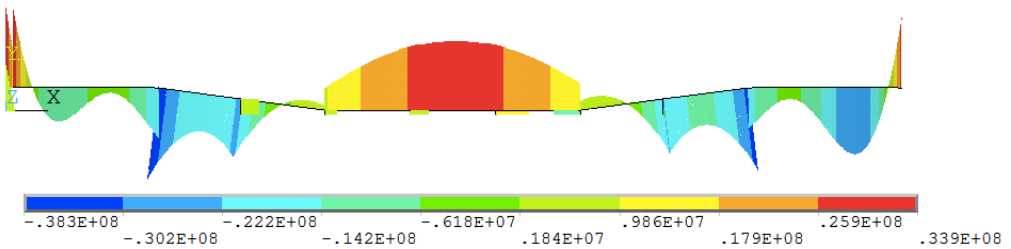


Figure A.152: Global Bending Moment M_Y in the Bridge Girder due to Low Tide

Global Bending Moment M_Z

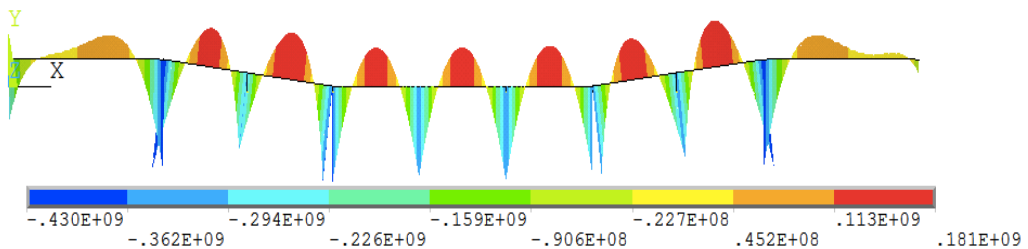


Figure A.153: Global Bending Moment M_Z in the Bridge Girder due to Low Tide

Global Shear Force V_y

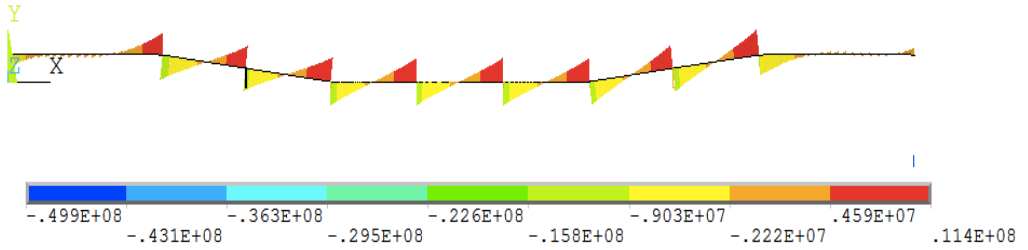


Figure A.154: Global Shear Force V_y in the Bridge Girder due to Low Tide

Global Shear Force V_z

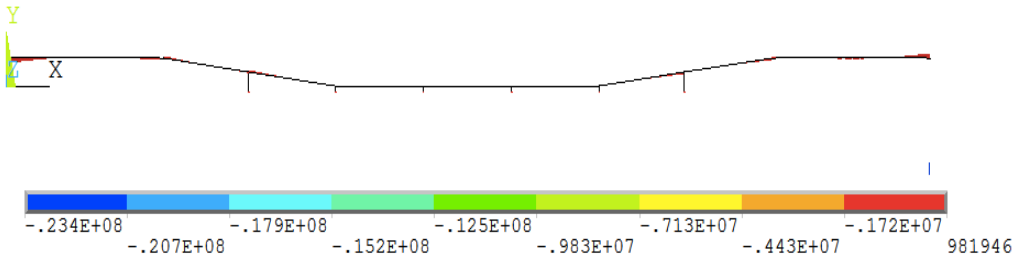


Figure A.155: Global Shear Force V_z in the Bridge Girder due to Low Tide

Global Von Mises Stress

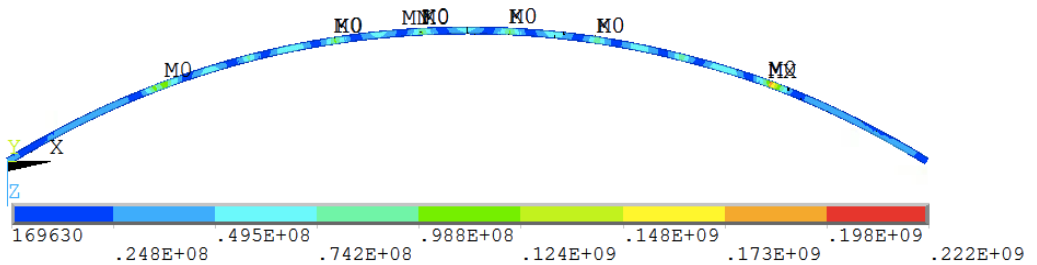


Figure A.156: Global Von Mises Stress in the Bridge Girder due to Low Tide

A.22 High Tide

X-component of Displacement

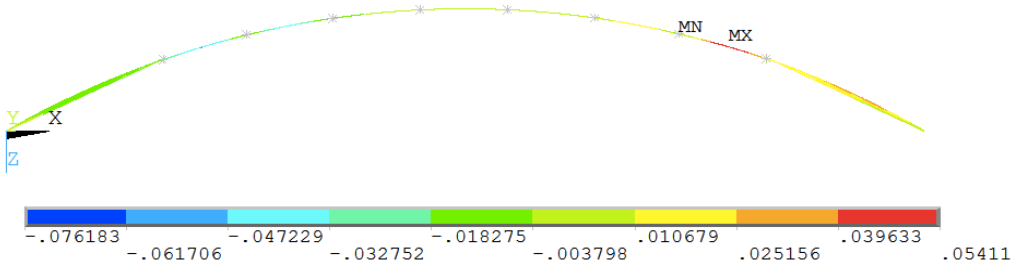


Figure A.157: X-component of Displacement in the Bridge Girder due to High Tide

Y-component of Displacement

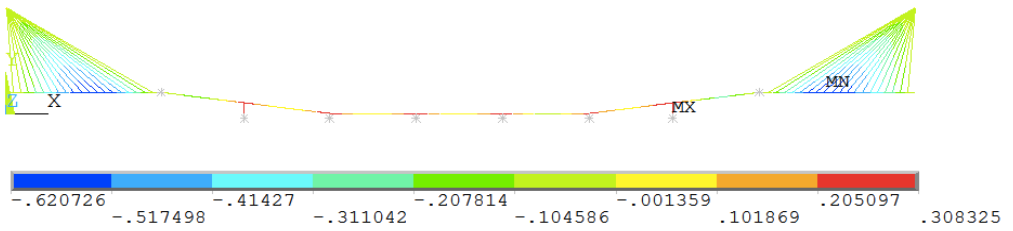


Figure A.158: Y-component of Displacement in the Bridge Girder due to High Tide

Z-component of Displacement

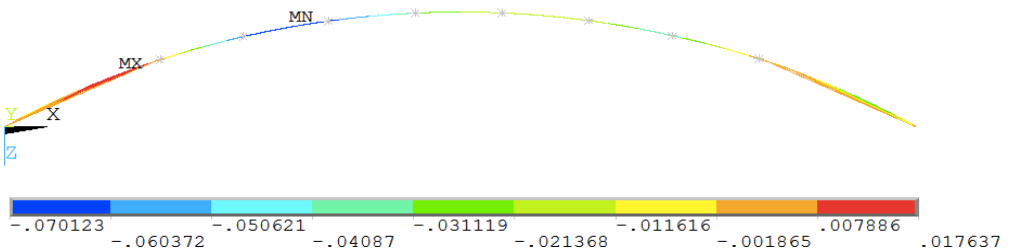


Figure A.159: Z-component of Displacement in the Bridge Girder due to High Tide

X-component of Rotation

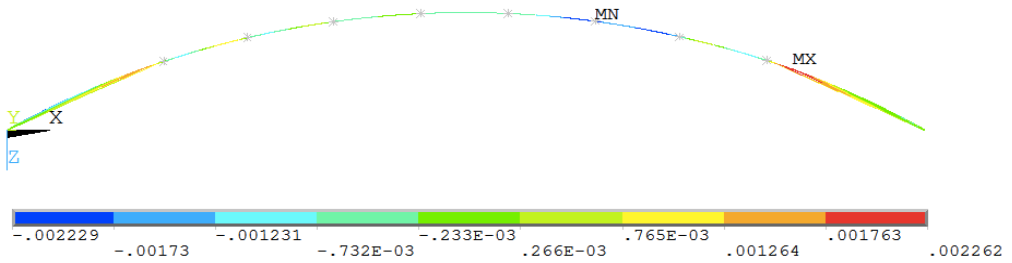


Figure A.160: X-component of Rotation in the Bridge Girder due to High Tide

Y-component of Rotation

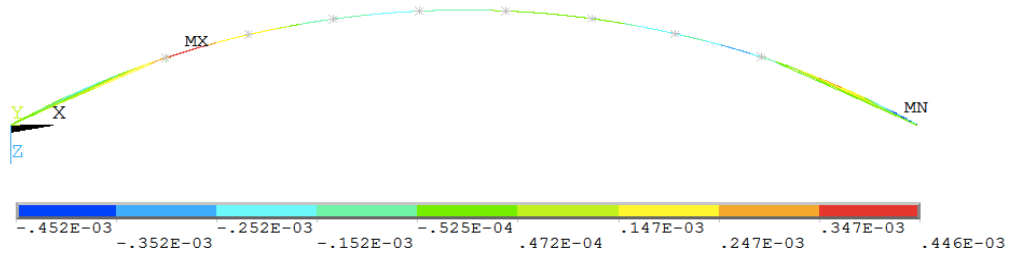


Figure A.161: Y-component of Rotation in the Bridge Girder due to High Tide

Z-component of Rotation

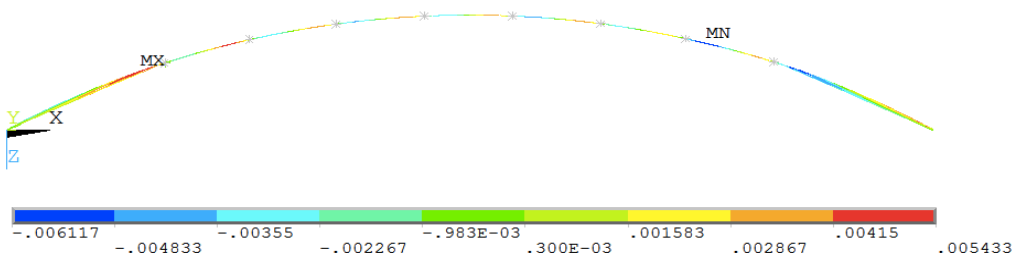


Figure A.162: Z-component of Rotation in the Bridge Girder due to High Tide

Global Bending Moment M_X

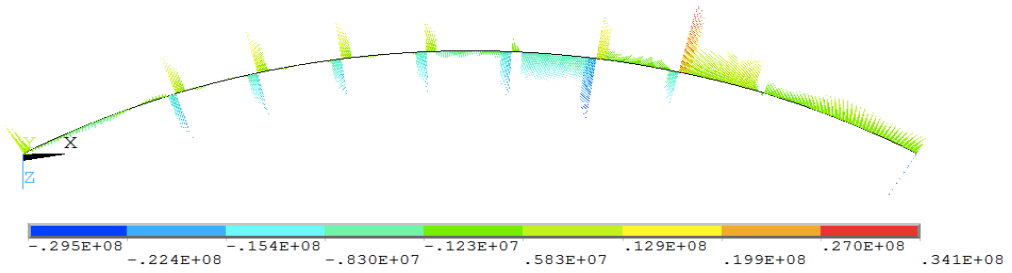


Figure A.163: Global Bending Moment M_X in the Bridge Girder due to High Tide

Global Bending Moment M_Y

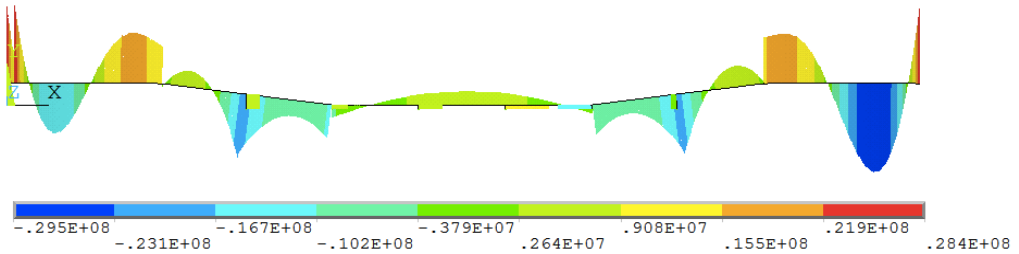


Figure A.164: Global Bending Moment M_Y in the Bridge Girder due to High Tide

Global Bending Moment M_Z

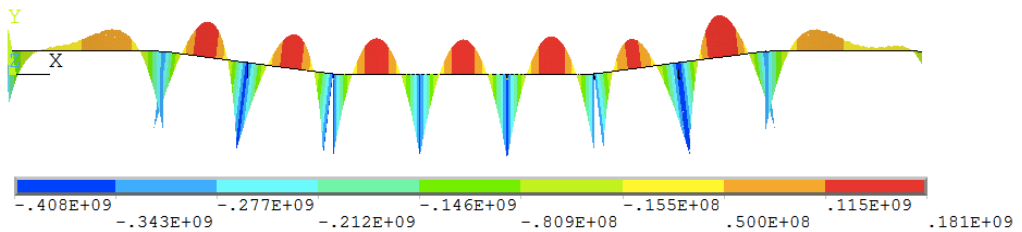


Figure A.165: Global Bending Moment M_Z in the Bridge Girder due to High Tide

Global Shear Force V_Y

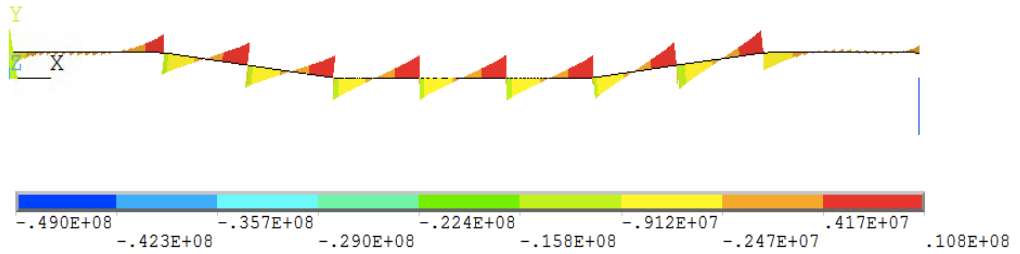


Figure A.166: Global Shear Force V_y in the Bridge Girder due to High Tide

Global Shear Force V_Z

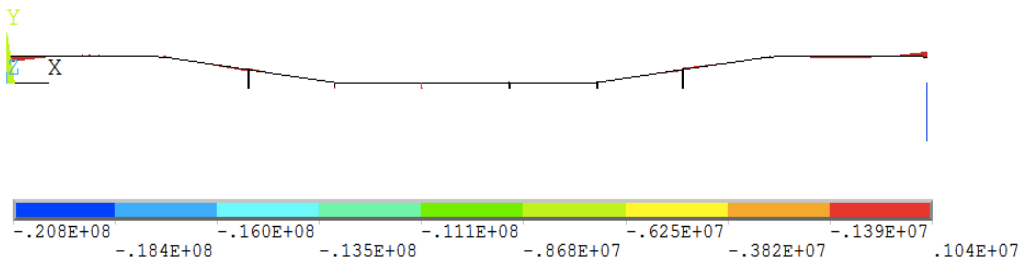


Figure A.167: Global Shear Force V_z in the Bridge Girder due to High Tide

Global Von Mises Stress

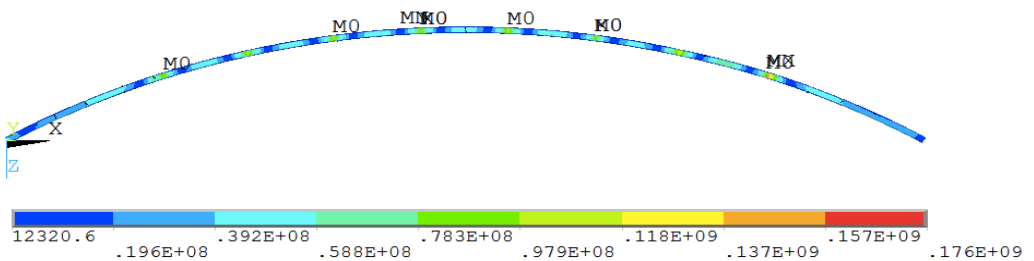


Figure A.168: Global Von Mises Stress in the Bridge Girder due to High Tide

A.23 Effect of Including High Bridge - Additional Plots

Global Displacements

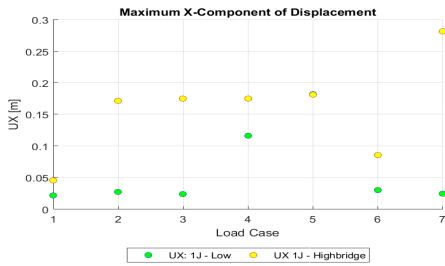


Figure A.169: Comparison of global rotations about the global x-axis for the I-jacket concept

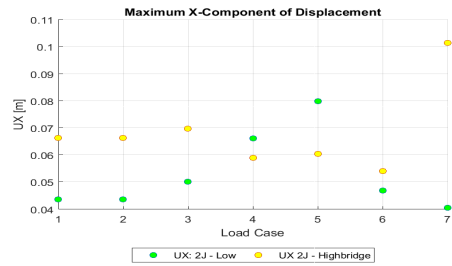


Figure A.170: Comparison of global rotations about the global x-axis for the II-jacket concept

Global Rotations

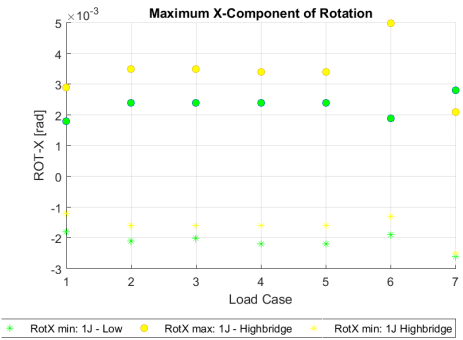


Figure A.171: Comparison of global rotations about the global x-axis for the I-jacket concept

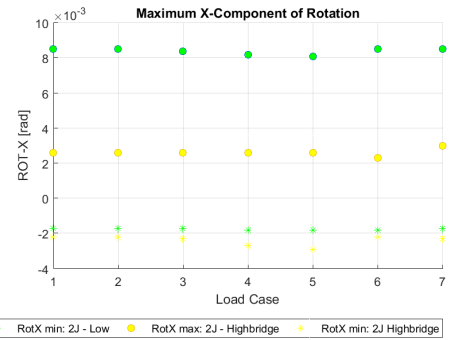


Figure A.172: Comparison of global rotations about the global x-axis for the II-jacket concept

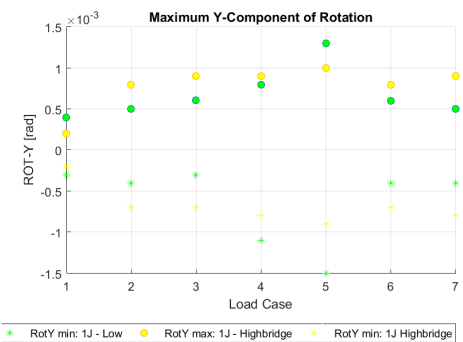


Figure A.173: Comparison of global rotations about the global y-axis for the I-jacket concept

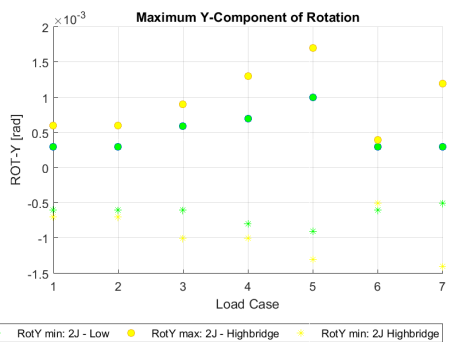


Figure A.174: Comparison of global rotations about the global y-axis for the II-jacket concept

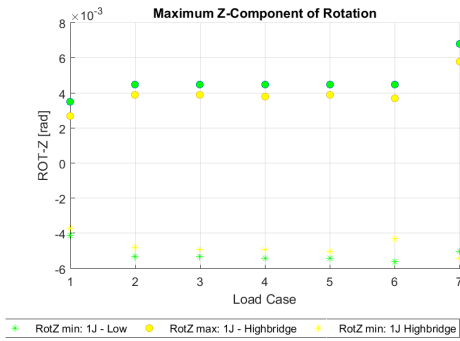


Figure A.175: Comparison of global rotations about the global z-axis for the I-jacket concept

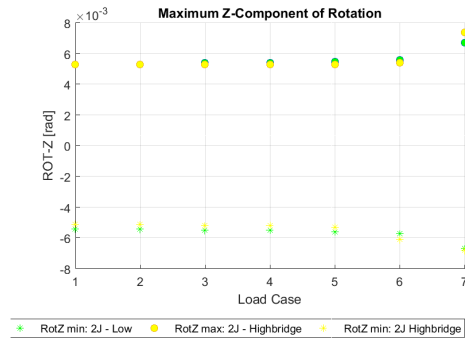


Figure A.176: Comparison of global rotations about the global z-axis for the II-jacket concept

Global Bending Moments

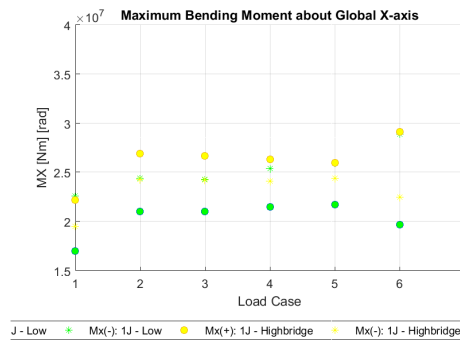


Figure A.177: Comparison of maximum and minimum global bending moment M_x for the I-jacket concept

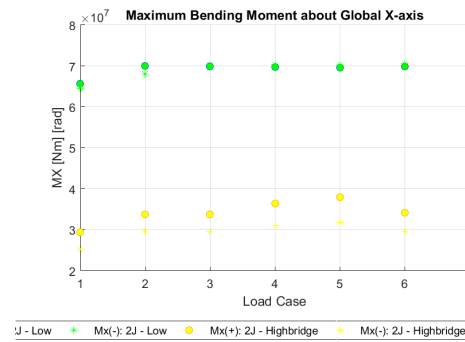


Figure A.178: Comparison of maximum and minimum global bending moment M_x for the II-jacket concept

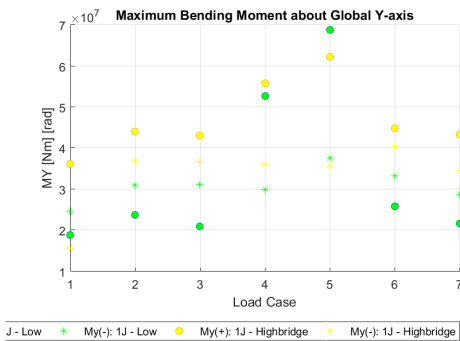


Figure A.179: Comparison of maximum and minimum global bending moment M_y for the I-jacket concept

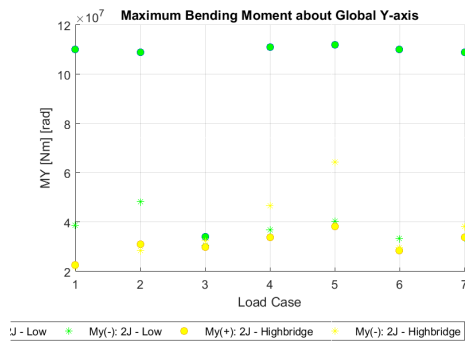


Figure A.180: Comparison of maximum and minimum global bending moment M_y for the II-jacket concept

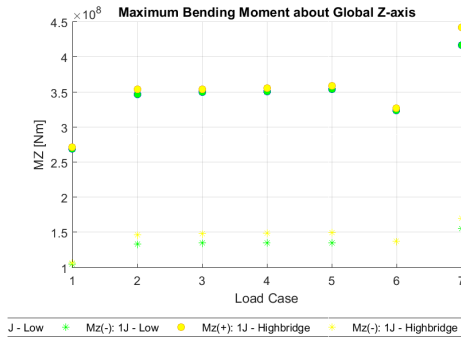


Figure A.181: Comparison of maximum and minimum global bending moment M_z for the I-jacket concept

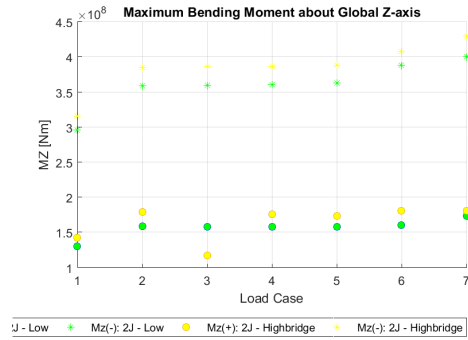


Figure A.182: Comparison of maximum and minimum global bending moment M_z for the II-jacket concept

A.24 Modal Analysis

A.24.1 I-Jacket: Modeshape 11-30

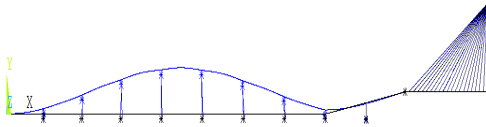


Figure A.183: Mode 11: Vertical, $T = 5.80$ s

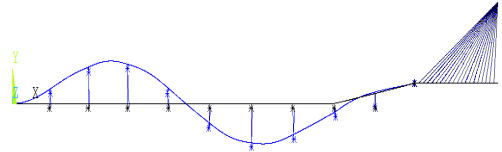


Figure A.184: Mode 12: Vertical, $T = 5.78$ s

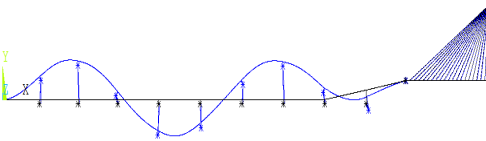


Figure A.185: Mode 13: Vertical, $T = 5.71$ s

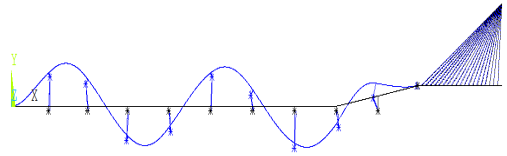


Figure A.186: Mode 14: Vertical, $T = 5.53$ s

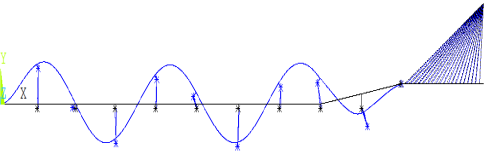


Figure A.187: Mode 15: Vertical, $T = 5.24$ s

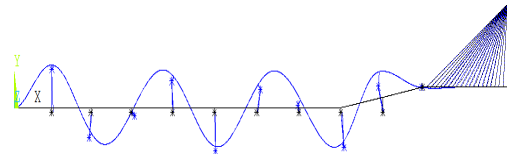


Figure A.188: Mode 16: Vertical, $T = 4.86$ s

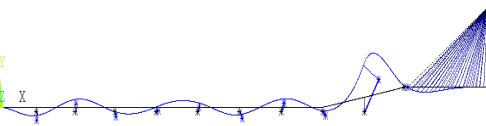


Figure A.189: Mode 17: Vertical, $T = 4.60$ s

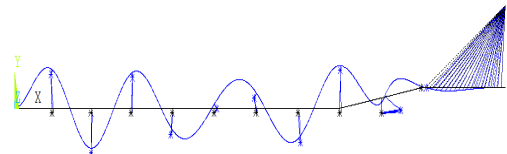


Figure A.190: Mode 18: Vertical, $T = 4.48$ s

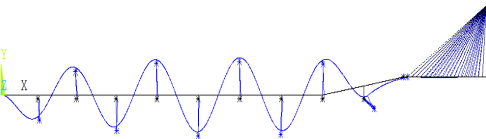


Figure A.191: Mode 19: Vertical, $T = 4.25$ s

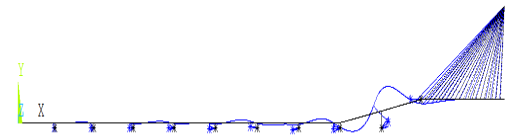


Figure A.192: Mode 20: Vertical, $T = 3.68$ s

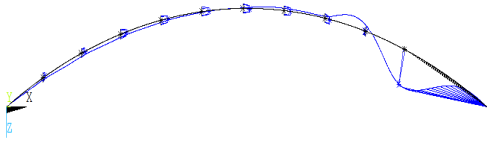


Figure A.193: Mode 21: Horizontal, $T = 2.87$ s

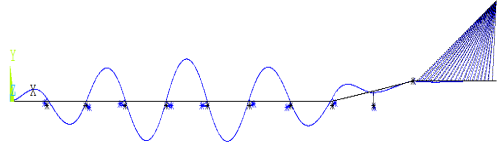


Figure A.194: Mode 22: Vertical, $T = 2.29$ s

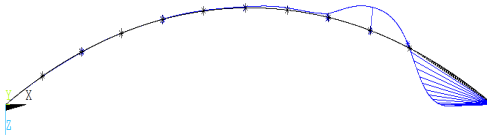


Figure A.195: Mode 23: Horizontal, $T = 2.20$ s

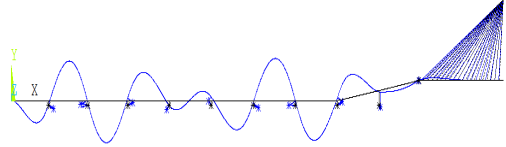


Figure A.196: Mode 24: Vertical, $T = 2.09$ s

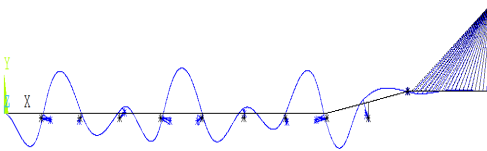


Figure A.197: Mode 25: Vertical, $T = 1.91$ s

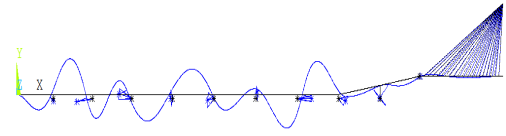


Figure A.198: Mode 26: Vertical, $T = 1.85$ s

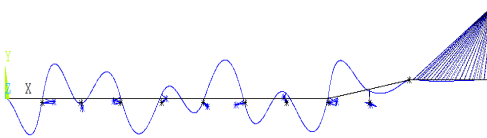


Figure A.199: Mode 27: Vertical, $T = 1.73$ s

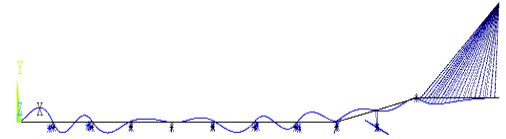


Figure A.200: Mode 28: Vertical, $T = 1.71$ s

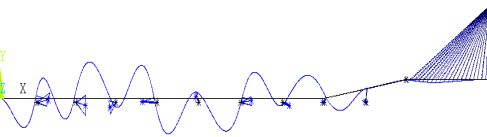


Figure A.201: Mode 29: Vertical, $T = 1.61$ s

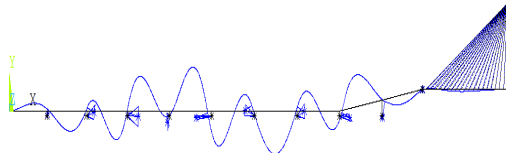
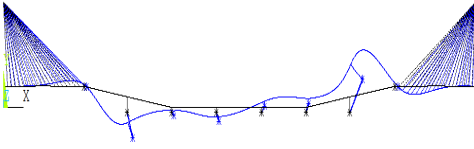
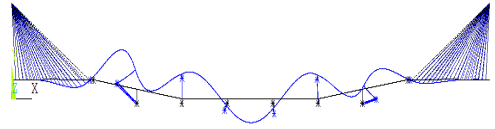
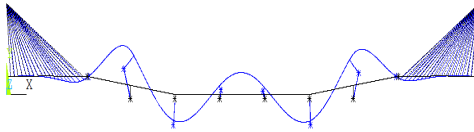
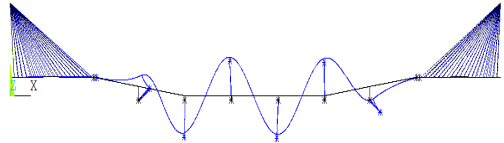
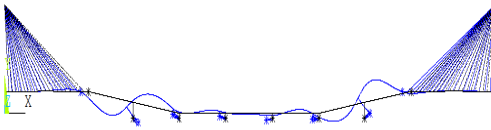
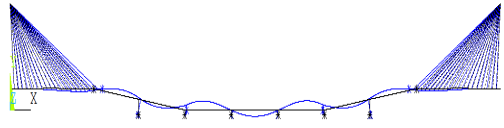
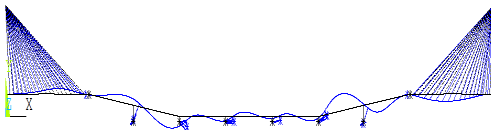
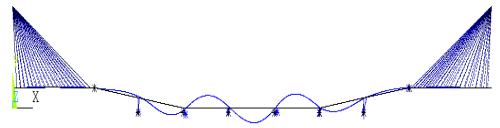
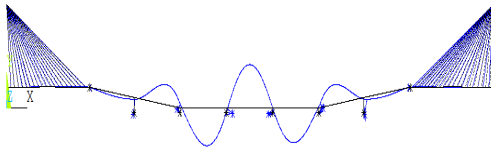
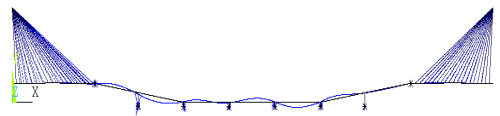


Figure A.202: Mode 30: Vertical, $T = 1.61$ s

A.24.2 II-Jacket: Modeshape 11-30

Figure A.203: Mode 11: Vertical, $T = 5.21$ sFigure A.204: Mode 12: Vertical, $T = 4.99$ sFigure A.205: Mode 13: Vertical, $T = 4.96$ sFigure A.206: Mode 14: Vertical, $T = 4.56$ sFigure A.207: Mode 15: Vertical, $T = 3.91$ sFigure A.208: Mode 16: Vertical, $T = 3.22$ sFigure A.209: Mode 17: Vertical, $T = 2.69$ sFigure A.210: Mode 18: Vertical, $T = 2.51$ sFigure A.211: Mode 19: Vertical, $T = 2.44$ sFigure A.212: Mode 20: Vertical, $T = 2.22$ s

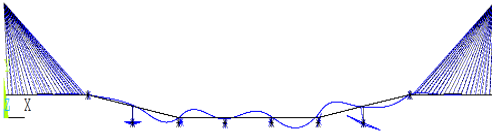


Figure A.213: Mode 21: Vertical, $T = 2.11$ s

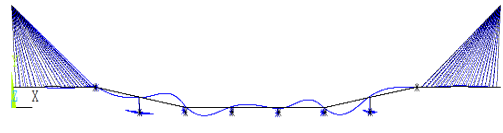


Figure A.214: Mode 22: Vertical, $T = 2.08$ s

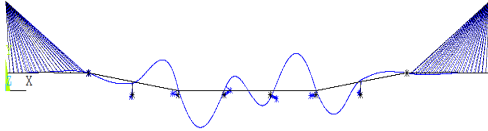


Figure A.215: Mode 23: Vertical $T = 2.01$ s

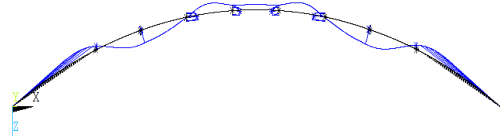


Figure A.216: Mode 24: Horizontal, $T = 1.84$ s

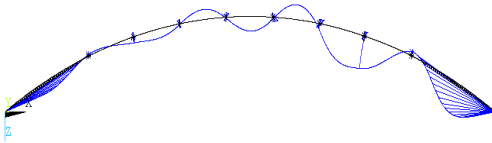


Figure A.217: Mode 25: Horizontal, $T = 1.63$ s

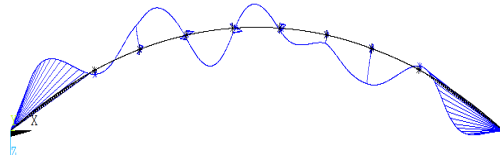


Figure A.218: Mode 26: Horizontal, $T = 1.56$ s

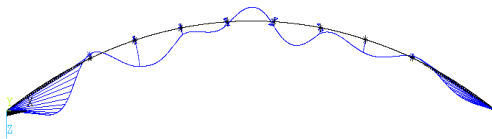


Figure A.219: Mode 27: Horizontal, $T = 1.48$ s

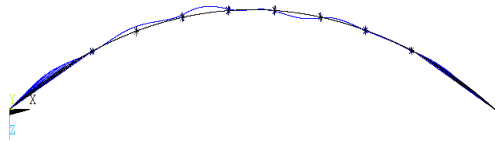


Figure A.220: Mode 28: Horizontal, $T = 1.39$ s

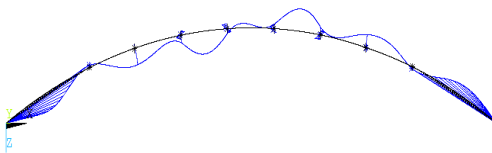


Figure A.221: Mode 29: Horizontal, $T = 1.38$ s

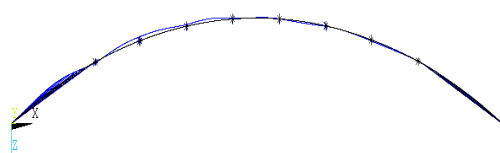


Figure A.222: Mode 30: Horizontal, $T = 1.35$ s

A.25 Coincidence with wave periods

A.25.1 Coincidence with wave periods for mode 1-30 (I-Jacket)

SET	FREQUENCY	PERIOD	Locally Wind Generated Sea									Swell		
			Z70			Z25/315			0/180			Z50-Z90		
			1 year	100 year	10 000 year	1 year	100 year	10 000 year	1 year	100 year	10 000 year	1 year	100 year	10 000 year
			[Hz]	[s]	≤5	≤6	≤7	≤5	≤6	≤7	≤5	≤6	≤7	6-18
1	1.23E-02	81.21	81.21	81.21	81.21	81.21	81.21	81.21	81.21	81.21	81.21	81.21	81.21	81.21
2	2.18E-02	45.86	45.86	45.86	45.86	45.86	45.86	45.86	45.86	45.86	45.86	45.86	45.86	45.86
3	3.90E-02	25.67	25.67	25.67	25.67	25.67	25.67	25.67	25.67	25.67	25.67	25.67	25.67	25.67
4	4.84E-02	20.67	20.67	20.67	20.67	20.67	20.67	20.67	20.67	20.67	20.67	20.67	20.67	20.67
5	5.88E-02	17.00	17.00	17.00	17.00	17.00	17.00	17.00	17.00	17.00	17.00	17.00	17.00	17.00
6	7.80E-02	12.81	12.81	12.81	12.81	12.81	12.81	12.81	12.81	12.81	12.81	12.81	12.81	12.81
7	0.10097	9.90	9.90	9.90	9.90	9.90	9.90	9.90	9.90	9.90	9.90	9.90	9.90	9.90
8	0.12452	8.03	8.03	8.03	8.03	8.03	8.03	8.03	8.03	8.03	8.03	8.03	8.03	8.03
9	0.14188	7.05	7.05	7.05	7.05	7.05	7.05	7.05	7.05	7.05	7.05	7.05	7.05	7.05
10	0.16828	5.94	5.94	5.94	5.94	5.94	5.94	5.94	5.94	5.94	5.94	5.94	5.94	5.94
11	0.17245	5.80	5.80	5.80	5.80	5.80	5.80	5.80	5.80	5.80	5.80	5.80	5.80	5.80
12	0.17299	5.78	5.78	5.78	5.78	5.78	5.78	5.78	5.78	5.78	5.78	5.78	5.78	5.78
13	0.17522	5.71	5.71	5.71	5.71	5.71	5.71	5.71	5.71	5.71	5.71	5.71	5.71	5.71
14	0.18078	5.53	5.53	5.53	5.53	5.53	5.53	5.53	5.53	5.53	5.53	5.53	5.53	5.53
15	0.19099	5.24	5.24	5.24	5.24	5.24	5.24	5.24	5.24	5.24	5.24	5.24	5.24	5.24
16	0.20577	4.86	4.86	4.86	4.86	4.86	4.86	4.86	4.86	4.86	4.86	4.86	4.86	4.86
17	0.21756	4.60	4.60	4.60	4.60	4.60	4.60	4.60	4.60	4.60	4.60	4.60	4.60	4.60
18	0.22341	4.48	4.48	4.48	4.48	4.48	4.48	4.48	4.48	4.48	4.48	4.48	4.48	4.48
19	0.2351	4.25	4.25	4.25	4.25	4.25	4.25	4.25	4.25	4.25	4.25	4.25	4.25	4.25
20	0.27167	3.68	3.68	3.68	3.68	3.68	3.68	3.68	3.68	3.68	3.68	3.68	3.68	3.68
21	0.34903	2.87	2.87	2.87	2.87	2.87	2.87	2.87	2.87	2.87	2.87	2.87	2.87	2.87
22	0.43631	2.29	2.29	2.29	2.29	2.29	2.29	2.29	2.29	2.29	2.29	2.29	2.29	2.29
23	0.45414	2.20	2.20	2.20	2.20	2.20	2.20	2.20	2.20	2.20	2.20	2.20	2.20	2.20
24	0.47787	2.09	2.09	2.09	2.09	2.09	2.09	2.09	2.09	2.09	2.09	2.09	2.09	2.09
25	0.52489	1.91	1.91	1.91	1.91	1.91	1.91	1.91	1.91	1.91	1.91	1.91	1.91	1.91
26	0.54191	1.85	1.85	1.85	1.85	1.85	1.85	1.85	1.85	1.85	1.85	1.85	1.85	1.85
27	0.57883	1.73	1.73	1.73	1.73	1.73	1.73	1.73	1.73	1.73	1.73	1.73	1.73	1.73
28	0.58595	1.71	1.71	1.71	1.71	1.71	1.71	1.71	1.71	1.71	1.71	1.71	1.71	1.71
29	0.61946	1.61	1.61	1.61	1.61	1.61	1.61	1.61	1.61	1.61	1.61	1.61	1.61	1.61
30	0.62097	1.61	1.61	1.61	1.61	1.61	1.61	1.61	1.61	1.61	1.61	1.61	1.61	1.61

Figure A.223: Conditionally formatted values of eigenperiods coinciding with wave periods with 1, 100 and 10 000 years return period from locally wind generated sea and swell.

A.25.2 Coincidence with wave periods for mode 1-30 (II-Jacket)

SET	FREQ.	PERIOD	Locally Wind Generated Sea									Swell		
			270			225/315			0/180			250-290		
			1 year	100 year	10 000 year	1 year	100 year	10 000 year	1 year	100 year	10 000 year	1 year	100 year	10 000 year
	[Hz]	[s]	≤ 5	≤ 6	≤ 7	≤ 5	≤ 6	≤ 7	≤ 5	≤ 6	≤ 7	6-18	6-18	6-18
1	0.0183	54.55	5276	5276	5276	5276	5276	5276	5276	5276	5276	5276	5276	5276
2	0.0321	31.20	3127	3127	3127	3127	3127	3127	3127	3127	3127	3127	3127	3127
3	0.0416	24.02	2170	2170	2170	2170	2170	2170	2170	2170	2170	2170	2170	2170
4	0.0558	17.93	16.14	16.14	16.14	16.14	16.14	16.14	16.14	16.14	16.14	16.14	16.14	16.14
5	0.0793	12.62	11.09	11.09	11.09	11.09	11.09	11.09	11.09	11.09	11.09	11.09	11.09	11.09
6	0.1079	9.27	8.73	8.73	8.73	8.73	8.73	8.73	8.73	8.73	8.73	8.73	8.73	8.73
7	0.1563	6.40	5.83	5.83	5.83	5.83	5.83	5.83	5.83	5.83	5.83	5.83	5.83	5.83
8	0.1683	5.94	5.81	5.81	5.81	5.81	5.81	5.81	5.81	5.81	5.81	5.81	5.81	5.81
9	0.1730	5.78	5.70	5.70	5.70	5.70	5.70	5.70	5.70	5.70	5.70	5.70	5.70	5.70
10	0.1791	5.58	5.46	5.46	5.46	5.46	5.46	5.46	5.46	5.46	5.46	5.46	5.46	5.46
11	0.1920	5.21	5.06	5.06	5.06	5.06	5.06	5.06	5.06	5.06	5.06	5.06	5.06	5.06
12	0.2005	4.99	4.87	4.87	4.87	4.87	4.87	4.87	4.87	4.87	4.87	4.87	4.87	4.87
13	0.2017	4.96	4.65	4.65	4.65	4.65	4.65	4.65	4.65	4.65	4.65	4.65	4.65	4.65
14	0.2194	4.56	3.49	3.49	3.49	3.49	3.49	3.49	3.49	3.49	3.49	3.49	3.49	3.49
15	0.2557	3.91	2.80	2.80	2.80	2.80	2.80	2.80	2.80	2.80	2.80	2.80	2.80	2.80
16	0.3105	3.22	2.62	2.62	2.62	2.62	2.62	2.62	2.62	2.62	2.62	2.62	2.62	2.62
17	0.3720	2.69	2.32	2.32	2.32	2.32	2.32	2.32	2.32	2.32	2.32	2.32	2.32	2.32
18	0.3980	2.51	2.22	2.22	2.22	2.22	2.22	2.22	2.22	2.22	2.22	2.22	2.22	2.22
19	0.4095	2.44	2.04	2.04	2.04	2.04	2.04	2.04	2.04	2.04	2.04	2.04	2.04	2.04
20	0.4509	2.22	1.88	1.88	1.88	1.88	1.88	1.88	1.88	1.88	1.88	1.88	1.88	1.88
21	0.4740	2.11	1.81	1.81	1.81	1.81	1.81	1.81	1.81	1.81	1.81	1.81	1.81	1.81
22	0.4809	2.08	1.76	1.76	1.76	1.76	1.76	1.76	1.76	1.76	1.76	1.76	1.76	1.76
23	0.4986	2.01	1.57	1.57	1.57	1.57	1.57	1.57	1.57	1.57	1.57	1.57	1.57	1.57
24	0.5439	1.84	1.46	1.46	1.46	1.46	1.46	1.46	1.46	1.46	1.46	1.46	1.46	1.46
25	0.6118	1.63	1.37	1.37	1.37	1.37	1.37	1.37	1.37	1.37	1.37	1.37	1.37	1.37
26	0.6417	1.56	1.34	1.34	1.34	1.34	1.34	1.34	1.34	1.34	1.34	1.34	1.34	1.34
27	0.6747	1.48	1.31	1.31	1.31	1.31	1.31	1.31	1.31	1.31	1.31	1.31	1.31	1.31
28	0.7215	1.39	1.29	1.29	1.29	1.29	1.29	1.29	1.29	1.29	1.29	1.29	1.29	1.29
29	0.7258	1.38	1.24	1.24	1.24	1.24	1.24	1.24	1.24	1.24	1.24	1.24	1.24	1.24
30	0.7384	1.35	1.20	1.20	1.20	1.20	1.20	1.20	1.20	1.20	1.20	1.20	1.20	1.20

Figure A.224: Conditionally formatted values of eigenperiods coinciding with wave periods with 1, 100 and 10 000 years return period from locally wind generated sea and swell.

A.26 Regular Wave Analysis: Additional Bending Moment Result Plots

Wave Period $T = 5$ s

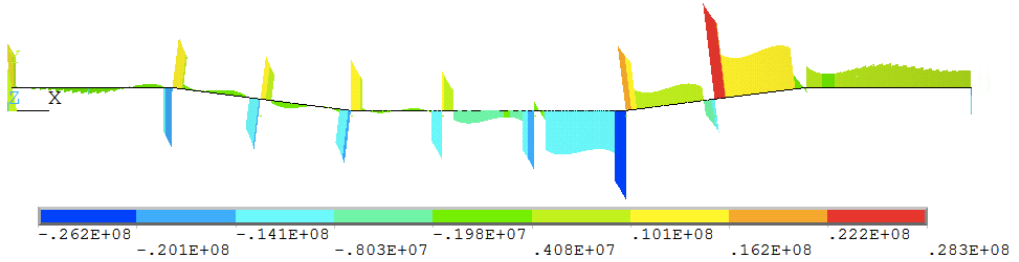


Figure A.225: Largest negative bending moment, M_x , at $T = 5$ s

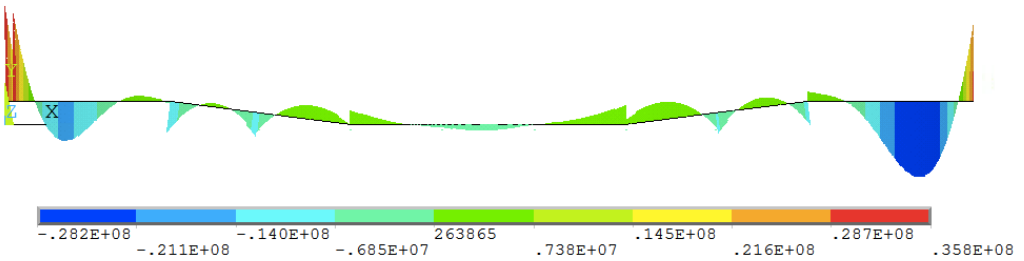


Figure A.226: Largest negative bending moment, M_y , at $T = 5$ s

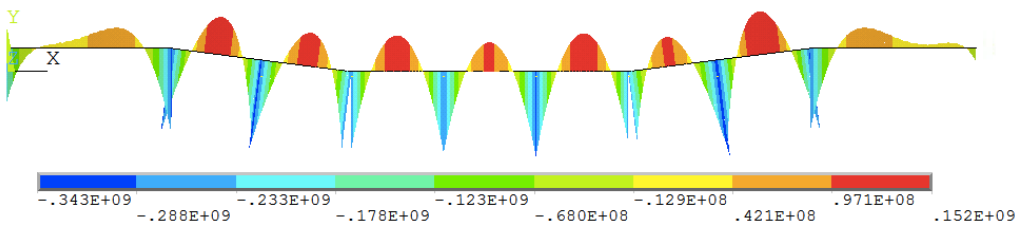


Figure A.227: Largest negative bending moment, M_z , at $T = 5$ s

Wave Period $T = 6$ s

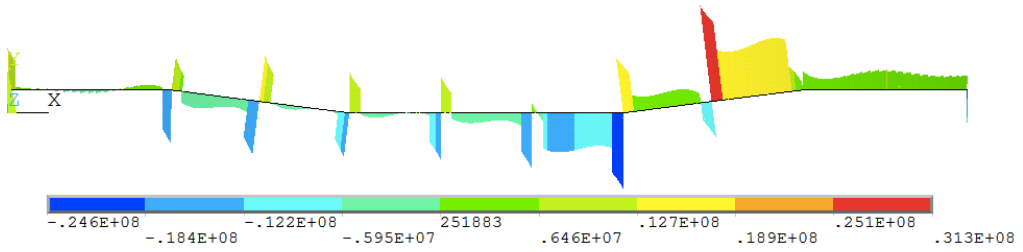


Figure A.228: Largest positive bending moment, M_x , at $T = 6$ s

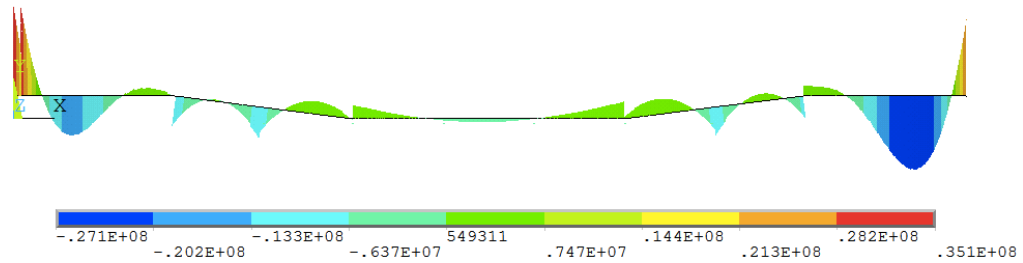


Figure A.229: Largest positive bending moment, M_y , at $T = 6$ s

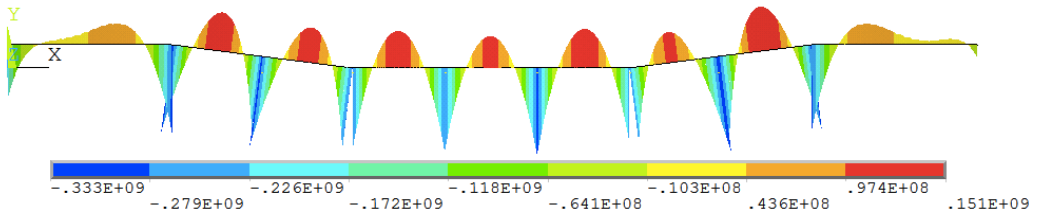


Figure A.230: Largest positive bending moment, M_z , at $T = 6$ s

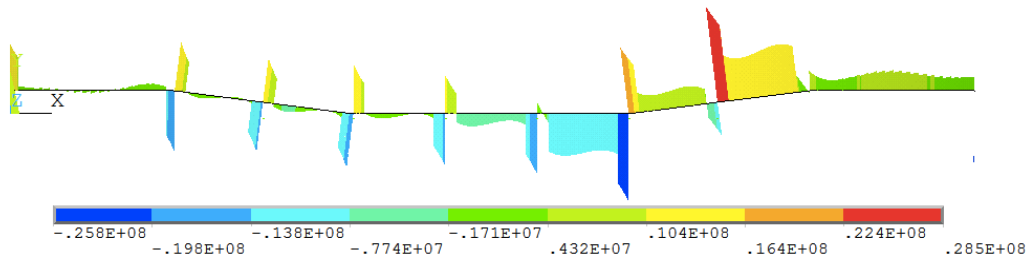


Figure A.231: Largest negative bending moment, M_x , at $T = 6$ s

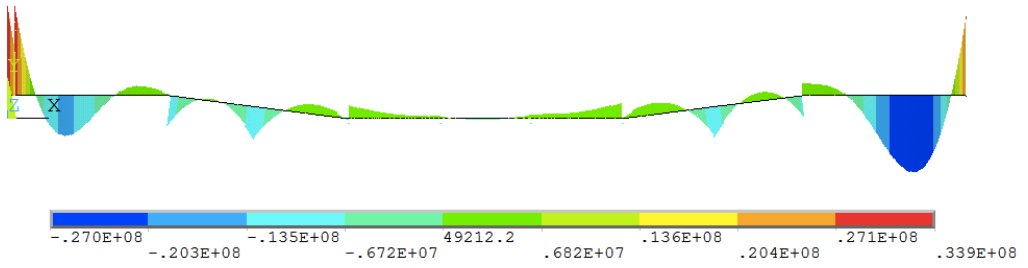


Figure A.232: Largest negative bending moment, M_y , at $T = 6$ s

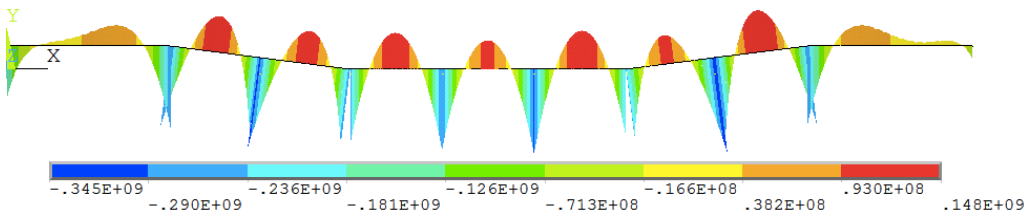


Figure A.233: Largest negative bending moment, M_z , at $T = 6$ s

A.27 Digital Appendix

The digital appendix includes:

ANSYS APDL and modeling files:

- Scripts as described in chapter 7 for concept 1 and concept 2 (*Digital_Appendix/ANSYS/*)
- Main scripts for postprocessing (*Digital_Appendix/ANSYS/Postprocessing*)
- Matlab scripts for calculations for static forces, regular wave forces and damping parameters. (*Digital_Appendix/ANSYS/MATLAB*)
- Calculations for delay (excel workbook *delay.xlsx*).

USFOS files:

- Control file (*head.dyn*)
- Model file (*stru-1_dyn.fem*)
- Animation of the collision (*animation.avi*)

